

# Stabilising Semiconducting Polymers Using Solid State Molecular Additives



**John Armitage**

Department of Physics

University of Cambridge

This dissertation is submitted for the degree of  
Doctor of Philosophy

Christ's College

February 2019



- The greatest enemy of knowledge is not ignorance, it is the illusion of knowledge.
  - Stephen Hawking

To Maria, for letting me live with my wife....

# Declaration

This dissertation is the result of my own work and includes nothing which is the outcome of work done in collaboration except as declared in the Preface and specified in the text. It is not substantially the same as any that I have submitted, or, is being concurrently submitted for a degree or diploma or other qualification at the University of Cambridge or any other University or similar institution except as declared in the Preface and specified in the text. I further state that no substantial part of my dissertation has already been submitted, or, is being concurrently submitted for any such degree, diploma or other qualification at the University of Cambridge or any other University or similar institution except as declared in the Preface and specified in the text. It does not exceed the prescribed word limit for the relevant Degree Committee.

Collaborators which have made specific contributions to this work include Iyad Nasrallah at Cambridge University (diF-TES ADT transistor measurements and arranging DFT simulations), Christian Bech Nielsen of University of London (synthesis of materials), Mahesh Kumar and Jean-Luc Bredas at King Abdullah University of Science and Technology (diF-TES ADT DFT simulations), Filipe Richeimer at National Physical Laboratory (scanning microscopy), Gosia Nguyen at Cambridge University (helped with device fabrication at end of PhD), Ian Jacobs at Cambridge University (Nuclear magnetic resonance analysis) and Dimitrios Simatos at Cambridge University along with the Chemistry department (Nuclear magnetic resonance measurements). Wherever these measurements and calculations are presented, they are clearly acknowledged in the corresponding figure captions.

John Armitage

February 2019

# Stabilising Semiconducting Polymers Using Solid State Molecular Additives

John William Armitage

## Abstract

Solution processed organic semiconductors contain extrinsic environmental species that cause device instabilities as they are difficult to remove during low temperature processing and are able to penetrate into organic electronics after fabrication. This dissertation is centered on the search for and development of solid state molecular additives to improve device stability associated with atmospheric defects in organic field effect transistors. To achieve this, an extended study was undertaken of the influence of over 95 different molecular additives expected to improve the stability characteristics of organic field effect transistors based on the literature.

This dissertation demonstrates that positive bias and light stress stability can be improved in both p-type diF-TES ADT and IDT-BT organic field effect transistors by incorporating solid state small molecular additives. Simulations predict that the additives improve stability by introducing a competitive recombination pathway in order to prevent the trapping of electrons in the LUMO of the semiconductor by atmospheric species. Improvements with the solid state molecular additives are achieved by controlling the LUMO and morphology of the additive polymer blend.

Secondly, improvements in the environmental and negative bias stress stability of organic field effect transistors are also observed with molecular additives. The solid state small molecular additives that significantly improve device characteristics are limited to a subset of molecules with similar structure to tetracyanoquinodimethane. It is demonstrated that this subset of solid state molecular additives correlates with a chemical reaction between the molecules and water. The chemical reaction appears to change the molecular additives into a new chemical species, plausibly consuming water,

modifying the pH and doping the semiconductor, resulting in improved organic field effect transistor characteristics.

Thirdly, machine learning techniques are used to accurately predict which solid state additives are capable of improving device performance. The machine learning algorithm uses neural passing networks for feature generation, due to its ability to capture physical plausible features such as functional groups. The algorithm screened over 1.5 billion molecular structures and found plausible molecular structures based on expert knowledge.

Fourthly, novel analogue neuromorphic computer architectures based on anti-ferromagnetic and analogue transistors are modeled. The proposed architecture presents both trainable anti-ferromagnetic based synapses for learning and non-trainable voltage controlled synapses for computationally demanding inferences. This dissertation suggests that combining both the fully controllable and trainable networks is a promising route forward for analog neuromorphic computers.

# Acknowledgements

First and foremost, I thank Professor Henning Sirringhaus for his supportive supervision, providing an impeccable research environment, demonstrating appropriate mannerisms when dealing with new ideas, helping me obtain funding for my PhD and most importantly taking a chance on me. I believe I have changed for the better due to your guidance, thanks.

Secondly, I would like to thank my funders Christ's College, FlexEnable and the Canadian Centennial Scholarship Fund for their financial support and for providing me with my industrial supervisor Jan Jongman. I would also like to express gratitude to my friends and colleagues for collaborating with me on this work: Dr. Iyad Nasrallah, Dr. Mark Nikolka, Dr. Leszek Spalek, Dr. Ian Jacobs, Dr. Guillaume Schweicher, Assistant Professor Mahesh Kumar, Professor Jean-Luc Bredas, Filipe Richeimer, Ivan Dimov, Malgorzata Nguyen and Dimitrios Simatos

I would like to thank the supporting staff Roger Beadle, Radoslav Chakalov, Thomas Sharp and Alex Crook for their constant practical knowledge of running a research lab. I would also like to thank Dr. Satyaprasad Senanayak and Dr. Moon Kang for letting me dabble in perovskite memristors and for discussing the future of neuromorphic computers respectively. I also greatly appreciate Dr. Jörg Wunderlich at the Hitachi Cambridge Laboratory and Dr. Deepak Venkateshvaran at Cambridge University for giving me the opportunity to work on analogue neuromorphic computers.

This work would not be possible without the continuous support from my parents Ian and Diana Armitage, my brothers Hugh and Grant Armitage, as well as my grandparents Pat and Bill Harris and Sheila and Frank Armitage. I would also like to thank my friends, if you ever read this you likely know who you are.

## Acknowledgements

---

Most importantly I would like to acknowledge my editor, and the reason I get out of bed in the morning, Mrs. Celia Charron, Senior Publishing Editor at the Royal Society of Chemistry and my wife.



# Contents

Declaration

Abstract

Contents

<b>1</b>	<b>Introduction</b>	<b>1</b>
1.1	Reliable organic electronics	1
1.2	Organic semiconductors	3
1.2.1	Charge transport	3
1.2.2	Doping in organic semiconductors	5
1.3	Thin film transistors	9
1.3.1	Architectures	9
1.3.2	Operation principles	10
1.4	Semiconductor stability	13
1.4.1	Deep traps	13
1.4.2	Redox reactions in organics	13
1.4.3	Mobile ionized water	16
1.4.4	Removal of atmospheric traps	18
1.5	Statistical experimental discovery	20
1.5.1	Vector representation of molecular structure	21
1.5.2	General insight for applying machine learning models	26
1.5.3	Applying machine learning to materials science	27
<b>2</b>	<b>Experimental methods</b>	<b>32</b>
2.1	Organic materials	32
2.1.1	Polymer semiconductors	32
2.1.2	Dielectrics	33

2.1.3	Molecular additives	34
2.2	Device fabrication procedures	36
2.2.1	Substrate cleaning	36
2.2.2	Photolithography for bottom contacts	36
2.2.3	Thin film fabrication	37
2.2.4	Transistor fabrication	38
2.3	Experimental characterization	38
2.3.1	Electrical characterization	38
2.3.2	Ultra violet to visible absorption spectroscopy	40
2.3.3	Charge accumulation spectroscopy	41
2.3.4	Nuclear magnetic resonance spectroscopy	45
2.3.5	Scanning probe microscopy	46
2.4	Statistical methods	46
2.4.1	Feature generation	46
2.4.2	Data used in machine learning	48
2.4.3	Predictive model generation	50
2.4.4	Database searching	53
<b>3</b>	<b>Searching for solid state additives</b>	<b>55</b>
3.1	Introduction	55
3.2	Searching for p-type solid state additives	56
3.3	Thermally stable carbon nanotube polymer blends	65
3.4	Discussion	66
<b>4</b>	<b>Understanding positive bias stress in organic semiconductors</b>	<b>68</b>
4.1	Introduction	68
4.2	Positive bias stress stability through molecular additives	69
4.2.1	Light stability in organic semiconductors	69
4.2.2	Improved PBS and NBS stability with small molecules	74

4.2.3	Solubility dependence of PBS	76
4.2.4	Spectroscopic behavior of IDT-BT films during PBS	80
4.3	Mobility of additives in IDT-BT	82
4.4	Proposed increased PBS with molecular additives	84
4.4.1	Additional chemical reactions	84
4.4.2	Trapping of electrons at TCNQ grain boundaries	85
4.4.3	Mobile ions	85
4.5	Molecular additive design rules for PBS	86
<b>5</b>	<b>The interaction of water and tetracyanoquinodimethane in OFETs</b>	<b>90</b>
5.1	Introduction	90
5.2	Adding water to solutions of IDT-BT with TCNQ	92
5.2.1	Improvement in OFETs with TCNQ and water	92
5.2.2	Spectroscopy of TCNQ water reactions	94
5.2.3	pH dependence of the TCNQ reaction	99
5.2.4	The relationship between pH of OSC in OFET and bias stability	100
5.3	Generality of the reaction	101
5.3.1	Solid state reactions of dopants in film	106
5.4	Implications	110
5.4.1	Consequences for doping additives	111
5.4.2	Consequences for non-doping reactive additives	111
5.4.3	Creating a robust stabilization additive	116
<b>6</b>	<b>Quantifying the search for molecular additives</b>	<b>118</b>
6.1	Introduction	118
6.2	Additive dataset	119
6.3	Feature and model selection	120
6.4	Predicting new chemical structures	125
6.5	Augmenting the search for additives	129

<b>7</b>	<b>Antiferromagnetics for analogue neuromorphic computing</b>	<b>131</b>
7.1	Introduction to analogue neuromorphic computing	131
7.2	Biological and artificial neurons	133
7.2.1	Neuron biology	133
7.2.2	Artificial neurons	134
7.2.3	Artificial neural networks	135
7.2.4	Learning paradigms	138
7.2.5	Summary	140
7.3	Analogue synapses	140
7.4	Antiferromagnetic counters	143
7.5	Methods	145
7.5.1	How learning occurs in memristor analogue computers	145
7.5.2	Modeling AFM counters	147
7.5.3	Circuit modeling	147
7.6	AFM synapse simulations	149
7.6.1	Simulating spike time dependent plasticity	149
7.6.2	Multilayer spiking rate networks	151
7.7	Conclusions and outlook of analogue neuromorphic computers	153
<b>8</b>	<b>Conclusion and outlook</b>	<b>156</b>
	<b>Appendix A</b>	<b>159</b>
	A.1 Minimum and maximum equivalence of Kullback-Leibler divergence and evidence lower bound	159
	<b>References</b>	<b>161</b>

# 1 Introduction

## 1.1 Reliable organic electronics

The field of organic electronics was initiated by a single event in 1977, the discovery of a highly conductive organic polymer, polyacetylene, which won Alan MacDiarmid, Alan Heeger and Hideki Shirakawa the Nobel prize in chemistry in 2000[1]. This discovery sparked the imaginations of scientists who developed a whole new field of electronics in which structural, optical, thermal, electrical, chemical and mechanical properties of materials could be adjusted due to the practically infinite chemical space. The promise of these electronics to date has not been fully realized but the field of organic electronics continues to be exciting as there is continuous improvement with no clear limitation on organic electronic properties.

To date, the most prolific use of organic electronics is based on the discovery of their electroluminescence properties in the 1990s, enabling a generation of organic light emitting diodes (OLEDs) used in large area displays. Organic small molecules are well suited for light emitting diodes as their tunable properties allow for the emission of a wider range of colors. This controllability of the optical phenomena of organic semiconductors (OSCs) has inspired a generation of printable organic solar panels with unique solution processing and flexible characteristics allowing for the integration of solar panels into novel products. The continuous increase in mobilities of OSCs even in highly amorphous polymer systems provides a promising way forward to fabricate printable shatterproof displays using uniform amorphous polymer OSCs, such as indacenodithiophene-co-benzothiadiazole (IDT-BT), as the semiconductor component in organic thin film field effect transistors (OFETs) such as backplane transistors as well as logic, amplifiers and sensors in applications such as smart packaging. The application of OFETs as amplifiers and sensors in biomedical implants is extremely promising especially for brain-computer interfaces because the uniquely soft mechanical characteristics of organic materials are essential for implants as scar tissue forms around stiff materials, forming an insulating barrier. Other promising applications of OSCs include thermoelectric applications where the low thermal conductivity, flexibility

and simple solution processing of OSCs could enable the production of cost effective devices capturing waste heat from hot water pipes in factories.

As the relevant organic semiconductor properties for practical device applications are incrementally improving, the problem of poor stability due to extrinsic environmental species becomes increasingly relevant. This poor stability is a major problem even in industrial organic semiconductor processes when fabricating OLEDs and other large area semiconductors such as amorphous and poly silicon, oxide, and perovskites semiconductors[2]–[4]. It is extremely difficult to continuously prevent the penetration of species and mitigate their damaging effects in low temperature processes. It is necessary to mitigate the damage caused by atmospheric contamination to realize roll-to-roll printing of organic electronic devices at low temperature in atmosphere. The work presented in this thesis is centered on the search and development of solid state molecular additives to improve device stability associated with atmospheric defects in OFETs using the highly amorphous polymer IDT-BT. This work has potential implications not only for OSCs but also other low temperature semiconductors which are susceptible to atmospheric defects.

**Chapter 1** provides an overview of the physics of transport and doping of OSC polymers in OFETs as well as the causes of instabilities due to extrinsic atmospheric species and how to mitigate their influence. As the organic synthesis and fabrication space is massive, the emerging field of statistical experimental discovery for material science is provided.

**Chapter 2** introduces organic semiconductors, additives and dielectrics in addition to device fabrication procedures and experimental characterization used in this work.

**Chapter 3** describes the search for over 90 potential stabilization additives selected following recent developments in the stabilization of polymer OSCs using molecular additives to further expand the understanding and library of molecular additives.

**Chapter 4** introduces the concept and routes to prevent positive bias stress (PBS) stability in p-type OSCs and design rules for solid state PBS stable molecular additives supported by experimental and theoretical evidence.

**Chapter 5** explores the chemical stability of all solid state molecular additives, which demonstrate improved device performance, with water and how the interaction influences OFET device characteristics.

**Chapter 6** explores how to use machine learning to quantify the search for new molecular additives.

**Chapter 7** introduces and explores the feasibility of antiferromagnetic counters in analogue neuromorphic computing.

**Chapter 8** provides the concluding remarks and key insights gained into solid state molecular additives for OSCs.

## 1.2 Organic semiconductors

Here we provide an introduction to transport and doping mechanisms in organic semiconductors.

### 1.2.1 Charge transport

Transport originates in organic polymers from the conjugation of  $\pi$ -bonds along the molecule[1]. In non-conjugated organic molecules the large overlap from the  $\sigma$ -bond results in a strong bond and large band gap between the bonding and antibonding orbitals. The reduced overlap of the pz-orbitals in a  $\pi$ -bond results in weaker bond interaction and a small band gap, allowing the propagation of  $\pi$ -bonds along a conjugated molecule, demonstrated in the molecule's canonical structures, resulting in charge transport. The hybridization of atomic orbitals is extended beyond nearest neighbor interactions through Hückel molecular orbital theory which predicts properties such as energy levels and geometries of the HOMO and LUMO due to hybridization of the whole atomic structure. The extension of Hückel's theory directly to a polymer would predict that as the number of orbitals increases, the energy difference between the states would decrease until a continuous band is formed suggesting polymers would be a conductor. Semiconducting characteristics develop due to preferential canonical structures resulting in a difference in bond lengths and electron concentrations in a periodic structure, known as Peierls distortion, creating a periodic potential and hence semiconducting behavior.

A general Hamiltonian ( $H_G$ ) describing the carrier transport in organic materials can be seen below in equation 1.1 to 1.4 [5].  $H_G$  can be separated into four components: one-

electron ( $H_{el}^0$ ), phonon-phonon ( $H_{ph}^0$ ), local electron-phonon ( $V_{el-ph}^{local}$ ) and non-local electron-phonon interactions ( $V_{el}^{non-local}$ ).

$$(1.1) \quad H_G = H_{el}^0 + H_{ph}^0 + V_{el-ph}^{local} + V_{el}^{non-local}$$

$$(1.2) \quad H_{el}^0 + H_{ph}^0 = \sum_j \epsilon_j a_j^\dagger a_j + \sum_{ij} J_{ij} a_i^\dagger a_j + \sum_{\vec{q}s} \hbar\omega_{\vec{q}s} (b_{\vec{q}s}^\dagger b_{\vec{q}s} + \frac{1}{2})$$

$$(1.3) \quad V_{el-ph}^{local} = \sum_{\vec{q}s} \sum_j \hbar\omega_{\vec{q}s} g_{jj,\vec{q}s} (b_{\vec{q}s}^\dagger + b_{-\vec{q}s}) a_j^\dagger a_j$$

$$(1.4) \quad V_{el}^{non-local} = \sum_{\vec{q}s} \sum_{i \neq j} \hbar\omega_{\vec{q}s} g_{ij,\vec{q}s} (b_{\vec{q}s}^\dagger + b_{-\vec{q}s}) a_i^\dagger a_j$$

where,  $a_j$  ( $a_j^\dagger$ ) is the annihilation (creation) of electrons from site  $j$ ,  $\epsilon_j$  is the energy of the charge sitting on molecular site  $j$ ,  $J_{ij}$  is the transfer integral describing the coupling of carriers between different molecules,  $b_{\vec{q}s}$  ( $b_{\vec{q}s}^\dagger$ ) is the annihilation (creation) of phonons with the wave vector ( $\vec{q}$ ) and polarization ( $s$ ),  $\hbar\omega_{\vec{q}s}$  is the energy of the phonon,  $g_{jj,\vec{q}s}$  is the phonon-electron interaction affecting the local energies and  $g_{ij,\vec{q}s}$  is the phonon-electron interaction affecting the non-local carrier transfer.

In an ideal system with absolutely no disorder the carriers would form Bloch states and the transport would be similar to that in inorganic systems. This is not realistic; even in perfectly crystallized organics there are mechanisms to introduce disorder and localize the carrier, destroying the Bloch states. One of the mechanisms is due to the weak van der Waals forces holding the organic molecules together, which enables large molecular vibrations. The large molecular vibrations constantly modify the coupling between two states on separate molecules ( $J_{ij}$ ), and this results in the transient localization of carriers[6], [7]. The term that describes the intermolecular vibration interactions is  $g_{ij,\vec{q}s}$ , which introduces dynamic disorder to  $J_{ij}$ . The dynamic disorder introduced in  $J_{ij}$  from transient localization is the dominant mechanism that inherently limits the room temperature mobility of small organic molecules[6], [8]–[10]. Static disorder in the value for  $J_{ij}$  can be caused by variations in intermolecular separation, relative orientation of molecules, the degree of conjugation, conformation of the molecules and Coulombic interactions.[5], [11], [12]

Further disorder can be present in  $\epsilon_j$ , which is known as energetic disorder, from the vibrational modes introduced from  $g_{jj,\vec{q}s}$  in an ideal system. This mechanism can be more intuitively understood as the energy needed to change the nuclei configuration in a molecule from the neutral to charged state, which is known as the reorganization energy



( $\lambda$ ). Charge transport limited by the reorganization energy, i.e. systems with very large  $\lambda$ , is modeled by the Marcus theory and is best described by Fratini et al. as the *“hopping motion of charge carriers which are self-trapped by their induced molecular deformations”*[6]. Other sources of energetic disorder include variations in molecular conjugation length, structural disorder, chemical defects, dipole interactions and conformation.

### 1.2.2 Doping in organic semiconductors

Doping occurs in inorganic semiconductors through the addition of atomic substitutional or interstitial defects in the band gap, which results in thermally generated carriers in the semiconductor. The concentration of the dopant allows the precise control of the Fermi level which is critical when fabricating electrical components. The number of added defects remains small, causing the band structure and the density of states to remain unchanged by the introduction of the dopant. Doping in organic semiconductors has significantly more complications as the inherently soft polymer can change geometries in the presence of a large dopant molecule, the dopants can thermally diffuse at room temperature, simple oxygen doping can result in degradation of polymers and the low dielectric constant of the organic semiconductor increases the electrical interaction between the dopant and free carrier[13]–[16].

These complications are a problem as doping provides a route to passivate intrinsic and extrinsic defects. Here, different forms of doping in organic semiconductors are examined, including ion pair formation, charge transfer states, Lewis acid base interactions, hydrogen doping and self-doped polymers.

The most common form of doping in organic semiconductors is related to the oxidation and/or reduction of the organic semiconductor by a neutral molecule resulting in a charge transfer and the formation of an ion pair, where an integer charge is on the dopant molecule and the opposite charge is on the semiconductor. A simple model would predict that if the ionization energy ( $IE$ ) of the donor molecule was less than the acceptor electron affinity ( $EA$ ), charge transfer would occur resulting in doping of the organic semiconductor. This is not always the case as the electrostatic energy (Madelung energy) between the ionized species reduces the net energy of the interaction between

the semiconductor and the molecule. The energy ( $E$ ) of the ion pair formation in a p-type semiconductor is the following:

$$(1.5) \quad E(\delta) = (IE - EA)p - k\langle e^2/r \rangle p^2$$

where,  $p$  is the degree of charge transfer,  $k$  is the electrostatic constant and  $r$  is the distance between the positive and negative charge. Intuitively, the Madelung energy represents the additional energy required to separate ions. The dependence of the doping energy on  $r$  explains the morphology dependent phenomena, such as the pressure dependence of ionization[17].

Charge transfer complexes are another form of doping that can occur when the difference between  $IE$  and  $EA$  is large, however, the formation of a charge transfer complex can still occur when the difference between  $IE$  and  $EA$  becomes small and/or unfavorable for the formation of ion pair doping. The specific rationale for why a system forms either ion pairs or charge transfer complexes is still unknown, however, evidence suggests it is a combination of the complex arrangement and inherent structure of the dopant and semiconductor[18]. The formation of a charge transfer complex is dependent not only on the relative energy but the relative overlap between the LUMOs and HOMOs of the dopant and organic semiconductor. An appropriate overlap of the orbitals can result in hybridization of the frontier orbitals resulting in the formation of bonding and antibonding supramolecular hybrid orbitals (Figure 1-1). For both p-type and n-type organic semiconductors this results in a new electron acceptor and donor state above and below the LUMO and HOMO, respectively, which acts as a dopant. This charge transfer complex behaves very similarly to dopants in inorganic systems where the electron donor and acceptor state is only slightly energetically below and above the conduction and valence band, respectively (Figure 1-1).

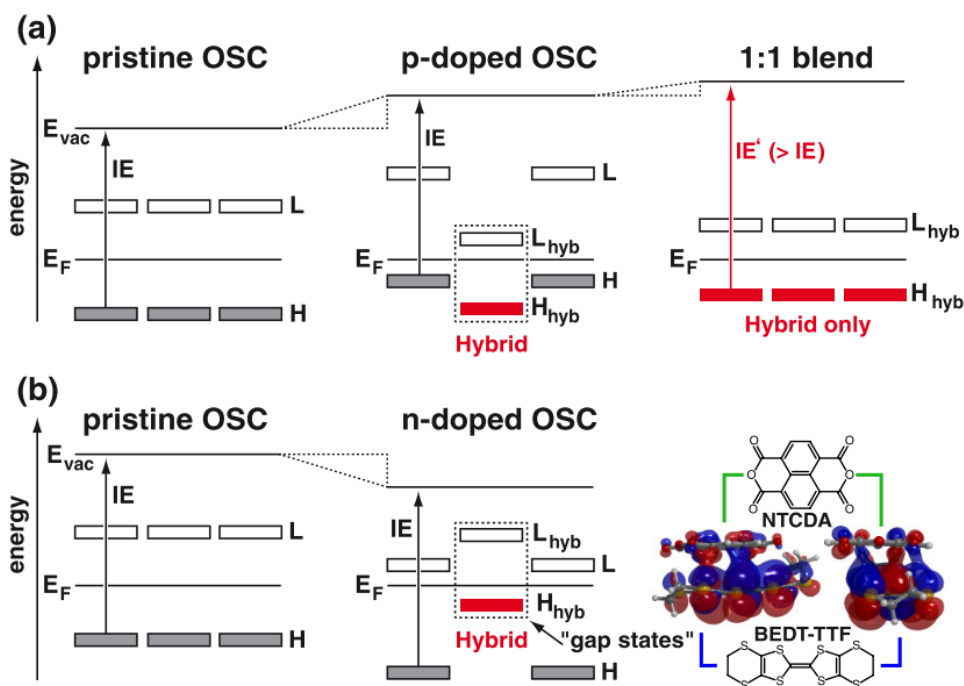


Figure 1-1: (a) Schematic energy-level diagram for molecular electrical p doping via OSC-dopant frontier-orbital hybridization.  $H_{hyb}$  and  $L_{hyb}$  denote the bonding and antibonding supramolecular hybrid orbital, respectively and  $IE'$  denotes the increased hybrid IE observed here in the 1:1 blend of OSC and dopant. (b) n-type doping proceeds in full analogy to (a); right: chemical structure and calculated bonding hybrid orbitals for the prototypical material pair 1,4,5,8-naphthalene-tetracarboxylic-dianhydride and bis(ethylenedithio)-tetrathiafulvalene. Image and caption from I. Salzman et al. [18].

The efficiency of the doping process is then determined by Fermi-Dirac statistics. In inorganic systems the dopant state is only a few meV below or above the conduction and valence band, which results in a large population of the dopant state being ionized, however, in organic semiconductors this is not the case, as the energy difference is significantly larger resulting in only a fraction of the charge transfer complexes being ionized at room temperature. This helps explain the low doping efficiencies in organic semiconductors. Experimental evidence of charge transfer complexes can also explain changes in the infrared and UV-VIS spectrum as well as the increase in ionization energy [18], [19].

A specific case of doping via charge transfer complexes is when the overlap of orbitals takes the form of a Lewis acids and base reaction[20]–[22]. Lewis acid base doping is practically interesting, as p-type doping of organic semiconductors with HOMOs around -5.3eV has been observed using the Lewis acid BCF which has a LUMO of -3.12eV, which would intuitively not result in doping due to the large energy barrier[21]. In the Lewis model, Lewis acids are capable of accepting an electron pair and a Lewis base has an unpaired electron pair that is not used in bonding and can be donated. A reaction between the appropriate Lewis acid and base results in a new molecule, known as the Lewis adduct, where the Lewis acid and base are linked through a coordinate covalent bond.

Another route for doping in organic semiconductors is through modification of the acidity and is observed in polymers such a polyaniline or PEDOT[14], [23], [24]. Protonic acid doping occurs through a cation proton incorporating itself into the polymer chain while the number of electrons on the polymer remains the same, resulting in a positively charged species. Protonic acid doping is unstable and easily reversible if the right pH is not maintained. This is demonstrated in systems such as PEDOT:PSS where modification of the pH results in a change in the work function and conductivity[25]. The correct state of protonic doping can be maintained in polymer systems by buffering the pH[14].

Self-doped polymers have a population of dopant molecules covalently bonded directly to the polymer. The dopant could be a neutral species which is capable of forming an ion pair or charge transfer complex, however, typically self-doped polymers contain an acidic functional group such as sulfonic acid which is capable of forming an ion pair with the polymer by releasing a cation in the presence of water. The proton of the acidic group can be replaced with any positive cation capable of dissociating with the polymer in water such as sodium or lithium. When the cation dissociates from the polymer, the electric field from the negative anion accumulates a hole on the polymer to shield the anion (Figure 1-2). Similarly, an injected hole could force deprotonation resulting in the persistent accumulation of the hole[14].

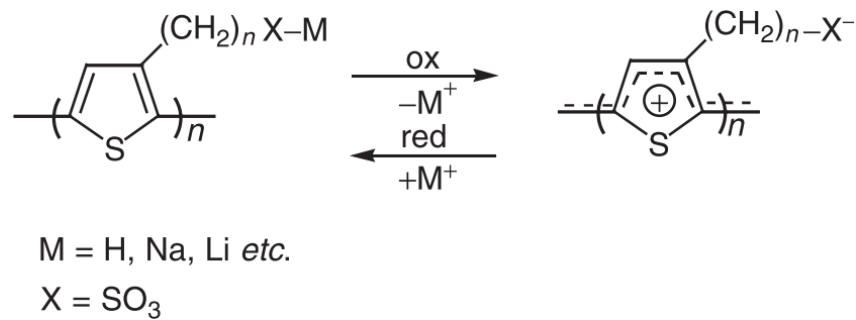


Figure 1-2: Oxidation-reduction reactions of polythiophene derivatives showing self-doping during the oxidation reactions. Image and caption from A. G. Macdiarmid et al. [24]

### 1.3 Thin film transistors

The mass production of high quality silicon occurs due to the remarkably effective Czochralski process, however, this process is limited in wafer size and does not allow the deposition of semiconductors on substrates. To compensate, a large variety of deposition techniques have been developed to deposit thin layers of semiconductors resulting in different transistor architectures known as thin film transistors. Here thin film transistor (TFT) architectures and their operation principles will be examined.

#### 1.3.1 Architectures

A TFT is a three terminal device that modulates the current between two electrodes by controlling the voltage on a third electrode. The third electrode, known as the gate, controls the conductivity of a region of the semiconductor by attracting charge carriers in the semiconductor via an electric field to the semiconductor insulator interface. The other two terminals, known as the drain and source, are located on opposite sides of the conductive channel controlled by the gate.

The most common transistor architectures are shown in Figure 1-3 and include staggered top-gate/bottom-contact and bottom-gate/top-contact as well as coplanar top-gate/top-contact and bottom-gate/bottom-contact structures. In this thesis, all OFETs presented will be based on the top-gate/bottom-contact TFT architecture.

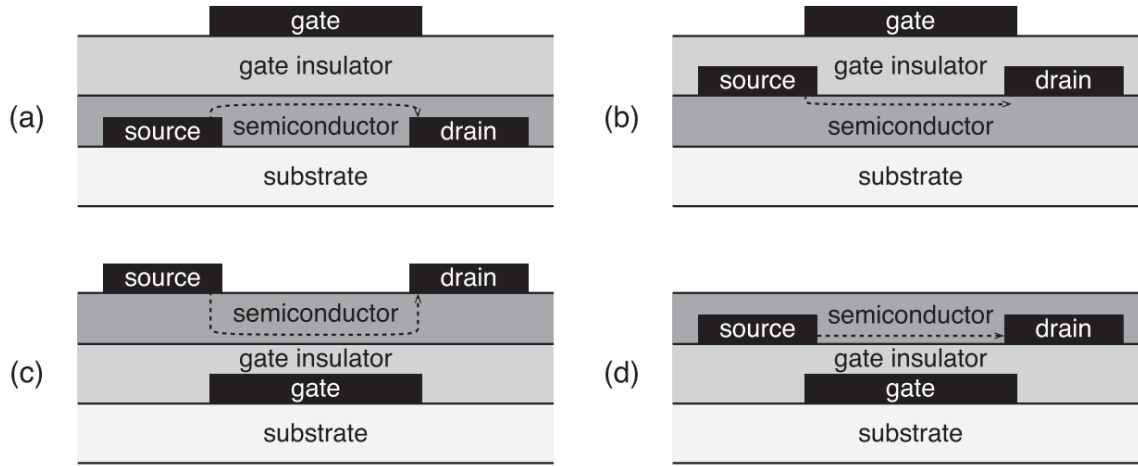


Figure 1-3: Different thin-film transistor configurations: staggered (a) top-gate/bottom-contact and (c) bottom-gate/top-contact; coplanar (b) top-gate/top-contact and (d) bottom-gate/bottom-contact. The charge flow in the channel is indicated with a dashed line. Image and caption from L. Herlogsson [26].

### 1.3.2 Operation principles

The current voltage relationship in OFETs can be described using the same mechanism which governs the charge transport in conventional inorganic MOSFETs. The minimum gate source voltage ( $V_{GS}$ ) at which there are sufficient accumulated carriers to form a conductive channel between the source and the gate source is known as the threshold voltage ( $V_{th}$ ).  $V_{th}$  is process dependent and can be related to the concentration of dopants, trapped charge and defects of the semiconductor. Any additional voltage after  $V_{GS} > V_{th}$  is directly related to the number of accumulated carriers in the OFET. The current through the transistors can be modelled through the gradual channel approximation, where the charge accumulated depth is assumed to be infinitesimally deep and the charge density from the source to the drain scales linearly with gate, drain and source voltage.

$$(1.6) \quad I_{DS} = \frac{\mu C_{ox} W}{L} \cdot \left( (V_{GS} - V_{th}) \cdot V_{DS} - \frac{V_{DS}^2}{2} \right)$$

where  $\mu$  is the mobility of the semiconductor,  $C_{ox}$  is the capacitance per unit area,  $W$  is the width of the transistor and  $L$  is the length of the channel (the distance between the source and the drain).

In the operation regime where  $V_{GS}$  is much greater than the drain source voltage ( $V_{DS}$ ) or  $V_{GS} - V_{th} \gg V_{DS}$ , the accumulated carriers are uniformly distributed at the insulator semiconductor interface, resulting in the current through the transistor scaling linearly with  $V_{DS}$ . As the current scales linearly with  $V_{DS}$  and  $V_{GS}$  in this regime, it is known as the linear regime (1.7).

$$(1.7) \quad I_{DS} = \frac{\mu C_{ox} W}{L} \cdot (V_{GS} - V_{th}) \cdot V_{DS}$$

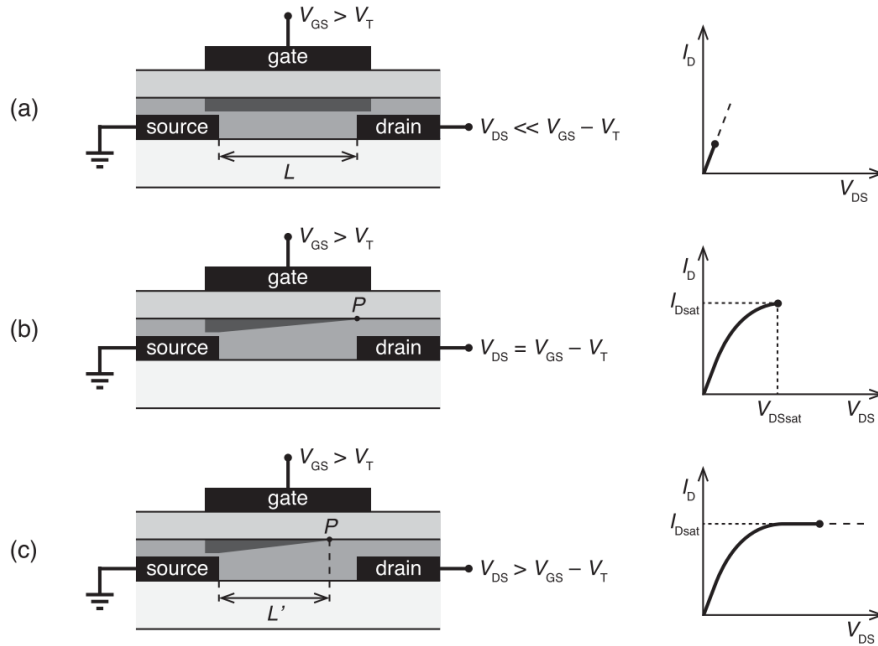


Figure 1-4: Illustrations of the charge distribution in the channel and current-voltage characteristics in the different operating regimes of field-effect transistors: (a) the linear regime; (b) the start of saturation at pinch-off; (c) the saturation regime. Image adapted from L. Herlogsson [26].

As  $V_{DS}$  approaches  $V_{GS} - V_{th}$  the accumulation near the drain electrode is consistently reduced until  $V_{DS} = V_{GS} - V_{th}$ . When no accumulation occurs at the drain, the physical point where no accumulation occurs is known as the pinch-off point ( $P$ ). As  $V_{DS}$  increases beyond  $V_{GS} - V_{th}$  the location of the pinch-off region moves slightly towards the source, changing the accumulation channel length ( $L'$ ) and creating a slightly larger depletion region between the pinch-off point and the drain where any additional increase in  $V_{DS}$  appears as an increase in the voltage drop across the narrow depletion region[27].

As the voltage across the accumulated channel remains unchanged and the accumulation channel length ( $L'$ ) is relatively independent of the increase in  $V_{DS}$ ,  $I_{DS}$  saturates. Hence, the operation regime of the transistor when  $V_{DS} \geq V_{GS} - V_{th}$  is known as the saturation regime (1.8).

$$(1.8) \quad I_{DS} = \frac{\mu C_{ox} W}{L} \cdot (V_{GS} - V_{th})^2 \left(1 + \frac{V_{DS}}{V_A}\right)$$

where  $V_A$  is the early voltage which includes the term for the modified channel length ( $L'$ ). Equations 1.7 and 1.8 enable the extraction of the mobility ( $\mu$ ) of the semiconductor. This is relevant for both industry and physics, however, the equations are only valid when the contact resistance is low. Unfortunately, this assumption is not valid for OFETs as the work functions of the intrinsic semiconductor and metal contacts do not align, forming a Schottky barrier at the interface. In addition any OSC between the contact and accumulation interfaces is resistive as it is not doped. Both effects result in high contact resistance invalidating equations 1.6 and 1.7 as accurate descriptions of current through the transistor. This can be avoided by doping the semiconductor at the contacts, however, in organic devices this is difficult to achieve in practice as the dopants are mobile.

Current through the transistor dominated by diode like contact resistance can result in significant overestimates of semiconductor mobility in the literature as the diode causes the current through the transistor to scale exponentially with  $V_{GS}$  and  $V_{DS}$ . Similarly, current through the transistor dominated by resistive like contact resistance causes a significant underestimate of the semiconductor mobility as  $V_{GS}$  and  $V_{DS}$  are overestimated. Choi et al. have proposed that along with the extracted mobility a reliability factor should be reported in the literature which aims to reveal the certainty of the extracted mobility. The reliability factor is the ratio of the maximum channel conductivity experimentally achieved in an OFET to the maximum channel conductivity expected in an equivalent but ideal FET with the claimed mobility and zero voltage threshold[28]. For other effects which obscure the mobility extraction please review Choi et al.'s article on critical assessment of charge mobility extraction in FETs[28].



### 1.4 Semiconductor stability

The next section discusses why organic electronics are limited by stability and how this can be prevented.

#### 1.4.1 Deep traps

A trap is formed any time there is a localization of charge, due to phenomena such as large reorganization energy. Traps are considered shallow when the fermi level is between the transport band and the trap states resulting in the equilibrium of free and trapped carriers determined by Fermi-Dirac statistics. The formation of a deep trap occurs when the charge is unable to escape the trap in a short time scale due to either a large energy mismatch or reorganization of the chemical species. The charges on these sites become inactive in transport and result in increased scattering of the free carrier and/or modifying the fermi level. Intrinsic common deep traps in inorganic semiconductors which can be present in organic semiconductors are radicals, which can form in organics due to UV light or bending of the organic[29], [30]. Here the focus is on deep traps formed by environmental species which are believed to dominate the deep traps in organic systems.

#### 1.4.2 Redox reactions in organics

In the literature, the most influential interaction between atmospheric species and organic semiconductors is believed to be the redox reaction. The charge transfer during the reduction-oxidation reaction (redox) of atmospheric species can result in the formation of deep traps or act as a dopant depending on the relative energy levels of the HOMO, LUMO and Fermi level. There can be a large recombination time of the atmospheric species due to the reorganization of the atmospheric species and large energy mismatch.

D. de Leeuw et al. have proposed that redox reactions involving the polymer and atmospheric species can be interpreted as the combination of two half reactions, where one reaction is the oxidation and the other reaction is the reduction. A subset of reduction chemical equations and their corresponding reduction potential ( $E_{Red}$ ) is

seen in Table 1. The oxidation chemical equation is the reverse of the reduction chemical equation. For the reactions involving moisture species, the reduction potential was determined in an aqueous solution with a pH of 7 referenced against a standard saturated calomel electrode (SCE)[31]. The reduction of superoxide ions ( $O_2^-$ ) was investigated in a dried aprotic medium against a platinum electrode[31]. The reduction of a neutral and positively charged organic molecule is approximated as the LUMO and HOMO energy, respectively, by omitting additional effects such as reorganization energy, polarization effects and excitation effects. As the reduction potentials are always relative to a reference electrode, here all reduction potentials are converted to a vacuum potential reference (absolute electrode potential in chemistry) which is used in physics for convenience.

Table 1: A selection of possible half reactions including polymers, involving oxygen, water, ozone, and hydrogen peroxide with their redox potentials referenced to an absolute electrode potential, where  $e$  is the elementary charge. Modified table from D. de Leeuw et al. [31]

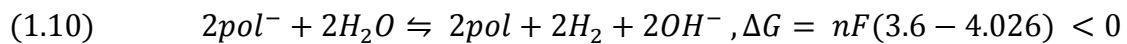
No.	Half Reaction	$E$ (Red. Vs Abs. electrode potential)
1	$pol + e^- \rightleftharpoons pol^-$	$E_{LUMO}/e$
2	$pol^+ + e^- \rightleftharpoons pol$	$E_{HOMO}/e$
3	$O_3 + 2H^+ + 2e^- \rightleftharpoons O_2 + H_2O$	-6.096 V
4	$H_2O_2 + 2H^+ + 2e^- \rightleftharpoons 2H_2O$	-5.802 V
5	$O_2 + 4H^+ + 4e^- \rightleftharpoons 2H_2O$	-5.255 V
6	$2O_2 + 4H^+ + 4e^- \rightleftharpoons 2H_2O_2$	-4.708 V
7	$2H_2O + 2e^- \rightleftharpoons H_2 + 2OH^-$	-4.026 V
8	$O_2 + e^- \rightleftharpoons O_2^-$	-3.784 V

The redox reaction model predicts whether the equilibrium of the reaction will move towards the products or the reactants by determining the Gibbs Free energy of the equilibrium, equation 1.9.

$$(1.9) \quad \Delta G = -nF(E_{Ox} - E_{Red})$$

where  $E_{Ox}$  is the reduction potential of the oxidation reaction. If  $\Delta G$  is negative the reaction will migrate towards the products, and the opposite is true if  $\Delta G$  is positive. As the reduction potential of the polymer is dependent on the energy of the LUMO and HOMO, this redox model would suggest that the energy levels of the HOMO, LUMO and fermi level would promote certain reactions towards the products or reactants. The charge trapping dependence of the HOMO and LUMO energy level resulting in deep traps preventing accumulation or acting as a dopant has been repeatedly demonstrated in both n-type and p-type organic semiconductors. For example Blom et al. reported that there is a universal electron trap in organic polymers around -3.6eV, and that reducing the LUMO energy level reduces the effect of the n-type trap[32]. Similarly, Takimiya et al. have shown p-type small molecules with high energy levels result in an increased susceptibility of oxidation of the small molecule by atmospheric species[33]. Nikolka et al. have demonstrated that reducing the HOMO in IDT-BT from -5.3 to -5.8 eV results in poor transport performance attributed to the stronger driving force of hole trapping in atmospheric traps[34]. The redox reaction model suggests that the only regime where the redox reactions would not influence charge transfer is when reduction potential of the desired transport orbital is equal to reduction potential of the atmospheric species. As the HOMO level is offset from the LUMO level, the redox reaction instability model would suggest the only route to produce ambipolar organic electronics is to remove atmospheric species from the organic.

An example of a thermodynamic favorable reaction, achieved by combining reactions 1 and 7, where electrons in the LUMO, at 3.6eV [35], of the IDT-BT polymer split water forming a deep trap, is seen below:



As the partial pressure of hydrogen gas in air is negligible, the hydrogen molecule will have a large entropic force, allowing the film to undergo a reaction that isn't reversible and having no route for the charge on the hydroxyl to recombine with the polymer, causing the hydroxyl to act as a deep trap. The entropy can be included in the reduction potential via the Nernst equation:

$$(1.11) \quad E_{Red} = E_{Red}^o + \frac{RT}{nF} \cdot \log \frac{[Ox]}{[Red]}$$

Where  $n$  is the number of electrons involved in the reaction,  $F$  is the Faraday constant,  $T$  is the temperature,  $R$  is the ideal gas constant,  $E_{Red}^o$  is the standard electrode potential,  $[Ox]$  is the activity of the oxidized form and  $[Red]$  is the activity of the reduced form. The Nernst equation is accurate at predicting the reaction kinetics for solutions as the activity of the species is known, but in thin films of hydrophobic organics the exact activity is difficult to obtain. Regardless, the Nernst equation shows that there is a critical activity of reactants and products for which the reduction potential changes the Gibbs free energy from positive to negative causing the reaction to become favorable. Furthermore, the Nernst equation predicts that the reduction potential of the charged species on either the LUMO or HOMO changes during accumulation or depletion of charge, which suggests that the only route to avoid instabilities is to remove atmospheric species from the organic[36]. Even though the redox reactions cannot be prevented without the removal of atmospheric species, the Nernst equation predicts that the Gibbs Free energy of the reactions can be modified by changing the activity of the reactants and products which would change certain electrical stress dynamics. For example reducing the pH of the organic would lower the activity of the hydroxyl species and increase the probability of negative polaron trapping by atmospheric species observed in equation 1.9.

Direct evidence proving redox reactions are the dominant mechanisms in organic semiconductors is difficult to achieve experimentally due to the small concentration of species in the film, however, there is indirect evidence in the literature and this work suggesting redox reactions are relevant [16], [36], [37].

### 1.4.3 Mobile ionized water

In general, mobile ions in semiconductors are typically undesirable as they are capable of inducing instabilities in the presence of an applied electric field[38]. Mobile ions result in instabilities in the device characteristics, as the ions migrate under an electric field applied to the device during operation and shield the applied electric field. After the applied electric field is removed, the electric field induced by the ions slowly dissipates as the ions slowly move back to the equilibrium distribution. In OFETs under gate

voltage stress, the electrical stress due to mobile ions would manifest as a threshold voltage shift. In any suitably synthesized deionized organic semiconductor, this mechanism of ion movement should not influence the bias instability, however, as water readily becomes thermally ionized hydronium cations and hydroxide anions, organic semiconductors with water can be susceptible to instabilities caused by mobile ions[39]. As mentioned in the previous section, through redox reactions there are other ways to generate ion species resulting in mobile ions[36]. The thermal ionization rate of water is  $2.6 \cdot 10^{-5} s^{-1}$  at room temperature, however, over the course of approximately ten hours each water molecule is expected to undergo ionization once[40], [41]. The concept of charge separation of ionized water is not new and provides the rationale for the conductivity of pure water.

An experimental technique to test the electrical stress characteristics with minimum water ionization is to reduce the generation of ionized water by lowering the temperature of the OFET. As the splitting of water forming ions is endothermic, the formation of ions reduces with temperature. The temperature dependence of the equilibrium constant ( $K_{eq}$ ) of water is described by the van't Hoff equation:

$$(1.12) \quad \frac{d}{dT} \ln K_{eq} = \frac{d}{dT} \ln \frac{[OH^-][H_3O^+]}{[H_2O]^2} = \frac{\Delta H^\ominus}{RT^2}$$

where T is temperature,  $\Delta H^\ominus$  is the standard enthalpy change of splitting of water,  $[OH^-]$  is the activity of hydroxide,  $[H_3O^+]$  is the activity of hydronium and  $[H_2O]$  is the activity of water. As  $\Delta H^\ominus$  is typically considered independent of temperature, the van't Hoff equation can be integrated showing that the ratio of the concentration of ionized water at different temperatures scales exponentially. In experiments the  $K_{eq}$  of water decreases by one order of magnitude between room temperature and 0°C[42]. Furthermore, the  $pK_{eq}$  ( $\ln(K_{eq})$ ) drops by two orders of magnitude between water and ice at the same temperature, suggesting that if ice forms in the OFET, there is complete suppression of ionization of water. However, it is unclear what the specific phase of water is inside the organic at room temperature and below zero degrees in the presence of an electric field.

Experimentally Kettner et al. demonstrated that reducing the temperature of DPP OFETs in a high vacuum suppresses the voltage threshold shift during both negative and positive gate bias stress stabilities, particularly because when the temperature is reduced below 0°C, complete suppression of bias stress is observed (Figure 1-5, left)[39]. Furthermore, Kettner et al. performed thermally stimulated current experiments (Figure 1-5, right) showing that the detrapping of carriers occurs only once, suggesting a single mechanism can be responsible for charge trapping. This evidence suggests that the DPP polymers tested by Kettner et al. are intrinsically trap-free and bias induced trapping appears to be dominated by a temperature dependent process, which strongly correlates with the suppression of ionized water.

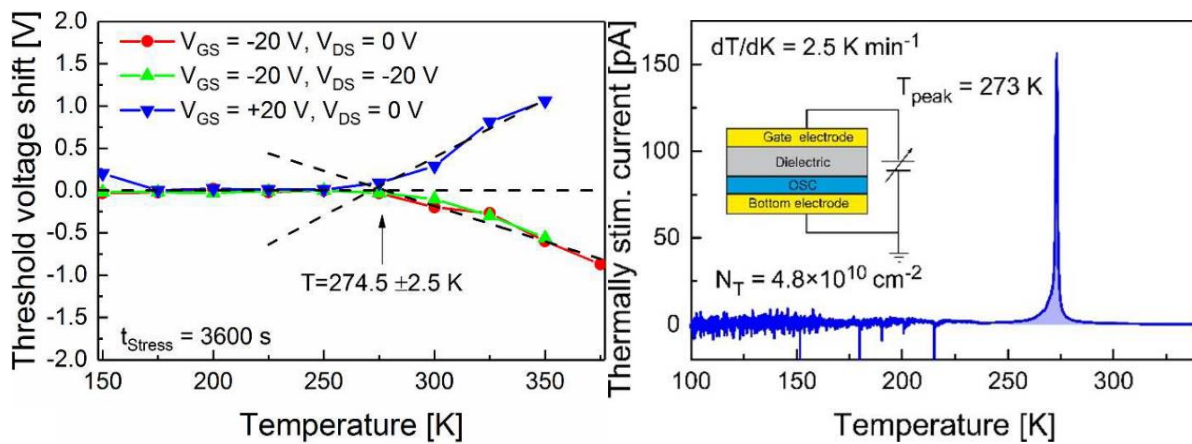


Figure 1-5: Left) Threshold voltage shift ( $\Delta V_{th}$ ) at various bias stress conditions indicated in the legend after 3600 s.  $\Delta V_{th}$  is shown as a function of the temperature during the stress. The dashed sloped lines are fits to the data in the high temperature regime. In addition, the  $\Delta V_{th}=0$  line is indicated. Right) Thermally stimulated current (TSC) trace of a MIS device. A schematic is shown in the inset. Trap filling was obtained by a bias-stress at 340 K for 10 000 s at  $V_G = -20\text{ V}$ . Image and caption modified from M. Kettner et al. [39].

## 1.4.4 Removal of atmospheric traps

As mentioned previously, trapping in organic semiconductors is dominated by environmental species and not intrinsic defects in the organic. A major engineering challenge is to find routes for removing atmospheric species from low temperature solution based processes and prevent the penetration of species during the lifecycle of the device. Here we will review routes to remove the effects of atmospheric species from

the semiconductor. A common route to remove atmospheric species is to passivate the traps by doping, however, this is undesirable for OFETs as it increases their off current. Other routes have been experimentally examined by Nikolka et al. showing that liquid and solid state additives are capable of improving device stability without doping the device[43].

The benefit from liquid additives is remarkable, showing near ideal device characteristics across a wide variety of polycrystalline and amorphous organic polymers. Nikolka et al. demonstrated that all of the liquid additives that work appear to be part of a family of molecules which form azeotropes with water. Molecules which form azeotropes with each other reduce the boiling point of a mixed solution, suggesting that as solvent boils off it will dehydrate the film and is able to dissolve and interact water in the film. Azeotropes form due to enthalpic interactions such as hydrogen bonding between solvents and water molecules. Furthermore Nikolka et al. argue that detectable empty voids within a polymer film generally exhibit a strong driving force to be filled, suggesting that either the additive may compete with water and displace water molecules from being in direct contact with the polymer because the additive-polymer interaction is more favorable than the water-polymer interaction, or the additive may interact strongly with residual water molecules within the voids such as to prevent the ability of water molecules to interact with the polymer. Through these mechanisms it is reasonable to assume that the liquid additives would modify stress related to redox reactions and mobile ions due to water. In the same article, Nikolka et al. predicted through simulations an additional water induced stress pathway where water near the backbone of IDT-BT induces energetic disorder through torsion of the backbone of the polymer. In this work they demonstrate improvements with solvent additives only in p-type regimes; due to the physical mechanism being related to the removal of water and not doping this mechanism should work for n-type devices as well.

To date no liquid additive has been discovered to produce long term stability as they are believed to leave the film. Fortunately, a similar performance improvement with no doping has also been observed for solid state additives which could provide a long term solution. In Nikolka et al.'s work on solid state additives they propose that the solid state additive improves device performance using the same physical mechanism responsible

for the similar observed improvement in liquid additives, however, evidence of void filling was only demonstrated for liquid additives and not solid additives. There is no evidence that the solid state additives form water complexes similar to the organic solvents which form azeotropes with water. Evidence was provided by Nikolka et al. that showed that solid additives do not inherently dope the polymer film, reproduced in this work, which makes it unclear what the specific mechanism is responsible for the observed device performance improvement[43].

The problem with understanding the solid and liquid state additives is that direct spectroscopic evidence is difficult due to the small quantities of atmospheric species and the small amounts of solid additives required to stabilize the film. As Nikolka et al. achieved a very high success rate for finding solid state molecules in their work, this suggests that there are likely a large number of unknown beneficial solid state additives which link the structure of the additives to performance. In this work we present a large data set of solid state molecular additives in order to gain a statistical understanding of the relationship between the structure of solid state additives and functionality. As the relationships between the structure of molecules and functionality are highly complex and understanding these relations is a critical component for the future of material science, the emerging field of statistical experimental discovery is discussed in the next section.

### 1.5 Statistical experimental discovery

A significant advantage of organic devices is that the chemical space of all possible synthesized materials are practically infinite[44]. A major scientific challenge is to efficiently search through this practically infinite space of possible candidates as the process is inherently unpredictable and time consuming. To improve the rate of discovery certain aspects can be simulated but this doesn't always work, and it can be too computationally demanding, as is the case in this thesis[43]. A promising route to improve the searching efficiency in material science is to augment computational and experimental discovery of novel materials by using machine learning techniques. At the core, machine learning techniques have provided an empirical route to efficiently map the quantifiable features of all prior experimental data to the outcome of an experiment



through statistical techniques to help predict the outcome of subsequent experiments. This concept is already in place in the field of drug discovery, as the complete biology system is an intractable problem, but there is a wealth of data linking the chemical properties of a drug to a biological response. The specific process of linking the properties of materials to relevant performance metrics using machine learning is known as quantitative structure-activity relationship (QSAR). Machine learning is particularly interesting for this work as the chemical properties of a material are determined by the chemical structure, suggesting that unknown chemicals can be related to the known structure of the molecule using machine learning. To understand how to apply artificial intelligence to searching, in this section we review the following: how to vector molecular structures to use in machine learning models, general insight into the effectiveness of machine learning models and how to apply machine learning models to real world data sets with small amounts of data.

### 1.5.1 Vector representation of molecular structure

Here we discuss the representation of molecular structures in a vector space which are compatible with machine learning algorithms. Intuitively the optimum basis set would be capable of encoding physical behavior, where molecules with similar physical behavior are located closer to each other than molecules that do not have similar behavior. If such a space was achieved, less data would be required to make valid predictions on untested molecules. Intuitively this could be thought of as lowering the Nyquist frequency of the space, which reduces the number of data points required to reproduce the space. This will be discussed in more detail later in this Chapter. Chemists attempt to build such a space by breaking the molecule into defined fragments known as functional groups which have a specific chemical behavior. Here we explore automatic routes to achieve such a mathematical space proposed in the literature. This includes physically implausible natural language encodings, such as one-hot and autoencoded smiles representation commonly used in the literature, as well as more physically relevant feature encoding such as neural graph fingerprints and Coulomb matrices.

All of the techniques discussed and used in this work start with the simplified molecular-input line entry system (SMILES). SMILES are 1D character representations which are unique for each molecular structure.

The specific SMILES for each molecular structure depend on the specific algorithm used to generate SMILES representation. SMILES are particularly useful as they can be uniquely converted to one-hot vectors and molecular graph encoding. In addition molecular structures can also be represented as Coulomb matrixes from SMILES, but relating the two is not unique.

### 1.5.1.1 One-hot encoding

As the SMILES representation is a string, it is common to convert the SMILES to a one-hot encoding vector which is used in machine learning text processing applications. One-hot encoding is a matrix representation where an element is assigned one if the index of the string (column index) corresponds to a character assigned to a row, otherwise it is assigned zero (Figure 1-6).

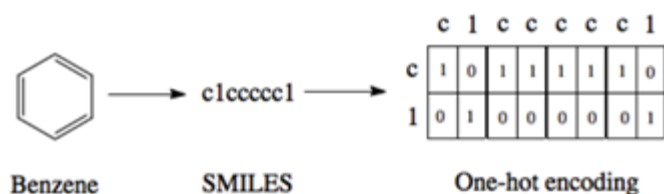


Figure 1-6: The SMILES and one-hot encoding for benzene. For simplicity only the characters present in benzene are shown in the one-hot encoding. In reality there would be a column for each character in the SMILES alphabet. Image and caption from R. Griffiths et al. [45].

### 1.5.1.2 Molecular graphs

Graphs are a mathematical structure which contain a set of nodes connected by edges. A molecular structure can be represented as a graph, where the nodes are atoms described by an atomic feature vector, the edges are the bonds describing how the

molecule is connected and the edge weights are bonds described by a bond feature vector. In practice the nodes, edges and edge weights are represented as a tensor.

The tensor representations of molecular graphs described above are not invariant to relabeling of atomic numbers. In chemical informatics this problem is addressed by creating a molecular fingerprint, a fixed length 1D vector, which is invariant to relabeling. State of the art conventional molecular fingerprints are extended-connectivity circular fingerprints (ECFP) [46], [47]. ECFP are non-ideal for all applications as they are sparse, have vector lengths on the order of a billion with only hundreds of non-zero elements and have structures which are near identical and are encoded as if they are completely different structures. One solution to creating appropriate fingerprints is to use convolutional neural networks on graphs[46]. These neural graph fingerprints (NGF) can be trained to generate specific fingerprints for a dataset as they are unique and differentiable[48]. The pseudocode of generating a NGF compared to an ECFP is seen in Figure 1-7.

<b>Algorithm 1</b> Circular fingerprints	<b>Algorithm 2</b> Neural graph fingerprints
1: <b>Input:</b> molecule, radius $R$ , fingerprint length $S$	1: <b>Input:</b> molecule, radius $R$ , <b>hidden weights</b> $H_1^1 \dots H_R^5$ , <b>output weights</b> $W_1 \dots W_R$
2: <b>Initialize:</b> fingerprint vector $\mathbf{f} \leftarrow \mathbf{0}_S$	2: <b>Initialize:</b> fingerprint vector $\mathbf{f} \leftarrow \mathbf{0}_S$
3: <b>for</b> each atom $a$ in molecule	3: <b>for</b> each atom $a$ in molecule
4: $\mathbf{r}_a \leftarrow g(a)$ $\triangleright$ lookup atom features	4: $\mathbf{r}_a \leftarrow g(a)$ $\triangleright$ lookup atom features
5: <b>for</b> $L = 1$ to $R$ $\triangleright$ for each layer	5: <b>for</b> $L = 1$ to $R$ $\triangleright$ for each layer
6: <b>for</b> each atom $a$ in molecule	6: <b>for</b> each atom $a$ in molecule
7: $\mathbf{r}_1 \dots \mathbf{r}_N = \text{neighbors}(a)$	7: $\mathbf{r}_1 \dots \mathbf{r}_N = \text{neighbors}(a)$
8: $\mathbf{v} \leftarrow [\mathbf{r}_a, \mathbf{r}_1, \dots, \mathbf{r}_N]$ $\triangleright$ concatenate	8: $\mathbf{v} \leftarrow \mathbf{r}_a + \sum_{i=1}^N \mathbf{r}_i$ $\triangleright$ <b>sum</b>
9: $\mathbf{r}_a \leftarrow \text{hash}(\mathbf{v})$ $\triangleright$ hash function	9: $\mathbf{r}_a \leftarrow \sigma(\mathbf{v}H_L^N)$ $\triangleright$ <b>smooth function</b>
10: $i \leftarrow \text{mod}(r_a, S)$ $\triangleright$ convert to index	10: $\mathbf{i} \leftarrow \text{softmax}(\mathbf{r}_a W_L)$ $\triangleright$ <b>sparsify</b>
11: $\mathbf{f}_i \leftarrow 1$ $\triangleright$ Write 1 at index	11: $\mathbf{f} \leftarrow \mathbf{f} + \mathbf{i}$ $\triangleright$ <b>add to fingerprint</b>
12: <b>Return:</b> binary vector $\mathbf{f}$	12: <b>Return:</b> <b>real-valued</b> vector $\mathbf{f}$

Figure 1-7: Pseudocode of ECFP (left) and NGF (right). Differences are highlighted in blue. Image is from D. Duvenaud et al. [46].

A NGF is an example of message passing, also known as belief propagation, a neural network dedicated to performing learning on graphical representations[49], [50]. Message passing neural networks have the general form where the state of the graphical node at interval time interval  $t$  is related to adjacent nodes at time interval  $t - 1$ .

### 1.5.1.3 Coulomb matrix

The Coulomb matrix for machine learning was introduced by Matthias Rupp et al. [51]

The Coulomb matrix ( $M$ ), equation 1.12, is defined by the set of nuclear charges  $\{Z_I\}$  and the set of atomic positions  $\{R_I\}$  of atoms in the molecule. Coulomb matrixes have been used as features to predict the electronic structure usually solved by the Schrödinger equation[51].

$$(1.13) \quad M_{IJ} = \begin{cases} 0.5 Z_I^{2.4} & \forall I = J \\ \frac{Z_I Z_J}{|R_I - R_J|} & \forall I \neq J \end{cases}$$

Coulomb matrixes are not used to represent molecular structure in this work as they are not uniquely represented by the SMILES representation and require simulations to predict  $R_I$ . Similar to molecular graphs, Coulomb matrixes defined above are not invariant when relabeling atomic numbers but there are techniques available to avoid this problem[52], [53].

### 1.5.1.4 Autoencoded latent space representation

The autoencoder is a form of unsupervised learning where an artificial neural network is used to generate a continuous compressed latent space representation. The latent space representation can be used as a compressed molecular fingerprint to generate a predictive model. Furthermore, latent space points optimizing the predictive model can be decoded to a molecular structure. The neural network achieves dimensionality reduction by training the network to act as an identity function while reducing the number of neurons representing the molecular structure at one point in the network pipeline. Autoencoders are interesting for this work involving the discovery of new molecular structures using small datasets, as the autoencoder could be trained on different large data datasets of relevant compounds to form appropriate molecular fingerprints.

Autoencoders can encode all of the molecular vector representations described above[49], [53], [54]. Here a SMILES autoencoder from Gomez-Bombarelli et al., Figure 1-8 [54], is described. In this instance an autoencoder is used to convert the high dimension SMILES one-hot encoding representation of the molecular structure to a

lower dimensional continuous latent space. In the work of Gomez-Bombarelli et al., the latent space representation of the molecular structure has been experimentally demonstrated to be continuous where molecules with a similar molecular structure are separated by a smaller Euclidean distance. As molecules with a similar structure cluster near each other, and assuming they have similar properties, then searching the latent space would provide an efficient method to find new molecular structures with similar properties. Points in the latent space could be decoded using the decoder section of the autoencoder to generate new molecular structures, which are not limited to known molecular libraries.

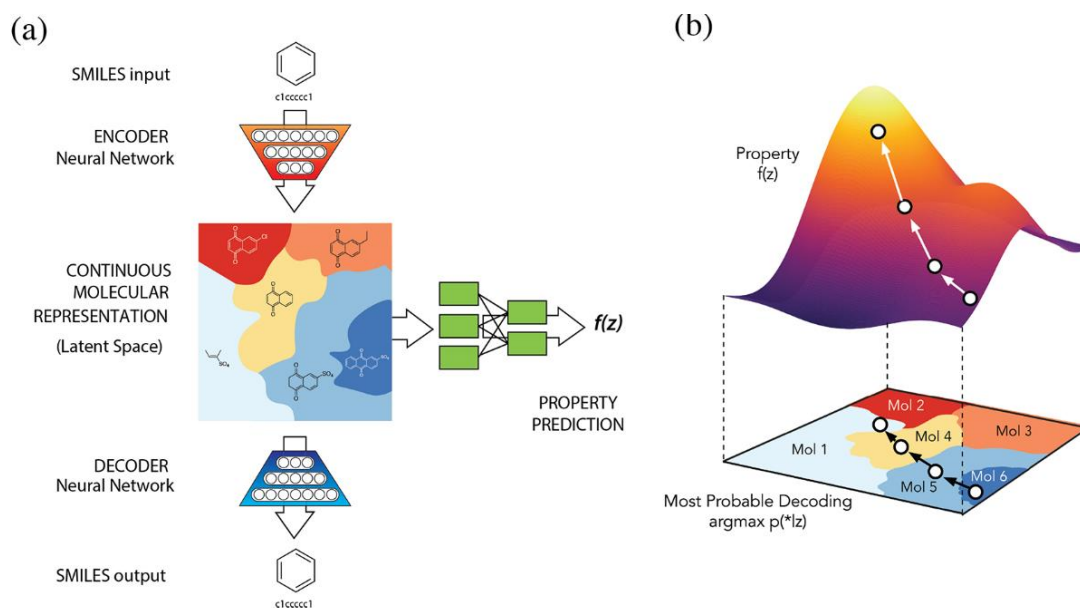


Figure 1-8: (a) A diagram of the autoencoder used for molecular design, including the joint property prediction model. Starting from the SMILES representation of a molecular structure, the encoder network converts each molecule into a vector in the latent space. Given a point in the latent space, the decoder network produces a corresponding SMILES string. A machine learning algorithm estimates the value of the target properties associated with each molecule. (b) Gradient-based optimization in continuous latent space. After training a machine learning model  $f(z)$  to predict the properties of molecules based on their latent representation  $z$ ,  $f(z)$  can be optimized with respect to  $z$  to find new latent representations expected to have high values of desired properties. These new latent representations can then be decoded into SMILES strings, at which point their properties can be tested empirically. Image and modified caption from R. Gomez-Bombarelli et al. [54]

## 1.5.2 General insight for applying machine learning models

Here we briefly discuss the theory of machine learning techniques and their recent advancement in mapping features to dependent variables. The most well known machine learning technique is linear regression. Linear regression finds a hyper plane ( $f(x)$ ) defined by a linear combination of the independent variables, which minimizes an error function, between  $f(x)$  and the dependent variable ( $y$ ).

$$(1.14) \quad f(x_j) = \sum_i \beta_i x_{i,j} + c, \quad E(y, x) = \frac{1}{N-1} \sum_{j=1}^N (y_j - f(x_j))^2$$

where  $i$  is the independent variable feature index,  $c$  is a constant,  $E(y, x)$  is the error function defined by the mean of the squared residuals,  $N$  is the number of training data and  $j$  is the index of the data point. Linear regression is extremely powerful as all continuous functions can be described as a linear combination of complete orthogonal basis sets, such as a Taylor or Fourier series. However, efficiently finding appropriate combinations of higher order terms becomes computationally intractable with complicated functions. These complicated functions are addressed with more advanced machine learning techniques, which use the same fundamental principles.

More advanced machine learning problems are optimized using an ensemble of decision tree (gradient boost) and/or neural network algorithms[55]. Decision tree algorithms are a machine learning technique based on an ensemble of weak predictors, for example a series of linear regression predictors[55]. At each split in the tree, the algorithms typically minimize an error function using a weak predictor and the remaining error is addressed by the following nodes. Decision tree algorithms have been demonstrated experimentally to be suited for applications with well-defined structured features, however, to the best of the author's knowledge there is no direct proof for this experimental observation[55]. An intuitive way to understand the effectiveness of decision tree algorithms is to assume that the space is non-continuous but sorted. An efficient route to sort such a space would be to perform a binary search which is analogous to the functionality of a decision tree. This would be difficult to achieve with a neural network because neural networks produce a continuous space. Decision trees start to perform worse with unstructured data, such as images, where higher order predictors are required.

Unstructured data are well classified by neural network algorithms, which can be rationalized due to their high model expressiveness. Model expressiveness can be described as the complexity of functions a model can capture, for example a polynomial with a high degree is more complex than that with a low degree[56]. Y. Gal demonstrates that certain regression models can have the same model expressiveness with less basis functions, demonstrating an increase in the efficiency of model expressiveness. Consider a polynomial regression model in a hierarchical structure where the regression model is composed  $L$  times. This results in a model which can capture polynomials up to degree  $(K - 1)^L$  but requires only  $K \cdot L$  basis functions. A similar flat model, a simple linear regression model, acquiring the same model expressiveness would require  $K^L$  basis functions[56].

### 1.5.3 Applying machine learning to materials science

In practical scientific lab settings, large quantities of data are limited due to the current artisan nature of sample fabrication. It is therefore unrealistic to produce very large datasets of relevant empirical results causing any machine learning model to have limited predictive capabilities. The problem of requiring large quantities of training data is further complicated in materials science when complete quantification of the whole process is near impossible, resulting in independent random fluctuations changing the outcome of an experiment. Consider a random fabrication process with  $N$  number of known variables. The expectation value of the number of known variables which randomly correlate with the change in material performance due to random fabrication error is  $N \left(\frac{1}{2}\right)^n$ , where  $n$  is the number of replicates of the same experiment. As large amounts of data and replicates are required for more accurate and precise machine learning algorithms to function, the materials science community needs to show more interest in developing high throughput synthesis and screening of materials.

The amount of available data also limits the upper bound of the model complexity. This becomes apparent by understanding how the number of independent pieces of information modifies the calculation of the mean squared error, also known as variance, which is minimized during the training of the machine learning algorithm.

$$(1.15) \quad \sigma^2 = \frac{1}{N-D} \sum_{j=1}^N (y_j - f(x_j))^2$$

where  $\sigma^2$  is the variance (square of the standard deviation),  $N$  is the number of independent data points,  $D$  is the number of parameters used to calculate  $f(x_j)$  and  $N - D$  is the number of independent pieces of information used to calculate  $\sigma^2$ . In many applications of machine learning, such as image recognition,  $N \gg D$ , however, this is not the case for the majority of applications in materials science where  $N$  is on the order of 100 to 1000 samples. When  $N = D$  the variance is undefined as the model has sufficient degrees of freedom to account for all of the degrees of freedom observed in the data. Therefore the minimum value of  $D$  is equal to  $N - 1$ . For a specific model the minimum value of  $D$  is equal to the number of hyper parameters tuned in order to optimize the model. Correcting the model variance by correcting for the number of independent pieces of information is a useful approach for the comparison of error between multiple machine learning algorithms with different numbers of hyper parameters.

Another limit on the minimum number of data points to generate a valid model is determined by the Nyquist criterion. The Nyquist criterion states that in order to correctly reproduce the space, the space needs to be evenly sampled with twice the maximum frequency inherent to the space. In electronic signal processing the Nyquist criterion is simple to verify as the sampling rate of the signal can be increased to determine whether any higher frequencies are present. In materials science it is very difficult to know whether the sampling frequency, related to the number of data point per unit of space, is sufficient to fully reproduce the space as it might not be practical to acquire more data points. However, this highlights the importance of appropriate feature generation. For example, if the dependent variable is smoothly varied with respect to the independent feature space result, less data is required to reproduce the space.

Even though it is unrealistic to produce very large datasets, machine learning techniques could be used to provide Bayesian inference in order to gain insight into the optimization of materials or processes. Next, we introduce Bayesian statistical models and how to perform Bayesian optimization using the models. Here we summarize the theoretical concepts of Bayesian statistics [56].



Given a training dataset of independent,  $X = \{x_1, \dots, x_N\}$ , and dependent,  $Y = \{y_1, \dots, y_N\}$ , variables, here we investigate how to build a probabilistic model,  $p(y^*|x^*, X, Y)$ , that determines the probability of a hypothesis ( $x^*$ ) having a specific outcome ( $y^*$ ). To achieve this, we can approximate through the process of Bayesian inference, equation 1.16.

$$(1.16) \quad p(y^*|x^*, X, Y) = \int p(y^*|x^*, w)p(w|X, Y)dw$$

Where  $p(y^*|x^*, w)$  defines the likelihood of  $y^*$  given  $x^*$  and model parameter  $w$  which is an additional variable describing some unobserved variable, also known as a latent variable. In addition, equation 1.13 includes the posterior distribution  $p(w|X, Y)$  defining the probability of  $w$  given the dataset  $\{X, Y\}$ . Examples of commonly used likelihood models are Gaussian and softmax functions used in regression and logistic problems, as seen below:

$$(1.17) \quad \begin{aligned} p(y^*|x^*, w) &= N(y^*, f^w(x^*), \sigma^2 I) && \text{(Gaussian for regression)} \\ p(y^* = l|x^*, w) &= \frac{\exp(f_l^w(x^*))}{\sum_{l'} \exp(f_{l'}^w(x^*))} && \text{(Softmax for classification)} \end{aligned}$$

Where  $f^w(x^*)$  is an arbitrary function where  $w$  can be optimized to generate an appropriate likelihood model  $p(y^*|x^*, w)$ . To determine  $p(y^*|x^*, X, Y)$ , one needs to find the optimal posterior distribution,  $p(w|X, Y)$ . Explicitly solving for  $p(w|X, Y)$  is intractable for most models but can be determined through Monte Carlo methods and approximated through variational inference. Monte Carlo methods estimate the probability distribution by generating a large number of samples until the true posterior converges in the large limit[57]. As these methods have large variance and require more computing time to approximate, here we will focus on variational inference.

Variational inference attempts to find a variational distribution,  $q_\theta(w)$ , which approximates the posterior distribution  $p(w|X, Y)$  by finding optimal parameters  $\theta$ . This can be achieved by minimizing the Kullback-Leibler divergence of  $q_\theta(w)$  and  $p(w|X, Y)$  with respect to  $\theta$ , as the Kullback-Leibler divergence is a statistical method to determine

the relative entropy (similarity) between two functions. Another route to determine  $p(w|X, Y)$  is to maximize the log of the evidence lower bound (ELBO)

$$(1.18) \quad \mathcal{L}_{VI}(\theta) = \int q_{\theta}(w) \log p(Y|X, w) dw - D_{KL}(q_{\theta}(w)||p(w)) \leq \log[p(Y|X)]$$

Where  $p(w)$  is the prior probability of  $w$  given expert knowledge and  $\mathcal{L}_{VI}(\theta)$  is the variational inference optimization objective function.  $\mathcal{L}_{VI}(\theta)$  is the analogue of the error term used in non-probabilistic regression. Maximizing  $\mathcal{L}_{VI}(\theta)$  is mathematically equivalent to minimizing the Kullback-Leibler divergence and is explicitly shown in Appendix A.

In Bayesian neural networks, there are many methods and tricks to solve  $\mathcal{L}_{VI}(\theta)$  [56]. In this work we use dropout as a Bayesian approximation. Dropout is a random process of excluding neurons during training and inference. When this technique is applied after every weight layer, the dropout neural network is mathematically equivalent to variational inference in deep Gaussian processes[58]. Next, we discuss how to use Bayesian statistics in Bayesian optimization.

Bayesian optimization is an iterative process involving a Bayesian model,  $p(y^*|x^*, X, Y)$ , for predicting the probability of the outcome of an experiment and an acquisition function for deciding which hypothesis to test next based on the Bayesian model[59]. After the hypothesis is tested,  $\{x_n, y_n\}$ , from the  $n$ th iteration, the model hyperparameters ( $\theta_n$ ) are updated with the updated dataset,  $X_{n+1} = \{X_n, x_n\}$  and  $Y_{n+1} = \{Y_n, y_n\}$ , and the process is repeated. An example acquisition function for selecting the next relevant hypothesis,  $x_{i,n}^*$ , from a set hypothesis,  $X^* = \{x_{1,n}^*, \dots, x_{m,n}^*\}$ , based on the largest expected improvement of  $y_n^*$  is seen below:

$$(1.19) \quad x_{i,n}^* = \operatorname{argmax}(\int \max(y^* - \max(Y_n), 0) \int p(y^*|\{X^*\}, w) q_{\theta_n}(w) dw dy^*)$$

Even though this process is based on purely empirical results and can provide some insight with small datasets, this process is not typically used in practice. In the literature, an organic photovoltaic blend was demonstrated to be optimized with Bayesian

optimization[60]. This thesis helps to demonstrate the effectiveness of Bayesian optimization for practical molecular discovery with realistically small datasets.

## 2 Experimental methods

This chapter provides information regarding the materials, fabrication and experimental characterization techniques used throughout this work.

### 2.1 Organic materials

The semiconducting and dielectric polymers used in this work are detailed in the next section.

#### 2.1.1 Polymer semiconductors

To investigate the device stability of amorphous polymers in this work an extended study was performed on the polymer indacenodithiophene-co-benzothiadiazole (IDT-BT) supplied by Professor Iain McCulloch from Imperial College London. IDT-BT is a highly amorphous polymer and has a high solubility in common organic solvents, a low energetic disorder and a mobility of  $\sim 1$  to  $3 \text{ cm}^2/\text{Vs}$ , which makes it a possible candidate for large area polymer transistor arrays. The remarkably high mobility is believed to be caused by the highly rigid backbone and low torsional potential which results in efficient transport along the polymer backbone[11]. The polymer has an optical band gap of  $1.7\text{eV}$ , HOMO of  $-5.3\text{eV}$  and LUMO of  $-3.6\text{eV}$ [35]. The side chains (R in Figure 2-1) can be modified; all experimental work was performed with C16 alkane side chain. Other organic semiconductors such as P3HT, diF-TES ADT, N220 and F8-BT were investigated and will be introduced appropriately.

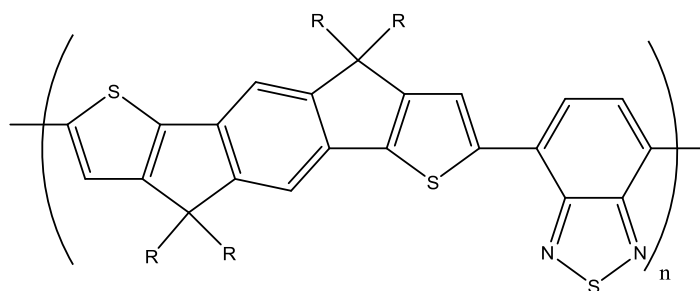


Figure 2-1: The chemical structure of indacenodithiophene-co-benzothiadiazole (IDT-BT).

### 2.1.2 Dielectrics

The interface between the dielectric and the semiconductor is important as it can affect the morphology of the semiconducting polymer films, density of deep traps and charge transfer through the semiconductor.[61], [62] Counterintuitively most high-k organic dielectrics are avoided as Veres et al. have demonstrated that the transport of charges in organic semiconductor is significantly reduced by high-k organic dielectrics[63]. This was attributed to disorder in the high-k dielectric creating random dipoles at the insulator and semiconductor interface, which increases the energetic disorder in the polymer film[63]. This thesis focuses on one dielectric polymer, poly(perfluorobutenylvinylether) (Cytop ®) used for p-type transport.

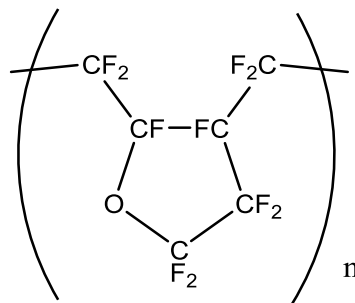


Figure 2-2: Chemical structure of Cytop ® monomer.

Cytop ® is an amorphous fluoropolymer that is transparent, hydrophobic and has good lamination properties and a low relative dielectric constant of 2.1. In IDT-BT p-type top gate bottom contact OFET applications, Cytop ® has been demonstrated to provide high mobility, environmental stability and electrical stability[43]. The Cytop ® grade used is CTL-809M, is dissolved in a non-disclosed fluorinated solvent CT-180 and supplied by Asahi Glass. Cytop appears to act as an electron trap, resulting in transport in OFETs and suppressing the n-type conductivity of ambipolar organic semiconductors resulting in p-type devices[64], [65].

## 2. Experimental methods

### 2.1.3 Molecular additives

As Nikolka et al. demonstrated, molecular additives are capable of improving the device stability in organic transistors[43]. A total of 95 different molecular additives were investigated in order to determine the relationship between the structure of the additive and the stability performance of the transistor. Molecular additives were chosen that have a diverse set of properties and functional groups in order to perform QSAR. Table 2 lists all of the molecular additives/families tested and their corresponding suppliers. The improvement and relevant features of the molecules will not be discussed here in detail and will be introduced wherever appropriate.

Table 2: List of molecular additives tested and their corresponding suppliers.

Molecule	Supplier	Molecule	Supplier
mono(alkoxycarbonyl)-tetrafluorotricyanoquinodimethanes	Adam Moule	benzodifurandione-based oligo(p-phenylene vinylene) derivatives	Christian Nielsen
2,6-diphenylcyclohexanone	Merck	Benzophenone	Merck
2-Fluorophenyl 2-nitrophenyl Ether	Merck	benzothieno-benzothiophene	Merck
1,3-Dimethyl-2-phenyl-2,3-dihydro-1H-benzimidazole	Merck	Branched PEI	Merck
1,3-Diphenyl-2-propanone	Merck	C60F36	Novald
1,4-Dicyanobenzene	Merck	Cyanoacrylates	Merck
10-Chloro-9-anthraldehyde	Merck	Deuterium oxide	Merck
2-(2H-Benzotriazol-2-yl)-4-(1,1,3,3-tetramethylbutyl)phenol	Merck	Dichlorobenzene	Merck
2-(2H-Benzotriazol-2-yl)-4,6-bis(1-methyl-1-phenylethyl)phenol	Merck	F2-BDOPV	Christian Nielsen
2-(2H-Benzotriazol-2-yl)-6-dodecyl-4-methylphenol	Merck	Fomblin Y	Merck
2-(tert-butyl)anthracene-9,10-dione	Christian Nielsen	Fumaronitrile	Merck
2,2'-(2-(tert-butyl)anthracene-9,10-diylidene	Christian Nielsen	HCL	Merck
2,2'-(perfluoronaphthalene-2,6-diylidene)dimalononitrile	Novald	Heptadecanenitrile	Merck
2,2-dimethylbiphenyl	Merck	Hexacyano-3-radialene	Christian Nielsen
2,3,5,6-Tetrafluoro-7,7,8,8-tetracyanoquinodimethane	Merck	hydrogen peroxide	Merck
2,4,7,9-Tetramethyl-5-decyne-4,7-diol, mixture of (+/-) and meso	Merck	KOH	Merck

## 2. Experimental methods

Table 2: List of molecular additives tested and their corresponding suppliers.

Molecule	Supplier	Molecule	Supplier
2,5-Difluoro-7,7,8,8-tetracyanoquinodimethane	TCI	Letrozole	Merck
2,5-Dimethyl-7,7,8,8-tetracyanoquinodimethane	TCI	Malononitrile	Merck
2-Chloro-4-nitroaniline	Merck	Molybdenum tris(1-(methoxycarbonyl)-2-(trifluoromethyl)ethane-1,2-dithiolene)	Merck
2-Fluoro-7,7,8,8-tetracyanoquinodimethane	TCI	Naphthalene-2-carbonitrile	Merck
3,3-dimethylbiphenyl	Merck	Phenylbenzotrile	Merck
3,4,7,8-Tetramethyl-1,10-phenanthroline	Merck	Poly(acrylonitrile-co-butadiene)	Merck
3,5-Di-tert-butyltoluene	Merck	Poly(acrylonitrile-co-methyl acrylate)	Merck
4,4'-(Hexafluoroisopropylidene)dianiline	Merck	Poly(Ethylene Glycol)	Merck
4,4'-Dichlorobiphenyl	Merck	Poly(ethylene succinate)	Merck
4,4-Dichlorodiphenyl Sulfone	Merck	Poly(methyl vinyl ether-alt-maleic acid)	Merck
4,4'-Dimethylbiphenyl	Merck	Poly(styrene-co-acrylonitrile)	Merck
4,4'-Di-tert-butylbiphenyl	Merck	Poly(vinylidene chloride-co-acrylonitrile)	Merck
4,5-Dioctyloxy-1,2-Benzenedicarbonitrile	Merck	Poly(vinylidene chloride-co-methyl acrylate)	Merck
4-4-Biphenyldicarbonitrile	Merck	Polyvinyl Alcohol	Merck
4-4'-Dimethoxybiphenyl	Merck	sebaconitrile	Merck
4-Dodecylbenzenesulfonic acid	Merck	Semiconducting Carbon Nanotubes	Merck
4-Dodecylbenzoic acid	Merck	Sodium Polyacrylate	Merck
4-methyl-2-biphenylcarbonitrile	Merck	Spiro	Merck
4-Phenoxybenzotrile	Merck	Stearonitrile	Merck
4-Phenyltoluene	Merck	Tetraethylene Glycol	Merck
6-tert-Butyl-2,3-naphthalenedicarbonitrile	Merck	Tetrathiafulvalene	Merck
7,7,8,8-Tetracyanoquinodimethane	Merck	Truxenone derivatives	Merck
9,10-anthraquinone	Christian Nielsen	Tween 20	Merck
Acetic Acid	Merck	$\alpha,\alpha',\alpha'$ -Tetramethyl-1,3-benzenedipropionitrile	Merck
Aminobenzotrile	Merck	Tetracyanoethylene	TCI

### 2.2 Device fabrication procedures

Here the OFET fabrication procedures are discussed. For the majority of this work, all transistors are fabricated using top-gate/bottom-contact device architectures with a channel width and length of 1 mm and 20  $\mu\text{m}$  respectively.

#### 2.2.1 Substrate cleaning

Substrates were cleaned by sonicating in deionized water with 2% volume Decon 90, deionized water, acetone and isopropyl alcohol for 10 minutes. Samples were then blow dried and placed in an oxygen plasma asher for 10 minutes at 300W.

#### 2.2.2 Photolithography for bottom contacts

The substrates were first cleaned using the standard processes. The positive photoresist LOR5B, supplied by MicroChem, was spun onto the substrate at 5000 rpm for 30s, annealed at 180°C for 5 minutes and thermally quenched on a cold metal block. A second layer of positive photoresist, S1813 supplied by MicroChem, was spun on top of the substrate at 5000 rpm for 30s, annealed at 120°C for 2 minutes and thermally quenched on a cold metal block. The photoresist coated substrates were then exposed to UV light for 14 seconds using a Karl Suss MJB3 mask aligner with the appropriate electrode design. The UV exposed substrates were then submerged in an MF319 developer, supplied by MicroChem, for 36 seconds followed by submerging the substrate in deionized water and then blow drying. The developed samples were then attached with double sided vacuum tape, supplied by Agar Scientific, to glass microscope slides, with the photoresist pointing away from the microscope slide, and then plasma ashed for 1 minute at 150C. The samples on the microscope slide were then placed in a metal evaporator where 3 nm of chromium and 20 nm of gold were deposited onto the substrates. The gold coated substrates were then removed from the microscope slides and placed in NMP, supplied by Sigma-Aldrich, for 12hrs to remove the residual photoresist from the substrates. Finally, the substrates were submerged in acetone, then



isopropyl alcohol, and then dried. The resulting bottom metal contacts were then stored in air until use.

### 2.2.3 Thin film fabrication

Here the fabrication procedure for all semiconductor and dielectric films used in devices and for spectroscopy is discussed. Unless stated otherwise, all thin dielectric and semiconductor films were spin coated from anhydrous organic solvents in an inert atmosphere where the atmospheric content of oxygen and moisture was maintained below 1 part per million. The specific solvent, spin coating parameters, and annealing times were optimized to maximize reproducibility and electrical performance.

IDT-BT was dissolved in 1,2-dichlorobenzene at 10g/L at room temperature overnight, preheated at 60°C for 15minutes directly before spin coating, spun at 500 rpm for 3s, 1500 rpm for 30s and 5000 rpm for 30s resulting in a film thickness of 50nm.

diF-TES ADT was dissolved in mesitylene at 15 mg/ml at room temperature overnight, spun at 1000 rpm for 60s on top of the substrate and annealed at 100°C for 2 minutes resulting in a film thickness of 30 nm. All diF-TES ADT devices were fabricated by Dr. Iyad Nasrallah, in the department of physics at Cambridge University.

For semiconductor containing molecular additives, solutions were mixed before spin coating with the appropriate quantity of molecular additive or fabricated films. The applied processes will be discussed where necessary.

Cytop solution supplied by Ashai Glass was diluted by mixing 1 part fluorinated solvent CT-180 with 3 parts Cytop CTL-809M. The diluted solution was spun at 500 rpm for 3s and then 2000 rpm for 20s, and then annealed at 90C for 2 minutes. The thickness of the Cytop layer is 500nm.

### 2.2.4 Transistor fabrication

Here, we discuss the fabrication procedure for p-type top-gate/bottom-contact devices. All top-gate/bottom-contact p-type devices were prepared on 0.7mm thick Corning 1737F glass substrates cut into 1.5 cm supplied by Precision Glass & Optics. The substrates were then cleaned and interdigitated bottom contacts were deposited using the procedures described above. The substrates were then plasma ashed at 300W for 10 minutes. The semiconducting layer followed by a Cytop layer were then deposited on top of the substrate using the procedures described above. Once the semiconductor layer was deposited the device was always maintained under a dry nitrogen atmosphere. A 30 nm aluminum gate electrode was evaporated on top of the cytop layer and patterned using a shadow mask.

## 2.3 Experimental characterization

Here all experimental characterization fabrication procedures used in this work are examined.

### 2.3.1 Electrical characterization

The electrical characterizations, such as transfer curves, output curves and a variety of stress characteristics of the transistors, were measured in an inert environment with 1 part per million oxygen and moisture by a Karl Suss probe station. The probe station was connected to an Agilent 4155B semiconductor parameter analyzer (SPA). The SPA was controlled by custom LabView software generated by unknown previous PhD students. All measurements were performed under orange light from the laboratory lights unless otherwise specified.

Unless stated otherwise, all the transfer and output characteristics were taken on p-type transistors with  $W/L$  of 50. The saturation and linear transfer curves were obtained by setting the drain source voltage at -5V and -50V respectively and sweeping the gate voltage forward and back from +20V to -50V in steps of 1V. The output curves at

different gate voltages from 0 to -50V in steps of -10V were measured by sweeping the drain source voltage from 0V to -50V in steps of -1V.

The procedure for quantifying the electrical stress of transistors used in OLED applications is described here. There are two regimes that have different stressing degradation and procedures: constant current stress and depletion stress.

Constant current stress, or negative bias stress for p-type devices, simulates the transistor constantly supplying the same current to an OLED in order to maintain a set light fluence. During the measurement, the transistor is kept in the saturation regime, similar to transistor backplane applications, by connecting the gate electrode to the drain electrode and controlling the drain voltage to maintain the same current through the transistor during the electrical stress for a set amount of time. The current value maintained through the OFET with channel  $W/L$  of 50 was 2.5  $\mu\text{A}$ , that 50 nA needs to be maintained through a transistor with a  $W/L$  of 1 for OLED applications[66]. Typical drain voltages are between -5V and -50V. After the set period of stress time the transistor gate, drain and source all grounded simulating transistor recovery. The degradation of the transistor is monitored by the change in parameters such as the voltage threshold, mobility and contact resistance by measuring either the transfer or output characteristics during the stress and recovery period.

Depletion stress, or positive bias stress for p-type devices, simulates the transistor in OLED applications where the transistor is turning off the pixel. During the measurement, the gate, drain and source are maintained at 50V, -5V and 0V respectively for a set amount of time after which the device recovery is measured. The drain voltage was chosen as it is representative of the voltages used during constant current stress. The gate voltage of 50V was chosen as the electric field through the Cytop is at the dielectric breakdown of Cytop. The same metric used for the constant current stress was used to quantify the stress and recovery of the device. To control the light exposure of the transistor during depletion stress, the orange laboratory lights were turned on and off.

### 2.3.2 Ultra violet to visible absorption spectroscopy

As light in the ultra violet and visible spectrum (UV-VIS) interacts with the electron cloud of matter, UV-VIS absorption techniques provide a simple way to probe changes in the quantum structures of molecules. UV-VIS is capable of detecting changes in the molecule such as the generation of charge transfer complex, ionization pairs, induced polarons and a general change in chemical structure.

Light interacts with matter in the UV-VIS region by changing the transition probability of electrons between occupied and unoccupied molecular orbitals. The transition probability of electrons in a single molecule can be described by Fermi's golden rule of oscillating electrons where the motion of atomic nuclei and electrons in a molecule can be separated (Born-Oppenheimer approximation). The probability of a single molecule absorbing a photon ( $\Gamma$ ) of specific energy ( $E$ ) can be described as a summation of all possible transition probabilities capable in the orbital states ( $\Omega$ ):

$$(2.1) \quad \Gamma(E) = \sum_{i,f \in \Omega} \frac{2\pi}{\hbar} |\langle \phi_f | H'(E) | \phi_i \rangle|^2 p_f$$

where  $\hbar$  is the reduced Planck constant,  $|\langle \phi_f | H'(E) | \phi_i \rangle|$  is the expectation of the transition probability from an initial state ( $i$ ) to a final state ( $f$ ) with an incident photon with energy  $E$ , and  $p_f$  is the density of final states. By neglecting reflection and interference effects due to inhomogeneous refractive indexes in the sample with thickness  $z$ , the transmission of a beam of light with energy  $E$  through materials which is absorbed with probability  $\Gamma(E)$  can be described by the Beer-Lambert Law:

$$(2.2) \quad T(E) = e^{-\sum_{i=1 \dots N} \Gamma_N(E) \cdot A_N \int_0^z n_i(z') dz'}$$

where  $N$  is the number of different chemical species with different  $\Gamma(E)$ ,  $A_N$  represents the geometric cross section of molecule  $i$  and  $n_i(z')$  is the density of molecule  $i$  at a particular layer,  $z'$ , in the sample. As the absorption spectrum is defined as a logarithm of the ratio of the transmission spectrum relative to the blank spectrum with no sample, the absorption spectrum scales linearly with the concentration of light absorbing species. Due to this linearity the absorption spectrum is particularly useful for determining the quantity of chemical species in a film or solution relative to other

samples. Unless stated otherwise all UV-VIS spectra of solutions and thin films were taken using a Shimadzu UV-3600 Plus spectrometer.

### 2.3.3 Charge accumulation spectroscopy

Charge accumulation spectroscopy (CAS) developed by Dr. Riccardo Di Pietro in his PhD thesis observes the change in the UV-VIS absorption spectrum of an OFET by accumulating charge carriers in the organic. All CAS OFETs are fabricated using the standard p-type top-gate/bottom-contact architecture, except that the active area of the transistor was increased by changing the channel width and length to 19.4 cm and 80  $\mu\text{m}$  respectively and replacing the aluminum gate with a semitransparent aluminum gate. The large area allows the full beam of the spectrometer to pass through an area of charge accumulation. The semitransparent electrode is deposited by evaporating 8 nm of aluminum and then exposed to an oxygen rich atmosphere resulting in a semitransparent conductive electrode.

CAS is particularly useful in being able to quantify the amount of carriers, polaron induced absorption and bleaching of charge carriers in the polymer HOMO. To conform to standard practices developed by Riccardo, the CAS spectrum is presented as the ratio of the change in the transmission spectrum ( $\Delta T$ ) after charge accumulation (gate voltage is non zero) to the initial spectrum ( $T$ ) before charge accumulation (gate voltage is zero). As the transmission spectrum through the sample is related to the Beer-Lambert Law, the CAS spectrum ( $\Delta T/T$ ) does not scale linearly with polaron induced absorption, however, as  $\Delta T/T \ll 1$  it is a reasonable approximation to scale  $\Delta T/T$  with polaron induced absorption. All CAS spectra were taken using an Agilent Cary 6000i UV-VIS-NIR double-beam Spectrophotometer. For clear examples of CAS spectra with high signal to noise, please refer to Dr. Iyad Nasrallah's PhD Thesis.

In this work, I am particularly interested in using the CAS setup in order to determine whether a charge transfer occurs between the IDT-BT semiconducting polymer and molecular dopant F4-TCNQ during positive gate bias stress (PBS). As it is neutral and ionized, F4-TCNQ has a distinct UV-VIS transmission spectrum. It is conceivable that measuring the change of the transmission spectrum before and after PBS would provide

## 2. Experimental methods

spectral evidence of the ionized F4-TCNQ during PBS[67]. This is challenging as large electrostriction, where the dielectric changes shape in the presence of an electric field, and uneven compression of the dielectric due to the electrostatic force between the gate and the channel of the semiconductor warps the shape of the dielectric during PBS. This is a particular problem when using the dielectric Cytop as it is more malleable in comparison to other dielectrics such as PMMA. The warped dielectric modifies the path of the light through the stack and can create interference effects and possibly change the capacitance[68].

To avoid electric field stress in the dielectric during PBS, the best practice was determined experimentally to prestress the dielectric with the same magnitude and distribution of electric field by applying negative gate bias stress (NBS) before applying PBS. To apply the same electric field across the dielectric during NBS and PBS stress the magnitude of the gate voltage during NBS and PBS was the same, the drain and source electrodes were grounded and the polymer was sufficiently doped to maintain some conductivity during PBS. The measurement protocol used to measure the UV-VIS spectrum before and after PBS with no dielectric stress effects is seen in Figure 2-3 and listed below:

1. Initially (T0) the transfer characteristics are measured.
2. Directly after the transfer measurement the gate voltage was set at -50V.
3. One hour later (T1) the UV-VIS spectrum and then the transfer characteristics were measured.
4. Directly after transfer characteristics were measured the gate voltage was set to 50V.
5. After 1 minute (T2) the gate voltage was set to -50V and the UV-VIS spectrum was measured and the transfer characteristics (T2).

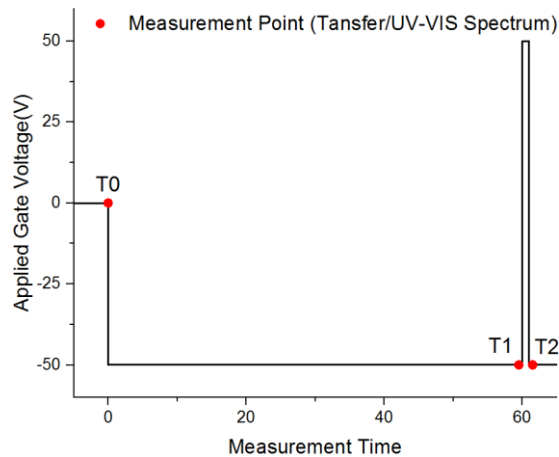


Figure 2-3: Measurement protocol to avoid electric field stress in polymer dielectric during PBS.

To demonstrate that this protocol is effective at mitigating dielectric stress effects in Cytop, the change in the UV-VIS spectrum of a F6-TCNNQ doped IDT-BT CAS OFET during the NBS and PBS (Figure 2-4 A) period of the stated PBS protocol was compared. Figure 2-4 A demonstrates that there is a large change in  $\Delta T/T$  during NBS compared to PBS which is expected as the dielectric should be stressed during the NBS period which mitigates further stress in the PBS period. The normal CAS spectrum during NBS is not observed as the spectrum is dominated by artifacts related to the warping of the dielectric. The minimal change in the PBS spectrum (Figure 2-4 A) compared to the CAS spectra (Figure 2-4 B) suggests minimal or no charge trapping has occurred during PBS, which is consistent with the stable voltage threshold of the transfer characteristics during NBS and PBS (Figure 2-4 C).

## 2. Experimental methods

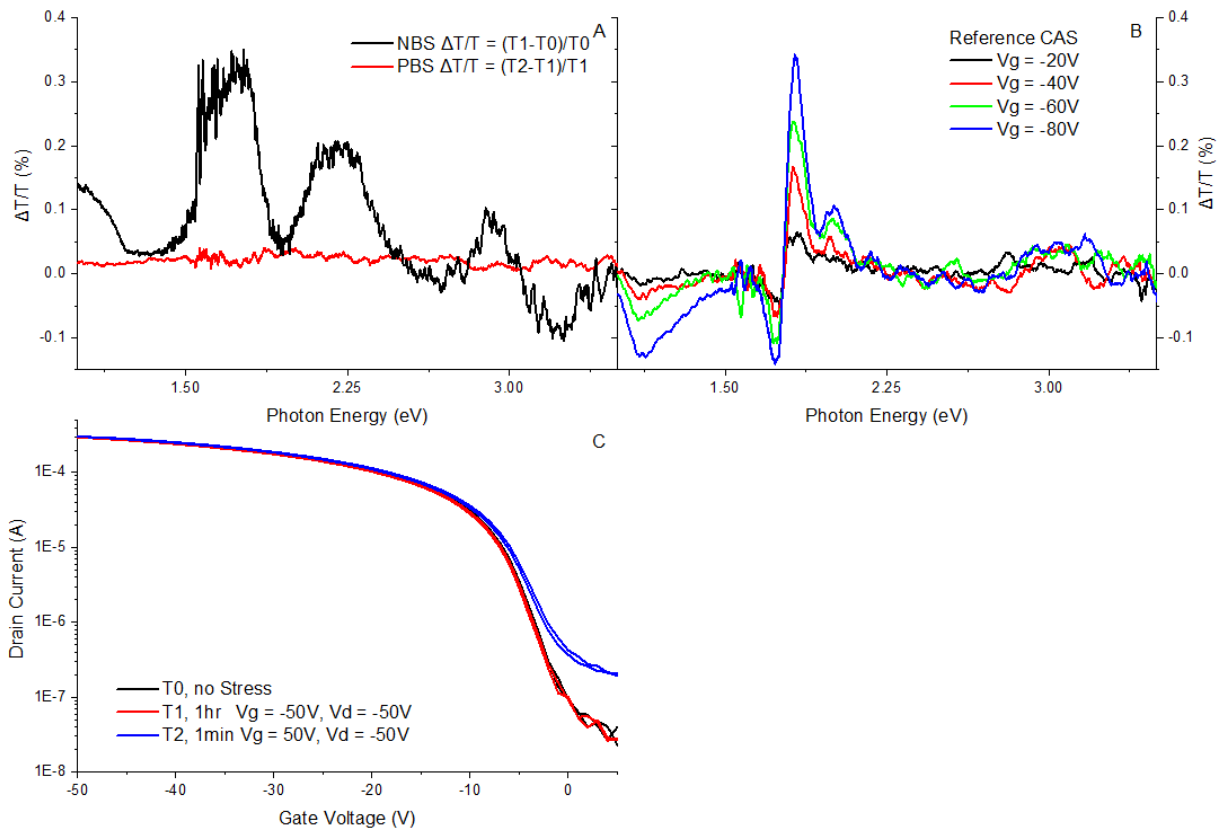


Figure 2-4: A) CAS spectrum of IDT-BT with 2 weight percent F6-TCNNQ at -20V compared to the percent change of transmission spectrum after PBS compared to directly before the stress  $\Delta T/T = (T2-T1)/T1$  B) Reference CAS spectrum of the same device after stress C) Transfer characteristics of the same device before stress, after NBS and after PBS.

### 2.3.3.1 Fourier transform infrared spectroscopy

Infrared spectroscopy detects intramolecular vibrations due to chemicals bonds present in the sample. Common vibrational modes observed in organic materials include stretching, scissoring, rocking, wagging and twisting. To determine the chemical structures responsible for a spectrum there are libraries of specific regimes where vibrational modes of certain structures reside, however, the exact vibrational mode will depend on the overall environment. An appropriate infrared absorption spectrum reference is Infrared and Raman Characteristic Group Frequencies: Tables and Charts[69].



Fourier transform infrared spectroscopy is a technique to measure the infrared absorption spectrum of a sample. The spectrometer uses a Michelson interferometer where a beam of coherent light is split into two paths; one beam is reflected off a stationary mirror and the other is bounced off a moving mirror. The two beams are then recombined and passed through the sample resulting in a beam of light where the constructive and destructive interface of each wavelength of light periodically depends on the position of the moving mirror and the absorption spectrum of the sample. The absorption spectrum is determined by computationally taking the Fourier transform of the detected combined light beam as a function of the moving mirror. The measurements were performed in standard atmosphere using a Thermo Fisher Scientific Nicolet iS10 FTIR instrument.

In this thesis FTIR spectroscopy was used to characterize the degree of charge transfer between molecular dopants containing nitrile groups and semiconducting polymers, and to confirm the chemical signature of chemical reaction byproducts. This was achieved by characterizing the CN stretch of nitrile groups on the dopant commonly associated with the formation of an ion pair and charge transfer complex[19], [43], [70].

### 2.3.4 Nuclear magnetic resonance spectroscopy

Nuclear magnetic resonance spectroscopy (NMR) uses a Zeeman Effect to split the energies of an atomic nucleus with non-zero spin into two energy levels by applying a strong magnetic field. The splitting of the energy levels allows the absorption of a perturbative radio frequency pulse which causes the nuclear spin to precess around the strong magnetic field. As the nuclear spin relaxes back to thermal equilibrium, it emits a detectable radio wave with a specific frequency dominated by the nucleus structure and weakly influenced by the local intramolecular magnetic field determined by other magnetic species in the film. This weak shift in the frequency is characteristic of specific compounds which can be used to classify the structure of the molecule. In this work NMR was used to help classify unknown chemical byproducts of chemical reactions of TCNQ with water.

All samples for NMR were fabricated by the author and will be described later in this work. All NMR measurements were performed by Dimitrios Simatos, Dr. Katharina

Marker and the NMR services in the chemistry department at Cambridge University. Analysis of the NMR was performed by Dr. Ian Jacobs and Malgorzata Nguyen in the physics department at Cambridge University.

### 2.3.5 Scanning probe microscopy

All scanning probe microscopy experiments including Atomic Force Microscopy, Conductive Atomic Force Microscopy and Microwave Scanning Microscopy were performed by Filipe Richheimer supervised by Dr. Fernando Castro in the National Physical Laboratory in London. All films were fabricated on silicon substrates with 100 nm of thermally evaporated gold at a rate of 0.1 Å/s to produce a uniform film with a surface roughness of 0.5 nm.

To determine the thickness of films above 100nm, a scratch was made in the polymer film and the thickness was measured using a Veeco Dektak IIA.

## 2.4 Statistical methods

Here we discuss the specifics of the features and data used in generating the machine learning model, selection of the machine learning model and the databases searched in this thesis to find new molecular structures. All software and data used in this thesis will be uploaded to <https://github.com/OE-FET> upon submission of papers related to this thesis. All software was written in python using the Scikit-learn, RDKit, Keras, NGF and Tensorflow libraries [71]–[75].

### 2.4.1 Feature generation

In this work we explored three different techniques to generate feature vectors based on molecular structure, one-hot encoding, variational autoencoders and neural graph fingerprints.

### 2.4.1.1 SMILES to one-hot encoding

For the specific algorithm of one-hot encoding method, please see Chapter 1. Valid characters include "7", "6", "o", "]", "3", "s", "(", "-", "S", "/", "B", "4", "[", ")", "#", "I", "l", "O", "H", "c", "1", "@", "=", "n", "P", "8", "C", "2", "F", "5", "r", "N", "+", "\\\" and \" \".

The maximum string length was set at 120. The resulting shape of a one-hot encoded SMILE was (35, 120). All SMILES were canonicalized in the Kekulize form using RDKit.

### 2.4.1.2 Variational auto encoders

The autoencoder latent space representation was generated from the Gómez-Bombarelli et al. autoencoder [54], [76]. The autoencoder was trained on 250,000 molecules randomly selected from the Zinc 15 data base in addition to molecular structures tested in this thesis. The variational autoencoder hyperparameters were identical to those of Gómez-Bombarelli et al. [54]. The input to the VAE is the SMILES one-hot encoding described above.

### 2.4.1.3 Neural graph fingerprint

A molecular graph representation of a molecule was generated by converting the SMILES representation to a molecular object in RDKit which was then converted to three tensors describing molecular graphs (atom nodes, edges and bond features).

RDKit does not handle the aromaticity correctly for all quinone structures. For example, the RDKit represents the ring in tetracyanoquinodimethane (TCNQ) as aromatic, which is not correct. To overcome this issue, aromaticity was redefined. Each atom in an aromatic molecular ring was checked to determine whether it was connected to another atom via a single bond or a double bond which was in another aromatic ring, or connected to one by a conjugated chain. If not, all bond features from the specific atom were set as non-aromatic.

The neural graph fingerprint (NGF) model used was an updated version of Keiser's implementation of Duvenaud et al. NGF [46], [74]. The inputs to the NGF generator are three tensors describing molecular graphs. The NGF generator was not trained and consists of small random weights between  $\pm 0.01$ . The NGF hyperparameters were the

## 2. Experimental methods

following: the graph convolution width was 16, fingerprint length was 200 and max circular radius was 5. The same atom and bond features were used to generate the NGF as the parameters used in extended-connectivity circular fingerprints [47].

### 2.4.2 Data used in machine learning

A list of all of the molecular solid state additives used to build the predictive model and their corresponding performance metrics can be seen in Table 3. If small molecules demonstrated any significant improvement in OFET performance with or without water that was caused by acidic doping or forming an azeotrope with water, they were classified as category 1, and everything else was classified as category 2. Additives not tested in this work are noted with the appropriate reference.

Table 3: Solid state molecular additives and corresponding performance metric used to build machine learning models.

Molecule	Category
Fumaronitrile	2
N-butyl acetate[34]	2
Isopropyl alcohol[34]	2
Ethanol[34]	2
Toluene[34]	2
Xylene[34]	2
Cyclohexane[34]	2
Chlorobenzene	2
Tetralin[34]	2
Benzene[34]	2
Methanol[34]	2
Butanedithiol[34]	2
(Methyl)naphthalene	2
Poly(ethylene succinate)	2
polyamine	2
2-(2H-Benzotriazol-2-yl)-4,6-bis(1-methyl-1-phenylethyl)phenol	2
2-(2H-Benzotriazol-2-yl)-4-(1,1,3,3-tetramethylbutyl)phenol	2
6-tert-Butyl-2,3-naphthalenedicarbonitrile	2
a,a,a'-Tetramethyl-1,3-benzenedipropionitrile	2
10-Chloro-9-anthraldehyde	2
4-Phenyltoluene	2
4,4'-Dimethylbiphenyl	2
Heptadecanenitrile	2
4,4'-Di-tert-butylbiphenyl	2
3,4,7,8-Tetramethyl-1,10-phenanthroline	2
4-Phenoxybenzonitrile	2

## 2. Experimental methods

Table 3: Solid state molecular additives and corresponding performance metric used to build machine learning models.

Molecule	Category
4,5-Dioctyloxy-1,2-Benzenedicarbonitrile	2
4,4'-(Hexafluoroisopropylidene)dianiline	2
2,4,7,9-Tetramethyl-5-decyne-4,7-diol,mixture of (+/-) and meso	2
2-Chloro-4-nitroaniline	2
2-(2H-Benzotriazol-2-yl)-6-dodecyl-4-methylphenol	2
Tetraethylene Glycol	2
Tween 20	2
4,4-Dichlorodiphenyl Sulfone	2
4,4'-Dichlorobiphenyl	2
4-4'-Biphenyldicarbonitrile	2
4-4'-Dimethoxybiphenyl	2
2,2-dimethylbiphenyl	2
2-Fluorophenyl 2-nitrophenyl Ether	2
3,3-dimethylbiphenyl	2
Phenylbenzotrile	2
4-methyl-2-biphenylcarbonitrile	2
Malononitrile	2
Naphthalene-2-carbonitrile	2
3,5-Di-tert-butyltoluene	2
Stearonitrile	2
2,6-diphenylcyclohexanone	2
1,3-Diphenyl-2-propanone	2
Poly(Ethylene Glycol)	2
Polyvinyl Alcohol	2
Cyanoacrylate	2
4-dodecylbenzoic acid	2
Benzophenone	2
Acetic Acid	2
benzodifurandione-based oligo(p-phenylene vinylene)	2
difluoro-benzodifurandione-based oligo(p-phenylene vinylene)	2
9,10-anthraquinone	2
2-(tert-butyl)anthracene-9,10-dione	2
2-(4-(dicyanomethyl)phenyl)-2-(tetrahydrofuran-2-yl)malononitrile	2
octyl 2-cyano-2-(4-(dicyanomethyl)phenyl)acetate	2
Aminobenzonitrile	2
4-dodecylbenzenesulfonic acid	2
2-Fluoro-7,7,8,8-tetracyanoquinodimethane	1
2,2'-(perfluoronaphthalene-2,6-diylidene)dimalononitrile	1
2,2',2''-(cyclopropane-1,2,3-triylidene)trimalononitrile	1
Tetrafluorotetracyanoquinodimethane	1
2,5-Difluoro-7,7,8,8-tetracyanoquinodimethane	1
t-Butyl-tetracyano-9,10-anthraquinodimethane	1
11,11-dicyano-9-anthraquino-10-methane	1
11,11,12,12-tetracyano-9,10-anthraquinodimethane	1
trimethyl 2,2',2''-(5H-diindeno[1,2-a:1',2'-c]fluorene-5,10,15-triylidene)(2E,2'E,2''E)-tris(2-cyanoacetate)	1
triethyl 2,2',2''-(5H-diindeno[1,2-a:1',2'-c]fluorene-5,10,15-triylidene)(2E,2'E,2''E)-tris(2-cyanoacetate)	1

Table 3: Solid state molecular additives and corresponding performance metric used to build machine learning models.

Molecule	Category
methyl 2-cyano-2-(4-(dicyanomethylene)cyclohexa-2,5-dien-1-ylidene)acetate	1
2,5-Dimethyl-7,7,8,8-tetracyanoquinodimethane	1
11,11,12,12-Tetracyanonaphtho-2,6-quinodimethane	1
Tetracyanoethylene	1
octyl 2-cyano-2-(4-(dicyanomethylene)cyclohexa-2,5-dien-1-ylidene)acetate	1
Tetracyanoquinodimethane	1

### 2.4.3 Predictive model generation

Here we build a series of neural networks with different hyperparameters to determine the robustness of the feature vector.

In large data sets, the data is broken into three disjoint sets: training, cross validation and test sets. The model is trained on the training set, the hyperparameters are optimized on the cross validation set and model performance is determined by the test set. As the total dataset of molecular additives is small, here we use the leave-one-out cross validation (LOOCV) to determine the overall performance of the network and do not use a cross validation set to optimize the hyperparameters. LOOCV operates as the following: for a data set of length  $n$ , LOOCV trains  $n$  models on  $n-1$  examples in the data and tests the specific model on the left out data point. The performance of the model is the summation of all of the  $n$  models. The LOOCV performance of the neural networks with different hyperparameters and molecular feature representation can be seen in Table 4. The optimal hyperparameters for each model can be seen in Table 5. Additional hyperparameters not optimized include `learning_rate:= 0.0005`, `beta_1 := 0.9`, `beta_2:= 0.999`, `epsilon:= 1E`, `schedule_decay:= 0.5`, and `hidden_layer growth_factor:= 0.5`. The best basis set appears to be the NGF and will be discussed in more detail in Chapter 6.

## 2. Experimental methods

Table 4: The LOOCV performance of the neural networks with different hyperparameters and molecular feature representation.

Neural network hyperparameters						SMILES		SMILES VAE		NGF	
Model	Dropout	Hidden Layers	Hidden Dim	regl2	Activation	True Positives	True Negatives	True Positives	True Negatives	True Positives	True Negatives
0	0	0	0	0.1	sig	0.52	0.98	0.76	0.92	0.88	1
1	0	0	0	0.1	relu	0.52	0.98	0.76	0.92	0.88	1
2	0	1	200	0.1	sig	0	1	0	1	0	1
3	0	1	200	0.1	relu	0.47	1	0.64	0.96	0.88	0.98
4	0	1	200	0.01	sig	0.58	0.98	0.7	0.96	0.88	1
5	0	1	200	0.01	relu	0.64	0.96	0.76	0.94	0.88	1
6	0	1	200	0.001	sig	0.64	0.96	0.76	0.94	0.88	1
7	0	1	200	0.001	relu	0.64	0.96	0.76	0.94	0.88	1
8	0	1	100	0.1	sig	0	1	0	1	0	1
9	0	1	100	0.1	relu	0.41	1	0.64	0.96	0.88	0.98
10	0	1	100	0.01	sig	0.58	0.98	0.76	0.96	0.88	1
11	0	1	100	0.01	relu	0.64	0.96	0.7	0.94	0.88	1
12	0	1	100	0.001	sig	0.64	0.96	0.76	0.92	0.88	1
13	0	1	100	0.001	relu	0.64	0.96	0.76	0.92	0.88	1
14	0	1	20	0.1	sig	0	1	0	1	0	1
15	0	1	20	0.1	relu	0.47	1	0.64	0.96	0.88	0.98
16	0	1	20	0.01	sig	0.58	0.98	0.76	0.92	0.88	1
17	0	1	20	0.01	relu	0.64	0.96	0.7	0.94	0.88	1
18	0	1	20	0.001	sig	0.64	0.96	0.76	0.92	0.88	1
19	0	1	20	0.001	relu	0.64	0.96	0.76	0.92	0.88	1
20	0	2	200	0.1	sig	0	1	0	1	0	1
21	0	2	200	0.1	relu	0	1	0.47	0.98	0.64	0.96
22	0	2	200	0.01	sig	0.52	0.98	0.64	0.96	0.88	0.98
23	0	2	200	0.01	relu	0.64	0.96	0.76	0.94	0.88	1
24	0	2	200	0.001	sig	0.64	0.96	0.76	0.94	0.88	1
25	0	2	200	0.001	relu	0.64	0.96	0.76	0.94	0.88	1
26	0	2	100	0.1	sig	0	1	0	1	0	1
27	0	2	100	0.1	relu	0	1	0.47	0.98	0.7	0.96
28	0	2	100	0.01	sig	0.52	0.98	0.64	0.96	0.88	0.98
29	0	2	100	0.01	relu	0.64	0.96	0.76	0.94	0.88	1
30	0	2	100	0.001	sig	0.64	0.96	0.76	0.94	0.88	1
31	0	2	100	0.001	relu	0.64	0.96	0.76	0.94	0.88	1
32	0	2	20	0.1	sig	0	1	0	1	0	1

## 2. Experimental methods

Table 4: The LOOCV performance of the neural networks with different hyperparameters and molecular feature representation.

Model	Neural network hyperparameters					SMILES		SMILES VAE		NGF	
	Dropout	Hidden Layers	Hidden Dim	regl2	Activation	True Positives	True Negatives	True Positives	True Negatives	True Positives	True Negatives
33	0	2	20	0.1	relu	0	1	0.41	0.98	0.58	0.96
34	0	2	20	0.01	sig	0	0.98	0.64	0.96	0.88	0.98
35	0	2	20	0.01	relu	0.64	0.96	0.7	0.94	0.88	1
36	0	2	20	0.001	sig	0.64	0.96	0.76	0.92	0.88	1
37	0	2	20	0.001	relu	0.64	0.96	0.76	0.92	0.88	1
38	0.1	0	0	0.1	sig	0.52	0.98	0.76	0.92	0.88	1
39	0.1	0	0	0.1	sig	0.52	0.98	0.76	0.92	0.88	1
40	0.1	1	200	0.1	sig	0	1	0	1	0	1
41	0.1	1	200	0.1	relu	0.35	1	0.64	0.96	0.88	0.98
42	0.1	1	200	0.01	sig	0.52	0.98	0.7	0.92	0.88	1
43	0.1	1	200	0.01	relu	0.64	0.96	0.76	0.94	0.88	1
44	0.1	1	200	0.001	sig	0.64	0.96	0.76	0.94	0.88	1
45	0.1	1	200	0.001	relu	0.64	0.96	0.76	0.94	0.88	1
46	0.1	1	100	0.1	sig	0	1	0	1	0	1
47	0.1	1	100	0.1	relu	0.41	1	0.64	0.96	0.88	0.98
48	0.1	1	100	0.01	sig	0.52	0.98	0.76	0.94	0.88	1
49	0.1	1	100	0.01	relu	0.64	0.96	0.7	0.94	0.88	1
50	0.1	1	100	0.001	sig	0.64	0.96	0.76	0.92	0.88	1
51	0.1	1	100	0.001	relu	0.64	0.96	0.76	0.92	0.88	1
52	0.1	1	20	0.1	sig	0	1	0	1	0	1
53	0.1	1	20	0.1	relu	0.41	1	0.64	0.96	0.88	0.98
54	0.1	1	20	0.01	sig	0.52	0.98	0.7	0.96	0.88	1
55	0.1	1	20	0.01	relu	0.64	0.96	0.76	0.94	0.88	1
56	0.1	1	20	0.001	sig	0.64	0.96	0.76	0.9	0.88	1
57	0.1	1	20	0.001	relu	0.64	0.96	0.76	0.92	0.88	1
58	0.1	2	200	0.1	sig	0	1	0	1	0	1
59	0.1	2	200	0.1	relu	0	1	0.41	0.98	0.58	0.96
60	0.1	2	200	0.01	sig	0.35	1	0.64	0.96	0.88	0.98
61	0.1	2	200	0.01	relu	0.64	0.96	0.76	0.94	0.88	1
62	0.1	2	200	0.001	sig	0.58	0.96	0.76	0.94	0.88	1
63	0.1	2	200	0.001	relu	0.64	0.96	0.76	0.94	0.88	1
64	0.1	2	100	0.1	sig	0	1	0	1	0	1
65	0.1	2	100	0.1	relu	0	1	0.47	0.98	0.58	0.96



## 2. Experimental methods

Table 4: The LOOCV performance of the neural networks with different hyperparameters and molecular feature representation.

Neural network hyperparameters						SMILES		SMILES VAE		NGF	
Model	Dropout	Hidden Layers	Hidden Dim	regl2	Activation	True Positives	True Negatives	True Positives	True Negatives	True Positives	True Negatives
66	0.1	2	100	0.01	sig	0.29	0.98	0.64	0.96	0.88	0.98
67	0.1	2	100	0.01	relu	0.64	0.96	0.7	0.94	0.88	1
68	0.1	2	100	0.001	sig	0.64	0.96	0.76	0.94	0.88	1
69	0.1	2	100	0.001	relu	0.64	0.96	0.76	0.94	0.88	1
70	0.1	2	20	0.1	sig	0	1	0	1	0	1
71	0.1	2	20	0.1	relu	0	1	0.29	0.98	0.52	0.96
72	0.1	2	20	0.01	sig	0	1	0.64	0.96	0.88	0.98
73	0.1	2	20	0.01	relu	0.58	0.96	0.76	0.92	0.88	1
74	0.1	2	20	0.001	sig	0.64	0.96	0.76	0.92	0.88	1
75	0.1	2	20	0.001	relu	0.64	0.96	0.76	0.9	0.88	1

Table 5: Neural network hyperparameters used for each neural network.

	Hidden Layers	Initial hidden Dimensions	Activation	Regl2	Dropout
SMILES	2	100	relu	0.01	0.1
SMILES VAE	2	100	relu	0.001	0.1
NGF	2	100	relu	0.01	0.1

### 2.4.4 Database searching

All tranches in the Zinc15 database were explored with weights below 500 Daltons in addition to the complete PubChem Database [77], [78]. Structures expected to work based on the predictive model were stored. To illustrate the confidence in the prediction, the Z-score was calculated for each molecule using the expectation value and standard deviation from both labels. The expectation value and standard deviation were approximated for each label by performing Monte Carlo dropout during the predicting phase [58].

## 2. Experimental methods

---

To find a range of different molecular structures that were predicted, the NGFs of the predicted structures were encoded using principle component analysis, reducing the dimensions from 200 to 50, and then clustered using k-mean. The number of clusters was optimized using the elbow method.

# 3 Searching for solid state additives

## 3.1 Introduction

As important semiconductor capabilities are continuously improving in solution processed electronic semiconductors such as perovskite, amorphous oxides and organic semiconductors, the future of solution based devices is promising. Consistently the major limiting factor for device application is that solution processed devices have poor stability. In the literature there is a lot of evidence that stability can be improved through encapsulation, doping and contact modification in solution processed semiconductors. In particular the work of Nikolka et al. on stabilising organic semiconductors is remarkable as using both liquid and solid state additives appears to significantly suppress the formation of traps responsible for device degradation creating near perfect device characteristics. The current understanding is that the liquid additives form azeotropes with water which displace and dissolve water in the film. Similarly, non-doping solid state additives compete with water to fill voids that would otherwise be filled with water and possibly bond water to their structure. As all low temperature solution processed semiconductors are susceptible to atmospheric defects, complete scientific understanding of the direct mechanisms responsible for improving stability could have far-reaching consequences for all solution based processes and make solution based semiconductors commercially viable.

In this chapter the knowledge of the role of solid state additives in stabilising semiconducting polymers is extended by investigating over 95 new molecular additives to determine how they stabilize semiconducting polymers. The large data set could provide understanding of how the mechanisms of the solid state additives function and what chemical structures to avoid, which cannot be practically determined by simulations[43]. Furthermore, as small molecule additives have been demonstrated by Nikolka et al. to be thermally unstable in semiconducting polymers, large molecular additives (polymer, polymerizing and CNT) which would interlace with the semiconducting polymer could provide improved thermal stability.

## 3.2 Searching for p-type solid state additives

In this section p-type IDT-BT OFETs are fabricated using the top-gate/bottom-contact architecture with 2 weight percent of the solid state additives. For polymer additives tested, the weight concentration was varied from 0.1 to 2 weight percent; and the optimum concentration is presented below. For the full list of molecular additives tested, please see the methods section. All additives were tested twice in different batches of OFETs to reduce the possibility that a mistake was performed during the processing. If any molecular additive demonstrated a significant improvement in device characteristics, two additional batches of devices were fabricated to confirm that the improvement was reproducible. Here we provide a brief comparison of devices with liquid and solid state stabilising additives to visually demonstrate the improvement in OFET performance (Figure 3-1 and Figure 3-2). To remove DCB from one of the OFETs the devices were annealed at 90C for 1hr with the sample and DCB was annealed for 1s to remove the bulk of the solvent. Consistent with the work of Nikolka et al. the OFETs with the liquid additives have more ideal transfer characteristics; for example the voltage threshold of OFETs with and without DCB is -7.3 and -28.6 V respectively.

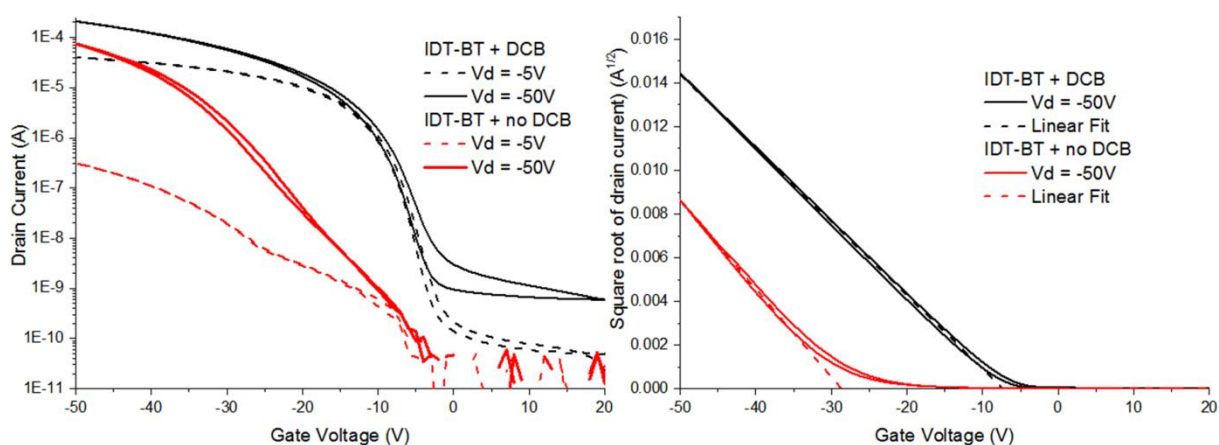


Figure 3-1: Left) Saturation and linear regime transfer curves of IDT-BT OFETs with and without DCB Right) Calculation of the voltage threshold by linearly fitting line to the square root of the drain current.

### 3. Searching for solid state additives

Similarly, the stabilising solid state additives improve the transfer characteristics even when the solvent is removed by heating the film at 90C for 1hr. As seen in Figure 3-2, the voltage threshold of OFETs with TCNQ, F2-TCNQ and F4-TCNQ increases by 16.1, 18.4 and 19.6 V, respectively, compared to those of the OFET without the additive.

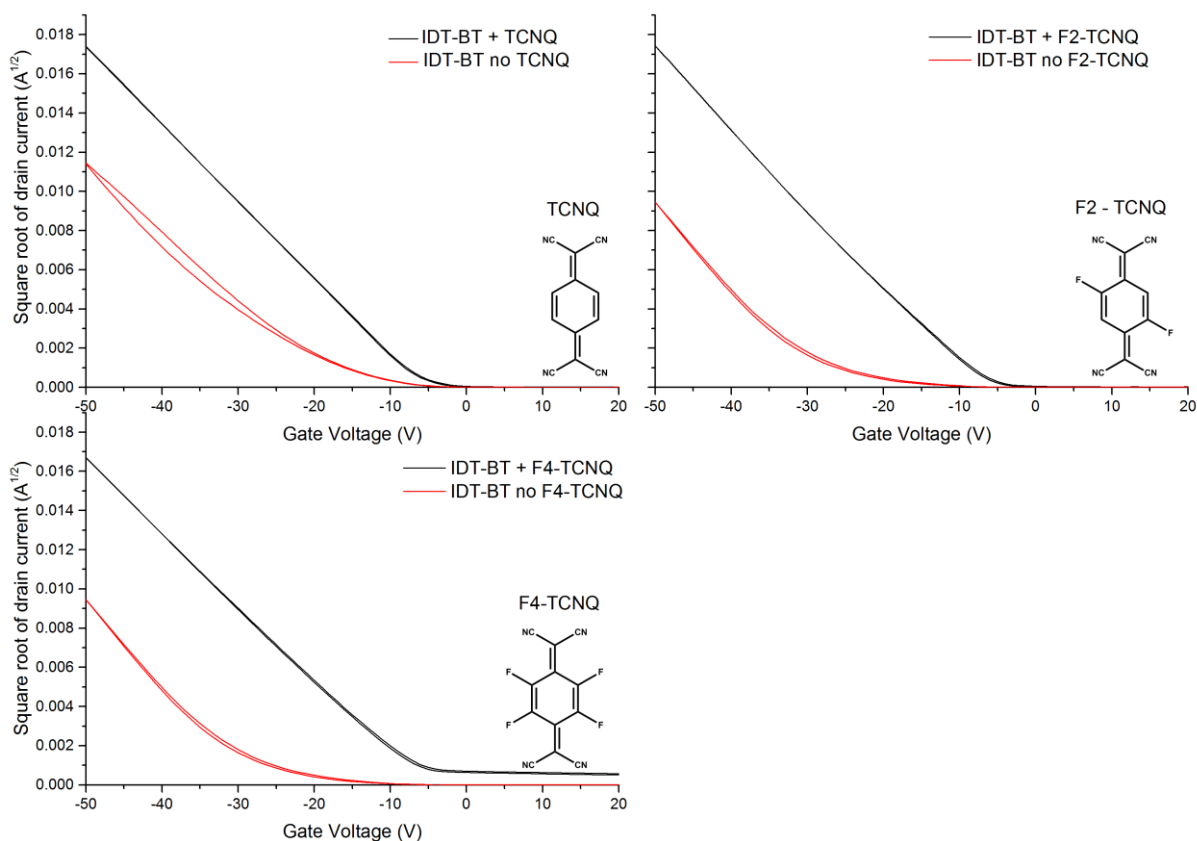


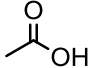
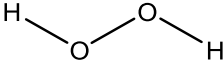
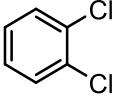
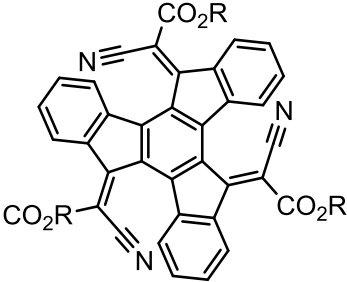
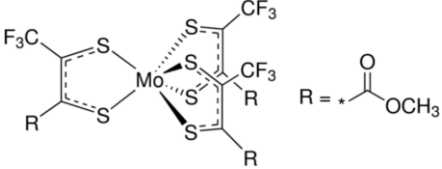
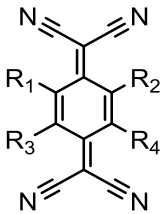
Figure 3-2: Linear plot of saturation transfer curves of IDT-BT OFETs with 2 weight percent TCNQ (Top Left), F2-TCNQ (Top Right), F4-TCNQ (Bottom), red lines, compared to reference samples without the solid state additive, black lines, with  $V_d = -50V$ .

As over 4000 transistors were manufactured, 95 different solid state additives were tested and as manufacturing fluctuations occurred during this investigation, direct comparison, similar to that in Figure 3-1, of the electrical characteristics was uninformative. To compare device improvement of the additives across all of the batches the relative saturation voltage thresholds of each sample in a batch was compared to a reference device in the same batch with identical processing parameters and no

### 3. Searching for solid state additives

molecular additive. The subset of molecules tested which demonstrate a statistically significant improvement in voltage threshold between batches is presented in Table 6.

Table 6: Subset of molecular additives with statistically significant voltage threshold shift greater than one standard deviation.

Name	Structure	$\Delta V_t$
<b>Acetic Acid</b> (non-dopant)		3.02±1.6
<b>Hydrochloric Acid</b> (dopant)	HCl	10.6±5
<b>Hydrogen peroxide</b> (dopant)		9.4±5
<b>1,2-Dichlorobenzene</b> (non-dopant) DCB		21±10
<b>Truexenone Derivates</b> (non-dopant) CN164 - R= CH3 CN112 - R= C2H5		CN164 3.75±1.8 CN112 2.8±1.3
<b>Molybdenum tris(1-(trifluoroacetyl)-2-(trifluoromethyl)ethane-1,2-dithiolene)</b> Mo(TFD)3 (dopant)		12±36
<b>Tetracyanoquinodimethane Derivates</b> TCNQ (non-dopant) R <sub>1</sub> , R <sub>2</sub> , R <sub>3</sub> , R <sub>4</sub> = H		TCNQ 11.12 ± 7.9
F <sub>1</sub> TCNQ (non-dopant) R <sub>1</sub> , R <sub>2</sub> , R <sub>3</sub> = H, R <sub>4</sub> = F		F <sub>1</sub> TCNQ 11.12 ± 7.9
F <sub>2</sub> TCNQ (dopant) R <sub>2</sub> , R <sub>3</sub> = H, R <sub>1</sub> , R <sub>4</sub> = F		F <sub>2</sub> TCNQ 12.5±6.8
F <sub>4</sub> TCNQ (dopant)		F <sub>4</sub> TCNQ 27.6±14.1

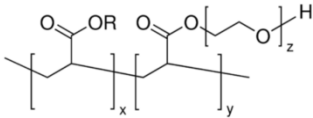
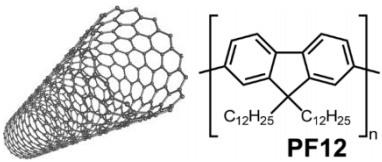
### 3. Searching for solid state additives

Table 6: Subset of molecular additives with statistically significant voltage threshold shift greater than one standard deviation.

Name	Structure	$\Delta V_t$
$R_1, R_2, R_3, R_4 = F$		
<b>tetrafluoro-tetracyanoquinodimethane</b>		F4-O
Derivates (dopants)		$27 \pm 12$
F4-O, R = Octane		F4-M
F4-M, R = Methyl		$18 \pm 8$
<b>2,2'-(perfluoronaphthalene-2,6-diylidene)dimalononitrile</b>		$9.7 \pm 4.2$
(dopant)		
F <sub>6</sub> TCNNQ		
<b>hexacyano-trimethylene-cyclopropane</b>		$13.1 \pm 6.7$
(dopant)		
CN6-CP		
<b>dicyano-9-anthraquino-10-methane</b>		$3.7 \pm 2.4$
(non-dopant)		
<b>tetracyano-anthraquinodimethane</b>		t-butyl-TCAQ
Derivates (non-dopants)		$13.4 \pm 7.3$
t-butyl-TCAQ, R = tert-butyl		
<b>Poly(ethylene succinate)</b>		$1.5 \pm 0.9$
(non-dopant)		
<b>Poly(vinylidene chloride-co-crylonitrile)</b>		$2.5 \pm 1.8$
(non-dopant)		

### 3. Searching for solid state additives

Table 6: Subset of molecular additives with statistically significant voltage threshold shift greater than one standard deviation.

Name	Structure	$\Delta V_t$
<b>Sodium Polyacrylate</b> (non-dopant)	 <p style="text-align: center;">R = H or Na</p>	$0.79 \pm 0.6$
<b>Single wall carbon nano-tubes</b> chirality (10,7) with wrapping polymer PF12 (unclear dopant, semiconductor)	 <p style="text-align: center;"><b>PF12</b></p>	$16.5 \pm 8.2$

The only solid state molecules which demonstrate a consistent improvement in the voltage threshold across all device batches are hydrochloric acid, a subset of the TCNQ derivatives, p-type dopants such as CN6-CP and MoTFD3 and the semiconducting CNT.

Similar to the work of Nikolka et al. the improvement in the voltage threshold is not limited to the solid state additives where the electron affinity of the solid state additive is sufficiently deep to dope the semiconducting polymer[43]. However, there is a significant voltage threshold increase around -5.3eV which corresponds with the molecular additive functioning as a dopant (Figure 3-3). The specific electron affinity values of the additives were taken from the cited references[79]–[84]



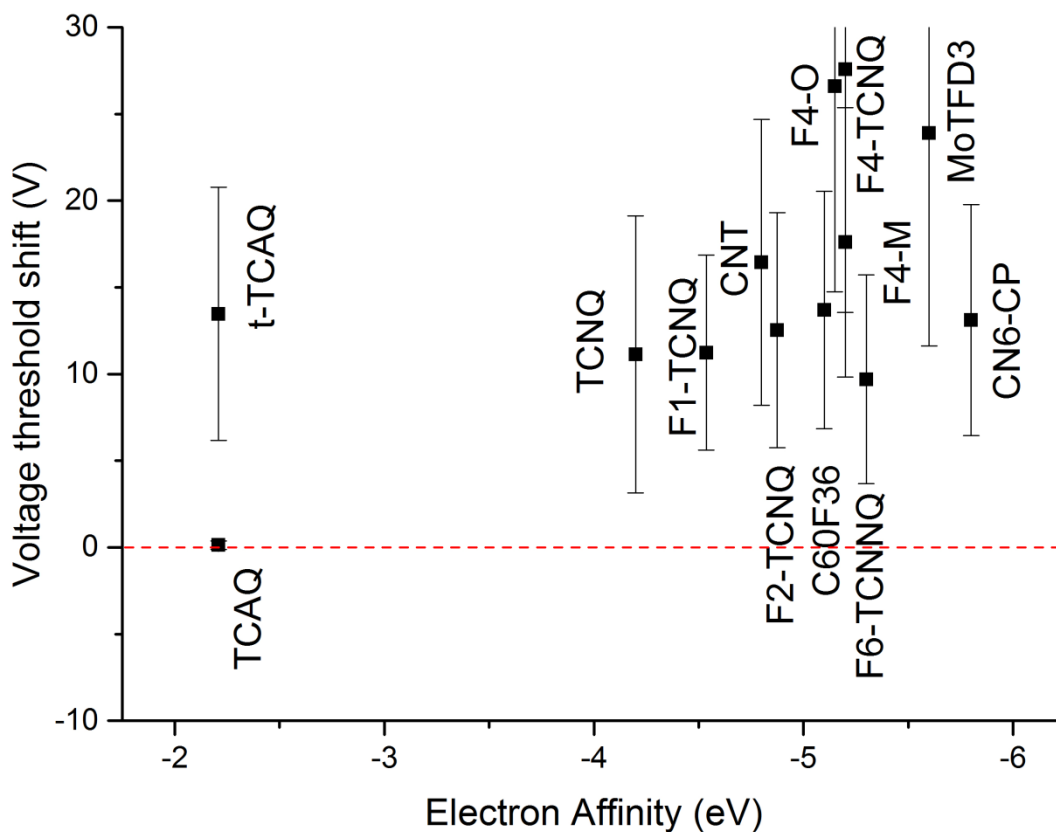


Figure 3-3: The dependence of the voltage threshold increase of the OFETs on the electron affinity of the additive.

All of the data relating molecular structures in the non-doping data set to the voltage threshold are presented here. To efficiently visually interpret the voltage threshold shift data of the non-doping molecular additives, the improvement of the voltage threshold against different independent variables is presented, such as mass of the molecule (Figure 3-4), mass ratio of specific functional groups (Figure 3-5) and pKa of the additive (Figure 3-6). The mass ratio of the functional groups for each molecule is calculated by the mass of the functional group times the mass of the functional group over the total molecular mass.

As seen in Figure 3-4 and Figure 3-5 there is no statistically significant trend relating the molecular mass of the additive as well as the mass ratio of ether, hydroxyl, ketone, ester, benzene, fluorine and chloride to either an increase or decrease in the voltage threshold shift, which suggests that these predictors do not inherently correlate with the voltage threshold shift and therefore are not suitable to generate a QSAR.

There is a significant trend in the mass ratio of nitrile functional groups to voltage threshold shift between 0.3 to 0.6, however, it is insufficient to build a useful predictive

### 3. Searching for solid state additives

model. Furthermore, based on this dataset it is not reasonable to build a more complicated statistical model based on the molecular structure of additives as molecules such as TCNQ, F1-TCNQ, DCAQ and t-butyl TCAQ improve device characteristics while molecules with near identical structure such as TCNNQ, TCNE, Dimethyl-TCNQ and TCAQ do not demonstrate device improvements.

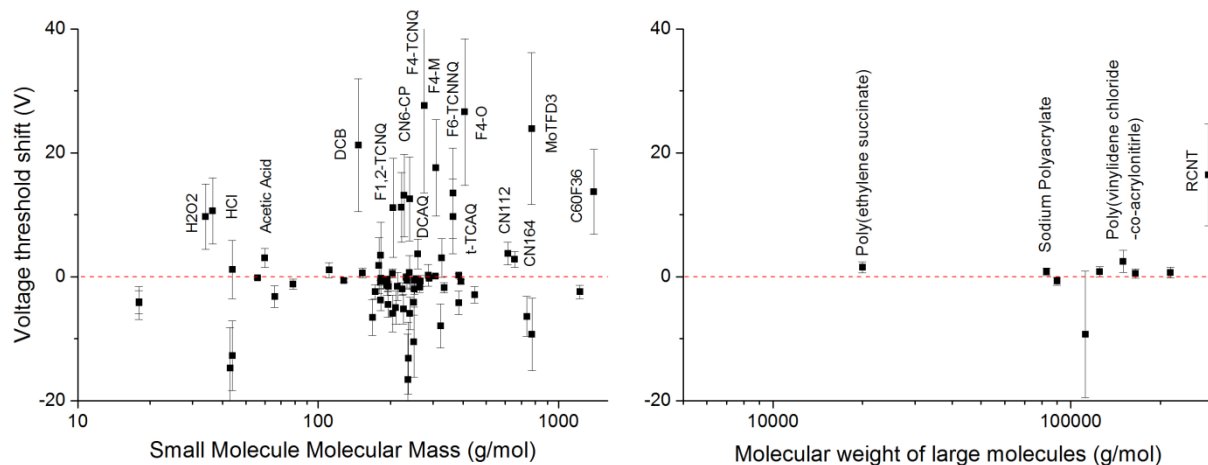


Figure 3-4: Voltage threshold shift as a function of the molecular mass of small molecules (left) and large molecules (right). Note: The molecular mass of carbon nanotubes (RCNT) is unknown, a value was assigned to present the voltage threshold shift along with the other large molecules. Molecules with statistically significant improvements in voltage threshold greater than one standard deviation are labeled.

### 3. Searching for solid state additives

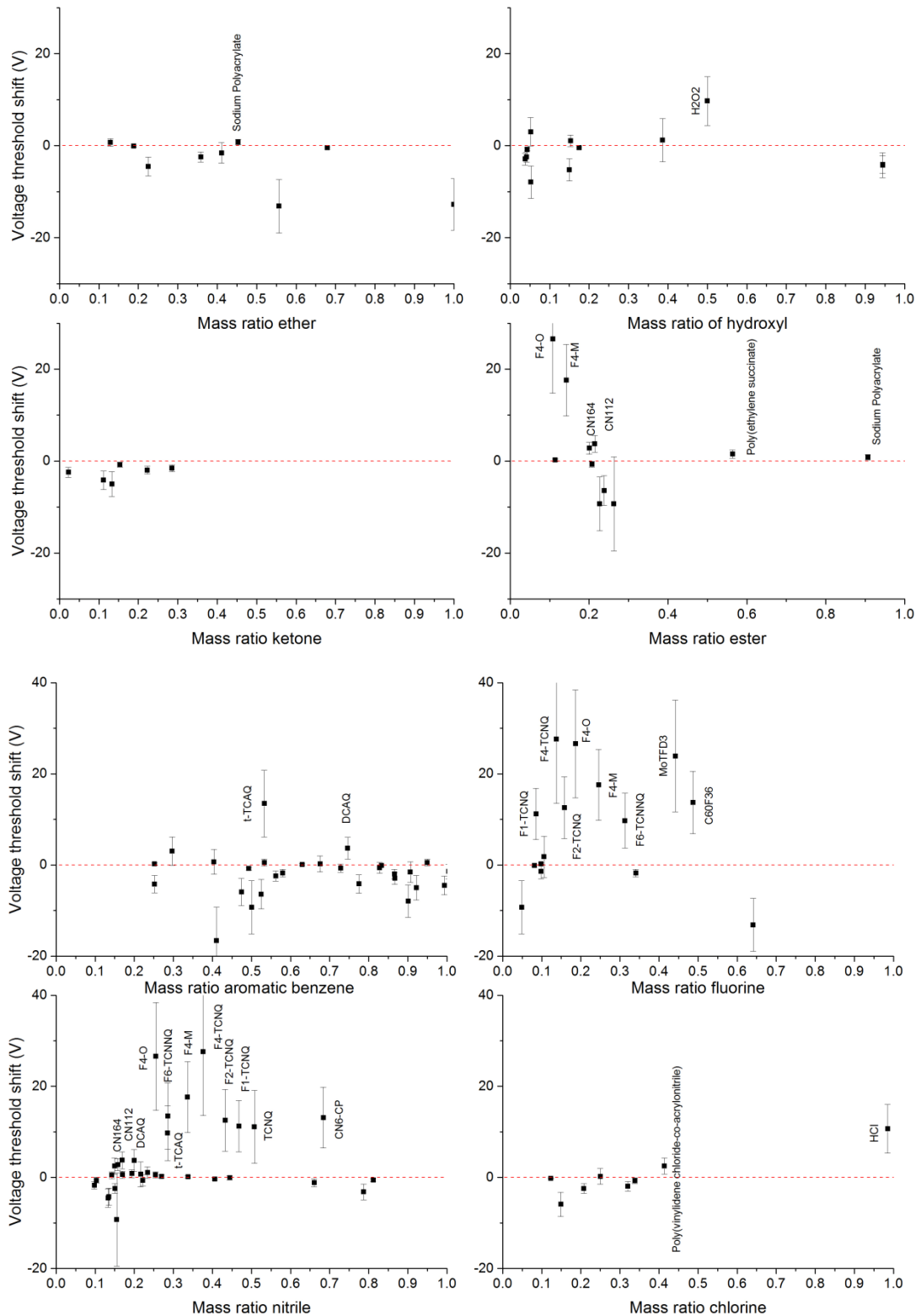


Figure 3-5: Voltage threshold shift dependence of OFETs on the mass ratio of ether, hydroxyl, ketone, ester, benzene, fluorine, nitrile and chlorine functional groups of non-doping molecular additives. Molecules with statistically significant improvements in voltage threshold greater than one standard deviation are labeled.

### 3. Searching for solid state additives

There is a trend that the voltage threshold shift increases with increasing acidity of the additive. The significant increase in voltage threshold shift of HCl also correlates with a rising off current of the OFET with HCL, suggesting that additives with very low pKa dope IDT-BT. Similarly, the voltage threshold shift due to the addition of the sulfuric acid additives could not be calculated as the film was completely metallic and did not exhibit semiconducting properties.

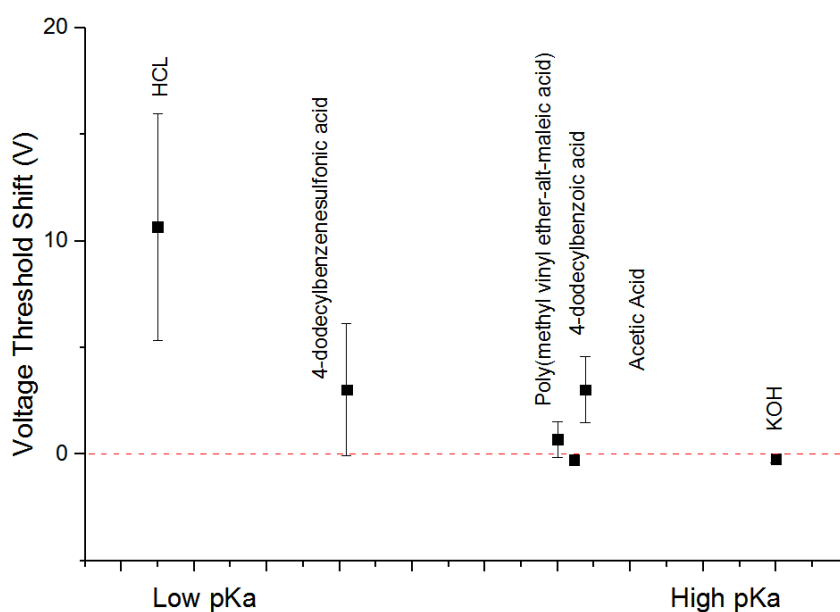


Figure 3-6: OFET voltage threshold shift with additives with varying pKa. The subset of additives presented here are all known acids or bases.

Through this search of over 90 additives, the significant improvement in device characteristics was determined to be related to a very small subset of molecular additives. The only large molecule that significantly improved device performance was the CNT. As small molecules tend to phase separate out of polymers at high temperatures, it is possible that CNT will not, due to its bulky nature. Thermal stability is critical for organic devices as promising applications include thermoelectric generators or form fitting sensors in hot environments, such as beside a combustion engine. Here we investigate whether CNTs are capable of improving the thermal stability of the molecular additive.

### 3.3 Thermally stable carbon nanotube polymer blends

The thermal stability of non-doped and doped CNT polymer blends in top-gate/bottom-contact OFETs was investigated. The polymer CNT films were fabricated by mixing 1 wt% CNT with the IDT-BT polymer solution in DCB as a reference. Doped films were fabricated by introducing 2wt% F2-TCNQ into the solution. The transfer characteristics of the OFETs were monitored as the OFETs were thermally stressed on the same hot plate at 90°C for up to 4 days. Here the linear transfer characteristics are presented in order to compare OFETs as the power dissipated by measuring the transfer characteristics through the doped CNT blend was sufficient to burn the OFET. Figure 3-7 demonstrates that after 1hr of annealing, the polymer CNT transfer characters were slightly degraded; however, further annealing did not significantly modify the transfer characteristics.

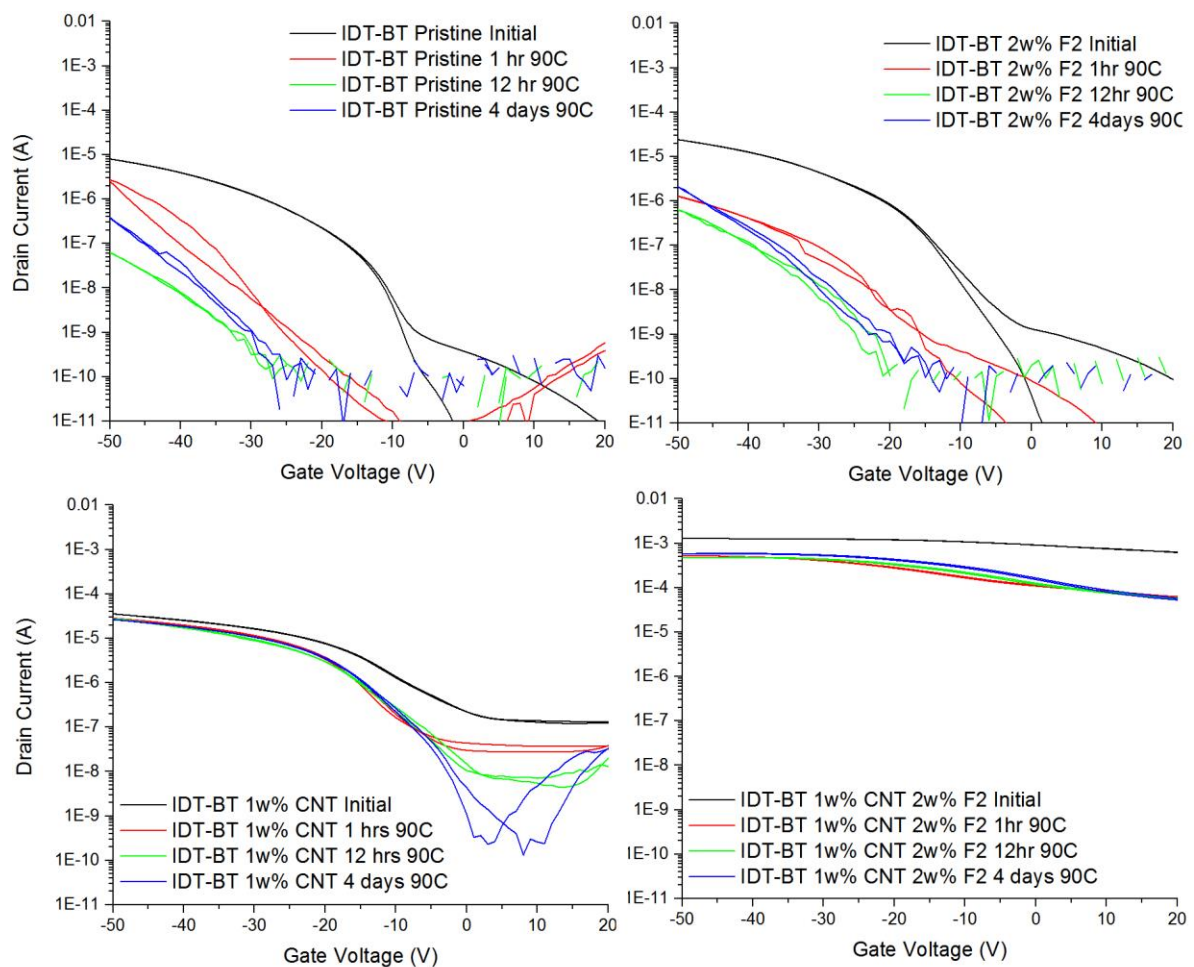


Figure 3-7: The evolution of linear transfer characteristics of doped and non-doped polymer CNT blends during annealing at 90°C.

### 3. Searching for solid state additives

This is in direct contrast to the polymer-only films which consistently degraded with time. There is an increase in the off current of the IDT-BT CNT blend, however, it is unclear what the direct cause is. It is plausible there are additional chemical species that form the blends doping the IDT-BT or perhaps the CNTs themselves.

#### **3.4 Discussion**

After searching through a large collection of molecular additives with different functional groups and properties, the only significant improvement observed with solid state additives is limited to that observed with very strong acids, a selection of TCNQ derivatives, dopants and the semiconducting CNT. The physics of how the CNTs are able to stabilize the polymer and what portion of the charge transport is due to the CNT network, are not known. The preliminary CNT data are included as they present exceptional thermal stability for both doped and non-doped systems.

The results of the extensive search of small molecule additives suggest that if filling the voids with solid state additives is the reason for the observed improvement, it is limited to a very small subset of molecules. Filling the voids could still be the rationale but it is unclear why solid state additives such as biphenyl derivatives with nitrile, methyl, and chloride functional groups which are highly soluble in DCB and near identical molecules to TCNQ and cyanoacrylates (the monomer of superglue, which rapidly polymerizes at room temperature when in contact with water) do not demonstrate any significant improvement. The main evidence for the solid state additive filling the void was that the size of the percent volume of detectable voids in the polymer film correlates with the percent weight of the solid state additive necessary to improve device characteristics. The simple void filling hypothesis is also not consistent with the later work of Nikolka et al. which demonstrates that solvents that do not form azeotropes with water, such as methyl naphthalene and methanol, do not improve device characteristics even though they are able to dissolve the polymer and move into voids[34]. In particular, no improvement in device performance with methanol is observed even though it is completely miscible in water.

### 3. Searching for solid state additives

Nikolka et al. then argue that solid state additives improve device stability because they contain nitrile groups which act as hydrogen bond acceptors, resulting in the additive bonding onto the solid state additive, similar to how liquid additives form azeotropes with water through hydrogen bonding. This does not appear to be the solid state mechanism as molecules such as tetracyanobenzene, fumaronitrile, aminobenzonitrile and dimethyl-TCNQ have similar functional groups but do not improve device characteristics.

Based on this work, it seems that the solid state additive TCNQ does not compete with water to fill the voids or interact with water through hydrogen bonding interactions. Building a statistical model to help predict the correct chemical structure of the additive based on molecular structure appears inappropriate for this dataset as there is an extremely limited number of molecules demonstrating device improvement while not doping the OFET. Molecules with near identical structure also behave differently. This suggests that molecular structure is a poor indicator of the ability of the additive to improve device performance, as it is likely operating below the Nyquist criterion to build an appropriate model. For example, there are 6 non-doping additives which appear to decrease the voltage threshold (F1-TCNQ, F2-TCNQ, CN164, CN112, DCAQ and t-butyl-TCAQ) while there are 5 additives with near identical structure (TCAQ, TCNE, TCNNQ, t-butyl-AQ and methyl-TCNQ) which do not. However, it is still possible to build a model with up to 12 degrees of freedom to predict molecules which could improve devices characteristics as there are 13 solid state small molecules which demonstrate improvements.

Upon further review of the literature it was revealed that TCNQ is highly reactive to moisture and turns into an acid. The possibility that TCNQ is improving device characteristics by reacting with water is explored in detail in Chapter 5. In this section of the work we will refer to TCNQ as a model system to better understand the mechanism. In Chapter 6 we build a statistical model generated using this data set and additional data, to accurately predict the improvement in device performance based on the structure of the solid state additive.

# 4 Understanding positive bias stress in organic semiconductors

## 4.1 Introduction

Prolonged environmental and operational stability is a necessary requirement for transistors operating in analogue circuit applications where consistent device characteristics are required to produce functioning analogue electronics. If transistors have poor stability, undesirable compensation circuits can be used to compensate for the degradation [85]. As the mobilities of organic semiconductors used in organic field effect transistors (OFETs) approach the usability limit for backplane transistors in OLED applications, consistent analogue device characteristics such as a stable voltage threshold are required in order to maintain a constant current through the OLED.

Two common forms of transistor operational stress, which can have different degradation mechanisms, occur when either the transistor is operated in an accumulation or a depletion mode, analogous to when the transistor is in a low or high resistance state, respectively. The operational stability of the transistor in both modes is essential in an OLED display where the transistor needs to control the specific current in accumulation mode and block current in depletion mode through the OLED in order to get a consistent dynamic range and deep blacks. There are many literature reports showing methods to mitigate stress related to carrier accumulation stress in organic transistors[21], [43], [86]–[88]. Accumulation stress is typically the focus of many studies as it provides evidence that the semiconductor has stable charge carriers. Depletion stress where the transistor is turned off, also known as positive bias stress (PBS) in p-type OFETs, is just as important for applications as accumulation stress when the transistor is on, also known as negative bias stress (NBS) in p-type OFETs, as transistors will operate a majority of the time in depletion mode in displays.



## 4. Understanding positive bias stress in organic semiconductors

A common source of stress in organic semiconductors is related to the inherent deep traps in the systems causing the semiconductor not to be an intrinsic semiconductor. In these non-intrinsic p-type semiconductors when the majority hole carriers are depleted, it is possible to generate minority electron carriers through injection or photoexcitation which are not readily able to recombine with a hole. The electron can then be trapped in the inherent deep traps of the semiconductor that make the semiconductor non-intrinsic, and the additional trapped charges result in undesirable shifts in the voltage threshold[89]–[97]. A common industrial practice to reduce depletion stress is to incorporate a light absorbing layer into displays therefore reducing light being absorbed by the transistor. Here we explore the generation and prevention of light induced stress in organic semiconductors and their implications for PBS.

### **4.2 Positive bias stress stability through molecular additives**

#### **4.2.1 Light stability in organic semiconductors**

Here we experimentally and theoretically investigate light stress in p-type OFETs. The inherent light stress of the *p*-type small molecule and polymer semiconductor diF-TES ADT and IDT-BT is investigated by fabricating OFETs and observing the change in their transfer characteristics by exposure to light. The fabrication procedures are the standard procedures for OFETs and can be found in the methods sections. However, the organic semiconductors were dissolved in hydrous solvents to observe the effects of moisture defects. To observe the effect of light on the transfer characteristics, the transfer characteristics were measured before and after the OFETs were stored in the dark and exposed to ambient light. For diF-TES ADT and IDT-BT OFETs this process was performed in a vacuum probe station and nitrogen probe station, respectively.

The results demonstrate that the diF-TES ADT OFET stored in the dark and then exposed to ambient light develops a positive switch on voltage (Figure 4-1 A), which is recovered after the device is stored in the dark (Figure 4-1 B). Similarly the IDT-BT OFET initially stored in ambient light has a high off current which is reduced by storing the device in the dark (Figure 4-1 B).

## 4. Understanding positive bias stress in organic semiconductors

By then re-exposing the device to light, the off current increases. This is consistent with literature reports where the light stability of *p*-type polymers and small molecule OFETs manifests as a positive switch-on voltage and/or a high off current in the transfer characteristics[89]–[97].

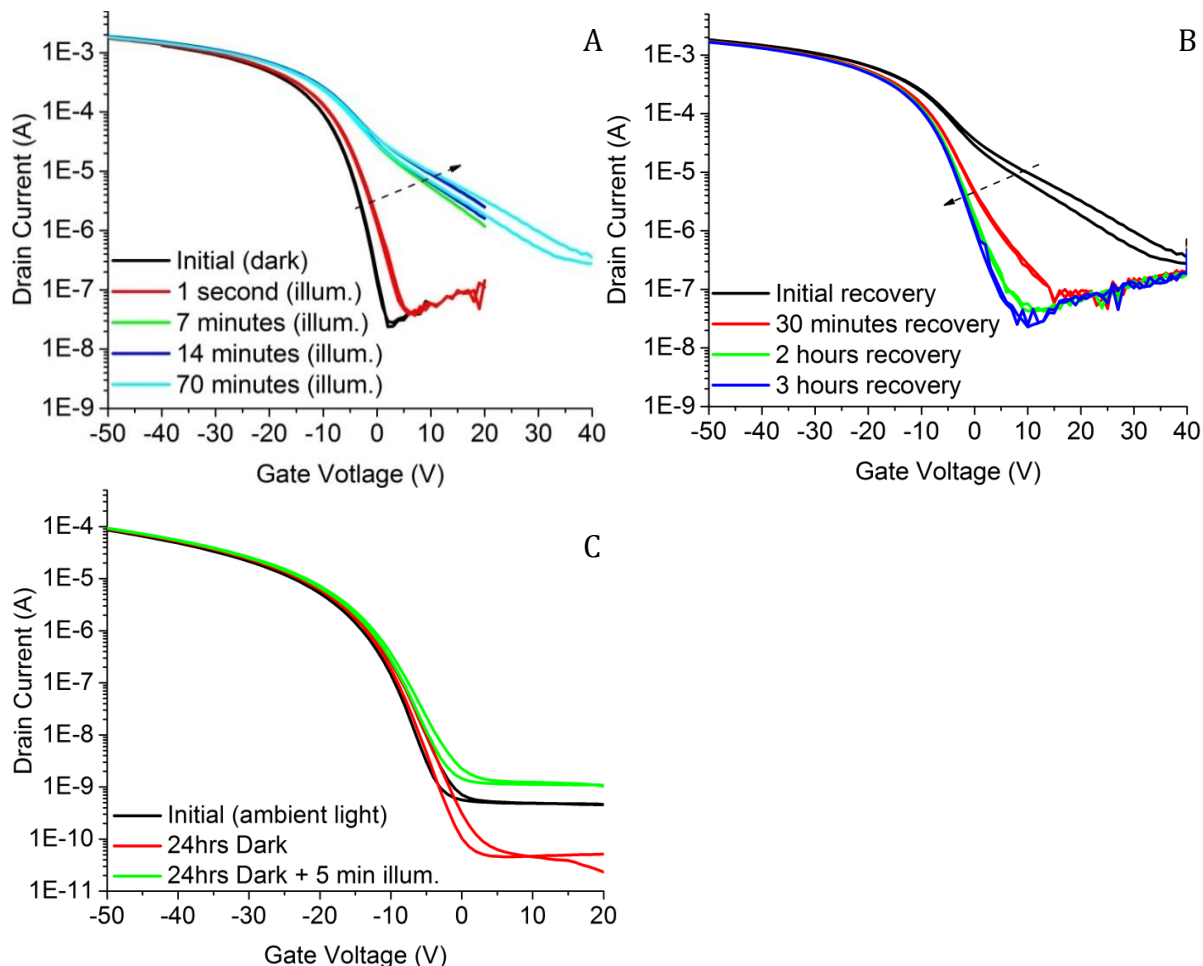


Figure 4-1: A) Transfer characteristics of a diF-TES ADT OFET initially stored in dark conditions and exposed to light. B) Recovery of the same OFET after exposure to light in the dark. C) Sequential transfer characteristics of an IDT-BT OFET initially exposed to light, stored in the dark and re-exposed to light.

To understand the mechanism for the electron trapping and the role of atmospheric species, the time evolution of photo excited diF-TES ADT small molecules was simulated. Recombination calculations were performed by Jean-Luc Bredas at KAUST using density functional theory of excited electrons in the small molecule diF-TES ADT. To determine the specific cause of the trap in the diF-TES ADT OFETs, simulations were performed in

## 4. Understanding positive bias stress in organic semiconductors

the presence or absence of water, diatomic oxygen and mesitylene (Figure 4-2).

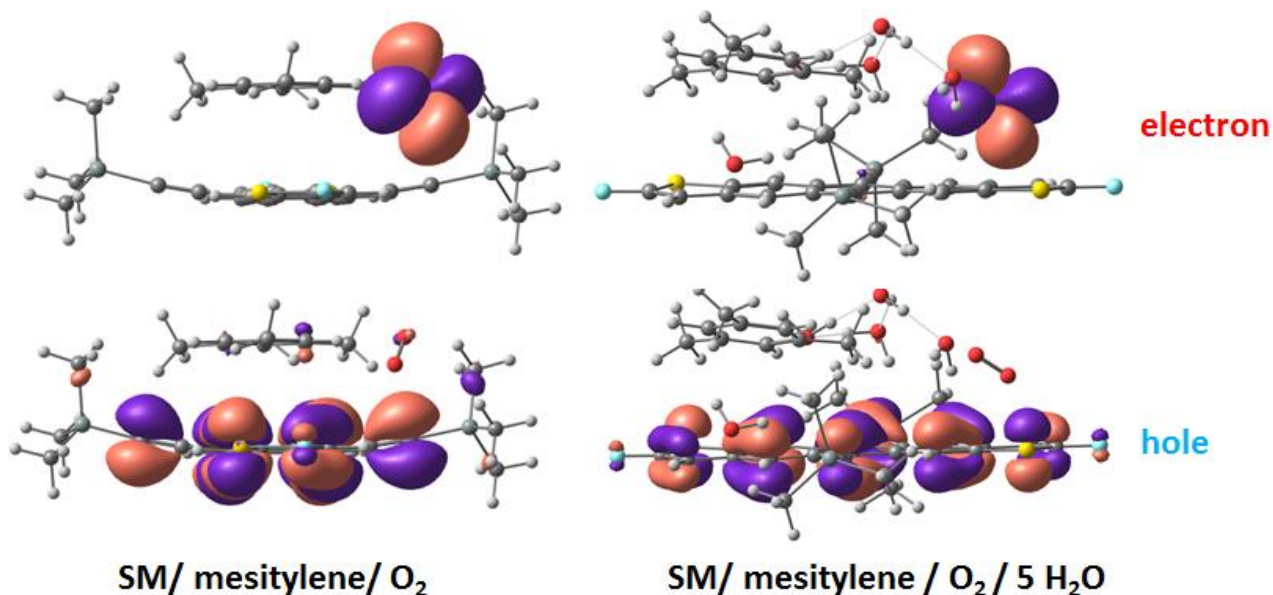
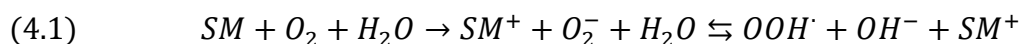


Figure 4-2: Left) Simulations involving diF-TES ADT (SM), mesitylene and oxygen (O<sub>2</sub>) showing the hole/electron wavefunction distribution of diF-TES ADT in an excited state where the hole is localised on the diF-TES ADT and the electron is localized on the O<sub>2</sub> forming superoxide (O<sub>2</sub><sup>-</sup>). Right) Identical simulation, but including water (H<sub>2</sub>O), showing the distribution of diF-TES ADT in an excited state where the hole is localised on the diF-TES ADT and the electron is localized on the O<sub>2</sub> forming superoxide (O<sub>2</sub><sup>-</sup>) which strongly interacts with water molecules.

The simulation predicts that photo excited electrons and excitons in the LUMO of diF-TES ADT small molecules (SM) become trapped on the oxygen-water complexes as the oxygen-water complexes have energy levels coinciding within the bandgap of the semiconductor. This is consistent with the literature, demonstrating that oxygen-water complexes constitute a universal electron trap in organic semiconductors with a trap energy level around 4 eV below the vacuum level[32]. The simulation predicts that oxygen is responsible for removing the electron from the LUMO of diF-TES ADT resulting in the oxygen molecule (O<sub>2</sub>) forming a superoxide molecule (O<sub>2</sub><sup>-</sup>). In the presence of water, the excess charge on the superoxide strongly interacts with water and can decompose forming a hydroperoxyl radical and hydroxyl ion, equation 4.1. The formation of superoxide in organic semiconductors and the decomposition of superoxide with water are both reported in the literature[16], [98], [99].

## 4. Understanding positive bias stress in organic semiconductors



Finally, the simulations predict that the detrapping/recombination time of the charges back into the HOMO of the semiconductor is very long (on the range of hours), due to the reorganization of the trap state.

As it has been demonstrated that light induced instabilities in OFETs are consistent with electron trapping, and as simulations of the electron trapping predict that the mechanism is related to redox reactions, here we examine whether solid state additives can compete with the atmospheric redox reactions to trap electrons which can easily recombine with holes in the HOMO. To investigate whether solid state additives could compete with atmospheric redox reactions to trap electrons, the transfer characteristics of diF-TES ADT OFETS in light without additives compared to those of OFETs with 2 weight percent TCNQ and F4-TCNQ are examined, as well as DFT simulations of the LUMO levels of clusters of diF-TES ADT with atmospheric species and the additive TCNQ. Experimentally the diF-TES ADT OFET with 2 weight percent TCNQ additive provides a permanent 0V switch-on voltage, relieving the effect of early switch-on observed in the OFET without the solid state additive (Figure 4-3, green). The OFET with 2 weight percent F4TCNQ begins to dope the organic semiconductor heavily (Figure 4-3, red), resulting in high OFF currents. These experimental results suggest that TCNQ is capable of reducing light induced stress caused by electron trapping in organic semiconductors, which is consistent with the literature on other semiconducting systems[99].

## 4. Understanding positive bias stress in organic semiconductors

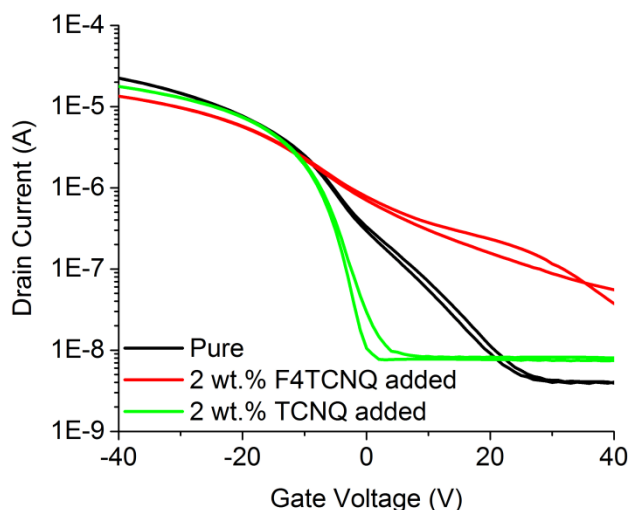


Figure 4-3): Transfer characteristics of a diF-TES ADT OFET in ambient light with 2 weight percent molecular additives F4-TCNQ and TCNQ.

Simulations support these claims showing that the combined LUMO of diF-TES-ADT, mesitylene and atmospheric species is located on the atmospheric species without TCNQ (Figure 4-4, green), and with TCNQ, the LUMO is on the TCNQ (Figure 4-4, red).

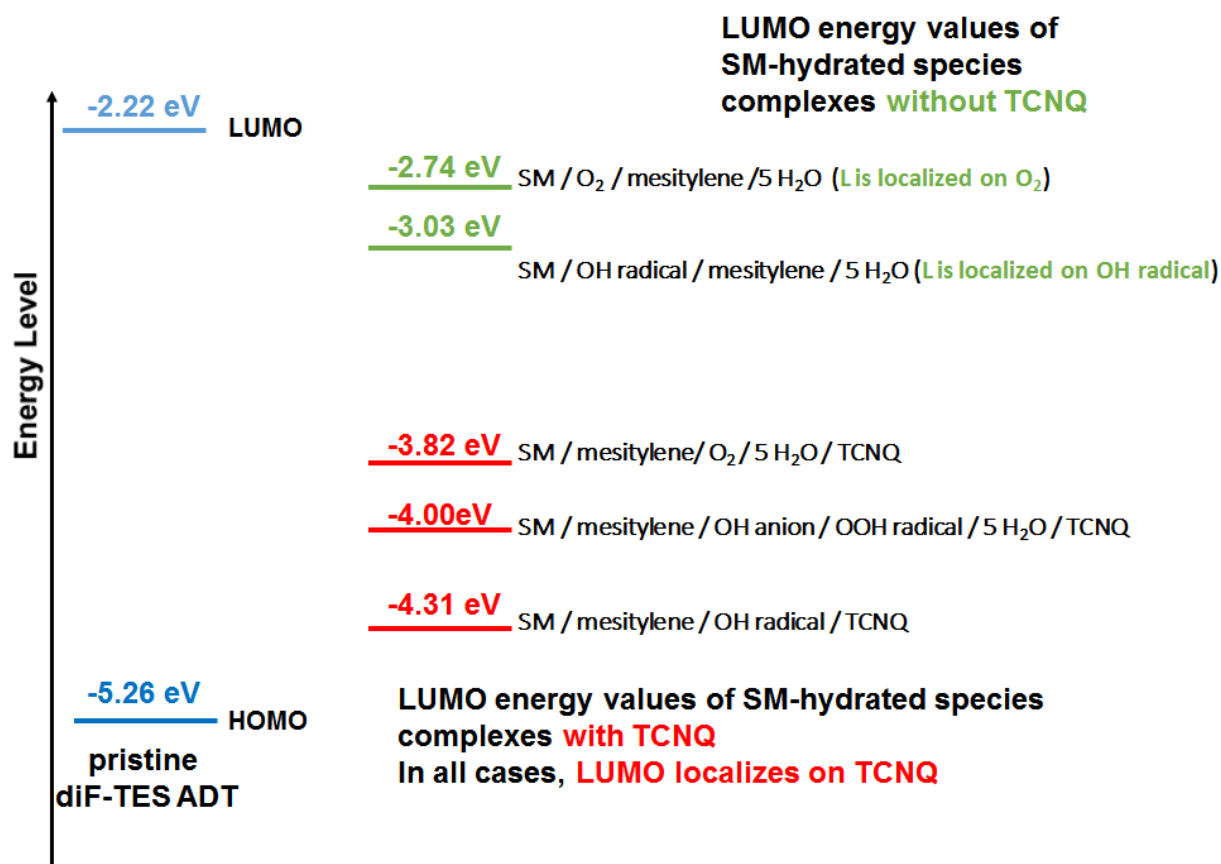


Figure 4-4: Energy level diagrams of the LUMO of different molecular systems including a combination of diF-TES-ADT, mesitylene, TCNQ and plausible moisture species.

## 4. Understanding positive bias stress in organic semiconductors

Recombination calculations were performed to determine the feasibility of electrons located in the LUMO of TCNQ and oxygen to recombine with holes located on the small molecule dif-TES-ADT. Recombination calculations were not carried out in the case of clusters where water was present due to complexity in the spin and multiplicities. The simulation predicts that electrons on the TCNQ recombine faster (compared to electrons on oxygen) with the holes on the organic semiconductor due to low reorganization energy and large electronic coupling between TCNQ and dif-TES-ADT. In this picture, the additive creates an efficient route for the excited electron to recombine with the hole in the HOMO of the semiconductor.

As previously shown in the literature, PBS of organic semiconductors seems to be related to the light instability of the organic semiconductors. Here it is shown that the addition of small molecules is capable of reducing light instability. It is then conceivable that the addition of suitable small molecules to organic semiconductors could reduce PBS.

### **4.2.2 Improved PBS and NBS stability with small molecules**

Here the possibility of reducing PBS in organic semiconductors by introducing a small molecule with a LUMO deeper than atmospheric traps to act as a competitive electron recombination center was investigated. Furthermore, it was determined whether the same additives observed in Chapter: 4 can be used to improve NBS in the same device. To determine whether molecular additives could reduce PBS and NBS in diF-TES ADT and IDT-BT OFETs, OFETs were fabricated with 2 weight percent molecular additives with LUMOs deeper than the atmospheric traps and then stressed using the PBS and NBS procedures described in the methods section. The CN6-CP samples were fabricated with 0.5 weight percent of the additive in order to maintain devices with similar on off ratios to other doped devices. In the IDT-BT OFETs the solvent content was controlled by annealing the IDT-BT transistor. All IDT-BT OFETs with additives had the solvent annealed out. The solvent was not annealed out of the diF-TES ADT OFETS as annealing these OFETs significantly changes the morphology.

## 4. Understanding positive bias stress in organic semiconductors

Figure 4-5 shows that the PBS in the p-type small molecule dif-TES-ADT (a) and the polymer IDT-BT without a stabilising solvent (b) is larger in ambient light (dashed red line) compared to the dark (dashed black line). There is also a general trend of additives with deeper LUMOs improving PBS in both dif-TES-ADT and IDT-BT (solid blue line). In particular, as the LUMO of the additive gets near or below the HOMO of the OSC, the PBS is reduced. The improvement in PBS with an additive with a deeper LUMO is consistent with the methodology of reducing light stress in dif-TES-ADT by providing an alternative recombination site. However, it is unclear whether the alternative recombination site is the additive or direct recombination with holes generated by p-type doping as F4-TCNQ, F6-TCNNQ and CN6-CP dope the OSC.

Interestingly, the off currents for the IDT-BTs OFETs doped with F6-TCNNQ and F4-TCNQ are of the same order of magnitude ( $\sim 10^{-7}$ A) but have drastically different positive bias stress. This suggests that the doping induced free carrier content is insufficient to predict the PBS stability of OFETs. Therefore, the poor performance in PBS due to TCNQ and F2-TCNQ in dif-TES-ADT and IDT-BT, respectively, is not definitively related to the additives not doping the OSC.

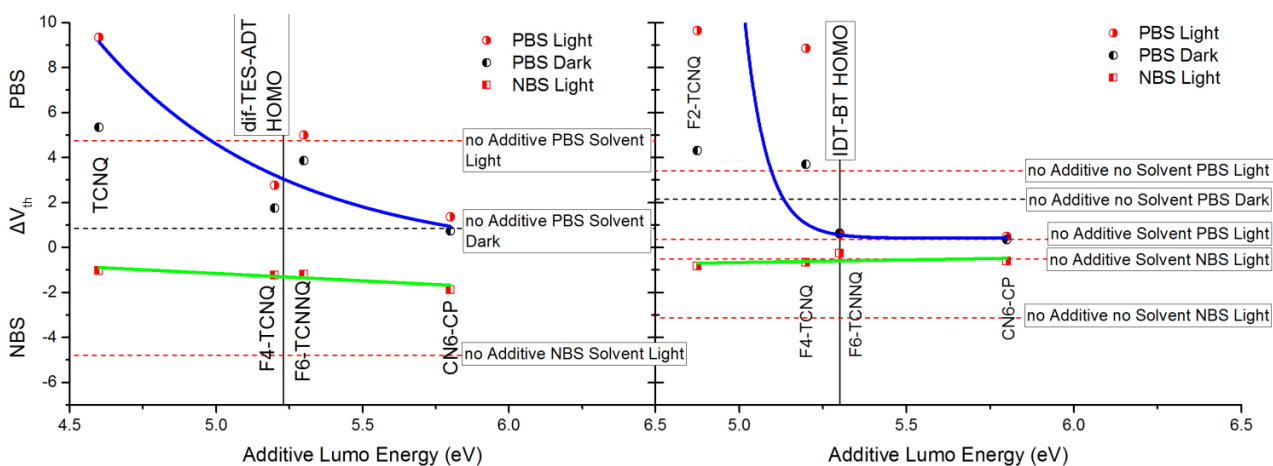


Figure 4-5: The threshold voltage shifts ( $\Delta V_{TH}$ ) due to positive and negative gate-bias stress in left) diF-TES ADT, a small molecule semiconductor and right) IDT-BT, a polymer semiconductor.

For the IDT-BT OFETs, it appears the solvent, DCB, improves PBS and NBS even though it does not act as a recombination site for photo excited electrons. This is not the case in

## 4. Understanding positive bias stress in organic semiconductors

diF-TES-ADT as including the solvent in the film does mitigate PBS or NBS. It is unclear what the direct discrepancy is but it could be related to the IDT-BT and diF-TES-ADT OSC being originally dissolved in anhydrous DCB and hydrous mesitylene, respectively.

Consistent with the results obtained by Nikolka et al., Figure 4-5 shows that the NBS in a p-type small molecule (a) and polymer (b) is reduced with the addition of molecular additives (solid green line) and is independent of the LUMO level[43]. This result demonstrates that it is possible to achieve NBS and PBS stable transistors with the incorporation of molecular additives.

It is interesting that TCNQ is capable of reducing the light stress stability in diF-TES ADT but TCNQ does not reduce PBS. This suggests that our current understanding regarding the interaction between small molecules and PBS is incomplete. Other important parameters are investigated next.

### **4.2.3 Solubility dependence of PBS**

During the investigation of the PBS stability dependence of different small molecules with varying LUMO energies it became apparent that there are parameters which dominate the PBS of the OFET in certain regimes. One possible parameter seems to be related to the solubility of the molecular additive. The role of the solubility in PBS by fabricating different polymer additive blends with additives which have similar structure and LUMO energies but highly different solubilities was investigated. The molecular additives examined are F4-TCNQ and its soluble derivatives F4MCTCNQ and F4OCTCNQ, seen in Figure 4-6, which both substitute a cyano group for a methyl and n-octyl ester, respectively. The experimental solubilities and LUMO of F4-TCNQ, F4MCTCNQ and F4OCTCNQ are 2.0, 113.8 and 204.1 mmol/L and 5.23, 5.14 and 5.12 eV, respectively[100]. To investigate how the additive solubility affects PBS, IDT-BT OFETs with 10 weight percent F4-TCNQ, F4OCTCNQ and F4MCTCNQ were fabricated and positive bias stressed (Figure 4-6). The results show that F4-TCNQ, F4MCTCNQ, and F4OCTCNQ in IDT-BT have voltage threshold shifts of 40V, 0.35V and 0.36V, respectively, in light.



## 4. Understanding positive bias stress in organic semiconductors

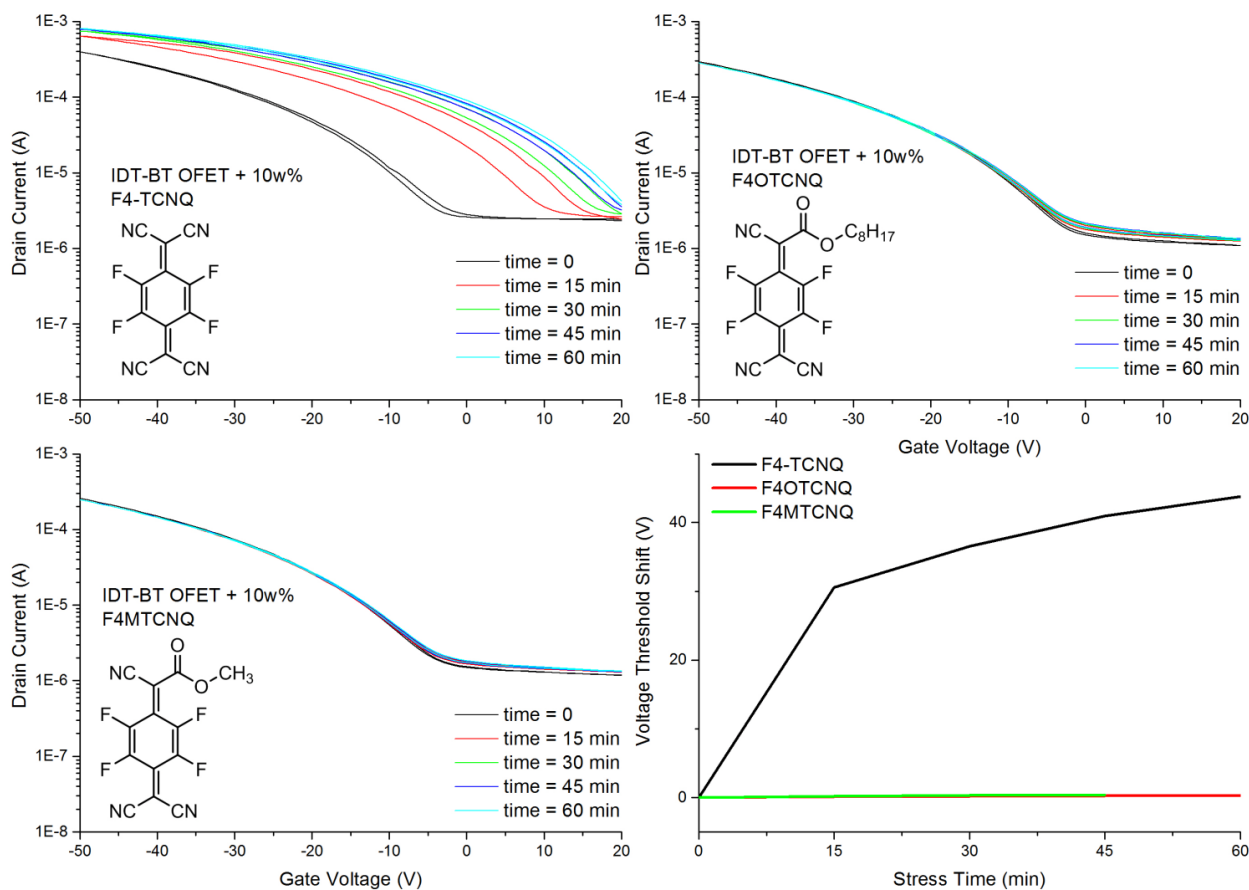


Figure 4-6: Positive bias stress of IDT-BT OFET with 10 weight percent of similar molecular additives with varying solubility in ambient light.

The improved benefit is not related to an increased LUMO potential, as the LUMO of F4MTCNQ and F4OTCNQ is less than that of F4-TCNQ. Similarly, the off currents in all devices are surprisingly similar (around 1  $\mu$ A), which suggests that the improvement observed with F4MTCNQ and F4OTCNQ is not related to the higher concentration of free holes allowing trap free recombination of the electrons. The improved PBS with F4MTCNQ and F4OTCNQ would then suggest that the solubility of the additive and/or another feature, such as morphology of the additive within the semiconducting film, has a very important role to play in positive bias stress. This suggests that it is unclear to what extent the role of the LUMO has on positive bias stress, as there appear to be regimes where the solubility can explain the observed positive bias stress. It is unclear then whether the increased PBS observed in F4-TCNQ, F2-TCNQ and TCNQ is caused by the morphology or LUMO level.

## 4. Understanding positive bias stress in organic semiconductors

Another route to investigate the PBS, due to solubility effects of the molecular additives, is to vary the weight concentration of the additive in the solution. The weight concentration would determine at which point during the spin coating of the film the molecular additive becomes fully saturated in the solution and crashes out, forming aggregates on the film. To investigate the dependence of the PBS on the concentration of the molecular additives in the IDT-BT solution, OFETs were fabricated with TCNQ, F2-TCNQ, F4-TCNQ, F6-TCNNQ, F4OCTCNQ and CN6-CP at varying weight concentrations.

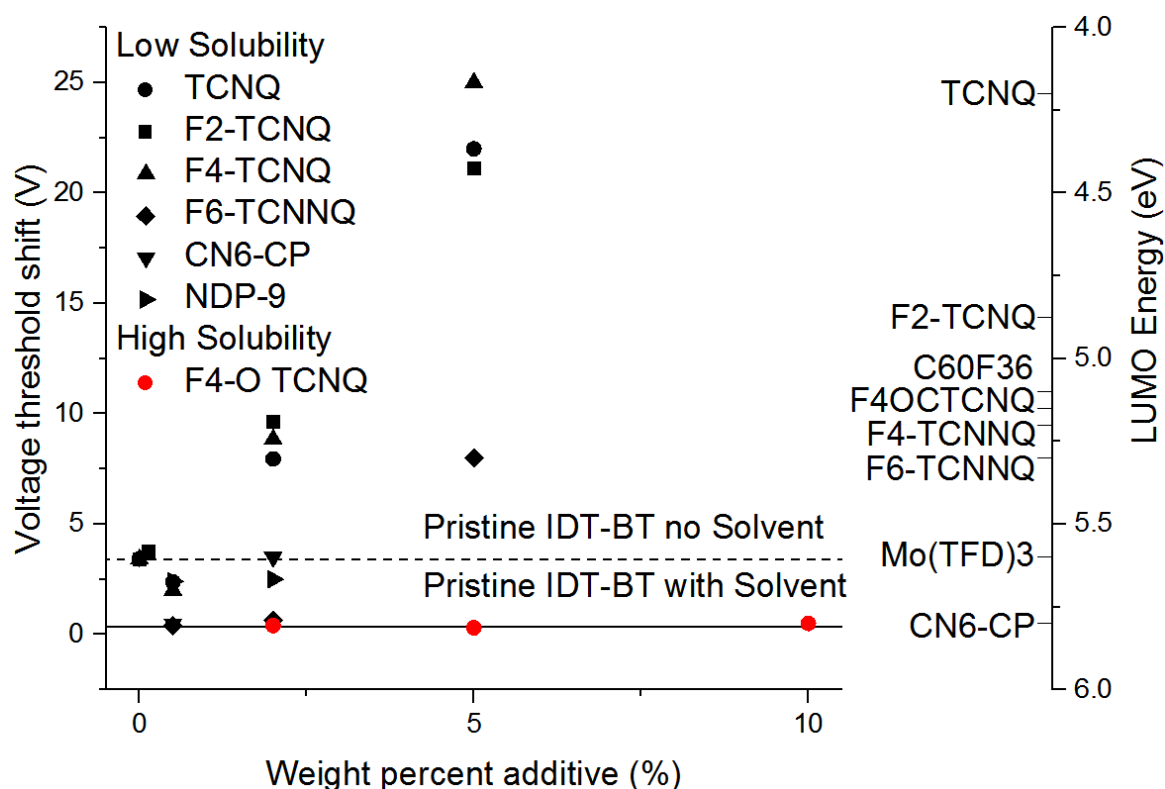


Figure 4-7: Left) Positive bias stress of IDT-BT OFETs with varying weight concentrations of molecular additives in ambient light. Right) LUMO energy of the additive.

The highly soluble F4OCTCNQ additive (red dots) and the solvent additive (solid black line) are able to stabilize PBS while showing no significant dependence of the PBS on weight percentage (Figure 4-7). For all other molecules investigated there is a significant increase in PBS with increasing weight percentage (black symbols). There is also a low concentration of TNCQ, F2-TCNQ and F4-TCNQ, around 0.5 weight percent,

## 4. Understanding positive bias stress in organic semiconductors

which reduces the PBS. This suggests that the limiting factor for TCNQ, F2-TCNQ and F4-TCNQ reducing PBS is low solubility.

To understand whether a phase transition of the additive polymer blends could be responsible for the increased PBS, the morphology of IDT-BT films was investigated, using AFM with varying weight concentrations of F6-TCNNQ before and after the onset of PBS in OFETs. The topology of an IDT-BT film with no additive, 2 weight percent F6-TCNNQ (PBS stable) and 5 weight percent F6-TCNNQ (PBS unstable) using AFM (Figure 4-8) was investigated. There is not a large difference in topology between a pristine film and a film with 2 weight percent F6-TCNNQ. However, films with 5 weight percent F6-TCNNQ have a large number of elevated regions (large white dots), which is consistent with the phase separation of polymer additive blends through the formation of additive aggregates on top of the polymer[101]. The generation of these regions appears to be directly correlated to the onset of increased PBS suggesting plausible causation. It is conceivable that the clusters of the additives form electron traps; this will be discussed in detail later. In the next two sections it will be determined whether the molecular additives are trapping additional charge or the mobile ions are responsible for increased positive bias stress.

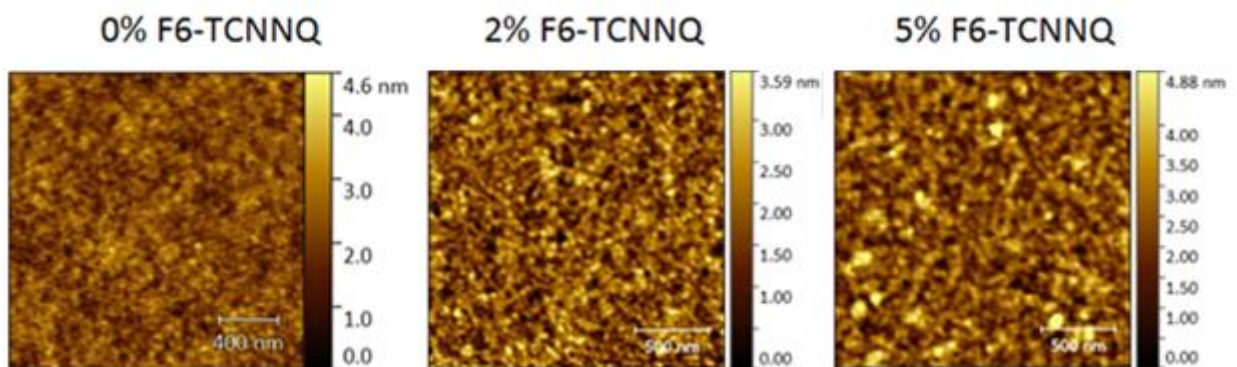


Figure 4-8: Topography of IDT-BT films with varying weight concentrations of F6-TCNNQ.

## 4. Understanding positive bias stress in organic semiconductors

### 4.2.4 Spectroscopic behavior of IDT-BT films during PBS

Here we examine whether F4-TCNQ is responsible for trapping electrons during PBS by measuring the change in the UV-VIS absorption spectroscopy. If the negative charging of F4-TCNQ is responsible for the observed increase in PBS, the anion of F4-TCNQ should be observed in the UV-VIS spectrum, as all the charged and neutral species have unique spectroscopic signatures[67]. The difference in the UV-VIS transmission spectrum of a 5 weight percent F4-TCNQ IDT-BT OFET before and after PBS is observed. As it is assumed that charge trapping causes the increased PBS, charge accumulation spectroscopy (CAS) was performed to confirm the spectroscopic signature of charge accumulation.

The results shown in Figure 4-9 A) demonstrate that there is a significant change in the differential of the UV-VIS transmission spectrum before and after PBS with peaks forming at 1.09, 1.72 and 1.81 eV. However, all of the peaks are also seen in the charge accumulation spectrum corresponding to polaron induced absorption, electro absorption and bleaching of the IDT-BT HOMO, respectively (Figure 4-9 D). This suggests that charge trapping is the responsible mechanism for the increasing PBS in IDT-BT OFETS with F4-TCNQ.

## 4. Understanding positive bias stress in organic semiconductors

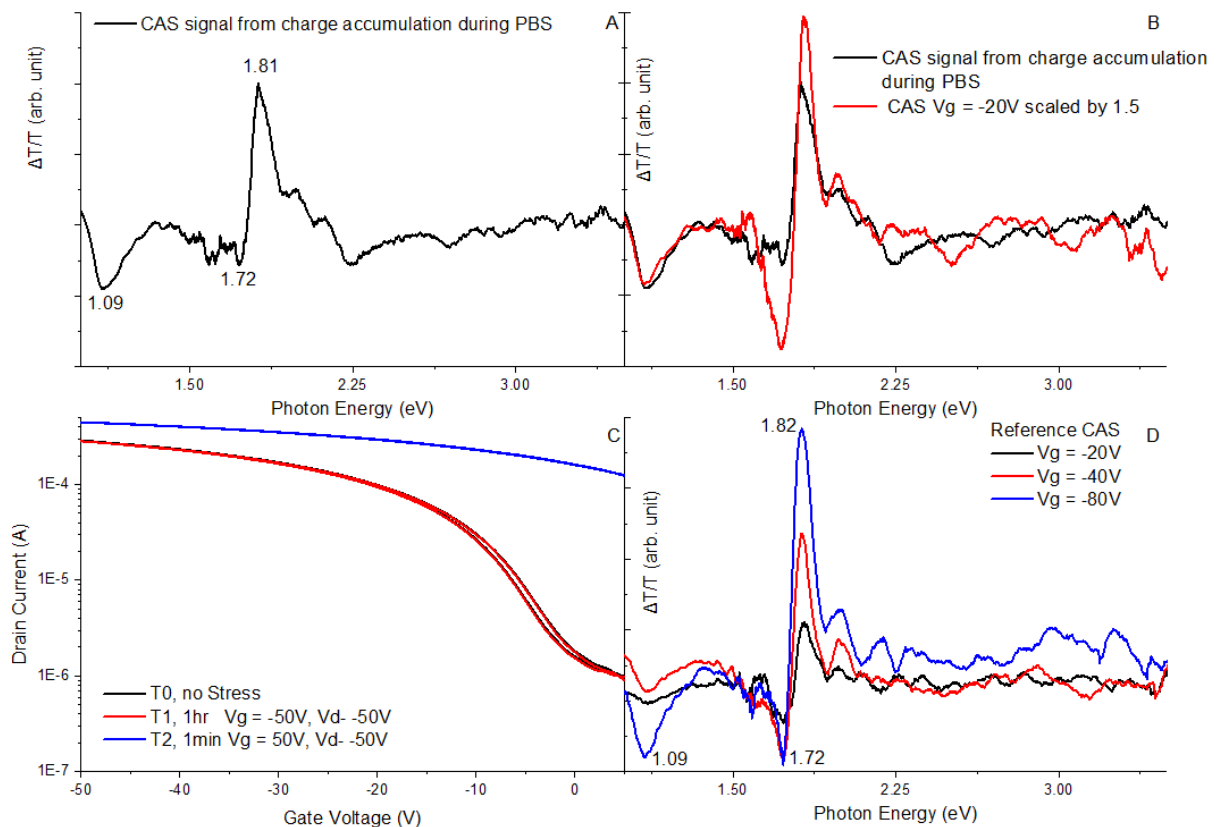


Figure 4-9: A) CAS from charge accumulating during PBS B) Stress  $\Delta T/T$  spectrum compared to CAS spectrum at  $V_g = -20V$  scaled by 1.5x C) Transfer characteristics of the same device before stress, after NBS and after PBS D) Reference CAS spectrum of the same device after stress.

As there is no significant generation and/or bleaching of any neutral or ionized F4-TCNQ peak in Figure 4-9, these results are inconsistent with the concept that F4-TCNQ is responsible for the observed electron trapping. Ionized peaks of F4-TCNQ are expected to be observed at 2.9, 2.45, 2.25, 1.6 and 1.45 eV[67]. However, it is conceivable that the F4-TCNQ aggregates are responsible for the increased PBS and are not observed due to light scattering off of the aggregates on the surface of the film, or that the optical cross section is likely to be smaller than the hole on the IDT-BT.

Interestingly, the polaron induced absorption of the difference in the UV-VIS transmission spectrum is a similar size and area to the  $V_g = -20V$  CAS spectrum scaled by 1.5x times, suggesting that approximately 30V of polarons have accumulated during PBS which is consistent with the voltage threshold shifting by 30V (Figure 4-9 B). Even though the polaron induced absorption is equal between the scaled and PBS spectrum,

## 4. Understanding positive bias stress in organic semiconductors

the relative amount of electroabsorption and bleaching of the IDT-BT is less. It is unclear whether this discrepancy is a real effect or is related to the measurement protocol.

### **4.3 Mobility of additives in IDT-BT**

The movement of dopants in polymer films is accelerated with thermal energy and electric fields[102], [103]. To determine whether dopants in IDT-BT are capable of moving laterally in a device under electrical stress, standard IDT-BT OFETs were fabricated with 2w% F4-TCNQ, F6-TCNNQ, Mo(TFD)<sub>3</sub> and CN6-CP, except that the process was stopped before adding the Cytop layer. Here the method of Muller et al. was used to determine whether ion movement is present in the polymer film by systematically increasing the drain voltage by 10V from 0V until significant ion movement was detected. Ion movement is inferred by the current being time dependent at a constant voltage[102]. The specific point at which the dopant migrates due to the electric field is difficult to define but all of the dopants appear to move between 4 to 8 V/um (Figure 4-10). This work suggests that dopants in IDT-BT appear to be mobile under electrical stress. However, it is not a direct measure of how the dopant moves with gate induced electric fields during PBS because the methodology of Muller et al. does not separate electric field effects from resistive heating effects. As non-doped IDT-BT is not conductive, a reference sample is not provided in Figure 4-10.

## 4. Understanding positive bias stress in organic semiconductors

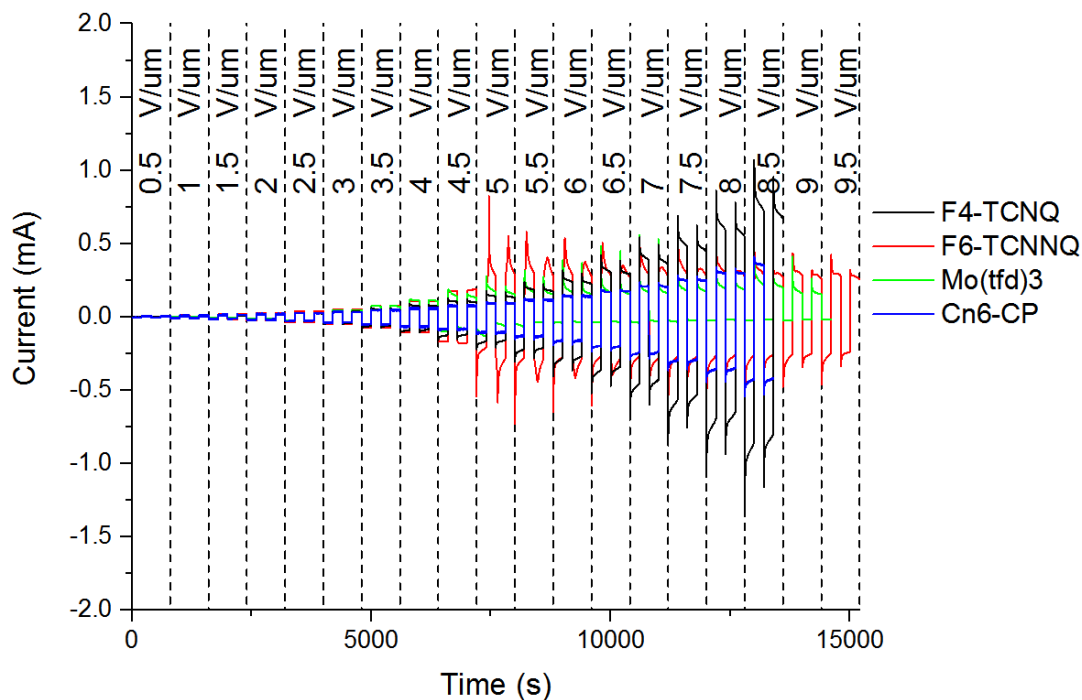


Figure 4-10: Current of various constant electric fields of alternating polarity for F4-TCNQ, CN6-CP, F6-TCNQ and Mo(TFD)3.

If mobile ions due to gate voltage are responsible for PBS, it is conceivable there would be a gate voltage dependence on the PBS, as there would be a minimal electric field to move the ions. To investigate the effect of gate voltage during PBS, standard OFETs were fabricated with different dopants and the transfer characteristics were measured after the same device was exposed to systematically increasing positive bias stress for 5 minutes. To remove any effect of resistive heating during PBS the drain source voltage was set at 0V.

Figure 4-11 (left) shows that there is no gate voltage dependence of the PBS when either the solvent and/or CN6-CP at 0.5 weight percent are present in the film and there is a regime below a gate voltage of 50V, where both Mo(TFD)3 and F6-TCNNQ reduce PBS compared to the pristine sample. There is a gate voltage dependence of the PBS in the IDT-BT film when no solvent is present and the additives TCNQ, F2-TCNQ, F4-TCNQ, F6-TCNNQ, C60F36 and Mo(TFD)3 are in the film. Interestingly, there appears to be a minimum onset voltage after which there is a linear increase in the PBS stress. This suggests that either the PBS occurs at a steady rate once a significantly strong electric field has been obtained, or the amount of total PBS shift is dependent on the gate

## 4. Understanding positive bias stress in organic semiconductors

voltage. To determine the cause, the same experiment was performed on another sample with a 4 hour stress interval, allowing the transistor to saturate the PBS before increasing the gate voltage. The results, in Figure 4-11 right), show that over the course of 4 hours the PBS starts to plateau demonstrating that there is a maximum PBS at a particular gate voltage. However, the maximum PBS voltage obtained during each stressing interval scales linearly with gate voltage. It is conceivable that the maximum PBS is related to the size of the depletion region, which in inorganic transistors is directly related to the magnitude of the gate voltage. The discrepancy between the voltage threshold shift between Figure 4-11 A and B is believed to be caused by process variations.

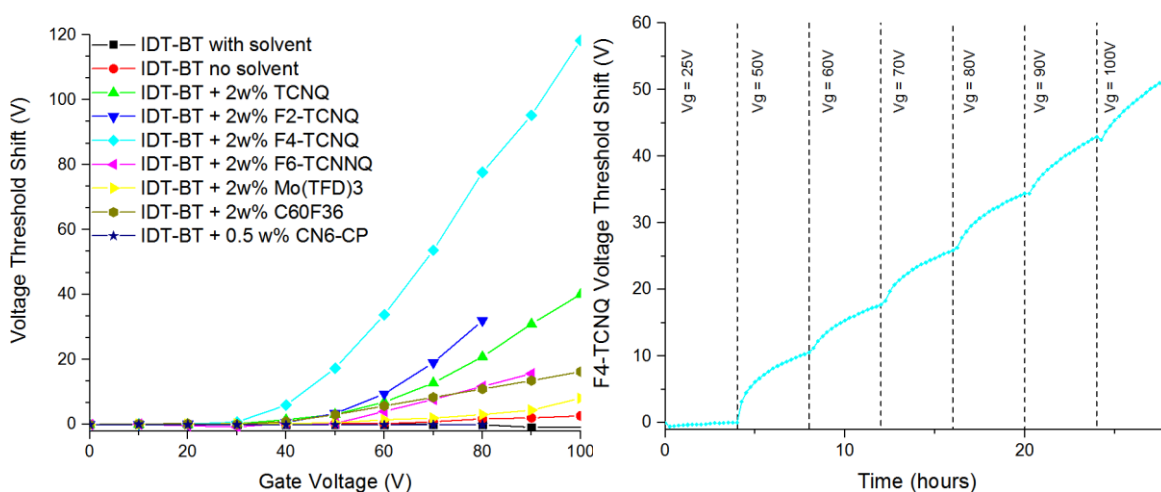


Figure 4-11: Left) PBS of IDT-BT OFETs with molecular additives at different gate voltages for 300s. Right) 4 hour PBS intervals of an F4-TCNQ IDT-BT OFET at different gate voltages.

### 4.4 Proposed increased PBS with molecular additives

Here possible mechanisms for the increased PBS with molecular additives are examined.

#### 4.4.1 Additional chemical reactions

There is literature showing that TCNQ based molecules are highly reactive[104]–[106]. Later in this report it is shown that TCNQ is not stable in the presence of hydroxyls. Hydroxyls can be generated in a film as they are a byproduct of a trapped electron on a



## 4. Understanding positive bias stress in organic semiconductors

super oxide decomposing by the thermal ionization of water. As TCNQ reacts with hydroxyls, this could modify the pH of the polymer film and change the trapping dynamics[31]. Similarly as TCNQ has an atmospheric degradation product that is an acid, the work of De Leeuw et al. would suggest that electron trapping is more favorable. Interestingly, as Kettner et al. have proposed, hydroxyl migration occurs during PBS and NBS, suggesting that during PBS hydroxyls should accumulate at the polymer dielectric interface where the hydroxyl could react with the large aggregates of TCNQ[39].

### **4.4.2 Trapping of electrons at TCNQ grain boundaries**

Dopants appear to accumulate at the surface, forming protruding islands of small molecules on an otherwise smooth polymer film[101]. During PBS it is possible that the electrons from the HOMO of the polymer are being more efficiently injected into the dopant aggregates as the dopant aggregates are closer to the gate electrode compared to the polymer. This would lead to electrons being injected across the small molecule/polymer phase boundary. Grain boundaries are typically filled with a higher density of traps compared to the bulk of the film. It is also conceivable that more atmospheric species are located at these grain boundaries between the polymer and the dopants suggesting that more chemical reactions are likely to occur.

### **4.4.3 Mobile ions**

This report has demonstrated the movement of dopants in IDT-BT through electrical stress, but has not demonstrated whether the additive diffusion is responsible for the increased PBS observed when some molecular additives are incorporated into the organic semiconductors. A possible route for mobile ions increasing PBS is whether the conductivity of the OSC is nonlinear with concentration of the dopant. Then it could be possible that accumulating the dopant systematically at the top of the OSC results in the total conductivity of the film increasing.

If mobile ions are responsible for poor PBS, it is unclear why NBS is not influenced by mobile ions. Here we will address why additives are particularly susceptible to PBS.

## 4. Understanding positive bias stress in organic semiconductors

Jacobs et al. have shown that this electrostatic interaction is important in binding the dopant to the OSC, as when the electrostatic interaction is chemically removed, the dopant is no longer bound to the OSC and becomes more mobile at room temperature without any electric field present[107]. Therefore it is conceivable that the efficiency at which the negative ion maintains a hole on the polymer would be directly related to the mobility of the dopant. During PBS, a complete depletion of all holes reduces the electrostatic interaction between the OSC and the additive, but the extent to which PBS is capable of depleting full and/or partial holes in the OSC is unknown. Similarly, if there are neutral additives in the bulk and if the additives trap a free electron without a positive charge pair on the OSC, there would be no electrostatic interaction between the OSC and the additive. With both the full depletion of the hole and the generation of a new anion, the anion would phase separate from the OSC and perhaps penetrate the dielectric.

### **4.5 Molecular additive design rules for PBS**

Based on this work, the following features of molecular additives appear to be relevant for reduced positive bias stress: the morphology/packing of the additive in the semiconductor, relative energy of impurity and additive in the film, and solubility of the additive and mobility of the additive. Here, the plausible LUMO level and the structural design rules of the additives to enable PBS stabilized OSCs are discussed. As all of the additives demonstrated consistent PBS improvement while doping the OSC, the conclusions of this section are speculative. However, we have presented some results which demonstrate that non-doping additives are capable of reducing PBS. For example TCNQ can reduce light stress and very small quantities of TCNQ and F2-TCNQ can slightly reduce PBS. To create a PBS and NBS stabilization additive, over the past two years we have been working with Christian Nielsen from Queen Mary, University of London, who has been trying to synthesize a solubilized form of F2-TCNQ. Soluble F2-TCNQ was chosen as an appropriate additive as F2-TCNQ is capable of improving NBS with no increase in the on-off ratio and as the soluble version of F4-TCNQ reduces PBS. For unknown reasons, the synthesis of soluble F2-TCNQ is extremely challenging and has not been achieved to date.

## 4. Understanding positive bias stress in organic semiconductors

Here we suggest possible design rules for future solid state PBS additives. The LUMO level needs to be carefully selected with respect to that of the water-oxygen trap level and the HOMO level of the organic semiconductor in order to ensure a trap free recombination pathway. In the following section, the water/oxygen trap level is referred to as  $E_A^{H_2O/O_2}$ , the electron affinity of the additive as  $E_A^{\text{additive}}$  and the ionization potential of the organic semiconductor as  $I_p^{\text{OSC}}$ :

- The LUMO of the additive level needs to be at least 0.1eV below the trap level of water-oxygen complexes, in order to act as a more energetically favorable trap site than the water-oxygen complexes. The trap level of the water-oxygen complexes is believed to be in the energy range between  $E_A^{H_2O/O_2} = 3.5\text{-}4\text{eV}$ , depending on the choice of organic semiconductor [32]
- The LUMO level of the additive needs to be significantly above the HOMO level of the organic semiconductor, preferably at least 0.1 eV above the HOMO level, in order not to induce a significant concentration of mobile hole charge carriers in the organic semiconductor by integral charge transfer doping, which would undesirably increase the transistor ON-current
- These two requirements can be summarized as:  $E_A^{H_2O/O_2} + 0.1 \text{ eV} < E_A^{\text{additive}} < I_p^{\text{OSC}} - 0.1\text{eV}$

Furthermore, the molecular additive is selected to interact strongly with the organic semiconductor. For example, by a charge transfer interaction so as to facilitate close intermolecular contact between the additive and the organic semiconductor in order to facilitate rapid recombination of trapped electrons on the additive with holes induced on the organic semiconductor. These holes can either be induced electrically by application of a negative gate voltage during operation or as highly localized holes, as opposed to mobile holes (that would increase the OFF current), through the molecular interaction between the additive and the organic semiconductor. To achieve the latter, the additive may be selected to induce a charge transfer complex as opposed to integer charge transfer with the organic semiconductor[108]. Alternatively, the additive may be selected such as to induce some integer charge transfer in the organic semiconductor in which the hole remains strongly Coulombically bound to the additive. Such a situation is favoured at low doping concentrations in organic semiconductors with a low degree of

## 4. Understanding positive bias stress in organic semiconductors

energetic disorder, where there is limited scope for ionization of the charge pairs created by charge transfer to separate in the energetic disorder landscape of the organic semiconductor[109]. In both cases the holes generated by the interaction between the organic semiconductor and the additive are not mobile, i.e. they do not generate a significant OFF-current, but their presence allows trapped electrons to recombine efficiently with holes induced on the organic semiconductor/additive complex.

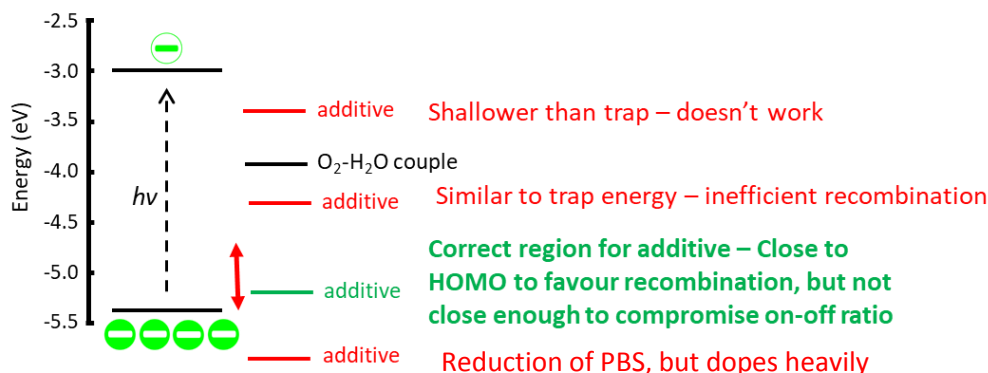


Figure 4-12: A comparison of the relative energy of the LUMO of the additive to the water-oxygen complex (O<sub>2</sub>-H<sub>2</sub>O couple), regarding the efficiency towards relieving PBS stress effects.

Maintaining an appropriate uniform morphology of the additive in an organic semiconductor blend is critical for obtaining a desirable PBS. However, maintaining the morphology is a difficult task as the additives electrically and thermally diffuse and aggregate at the semiconductor dielectric interface[101], [103], [110]. Here are the following structural design rules to help improve and maintain the morphology.

- The additive needs to be highly soluble in order to prevent the additive from crashing out of the solution and forming aggregates.
- The additive should contain bulky side chains and/or become cross linked, in order to prevent the mobility and aggregation of the additives during thermal and electrical stress as well as during the formation of the polymer film.
- The additive should be capable of introducing partial or complete charge, in order to increase the electrostatic interaction between the additive and the

## 4. Understanding positive bias stress in organic semiconductors

organic semiconductor during thermal and electrical stress as well as during the formation of the polymer film.

### **Contributions**

Iyad Nasrallah from Cambridge University

Fabricated and performed electrical measurements on all diF-TES ADT OFETS

Mahesh Kumar and Jean-Luc Bredas from KAUST

Performed all DFT simulations

Filipe Richeimer at National Physical Laboratory

Performed all scanning microscopy

# 5 The interaction of water and tetracyanoquinodimethane in OFETs

## 5.1 Introduction

In the past two decades mobilities of amorphous semiconducting polymers have gone beyond  $1\text{cm}^2\text{V}^{-1}\text{s}^{-1}$ , making organic field effect transistors (OFETs) suitable candidates for flexible transistors used in applications that include organic light emitting diode (OLED) backplanes, analogue amplifiers and logic circuits. The current challenge of incorporating OFETs into real world analogue applications is stabilising the electrical characteristics such as voltage threshold, because device applications such as OLEDs are extremely sensitive. Techniques such as doping by either small molecules or oxygen have shown improved transistor characteristics, however, weak doping methods result in an undesirable increase in the off current and oxygen doping techniques are not OLED process compatible.

Nikolka et al. have demonstrated that a subset of non-doping liquid and solid state additives are capable of reducing the voltage threshold shift in IDT-BT OFETs without increasing the off current[34], [43]. The liquid additives were all organic solvents capable of forming azeotropes with water, and the suggested mechanism is that the solvent is capable of removing water from the film when it slowly evaporates. In addition, the solvent is able to effectively act as a desiccant by dissolving water and reduces the exposure of the water to the semiconducting polymer. Remarkably, the benefits of solvent washing steps were observed even after the solvent was baked out of the film, suggesting that the solvents are capable of providing long lasting benefits due to the removal of water[34].

The exact mechanisms of solid state additives are not well understood in comparison, but there is extensive evidence that the solid additives do not dope the films, which is further reproduced in this work. The suggested mechanism by Nikolka et al. is that small molecules compete with water to fill up the voids in the polymer, therefore reducing the

## 5. The interaction of water and tetracyanoquinodimethane in OFETs

number of traps and/or weak hydrogen bonding between the additive and water. This assertion was primarily based on correlational evidence that the size of the voids in the polymer film is on the same scale as the volume of the additive required to improve device characteristics, and weak hydrogen interactions between the liquid additives and water are responsible for the azeotrope affect. In this work an extensive review of “inert” small molecules suggests that either filling the voids is insufficient to improve the device performance, or the filling of voids is limited to a very small number of molecules. One assumption that is made by Nikolka et al. is that TCNQ is stable in the film and during the processing of the solution in the glove box. However, there are multiple reports stating that neutral and charged species of TCNQ react with H<sub>2</sub>O, O<sub>2</sub> and general radical species to produce a wide variety of small molecules in both solution and solid state[104]–[106], [111], [112]. A commonly proposed byproduct is an acidic derivative of TCNQ known as dicyano-p-toluoylcyanid (DCTC)[105], [106], [111], [112]. Particularly, relevant work by Qi et al. has shown that a single layer of TCNQ in solid state is extremely reactive to oxygen and moisture species forming a permanent negative ion[106]. The structure of DCTC<sup>-</sup> is seen below in Figure 5-1 from [111]

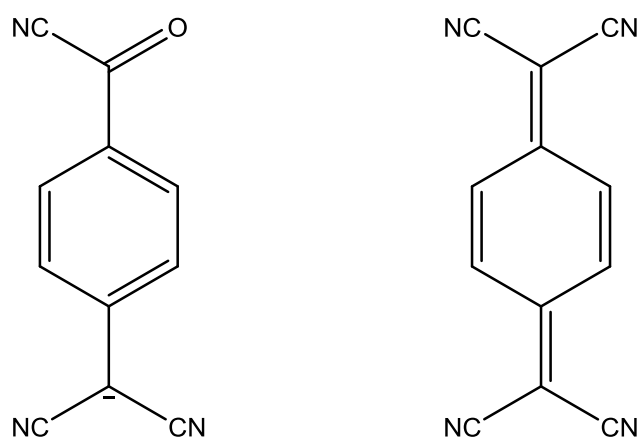


Figure 5-1: The chemical structure of Left) DCTC<sup>-</sup> and Right) TCNQ.

The chemical reactions of TCNQ suggest a series of possible desirable effects such as modifying the pH, removing atmospheric species and forming a dopant could modify the device performance[104], [106], [113]. Here we investigate whether the degradation of TCNQ with other species and the possible generation of new chemical species and/or depletion of others is related to the improved device stability.

## 5. The interaction of water and tetracyanoquinodimethane in OFETs

### 5.2 Adding water to solutions of IDT-BT with TCNQ

#### 5.2.1 Improvement in OFETs with TCNQ and water

The introduction of water into solutions of blended IDT-BT and TCNQ has been investigated to determine whether a water induced reaction mentioned in previous work could possibly result in improved OFET performance. To investigate this hypothesis, OFETS were fabricated using the semiconducting polymer IDT-BT with and without water and/or TCNQ using the same measurement protocol below:

- Solutions were mixed in an inert nitrogen environment and then moved into ambient atmosphere where water was added to the appropriate solutions.
- All solutions with TCNQ contained 4 weight percent TCNQ
- All solutions were then heated at 90C for 1hr in a sealed vial.
- Samples were then spun in air and annealed in the glovebox at 90C for 60 minutes to remove additional solvent.

Unexpectedly, the solutions where water was added to the devices (blue) with 4w% TCNQ have improved device characteristics compared to devices without water and TCNQ (black), with water (red) and with TCNQ but without water (green, Figure 5-2 A). The film with water and TCNQ has the highest on current and a voltage threshold closer to zero, while maintaining a high on-off ratio. However, there are devices where there is a high off current, which is indicative of doping.



## 5. The interaction of water and tetracyanoquinodimethane in OFETs

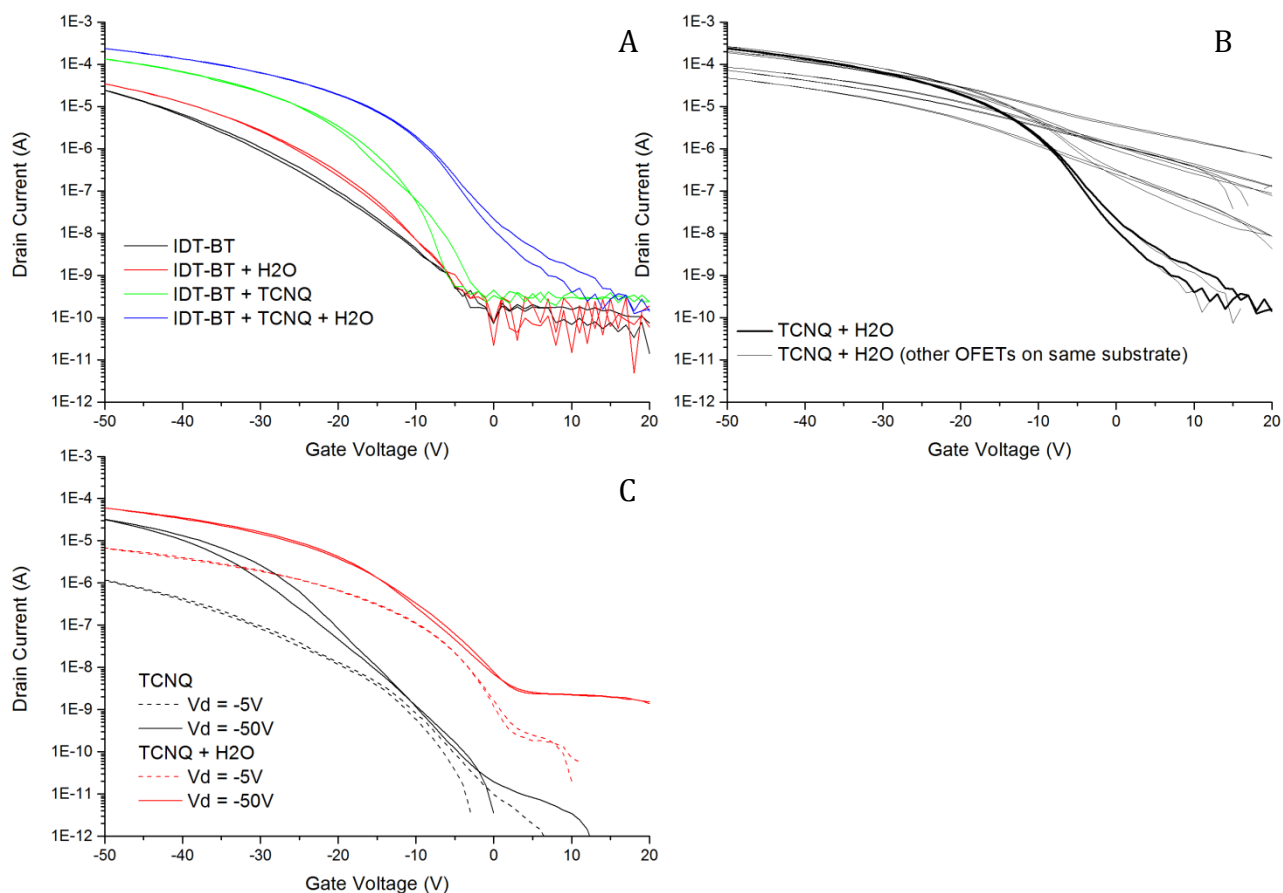


Figure 5-2: A) Transfer curves of IDT-BT OFETs with and without 4w% TCNQ blended with and without 30% volume water and heated at 90C. B) Variation of OFETs with TCNQ + water on the same substrate. C) Another batch of IDT-BT OFETs with 4w% TCNQ with and without water.

Due to the addition of the bulk water (30% volume) the films are non-uniform but result in a large device variation across the chip (Figure 5-2 B). However, these results have been repeated multiple times and show consistent device improvement and/or doping when both H<sub>2</sub>O and TCNQ are present in the solution. This is demonstrated in a second batch of devices with identical processing (Figure 5-2 C). This result indicates that the mechanism for TCNQ stabilising the OFET is related to water interacting with TCNQ. To provide insight about what interaction is occurring between TCNQ and water, the evolution of the solution and films of TCNQ with spectroscopy is examined.

## 5. The interaction of water and tetracyanoquinodimethane in OFETs

### 5.2.2 Spectroscopy of TCNQ water reactions

To understand the interaction between water and TCNQ, the evolution of the UV-VIS, infrared and NMR spectra of TCNQ films and solutions upon reaction with water was investigated.

First, the UV-VIS spectrum of TCNQ dissolved in DCB and then heated in the presence of water was characterized. The procedure of heating TCNQ in the presence of water was identical to the process used to obtain improved OFETs, but without using IDT-BT in the DCB solution. As both the DCB and water phase of the solution contained particulate matter, the solution was filtered using a hydrophilic filter to remove undissolved particulate matter. The UV-VIS spectrum of the water and DCB phase of the solution before and after heating is presented in Figure 5-3. Over the course of an hour, the DCB phase appears to remain the same, while there is a new peak in the water phase appearing at 600nm, suggesting the development of a new chemical structure in the water phase.

The time evolution of the TCNQ UV-VIS spectrum dissolved in acetonitrile in the presence of water at room temperature was also characterized. Acetonitrile was chosen as it is miscible with water and molecules with nitrile functional groups are highly soluble in it, which allows the real time observation of the interaction between water and TCNQ in the solution[114]. To achieve this, TCNQ was dissolved in acetonitrile at 0.02mg/ml and the evolution of the UV-VIS spectrum was continuously monitored after 10% volume water was added to the solution. The evolution of the acetonitrile UV-VIS spectrum of TCNQ in the presence of water (Figure 5-2) is consistent with the literature reports, showing that an absorption peak develops at 480nm which is attributed to TCNQ reacting with water from DCTC [112].

As the change in the UV-VIS spectra of the TCNQ solution in both DCB and acetonitrile in the presence of water shows a similar interaction, in other sections of the report, processing will occur in acetonitrile, as it provides cleaner processing to characterize the interaction between TCNQ and / or similar molecules with water. It is unclear why the UV-VIS peak differs between the water reaction in DCB and acetonitrile. It is possible

## 5. The interaction of water and tetracyanoquinodimethane in OFETs

that the reaction in acetonitrile compared to that in DCB results in different chemical species.

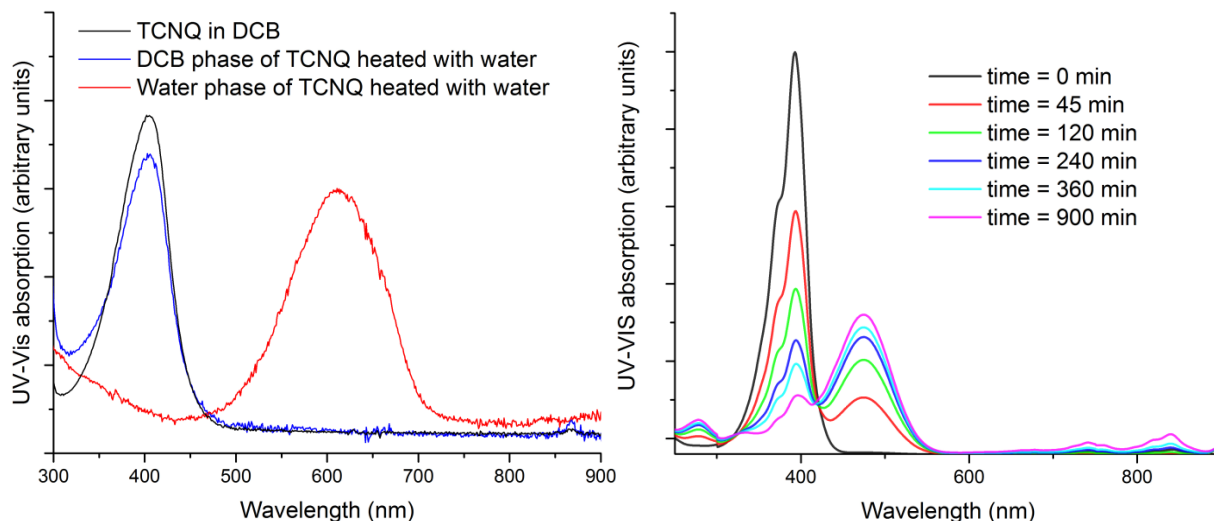


Figure 5-3: Left) The UV-VIS spectrum of TCNQ before and after heating in the presence of water. Right) The UV-VIS spectrum of TCNQ dissolved in acetonitrile at 0.02mg/ml over 12hrs in the presence of 10% volume water at room temperature.

Secondly, the infrared spectra of TCNQ dissolved in DCB and then heated in the presence of water was characterized. The procedure of heating the TCNQ in the presence of water was identical to the process used to obtain improved OFETs, but without IDT-BT being dissolved in the DCB. The DCB and water phase of the heated solutions were then drop casted onto separate double sided polished silicon substrates. The samples were then baked at 90C in air for 50 minutes to remove bulk water and solvent present in the film. For a reference, a sample of pure TCNQ was also fabricated (Figure 5-4 black). Finally, the infrared absorption spectrum was measured using an FTIR measurement system.

The FTIR spectrum of the water phase of the TCNQ heated solution (Figure 5-4 green) includes similar peaks to the reference DCTC<sup>-</sup> spectrum (Figure 5-4 blue) found in the literature[112]. The reacted water phase TCNQ spectrum has peaks around 835, 1576, 1650 and 2130-2195 which correlate with the formation of a benzene ring, the formation of the conjugated cyano-substituted double bond (marked C=C), the

## 5. The interaction of water and tetracyanoquinodimethane in OFETs

formation of a C=O vibration bond and the presence of nitrile stretching associated with a charged TCNQ molecule, which are also all found in DCTC<sup>-</sup>[112]. In the present FTIR spectrum there appears to be additional peaks and boarding of certain peaks making it difficult to detect all of the DCTC<sup>-</sup> specific peaks reported in the literature. However, it is reasonable that this should be the case as there are many possible reaction products and intermediates[105]. The DCB phase possibly contains some DCTC<sup>-</sup> (Figure 5-4 red); however, it may be in significantly reduced quantities compared to the water phase.

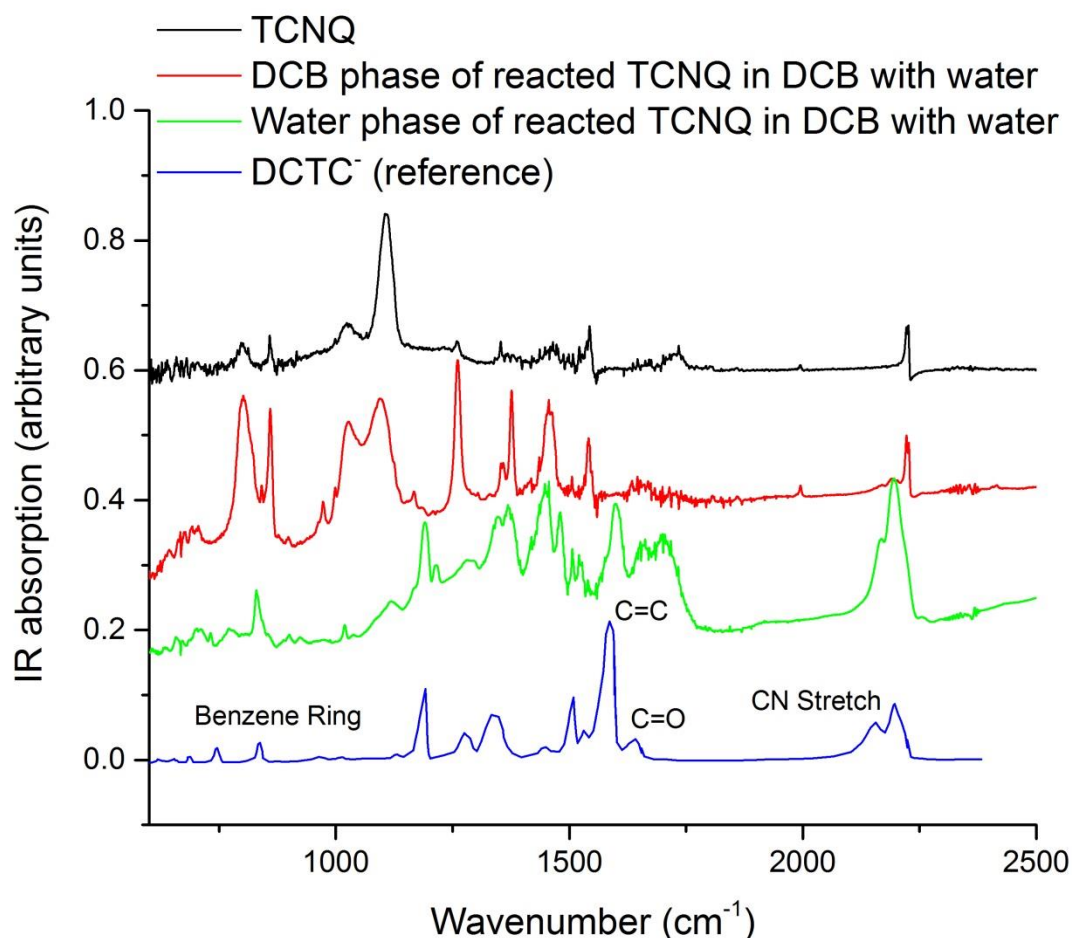


Figure 5-4: FTIR spectrums of pristine TCNQ (black), DCB (red) and water (green) phase of reacted TCNQ in DCB with water compared to a reference FTIR spectrum of DCTC<sup>-</sup> adapted from the M. Harris [112].

To determine whether an ionized species of TCNQ, DCTC or some intermediate product is present in the improved OFETs, a solution using the same process to achieve optimal

## 5. The interaction of water and tetracyanoquinodimethane in OFETs

device performance was spun onto a silicon substrate and compared to an identical fabrication procedure without water. The IDT-BT films were then measured in the FTIR. The FTIR spectra demonstrate the presence of a CN stretch when the solution contained water and was heated (Figure 5-5 red) which is indicative of a charged TCNQ derivate ( $2160\text{ cm}^{-1}$ ) compared to the reference sample without water (Figure 5-5 black) which only contains the neural peak ( $2225\text{ cm}^{-1}$ )[19].

The CN stretch implies that some ionized version of a TCNQ species is present in the IDT-BT film.

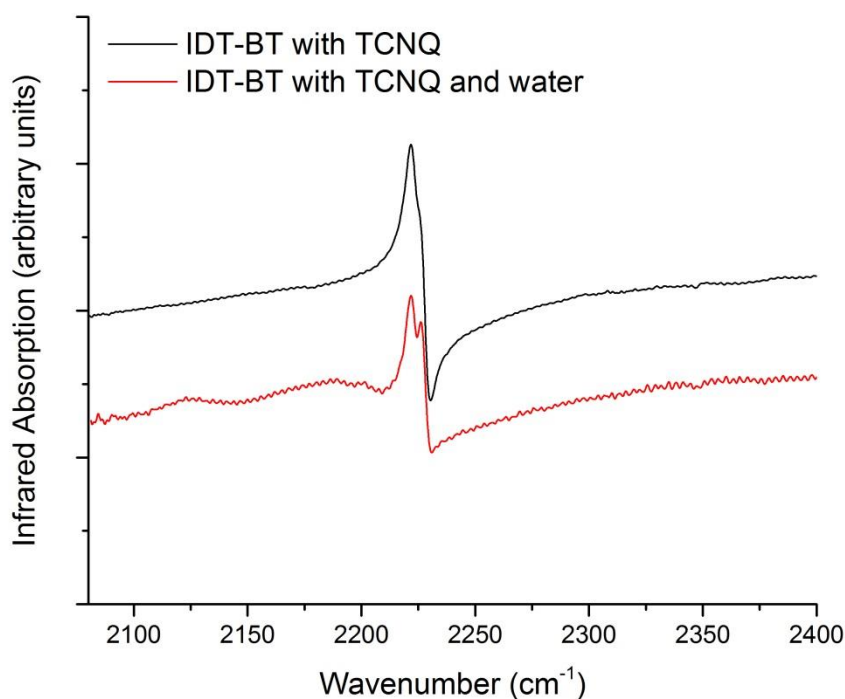


Figure 5-5: FTIR spectrum of the CN stretch region of an IDT-BT film fabricated under identical processing conditions as the IDT-BT OFETs with and without 30% volume water.

Thirdly, the NMR spectra of TCNQ dissolved in acetonitrile at 2g/L with 10% volume water and then heated at 90°C in a contained glass vial for 24hrs were characterized. Acetonitrile was used as the solvent as it is easy to process. The solutions were then dried at 70°C for 12hrs to remove the bulk water and acetonitrile before dissolving and

## 5. The interaction of water and tetracyanoquinodimethane in OFETs

filtering in deuterated acetonitrile (Figure 5-6 bottom). For comparison TCNQ was dissolved directly in deuterated acetonitrile at 2g/L (Figure 5-6 top).

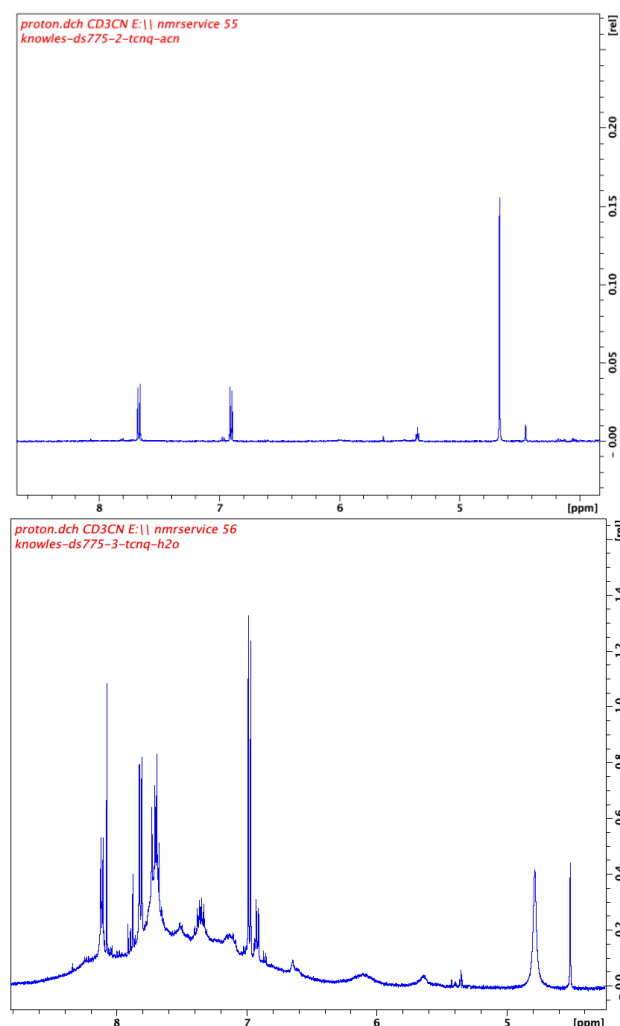


Figure 5-6: Proton NMR spectra of top) TCNQ and bottom) reacted TCNQ with water dissolved in deuterated acetonitrile.

The significant change in the proton NMR spectrum between TCNQ, and TCNQ reacted with water in acetonitrile, demonstrates new molecular spectra which appear after the TCNQ has reacted with water making it difficult to narrow down a specific chemical structure responsible for device improvement. The broad baseline hump under the sharp peaks in the water-reacted spectrum is either occurring due to inhomogeneous broadening, where there are different molecules which together average to one broad peak, or homogenous broadening, where the intrinsic line width of some of the species increases due to aggregation or polymerization of the species. As the chemical reaction

## 5. The interaction of water and tetracyanoquinodimethane in OFETs

is complex, next we attempt to determine whether TCNQ can plausibly react with moisture-oxygen species related to deep traps.

### 5.2.3 pH dependence of the TCNQ reaction

To the best of the author's knowledge, the pH dependence of chemical reactions involving TCNQ has not been characterized. The pH dependence is relevant since the literature consistently suggests that vague moisture-oxygen complexes form deep traps such as hydroxyl and hydronium ions in the polymer[31], [32], [36], [39]. To investigate the pH dependence of the TCNQ water reaction, TCNQ was dissolved at 0.2g/L in acetonitrile and 10x molar concentration water was added with hydrochloric acid, water without any acid or base and potassium hydroxide to result in solutions with pH 1, 7 and 13, respectively, along with a reference sample dissolved in anhydrous acetonitrile. After the UV-VIS spectra were measured, hydrochloric acid was slowly added to the TCNQ solution containing potassium hydroxide until the visible spectrum stabilized.

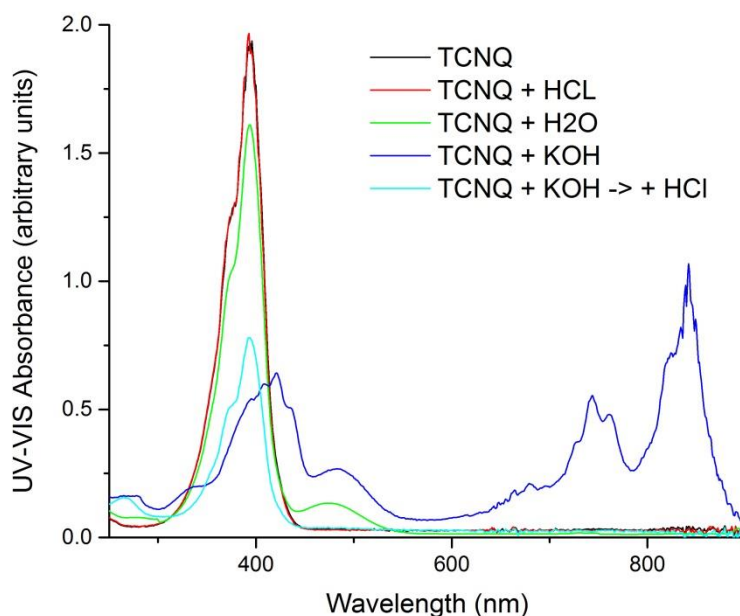


Figure 5-7: pH dependence of the TCNQ water reaction.

In the UV-VIS spectrum there is not a significant difference between the sample in anhydrous acetonitrile (Figure 5-7 black) compared to the sample with hydrochloric

## 5. The interaction of water and tetracyanoquinodimethane in OFETs

acid (Figure 5-7 red). This is in direct contrast to the UV-VIS spectra of TCNQ in acetonitrile with water and potassium hydroxide (Figure 5-7 green and blue, respectively). The solution with water shows a minor change while the solution with potassium hydroxide changes considerably. When hydrochloric acid is titrated into TCNQ in acetonitrile solution with potassium hydroxide solution, the UV-VIS spectrum reverts back to one similar to the spectrum of TCNQ dissolved in anhydrous acetonitrile (Figure 5-7 cyan); however, the neutral TCNQ absorption at 400 nm is significantly smaller. These results indicate that the interaction between TCNQ is pH dependent and irreversible.

### **5.2.4 The relationship between pH of OSC in OFET and bias stability**

It is unclear what exact chemical species are generated when heating TCNQ in the IDT-BT film in the presence of water. However, if an acid is produced it is possible that the acid could change the nature of the atmospheric traps present in the film and possibly dope the polymer. If the generation of an acid is the root of the increased device performance, it is conceivable that the addition of a different acid with a completely different chemical structure would also lead to improved IDT-BT OFET characteristics. In Chapter 3, Searching for solid state additives, it was demonstrated that HCL, 4-dodecylbenzenesulfonic acid and acetic acid all lead to increased device performance while potassium hydroxide and neutral water decrease device performance.

Here, we investigate in greater detail how hydrochloric acid, water and potassium hydroxide affect the NBS and PBS stability. To investigate how pH affects the stability, IDT-BT OFETs were fabricated, and before depositing the Cytop layer the annealed polymer film was washed in hydrochloric acid, water or potassium hydroxide with a pH of 1, 7 and 14 respectively in atmosphere for two minutes followed by a 10s anneal at 90C to remove bulk water. The evolution of the OFET transfer curves was then monitored during NBS and PBS (Figure 5-8).



## 5. The interaction of water and tetracyanoquinodimethane in OFETs

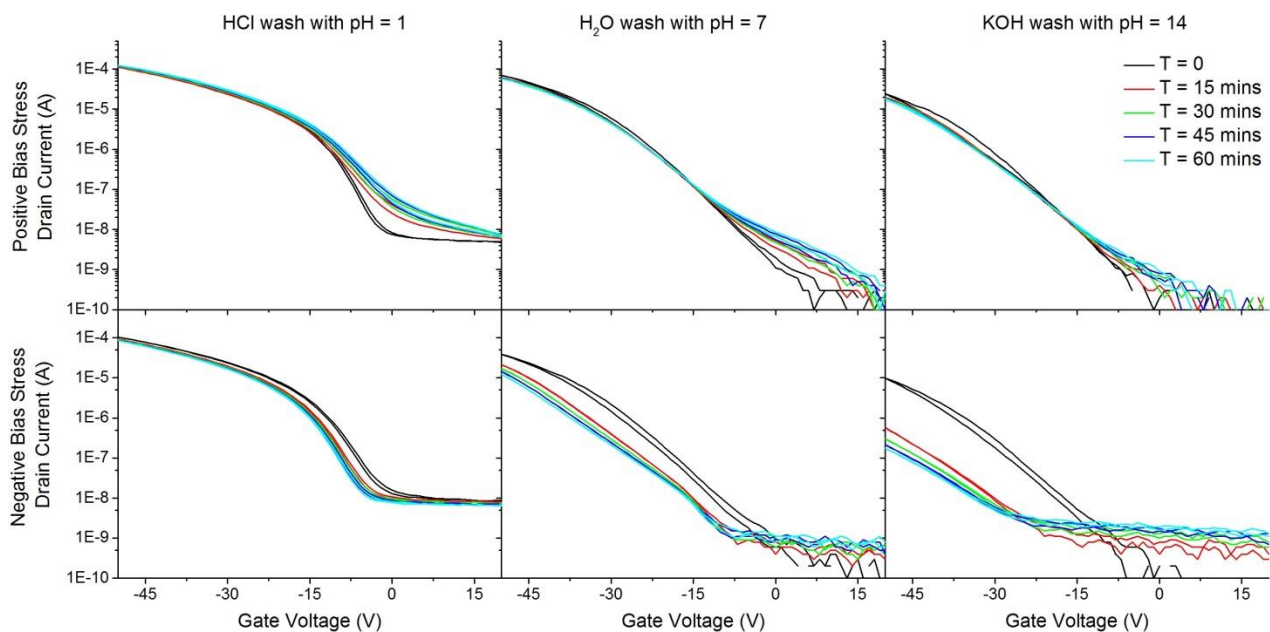


Figure 5-8: PBS and NBS stability of fabricated transistors washed with hydrochloric acid, water or potassium hydroxide solution.

The devices exposed to more acidic solutions had a consistent increase in PBS and a reduced NBS. The voltage threshold decrease due to PBS with the hydrochloric wash over a period of 1hr was approximately 3V, while the water and potassium washed devices had negligible PBS. The NBS of devices exposed to hydrochloric acid, water and potassium hydroxide were -2.5, -5 and -15V, respectively. The degraded transfer characteristics with the potassium hydroxide are indicative of high concentration of hydroxide acting as traps, which becomes pronounced during negative bias stress due to the accumulation of holes. Similarly, the improvement of NBS with hydrochloric acid is indicative of low concentrations of hydroxide or modification of the Gibbs free energy to reduce hole trapping during NBS. These results suggest that both NBS and PBS are very pH dependent.

### 5.3 Generality of the reaction

The interaction between TCNQ and water should not be limited to TCNQ and should be observed with other materials of similar structures to TCNQ. Intuitively these molecules

## 5. The interaction of water and tetracyanoquinodimethane in OFETs

should result in increased device performance relative to devices without the molecular additive. Here, we investigate whether molecules of similar structure previously reported by Nikola et al. undergo a similar reaction with water and display improved device characteristics[34], [43].

The subset of molecules investigated with similar structure to TCNQ include 11,11-dicyano-9-anthraquino-10-methane (DCAQ), 11,11,12,12-tetracyano-9,10-anthraquinodimethane (TCAQ), 2,5-difluoro-7,7,8,8-Tetracyanoquinodimethane (F2-TCNQ), 2,3,5,6-tetrafluoro-7,7,8,8-tetracyanoquinodimethane (F4-TCNQ), 2,2'-(perfluoronaphthalene-2,6-diylidene) dimalononitrile (F6-TCNNQ) and Hexacyano-3-radialene (CN6-CP) along with the soluble version of TCAQ (2,2'-(2-(tert-butyl)anthracene-9,10-diylidene) dimalononitrile or t-Bu-TCAQ), which includes a tert-butyl side chain. 9,10-anthraquinone (AQ) and the soluble version (2-(tert-butyl)anthracene-9,10-dione or t-Bu-AQ) with tert-butyl side chains were used as a reference and should not undergo a similar chemical reaction to TCNQ, as they do not include any nitrile groups.

To characterize the relationship between the molecular additives and water, the UV-VIS spectrum and FTIR spectrum were measured after the dopant was dissolved in 2g/L acetonitrile with the presence of 10% volume water and heated at 90C on a hotplate for an extended period of time. The UV-VIS spectra of the solutions were obtained before the water was added, 1hr after and 24hrs after water was added, then heated at 90C. The FTIR spectra of the drop cast additives were obtained before the water was added and 24hrs after the water was added, then heated at 90C. To observe the improvement in OFET transistors with the molecular additives the same procedure of heating TCNQ in the presence of water to obtain improved OFETs was used. All of these results can be seen in Figure 5-9 and Figure 5-10 for non-dopants and doping molecular additives, respectively.

## 5. The interaction of water and tetracyanoquinodimethane in OFETs

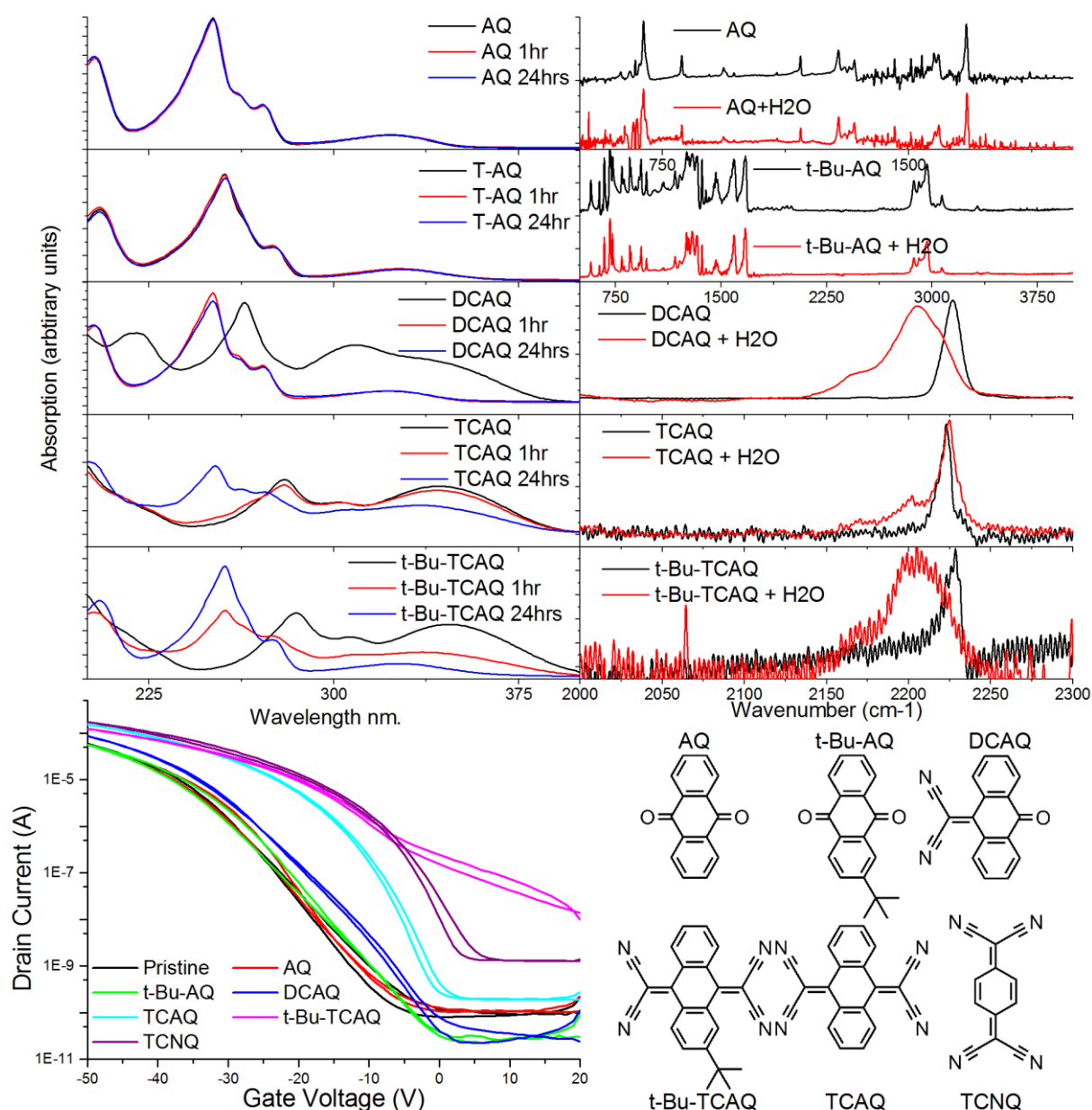


Figure 5-9: A) The change in the UV-VIS spectrum of AQ, t-Bu-AQ, DCAQ, TCAQ and t-Bu-TCAQ in 2g/L acetonitrile upon the addition of water and heated at 90C. B) The relevant change in the FTIR spectrum of AQ, t-Bu-AQ, DCAQ, TCAQ and t-Bu-TCAQ in 2g/L acetonitrile upon the addition of water and held at 90C for 24hrs. C) The resulting transfer curves of an IDT-BT OFET blended with 4w% AQ, t-Bu-AQ, DCAQ, TCAQ, t-Bu-TCAQ and TCNQ with the addition of 30% water and heated at 90C for 1hr compared to a reference sample. D) Chemical structure of AQ, t-Bu-AQ, DCAQ, TCAQ and t-Bu-TCAQ.

## 5. The interaction of water and tetracyanoquinodimethane in OFETs

Similar to the TCNQ water interaction results, it appears that all of the non-doping molecules which showed a change in the UV-VIS spectrum and a CN stretch in the FTIR, such as DCAQ, TCAQ and t-Bu-TCAQ, result in increased device performance compared to the reference samples (Figure 5-9). Molecules such as AQ and t-Bu-AQ with no nitrile functional groups do not show any significant change in the UV-VIS or FTIR spectrum, suggesting that there is no significant and/or similar interaction between them and the water in comparison to DCAQ, TCAQ, TCNQ and t-Bu-TCAQ. These results are mostly consistent with those of Nikolka et al., which showed that DCAQ and t-Bu-TCAQ result in device improvement while the addition of TCAQ, AQ and t-Bu-AQ do not. Nikolka et al. suggested that TCAQ did not lead to device improvement as it has a poor solubility (<2g/L) compared to other TCNQ additives which resulted in it not being able to fill the voids. The current results suggest that if TCAQ reacts with water, a new species is capable of stabilising the transistor.

Similar to all of the non-doping water interaction results, it appears that all of the doping molecules (F2-TCNQ, F4-TCNQ, F6-TCNNQ and CN6-CP) with similar molecular structure to TCNQ undergo a similar interaction with water (Figure 5-10). This demonstrates that an interaction occurs directly between water and similar TCNQ dopants, and could be related to the observed environmental stability of organic devices with dopants present. This is in contrast to the concept that device stability is based purely on the electrical passivation of traps using similar doping techniques found in inorganic semiconductors. This work would then suggest that these dopants could passivate electrical traps via doping the polymer and possibly further reduce traps by interacting directly with water, a common source of deep traps in organic devices.

## 5. The interaction of water and tetracyanoquinodimethane in OFETs

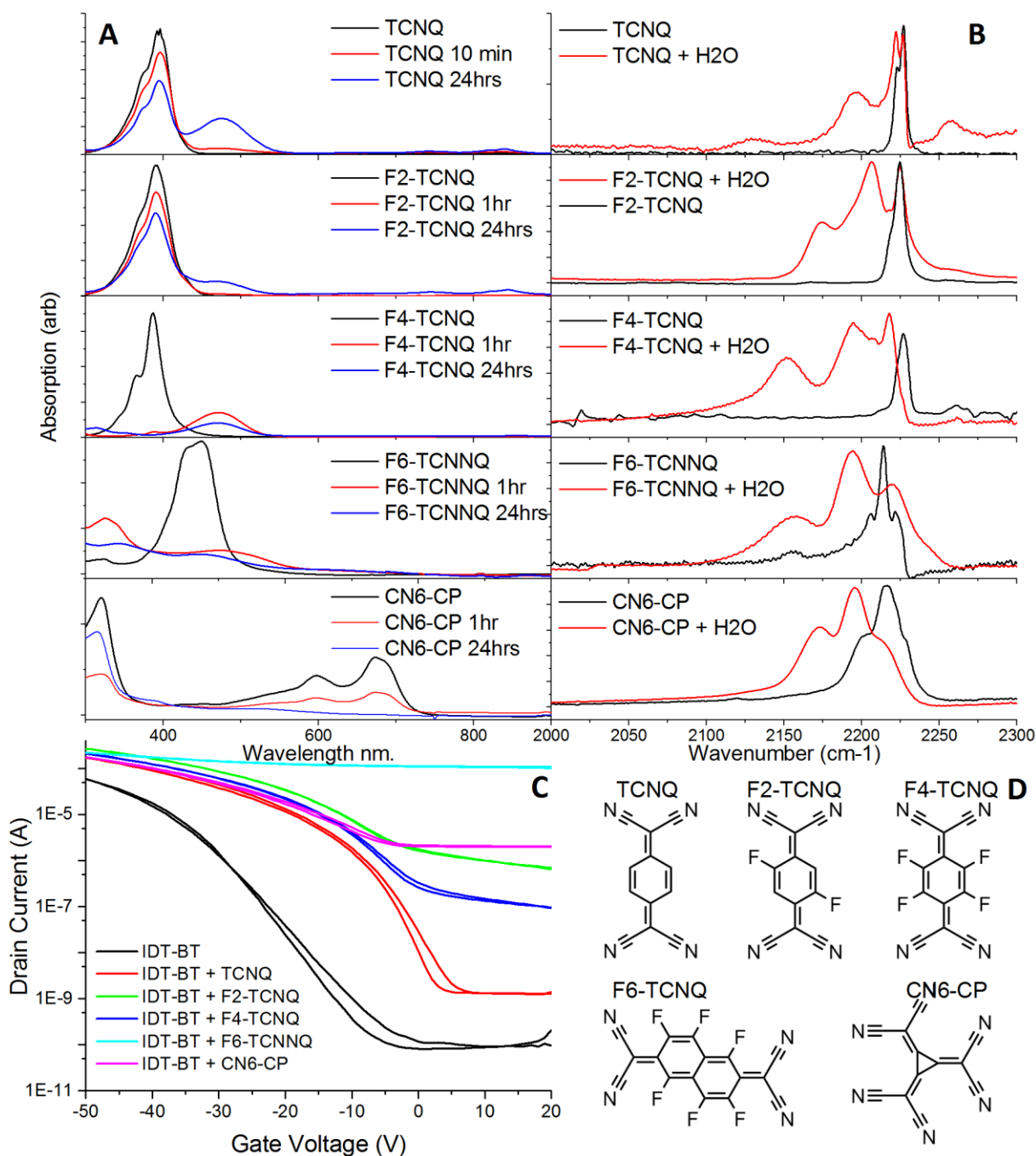


Figure 5-10 A) The change in the UV-VIS spectrum of TCNQ, F2-TCNQ, F4-TCNQ, F6-TCNNQ and CN6-CP in 2g/L acetonitrile upon the addition of water and heated at 90°C. B) The relevant change in the FTIR spectrum of TCNQ, F2-TCNQ, F4-TCNQ, F6-TCNNQ and CN6-CP in 2g/L acetonitrile upon the addition of water and held at 90°C for 24hrs. C) The resulting transfer curves of an IDT-BT OFET blended with 4w% TCNQ, F2-TCNQ, F4-TCNQ, F6-TCNNQ and CN6-CP with the addition of 30% water and heated at 90°C for 1hr compared to a reference sample. D) Chemical structure of TCNQ, F2-TCNQ, F4-TCNQ, F6-TCNNQ and CN6-CP.

## 5. The interaction of water and tetracyanoquinodimethane in OFETs

As it has been demonstrated in this section, there is a clear relationship between device improvement and molecular additive structure. Next, the possibility of building a predictive model to help augment the discovery of new molecular structures is examined.

### **5.3.1 Solid state reactions of dopants in film**

Through this study it has been shown that TCNQ and similar molecules undergo an interaction between moisture species when dissolved in a solvent in the presence of water. It is unclear to what extent TCNQ and similar molecules will provide further passivation effects by interacting with the moisture defects in solid state. To investigate the solid state interaction between the molecular additives and atmospheric conditions in IDT-BT films, films of IDT-BT with 4 weight percent of fresh solution of TCNQ, F2-TCNQ and F4-TCNQ were fabricated on double sided silicon substrates using identical process conditions to those for the OFETS without the presence of any water. For a reference, fresh solutions of TCNQ, F2-TCNQ and F4-TCNQ in acetonitrile at 2g/l were drop casted onto double sided silicon substrates. FTIR scans were performed on the initial samples in atmospheric conditions and again three months after fabrication while being exposed to atmospheric conditions. The time evolution of the FTIR spectrum of IDT-BT films with molecular additives in air is compared to a reference sample of the molecular additive not exposed to air in Figure 5-11.

## 5. The interaction of water and tetracyanoquinodimethane in OFETs

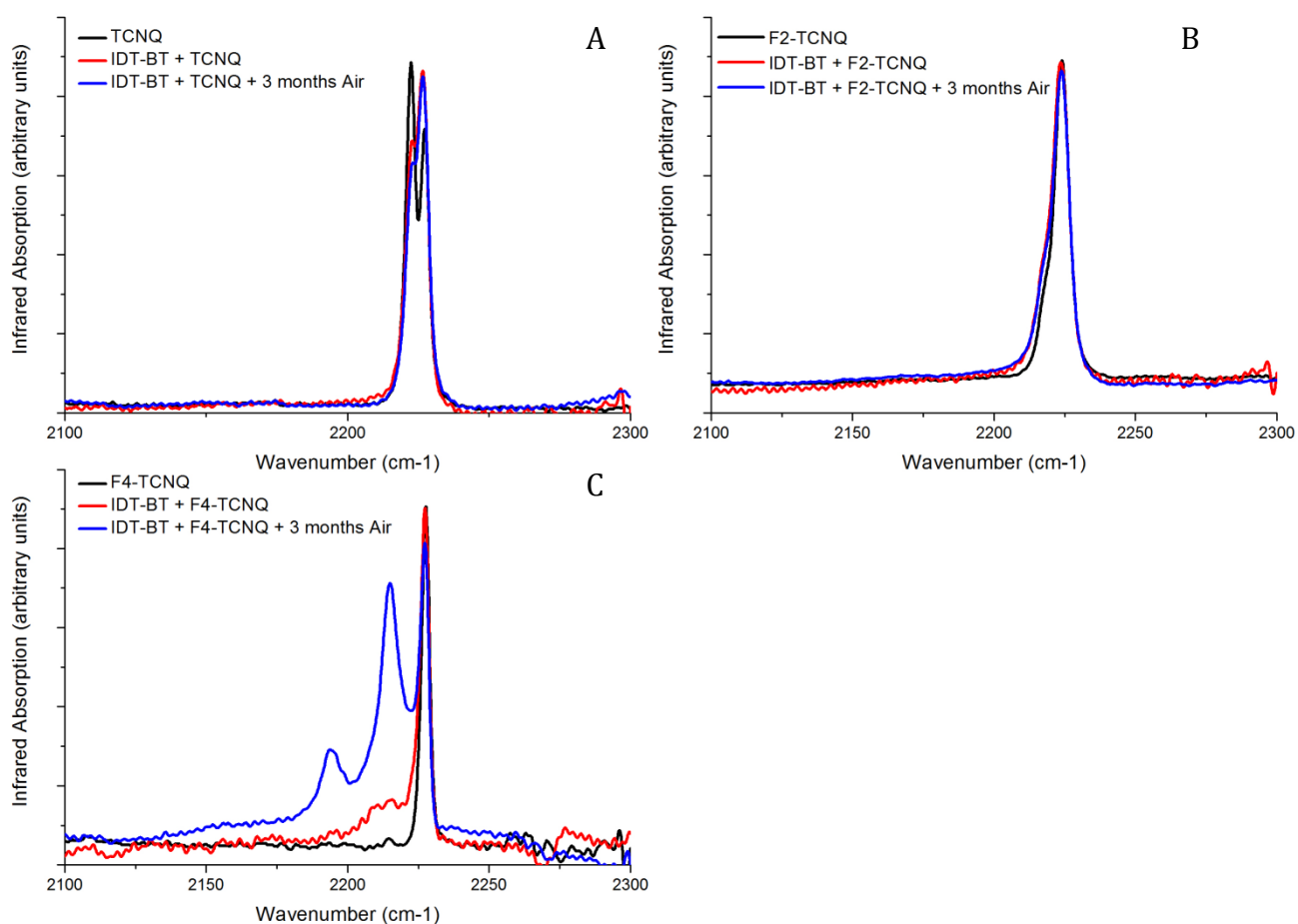


Figure 5-11: Influence of moisture atmospheric species on A) TCNQ, B) F2-TCNQ and C) F4-TCNQ.

As no CN stretch appears when TCNQ is mixed into IDT-BT, this indicates that TCNQ and IDT-BT do not undergo a charge transfer (Figure 5-11 A). As no CN stretch appears after 3 months in the TCNQ IDT-BT FTIR spectrum, this suggests that TCNQ does not interact with water significantly after the film has formed. As a CN stretch initially appears after the F2-TCNQ IDT-BT film is formed, this suggests that F2-TCNQ forms a charge transfer complex with IDT-BT (Figure 5-11 B). Since the F2-TCNQ CN stretch does not change after exposure to moisture, this suggests that just like TCNQ, F2-TCNQ does not significantly interact with water after the film has formed. Just like F2-TCNQ, a CN stretch appears in the F4-TCNQ and IDT-BT films initially after the film is formed. This suggests that F4-TCNQ forms a charge transfer complex with IDT-BT (Figure 5-11 C). Unlike TCNQ and F2-TCNQ, the CN stretch of F4-TCNQ significantly changes after exposure to moisture, indicating that F4-TCNQ might continuously interact with

## 5. The interaction of water and tetracyanoquinodimethane in OFETs

moisture in the solid state. From this result it is unclear whether F4-TCNQ is interacting with moisture in the solid state or whether over time F4-TCNQ dopes the polymer more.

Next we resolve whether F4-TCNQ interacts directly with water in the solid state or whether it dopes the polymer more over time in an inert atmosphere. To distinguish whether F4-TCNQ is capable of interacting with water at room temperature in the solid state, the time evolution of the UV-VIS spectrum of 2ml of water with 8 mg of undissolved particulates F4-TCNQ and TCNQ was monitored at room temperature for 12hrs.

Over time the TCNQ UV-VIS spectrum in water develops a peak at 397 nm which is indicative of the presence of neutral TCNQ dissolved in water (Figure 5-12 A)[67]. In the F4-TCNQ solution, peaks develop at 331, 751 and 851 nm in the UV-VIS spectrum, representing the development of new non neutral chemical species (Figure 5-12 B) [67]. Furthermore, after leaving the solutions at room temperature for 1 week a litmus paper test indicated that the solution with F4-TCNQ was acidic while TCNQ remained neutral. These results strongly indicate that F4-TCNQ interacts directly with water in the solid state in comparison to TCNQ.

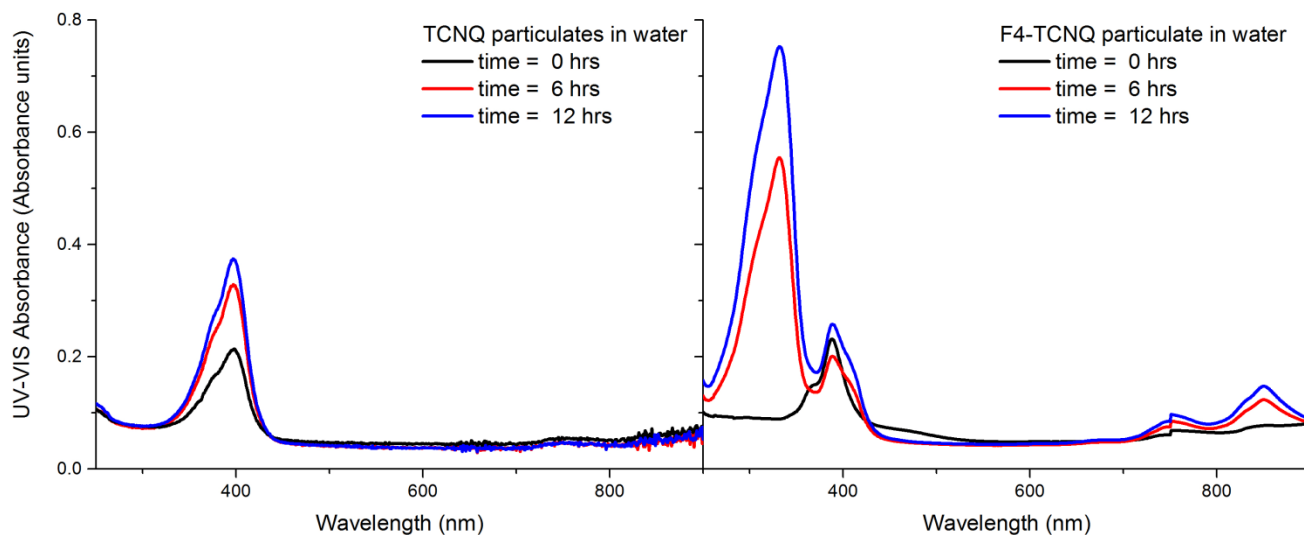


Figure 5-12: The evolution of the UV-VIS spectrum of left) TCNQ and right) F4-TCNQ particulates in water.

To determine whether F4-TCNQ dopes the polymer more over time, the supplementary information of Nikolka et al. regarding the environmental stability of IDT-BT films with the molecular additive F4-TCNQ has been reviewed. Their work demonstrates that the



## 5. The interaction of water and tetracyanoquinodimethane in OFETs

off current of IDT-BT OFETs doped with 2 weight percent F4-TCNQ does not significantly change when exposed to atmosphere for 24hrs followed by a dry nitrogen environment for an additional 24hrs. This is inconsistent with the FTIR spectrum of the 5 weight percent F4-TCNQ IDT-BT film from the work of Nikolka et al., which demonstrates significantly more F4-TCNQ molecules developing a CN stretch after exposure to atmosphere for 72hrs. Furthermore, Nikolka et al. demonstrate that OFETs with 10 weight percent F4-TCNQ, after storage in nitrogen over 2 years, have negligible off currents but maintain good transfer characteristics. In summary, these results indicate that F4-TCNQ does not inherently dope the polymer more over time, suggesting that the increase in the CN stretch is related to a solid state interaction between F4-TCNQ and atmospheric species, which does not readily occur with TCNQ and F2-TCNQ.

## 5. The interaction of water and tetracyanoquinodimethane in OFETs

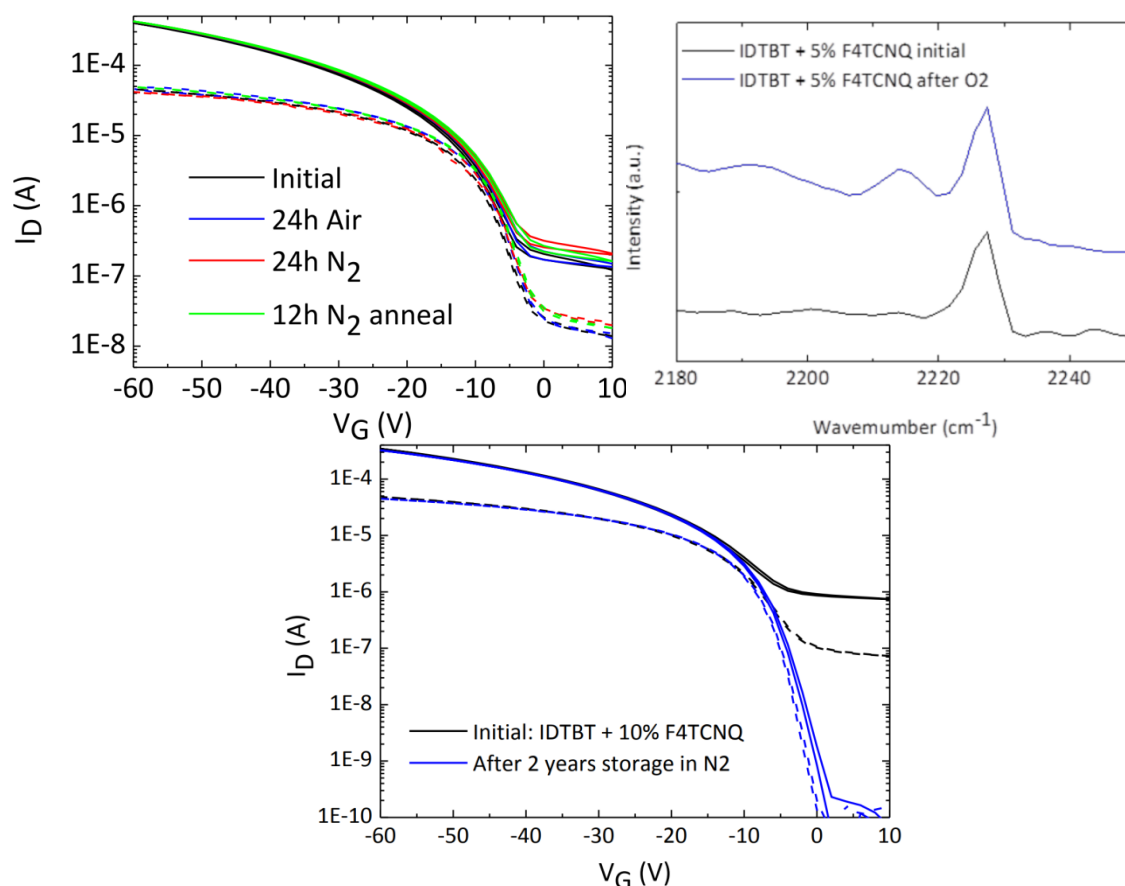


Figure 5-13: Top Left) The transfer characteristics of IDT-BT films with 2 weight percent F4-TCNQ exposed to different atmospheric conditions for extended periods of time. Top Right) Evolution of the FTIR spectra of IDT-BT films with 5 weight percent F4-TCNQ exposed to atmosphere for 72hrs. Bottom) The evolution of the transfer characteristic of IDT-BT films with 10 weight percent F4-TCNQ after 2 years of storage in a nitrogen glovebox. Images taken from G. Malliaras et al. [43].

### 5.4 Implications

The implications of this work for inherently doping and non-doping reactive solid state additives are discussed. Inherently doping reactive additives are characterized as molecules which have a sufficiently deep LUMO that can dope the polymer through some direct charge transfer mechanism as well as undergo a reaction with water. This category would include molecules such as CN6-CP, F4-TCNQ and F6-TCNNQ. Non-doping reactive additives are characterized as molecules which do not have a sufficiently deep LUMO that can dope the polymer through a direct charge transfer mechanism but

## 5. The interaction of water and tetracyanoquinodimethane in OFETs

undergo a reaction with water that can dope the polymer or remove moisture defects. This category would include molecules such as TCNQ, TCAQ and DCAQ. For convenience, for the rest of this work we will refer to inherently doping and non-doping reactive solid state additives as reactive doping and non-doping additives.

### **5.4.1 Consequences for doping additives**

As demonstrated previously, there is a class of reactive dopants with similar nitrile structures which reacts and/or undergoes a charge transfer with moisture species in solution and in solid state. The doping efficiency of these reactive dopants in semiconducting polymers is typically low with high doping efficiencies approaching 13% [115], [116]. The majority of dopants in the OFET do not dope the organic but can interact with water defects in the device directly and possibly change the nature of the atmospheric defects. This suggests that improved bias and environmental stress stability of reactive dopant additives could be a combination of doping the OSC and reacting with water, modifying the defects [43], [117].

It is curious that there are other dopants such as C30F36 and Mo(Tfd03) which are both able to dope IDT-BT but might not have the same interaction between the nitrile dopants and water due to the significant change in structure. It is unclear whether C30F36 and Mo(Tfd03) exhibit different long term environmental stabilities.

### **5.4.2 Consequences for non-doping reactive additives**

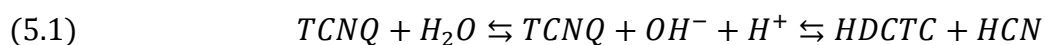
This report demonstrates that non-doping reactive additives, such as TCNQ, are able to stabilize p-type transport by undergoing chemical reactions with moisture species. The NMR and FTIR data demonstrate a mixture of chemical species produced in the reaction of TCNQ with water. It is unclear what specific species or group of species are responsible for the improved device characteristics. However, the understanding that a chemical reaction is involved with TCNQ improving device characteristics is a critical step forward in finding new materials to stabilize OFETs. As it is unclear what chemical combination is responsible for improved device characteristics, here we hypothesize what plausible ways TCNQ and possible TCNQ reaction byproducts could result in

## 5. The interaction of water and tetracyanoquinodimethane in OFETs

improved device characteristics such as consuming moisture species, maintaining a low pH and stabilising through doping[104], [106], [113].

### 5.4.2.1 Consumption of moisture species

Nikolka et al. have also demonstrated that the removal of water in p-type IDT-BT transistors through desiccants improves device characteristics[43]. The improvement through the dehydration of the polymer film would suggest that if TCNQ is only consuming water, it would result in improved device characteristics. Two possible stoichiometry balanced chemical reactions involving water reacting with TCNQ to form DCTC and 2-(4-(dicyanomethyl)phenyl)-2-hydroxymalononitrile (DCHM) are presented below:



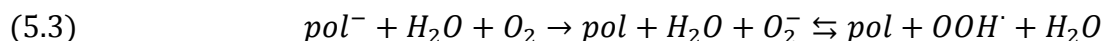
Possible mechanisms for device improvement through dehydration include the removal of redox reactions, radicals, thermally ionized water and high dielectric defects.

D. de Leeuw et al. have proposed that it is impossible to engineer the HOMO and LUMO level of the organic systems such that the redox reactions from both the HOMO and LUMO are in an equilibrium and/or are thermodynamically unfavorable during accumulation and depletion of charge[31], [36]. Therefore, the only route to prevent atmospheric species redox reactions is to remove atmospheric species.

Radicals present in the chemical structure of a semiconductor will act as deep traps localized in the middle of the band gap of semiconductors. Controlling radicals in the structure of amorphous silicon by the addition of hydrogen is critical as the large number of radical defects in amorphous silicon creates “*very high defect density which prevents doping, photoconductivity and other desirable characteristics of a useful semiconductor*”[2]. The consequence of having radicals generated in the film due to the

## 5. The interaction of water and tetracyanoquinodimethane in OFETs

formation of superoxide is problematic as any chemical reaction between a radical and a non-radical species is itself a radical, suggesting that once a radical reaction has been initiated it is difficult to stop, equation 5.3. It is plausible that radical chemistry occurs in the polymer as superoxides are known to form in organic systems and will decompose with water forming a hydroperoxyl radical and the hydroxyl anion[98].



Simulations by Nikolka et al. have shown that holes in the IDT-BT HOMO are capable of oxidizing a hydroxyl species, possibly resulting in a neutral radical hydroxyl species. The concept of radical initiated degradation has been observed by Jacobs et al. in organic photovoltaics (OPVs). Jacobs et al. demonstrated that even though 1,8-diiodocatane has been shown to improve the mixing of organic blended OPVs, under illumination it acts as a radical initiator resulting in a series of reactions increasing the radical concentration in the film and resulting in long term defects even after it has been removed[118]. As TCNQ is highly chemically reactive to both hydroxyls and a broad species of radicals, it is plausible that TCNQ or DCTC would be able to react with the moisture or reaction products, consuming the water induced defect species in the organic.

Kettner et al. have demonstrated that both NBS and PBS in polymers are generated by the separation of thermally generated species at 273K which are believed to be protons and hydroxyls. This suggests that if water was removed from the polymer, this process of thermally separating ionized water would be stopped. Furthermore, as free hydroxyls are produced during the process, these hydroxyl ions could react with the TCNQ and prevent a reaction with the hole in the polymer resulting in a deep trap or chemical defect site.

If mobile ionized water is responsible for PBS and NBS, a possible route to improve stress would be to reduce the mobility of the ions. Proton cation migration in non-polar proteins is commonly studied in biochemistry[119]. It appears that protons do not wander through a hydrophobic protein but transfer along a Grotthuss chain. A Grotthuss chain is a network of water molecules which allows protons to hop between them very

## 5. The interaction of water and tetracyanoquinodimethane in OFETs

rapidly. Interestingly, Nikolka et al. have demonstrated that solvents which act as azeotropes allow the solvent to remove water from the film and dissolve water in the film, which suggests that disrupting a Grotthuss chain by removing some water instead of removing all water might be sufficient to reduce the bias stress.

Organic semiconductors have a low relative permittivity of 2.3 while water has a large relative permittivity of 78.7. This would suggest that the water molecules will strongly influence the local electric field, resulting in increased energetic disorder on the polymer. Calculations from Nikolka et al. have shown that the high relative permittivity of water is capable of introducing torsion into the IDT-BT polymer backbone, resulting in increased energetic disorder[43]. Furthermore, a few monolayers of water at the electrode would reduce the strength of the electric field in the water layer, increasing the injection potential. Therefore, removing the water would reduce the energetic disorder observed by a charge carrier on the polymer.

The complete removal of water does not appear to be the dominant mechanism, as experimentally we have demonstrated that TCNQ reacting in the presence of water improves device characteristics without removing bulk water. This suggests other mechanisms such as modification of the pH in the voids of the polymer or that the additive doping converting to a dopant is responsible for the observed device improvement.

### **5.4.2.2 Stabilization through acidity**

In this work we have demonstrated that acids, such as hydrochloric acid, improve negative bias stress. Here different possible mechanisms are examined that are pH dependent, including radical passivation, hydrogen doping and modifying the redox chemistry. It should be noted that TCNQ is not an acid but can be turned into one, suggesting that if just pure TCNQ is incorporated into the film it will not necessarily maintain a strongly acidic environment until it has reacted with the appropriate species.

As described above, radicals will form traps in both organic and inorganic semiconductors, destroying semiconducting properties [2], [118]. Passivation of radicals

## 5. The interaction of water and tetracyanoquinodimethane in OFETs

in amorphous silicon during the fabrication process is due to the addition of either a radical or a hydrogen cation[2]. The hydrogen cation can passivate defect sites in amorphous silicon by undergoing a Lewis acid base reaction with a dangling silicon bond that has trapped an electron. A similar reaction could possibly occur in organic semiconductors suggesting that an acidic environment would constantly remove radical defects. As there is no experimental evidence for this mechanism, it is more plausible that a form of observed acidic doping is responsible.

Both the work of Nikolka et al. and this work have demonstrated that pure TCNQ by itself does not dope IDT-BT, however, TCNQ can result in highly doped films. Direct hydrogen doping of IDT-BT has not been reported but hydrogen doping has been observed in many polymer systems due to the direct integration of a positive proton onto the polymer backbone[14], [120]. Typically hydrogen doping will occur due to electrophilic aromatic substitution or a Lewis acid base reaction. Interestingly, Panidi et al. have reported IDT-BT doping through a Lewis acid base interaction by incorporating a strong Lewis acid tris (pentafluorophenyl) borane[21]. This suggests that highly acidic environments could directly dope IDT-BT through a similar Lewis acid base interaction.

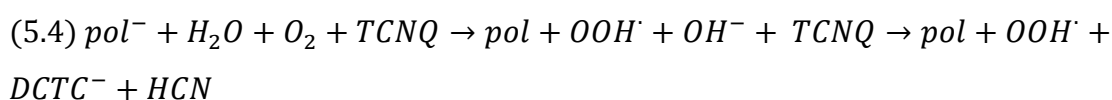
As D. de Leewu et al. have proposed that redox reactions are responsible for hole trapping in OSCs, it is conceivable that controlling the pH would change the Gibbs free energy of certain traps[31], [36]. For example, making a p-type semiconductor highly acidic would reduce the activity of hydroxyl ions, which are believed to be hole traps in IDT-BT. Furthermore, increasing the activity of hydronium ions would result in a decrease and increase in the Gibbs free energy of redox reactions involved in the generation of hydronium and hydroxyl ions. This would result in a net increase in trapped negative charges indistinguishable from doping. An important region where modifying the pH could have drastic effects would be at the metal electrode OSC interface. If there is a monolayer of water at this interface, all of the current through the device has to go through the monolayer of water and modifying the pH of the water at this location to favor electron trapping would reduce moisture based hole traps without doping the bulk of the semiconductor.

## 5. The interaction of water and tetracyanoquinodimethane in OFETs

As the acidic derivate of TCNQ modifies the pH, the acidic molecule would disturb the redox reaction equilibrium, resulting in doping the polymer by Lewis acid doping. This would suggest that TCNQ stabilizes through acidity by hydrogen doping. Next we will examine the possibility of doping through other mechanisms.

### 5.4.2.3 Stabilization through doping

Both the work of Nikolka et al. and this work has demonstrated that pure TCNQ by itself does not dope IDT-BT. However, we have shown that TCNQ can dope IDT-BT by reacting with water. In the film TCNQ could form a dopant by reacting with atmospheric species, after an initial charge transfer onto an atmospheric trap. Here we propose one plausible chemical reaction, equation 5.4, which would result in the formation of a deep electron.



As this doping mechanism modifies the pH in the process by TCNQ reacting with a hydroxyl ion, this mechanism is hard to distinguish between acidic doping. This thesis proposes that TCNQ stabilizes the polymer by reacting with water and modifying the pH.

### 5.4.3 Creating a robust stabilization additive

Here we have demonstrated that TCNQ is capable of improving device characteristics by reacting with water to form a new chemical species which modifies the pH. As TCNQ is not highly reactive to water in the solid state, more reactive molecules or inherently acidic compounds should be investigated. One method to generate more reactive molecules would be to lower the LUMO level of the additive resulting in an increased Gibbs free energy of the chemical reaction. However, a reduced LUMO level would result in increased doping of the OSC, which is undesirable. Another route to improve reactivity would be to find additives which are photo reactive. Preliminary results



## 5. The interaction of water and tetracyanoquinodimethane in OFETs

demonstrate that F4-TCNQ and TCNQ are more reactive with water in solutions in the presence of UV.

Furthermore, this Chapter has demonstrated that the improvement in device performance appears to be related to the structure of the solid state additive, which suggests one could generate a machine learning model to predict the performance of additives based on structure. A predictive machine learning model would enable high throughput screening of molecular additives to find new chemical structures, capable of acting as reactive non doping solid state additives. Next we explore whether it is possible to build a machine learning model to predict additional molecules based on our current dataset.

### **Contributions**

Dr. Ian Jacobs from Cambridge University

Performed all NMR analysis

Gosia Nguyen from Cambridge University

Helped fabricate TCNQ OFETs

# 6 Quantifying the search for molecular additives

## 6.1 Introduction

A promising aspect of organic electronics is their near infinite chemical structural variations which exhibit a range of tunable thermal, optical, electrical and mechanical properties. In practice, realizing this promise is extremely complicated, resulting in the increment in device performance being driven by expensive and time consuming empirical measurements and not analytical predictions. Solid state stabilization additives for stabilising amorphous p-type IDT-BT OFETs are an example of a complicated material system where the specific mechanism and incorporation of solid state additives is unknown. This results in new scientific discoveries being led by empirical results.

Even though the specifics of the interactions between the polymer and solid state additives are unknown, here we attempt to relate the structure of the molecular additives to improved device performance using machine learning. This is conceivable, as there appears to be a relationship between the structure of the additive and the improvement in device stability, as demonstrated in Chapter 5. Here we investigate whether it is possible to build a machine learning model relating structure to observed device improvement using all of the empirical results in this thesis. Furthermore, we examine whether it is possible to set up Bayesian optimization in order to efficiently search for new molecular structures.

### 6.2 Additive dataset

The dataset used to build the machine learning models is based on all additives tested in the work of Nikolka et al. as well as this thesis[34], [43]. Molecules are classified into two categories: Category 1, molecules which demonstrate a consistent improvement in device characteristics correlating with a reaction with water, and Category 2, all other molecules tested. Consistent improvement in device characteristics is defined as a consistent reduction in voltage threshold due to the incorporation of molecular additives. Both acidic molecules (4-Dodecylbenzenesulfonic acid, acetic acid, hydrochloric acid, sulfuric acid and THF-TCNQ) and molecules that form azeotropes with water (1,2 dichlorobenzene, toluene, acetonitrile, n-butyl acetate, isopropyl alcohol, ethanol, xylene, cyclohexane, chlorobenzene, tetralin and benzene) and demonstrate consistent improvement in device characteristics with the addition of the molecule are classified in the 2<sup>nd</sup> category as the mechanism improving device characteristics is related to a different mechanism.

Here we demonstrate the categorization on a subset of molecules. Figure 6-1 presents the improvement in OFET characteristics with dimethyl TCNQ, TCNNQ, and TCNE heated in a solution in the presence of water. These additives are characterised as category 1, an additive which is capable of reducing the voltage threshold and reacts with water, as the transfer curves from the devices with the additives has a voltage threshold closer to zero. The voltage threshold demonstrated in (Figure 6-1) as the OFET with the additive (red) is always on the right hand side of the graph, indicative of a reduction in the voltage threshold. The voltage threshold was extracted by fitting a line to the square root of the drain current.

## 6. Quantifying the search for molecular additives

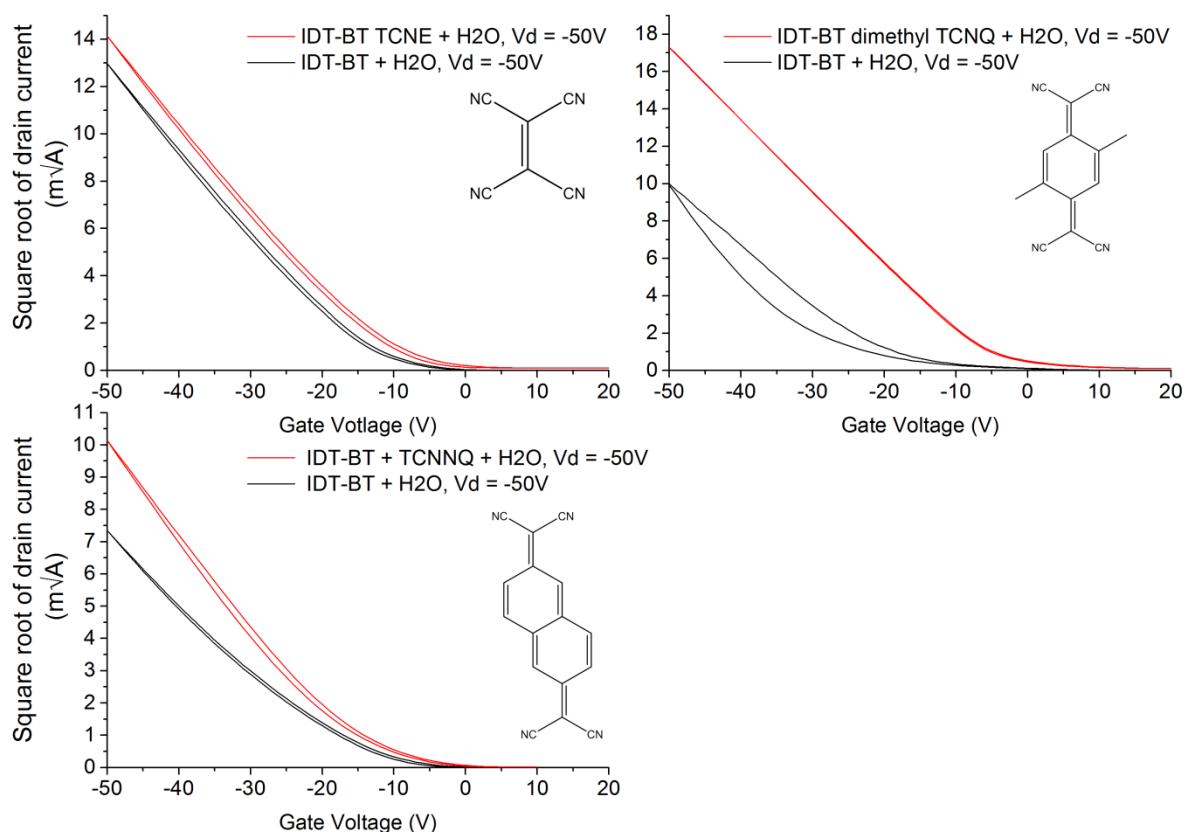


Figure 6-1: Improvement in OFET characteristics with Top Left) TCNE, Top Right) Dimethyl TCNQ, and Bottom) TCNNQ classified as Category 1

### 6.3 Feature and model selection

Here we explore the performance of neural network models capable of classifying molecular additives using different vector representations of molecular structure as input features. The vector representation of molecular structures tested includes one-hot encoding of the SMILES, a variational autoencoder SMILES representation generated from Gomez et al. and small random weight neural graph fingerprints from Duvenaud et al.[46], [54]. For specific information regarding the vector representation of molecular structures and selecting the hyperparameters please refer to the introduction and methods section.

The performance of the predictive neural network using the one-hot SMILES, SMILES VAE latent space and Neural Graph Fingerprint (NGF) representations as the input

## 6. Quantifying the search for molecular additives

vector for each molecular structure in the dataset can be seen in Figure 6-3 and Figure 6-4. The overall performance of the input vector trained on the neural network is presented in Table 7. The performance and hyperparameters were optimized using the leave-one-out cross validation metric as shown in Table 8.

Table 7: Overall performance of the predictive neural network using the one-hot SMILES, SMILES VAE latent space and NGF representations as the input vector.

		<b>Actual Positive</b>	<b>Actual Negative</b>
<b>SMILES</b>	<b>Positive Prediction</b>	10/16 (64%)	6/16 (36%)
	<b>Negative Prediction</b>	3/62 (4%)	59/62 (96%)
<b>SMILES VAE</b>	<b>Positive Prediction</b>	12/16 (76%)	4/16 (24%)
	<b>Negative Prediction</b>	4/62 (6%)	58/62 (94%)
<b>NGF</b>	<b>Positive Prediction</b>	14/16 (88%)	2/16 (12%)
	<b>Negative Prediction</b>	0/62 (0%)	62/62 (100%)

The NGF algorithm will be used for the rest of the dissertation as it has the lowest corrected variance (NGF 0.0013, SMILES VAE 0.021, SMILES 0.025) and is capable of categorizing the most additives correctly (Table 7). The variance was calculated with the adjusted number of independent pieces of information ( $73 = 78 - 5$ ). It is believed that the NGF provides the best feature sets as it can capture physical behavior by uniquely labeling physically relevant structures such as functional groups. This allows molecular structures with similar functional groups to be located closer in the feature space compared to completely different structures. This similarity would result in less data in order to fulfill the Nyquist criterion.

In direct contrast to the NGF both the SMILES and SMILES VAE features of near identical similar molecular structures can be considerably different. Consider the SMILES of TCNQ, methyl-TCNQ and F<sub>1</sub>-TCNQ. Each molecule has a near identical molecular structure, however, the canonical SMILES representations of methyl-TCNQ are

## 6. Quantifying the search for molecular additives

considerably different than the SMILES of both TCNQ and F<sub>1</sub>-TCNQ. This would result in molecules with near identical structures (and assumed properties) to be located in completely different locations of the space resulting in more experimental data to fulfil the Nyquist criterion. This is a known problem with the SMILE representation of molecules and it cannot be fixed as a string is a 1D representation[49]. This random distribution of SMILES is believed to be responsible for providing worse performance compared to the NGF.

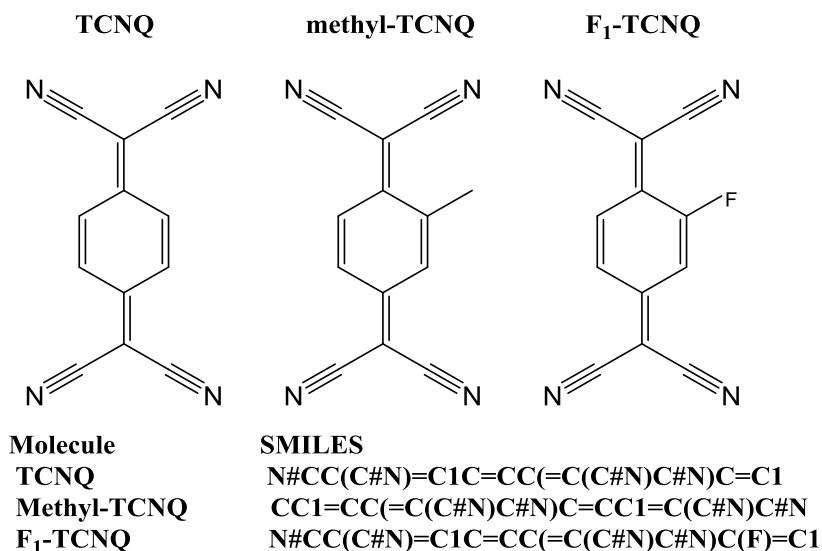


Figure 6-2: Molecular graph structure and SMILES of TCNQ, methyl-TCNQ and F<sub>1</sub>-TCNQ.

Table 8: The hyperparameters of the optimum neural networks. .

	Hidden Layers	Initial hidden Dimensions	Activation	Regl2	Dropout
<b>SMILES</b>	2	100	relu	0.01	0.1
<b>SMILES VAE</b>	2	100	relu	0.001	0.1
<b>NGF</b>	2	100	relu	0.01	0.1

## 6. Quantifying the search for molecular additives

Smiles	Predict 0 Actual 0	Predict 0 Actual 0	Predict 0 Actual 0	Predict 0 Actual 0	Predict 0 Actual 0
Smiles VAE	Predict 0 Actual 0	Predict 0 Actual 0	Predict 0 Actual 0	Predict 0 Actual 0	Predict 0 Actual 0
NGF	Predict 0 Actual 0	Predict 0 Actual 0	Predict 0 Actual 0	Predict 0 Actual 0	Predict 0 Actual 0
Smiles	Predict 0 Actual 0	Predict 0 Actual 0	Predict 0 Actual 0	Predict 0 Actual 0	Predict 0 Actual 0
Smiles VAE	Predict 0 Actual 0	Predict 0 Actual 0	Predict 0 Actual 0	Predict 0 Actual 0	Predict 0 Actual 0
NGF	Predict 0 Actual 0	Predict 0 Actual 0	Predict 0 Actual 0	Predict 0 Actual 0	Predict 0 Actual 0
Smiles	Predict 0 Actual 0	Predict 0 Actual 0	Predict 0 Actual 0	Predict 0 Actual 0	Predict 0 Actual 0
Smiles VAE	Predict 0 Actual 0	Predict 0 Actual 0	Predict 0 Actual 0	Predict 0 Actual 0	Predict 1 Actual 0
NGF	Predict 0 Actual 0	Predict 0 Actual 0	Predict 0 Actual 0	Predict 0 Actual 0	Predict 0 Actual 0
Smiles	Predict 0 Actual 0	Predict 0 Actual 0	Predict 0 Actual 0	Predict 0 Actual 0	Predict 0 Actual 0
Smiles VAE	Predict 0 Actual 0	Predict 0 Actual 0	Predict 0 Actual 0	Predict 0 Actual 0	Predict 0 Actual 0
NGF	Predict 0 Actual 0	Predict 0 Actual 0	Predict 0 Actual 0	Predict 0 Actual 0	Predict 0 Actual 0
Smiles	Predict 0 Actual 0	Predict 0 Actual 0	Predict 0 Actual 0	Predict 0 Actual 0	Predict 0 Actual 0
Smiles VAE	Predict 0 Actual 0	Predict 0 Actual 0	Predict 0 Actual 0	Predict 0 Actual 0	Predict 0 Actual 0
NGF	Predict 0 Actual 0	Predict 0 Actual 0	Predict 0 Actual 0	Predict 0 Actual 0	Predict 0 Actual 0
Smiles	Predict 0 Actual 0	Predict 0 Actual 0	Predict 0 Actual 0	Predict 0 Actual 0	Predict 0 Actual 0
Smiles VAE	Predict 0 Actual 0	Predict 1 Actual 0	Predict 0 Actual 0	Predict 0 Actual 0	Predict 0 Actual 0
NGF	Predict 0 Actual 0	Predict 0 Actual 0	Predict 0 Actual 0	Predict 0 Actual 0	Predict 0 Actual 0
Smiles	Predict 0 Actual 0	Predict 0 Actual 0	Predict 0 Actual 0	Predict 0 Actual 0	Predict 0 Actual 0
Smiles VAE	Predict 0 Actual 0	Predict 0 Actual 0	Predict 0 Actual 0	Predict 0 Actual 0	Predict 0 Actual 0
NGF	Predict 0 Actual 0	Predict 0 Actual 0	Predict 0 Actual 0	Predict 0 Actual 0	Predict 0 Actual 0
Smiles	Predict 0 Actual 0	Predict 0 Actual 0	Predict 0 Actual 0	Predict 0 Actual 0	Predict 0 Actual 0
Smiles VAE	Predict 0 Actual 0	Predict 0 Actual 0	Predict 0 Actual 0	Predict 0 Actual 0	Predict 0 Actual 0
NGF	Predict 0 Actual 0	Predict 0 Actual 0	Predict 0 Actual 0	Predict 0 Actual 0	Predict 0 Actual 0

Figure 6-3: Predicted and actual label of each molecular additive tested using the one-hot SMILES, SMILES VAE latent space and Neural Graph Fingerprint (NGF) representations as the input vector to the optimized neural network.

## 6. Quantifying the search for molecular additives

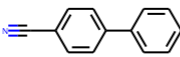
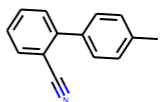
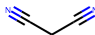
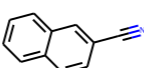
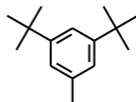
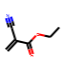
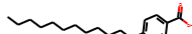
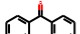

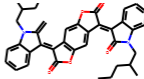
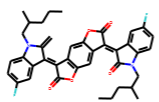
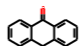
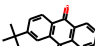
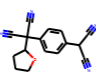
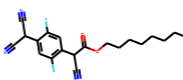
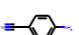
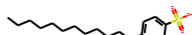
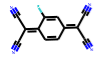
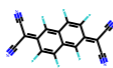
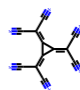
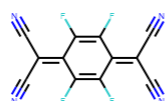
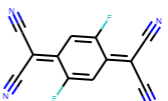
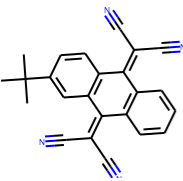
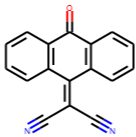
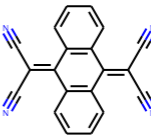
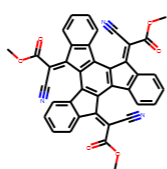
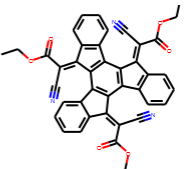
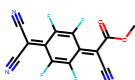
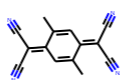
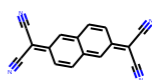
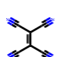
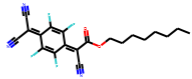
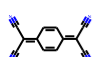
					
Smiles	Predict 0 Actual 0	Predict 0 Actual 0	Predict 0 Actual 0	Predict 0 Actual 0	Predict 0 Actual 0
Smiles VAE	Predict 0 Actual 0	Predict 0 Actual 0	Predict 0 Actual 0	Predict 0 Actual 0	Predict 0 Actual 0
NGF	Predict 0 Actual 0	Predict 0 Actual 0	Predict 0 Actual 0	Predict 0 Actual 0	Predict 0 Actual 0
					
Smiles	Predict 0 Actual 0	Predict 0 Actual 0	Predict 0 Actual 0	Predict 0 Actual 0	Predict 0 Actual 0
Smiles VAE	Predict 0 Actual 0	Predict 0 Actual 0	Predict 0 Actual 0	Predict 0 Actual 0	Predict 0 Actual 0
NGF	Predict 0 Actual 0	Predict 0 Actual 0	Predict 0 Actual 0	Predict 0 Actual 0	Predict 0 Actual 0
					
Smiles	Predict 0 Actual 0	Predict 0 Actual 0	Predict 1 Actual 0	Predict 1 Actual 0	Predict 1 Actual 0
Smiles VAE	Predict 0 Actual 0	Predict 0 Actual 0	Predict 0 Actual 0	Predict 1 Actual 0	Predict 1 Actual 0
NGF	Predict 0 Actual 0	Predict 0 Actual 0	Predict 0 Actual 0	Predict 0 Actual 0	Predict 0 Actual 0
					
Smiles	Predict 0 Actual 0	Predict 0 Actual 0	Predict 1 Actual 1	Predict 1 Actual 1	Predict 0 Actual 1
Smiles VAE	Predict 0 Actual 0	Predict 0 Actual 0	Predict 1 Actual 1	Predict 1 Actual 1	Predict 1 Actual 1
NGF	Predict 0 Actual 0	Predict 0 Actual 0	Predict 1 Actual 1	Predict 1 Actual 1	Predict 1 Actual 1
					
Smiles	Predict 1 Actual 1	Predict 1 Actual 1	Predict 0 Actual 1	Predict 1 Actual 1	Predict 1 Actual 1
Smiles VAE	Predict 1 Actual 1	Predict 1 Actual 1	Predict 0 Actual 1	Predict 1 Actual 1	Predict 1 Actual 1
NGF	Predict 1 Actual 1	Predict 1 Actual 1	Predict 1 Actual 1	Predict 0 Actual 1	Predict 1 Actual 1
					
Smiles	Predict 0 Actual 1	Predict 0 Actual 1	Predict 1 Actual 1	Predict 0 Actual 1	Predict 1 Actual 1
Smiles VAE	Predict 1 Actual 1	Predict 0 Actual 1	Predict 1 Actual 1	Predict 0 Actual 1	Predict 1 Actual 1
NGF	Predict 1 Actual 1	Predict 1 Actual 1	Predict 1 Actual 1	Predict 1 Actual 1	Predict 1 Actual 1
					
Smiles	Predict 0 Actual 1	Predict 1 Actual 1	Predict 1 Actual 1		
Smiles VAE	Predict 0 Actual 1	Predict 0 Actual 1	Predict 1 Actual 1		
NGF	Predict 0 Actual 1	Predict 1 Actual 1	Predict 1 Actual 1		

Figure 6-4: Predicted and actual label of each molecular additive tested using the one-hot SMILES, SMILES VAE latent space and Neural Graph Fingerprint (NGF) representations as the input vector to the optimized neural network.



### 6.4 Predicting new chemical structures

Here, we report a series of molecular structures predicted to work based on our optimal NGF machine learning model. To illustrate the confidence in the prediction, the Z-score was calculated for each molecule using the expectation value and standard deviation from both labels. The expectation value and standard deviation were approximated for each label by performing Monte Carlo dropout during the prediction phase [58]. The molecular structures presented in Figure 6-5 were proposed using expert knowledge. It should be noted that both HAT-CN6 and DDQ are known organic molecular dopants which were not tested in this work but predicted to work based on our model[84].

The molecular structures presented in Figure 6-6 and 6-7 were discovered by searching the complete Zinc 15 (1.35 billion molecules) and PubChem (125 million molecules) databases. Only a subset of all molecular structures predicted to improve device characteristics are included below as the model predicted that approximately 1 in 1,250 molecules could improve device performance, resulting in a total of approximately 1.2 million predictions. Here we cluster the predicted molecules into 6 clusters in order to view different molecular structures predicted to work. The clusters were determined by generating the neural graph fingerprints for each predicted molecule and used k-means to generate clusters. The molecules in each subset were then sorted based on their Z-score, and the top 8 distinct molecular structures from each cluster are presented.

## 6. Quantifying the search for molecular additives

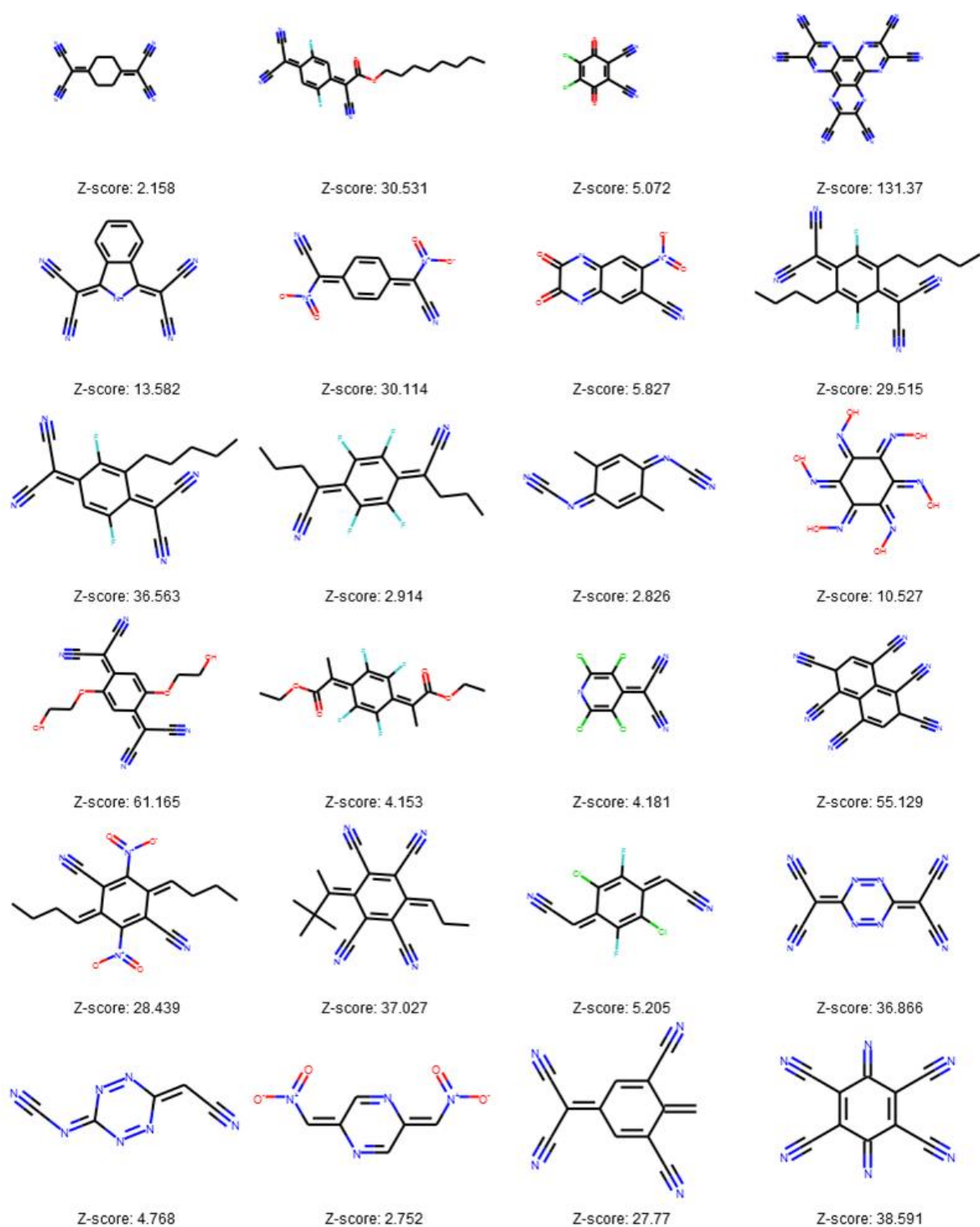


Figure 6-5: Molecular structures selected to function as an additive through expert knowledge and predicted to work by the predictive model.

## 6. Quantifying the search for molecular additives

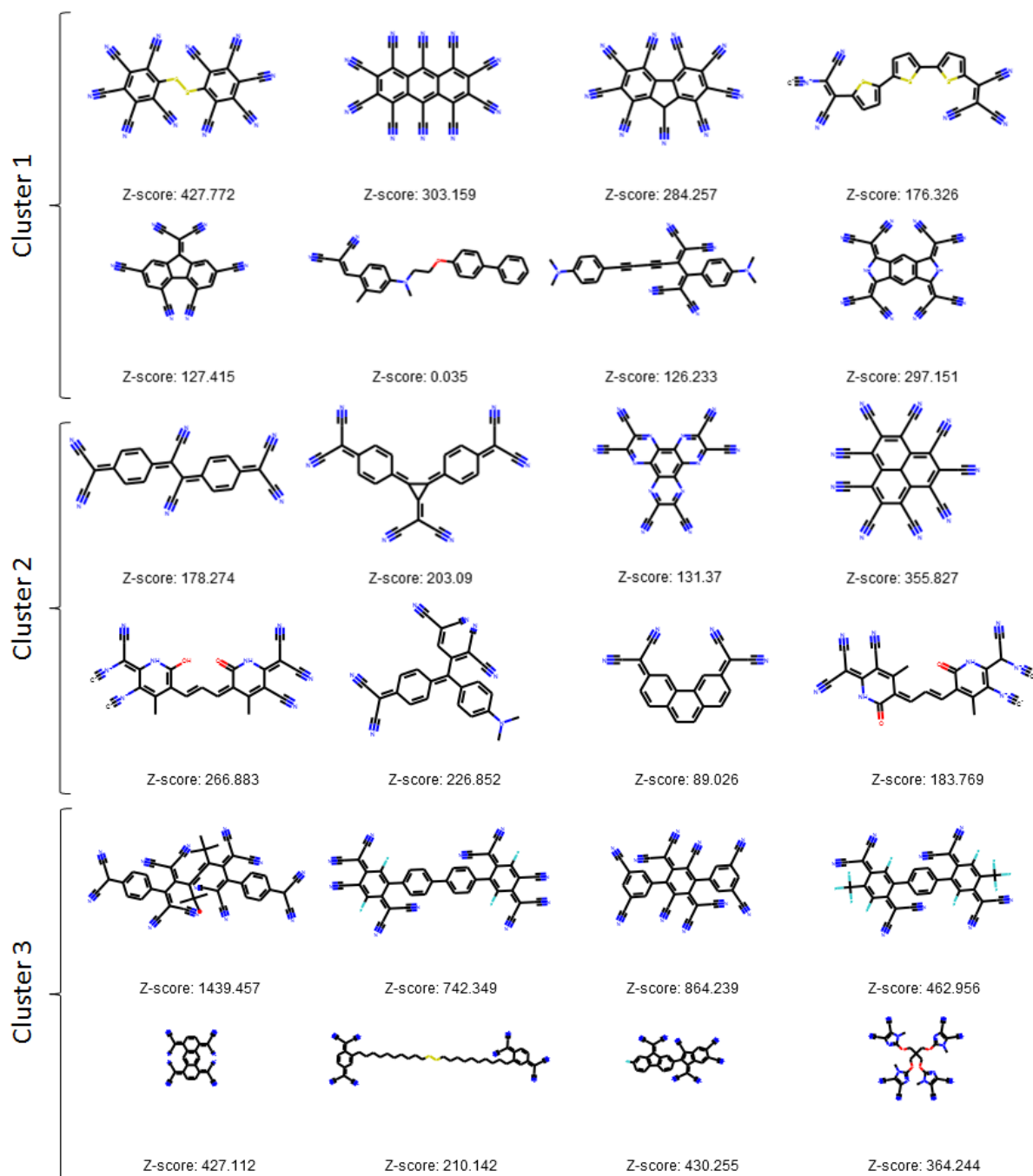


Figure 6-6: Clusters 1 to 3 of the top ranked molecular structures from the Zinc15 and PubChem database.

## 6. Quantifying the search for molecular additives

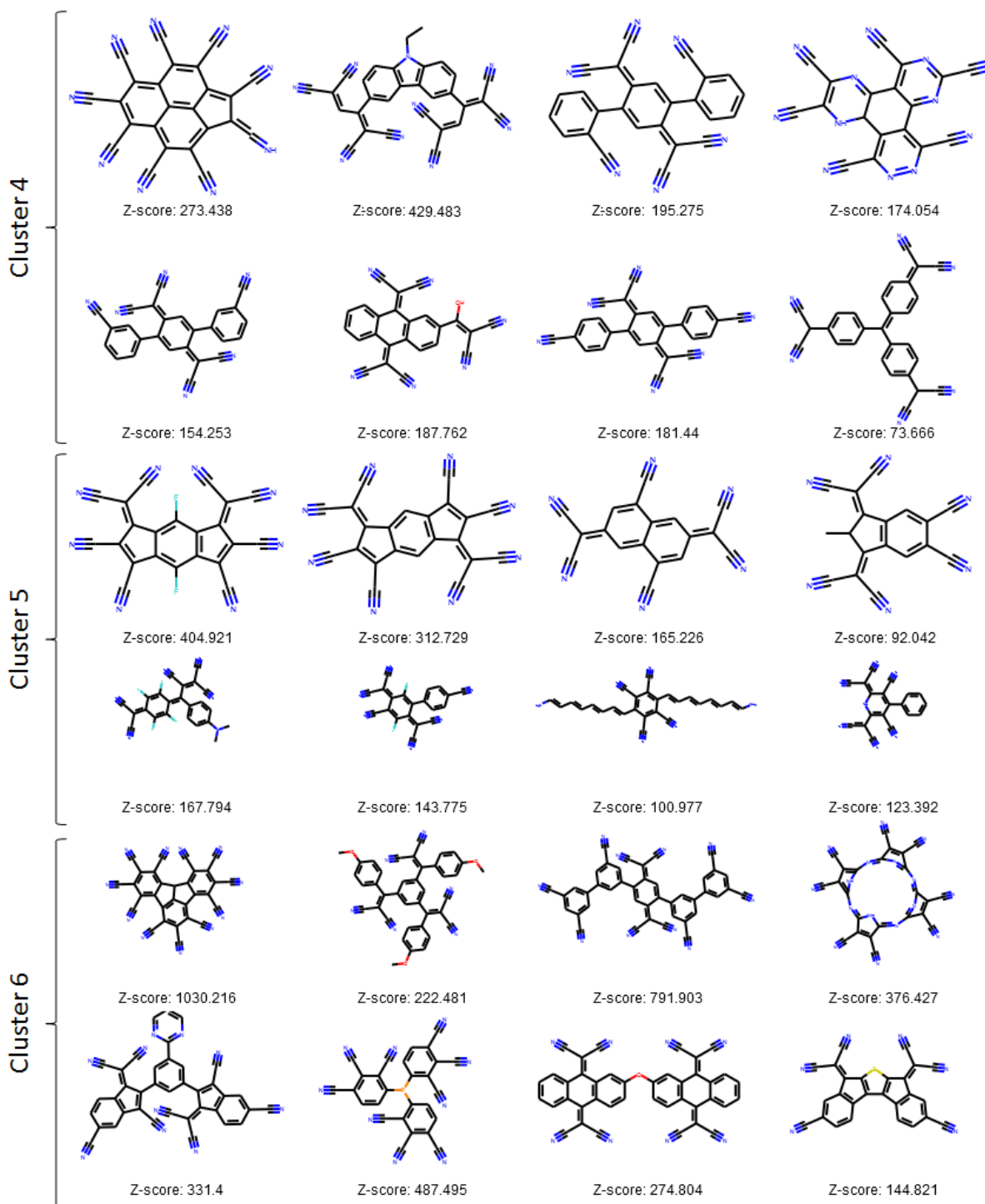


Figure 6-7: Clusters 4 to 6 of the top ranked molecular structures from the Zinc15 and PubChem database.

### 6.5 Augmenting the search for additives

Here we demonstrate that it is possible to predict molecular additives capable of improving device characteristics based on molecular structure. As the model predicts HAT-CN6 and DDQ, which are known molecular dopants but were not tested at all in this work, this suggests that the model is working appropriately[84]. Furthermore, DDQ is well known to react with water in ambient conditions and is stable in acidic conditions, which is indicative of all additives tested[121].

It is conceivable that the model predicted thousands of false positives as the training set used to build the predictive model is small. This is not a fundamental flaw as the model will improve with each additional additive tested through a Bayesian optimization process. However, the model should provide insight to help experimentalists prioritize testing molecular structures.

To build a more accurate model to predict suitable molecular additives, it is proposed that further research should investigate routes to estimate the additive's ability to blend into the organic polymer and the possibility of using autoencoders to generate improved fingerprints and allow for automatic optimization of molecular structure.

Instead of directly measuring the additive's ability to blend into the polymer, perhaps an appropriate indicator is the additive's octane/water partition coefficient. The partition coefficient is the relative concentration of the additive in each phase of a two-phase solution. This is a standard metric used in drug discovery, where the two phases are octane and water, to determine how the molecule will interact in polar and non-polar compounds. As the organic polymer is non-polar, predicting molecules which would blend into non-polar compounds, such as octane, could provide insight into the additive's ability to blend into the polymer. Furthermore, as this metric is very important to drug discovery, large databases such as Zinc15 and PubChem include partition coefficient estimates or experimental values. Future work should investigate probabilistic models to determine the partition coefficient based on structure and leverage big data from drug discovery databases.

## 6. Quantifying the search for molecular additives

As this thesis suggests, NGFs are reasonable fingerprints for molecular structure. However, they use small untrained random weights which are potentially not optimized to encode molecular structure. Future work should investigate graphical autoencoders to determine whether they can generate more appropriate fingerprints, such as junction tree variational autoencoders[49]. In addition, the autoencoder latent space has the potential to be systemically searched to find new molecular structures which are not in present in any online database. This could be achieved autonomously as an algorithm could systematically search through the latent space and find optimal molecules which maximize solubility and the additive's ability to react with moisture. Furthermore, one could leverage large databases to generate sophisticated autoencoders.

# 7 Antiferromagnetics for analogue neuromorphic computing

At the beginning of my doctoral work on stabilising semiconducting polymers, it became clear that for most practical purposes the organic device is a black box, and the most promising route to determine the mechanism of the solid state additives was to perform statistical techniques on large datasets. In preparing for this work, I reviewed the field of statistical based learning. With my new knowledge of statistical based learning and background in engineering and the physical limits of analogue circuits, I was approached by Dr. Deepak Venkateshvaran and Dr. Joerg Wunderlich to help them perform a feasibility study to determine whether antiferromagnetic (AFM) counters could be used as an artificial synapse in neuromorphic computing. I was very excited about this opportunity and decided to spend a considerable amount of my spare time on this study. This chapter contains the results of this feasibility study. To the best of the author's knowledge this is the first report investigating routes to implement neuromorphic computing with AFM counters.

## 7.1 Introduction to analogue neuromorphic computing

Digital computers have been extremely successful as they are Turing completeness machines, meaning that a sufficiently large one would be capable of performing any algorithm. Even though digital computers are Turing complete, this does not mean that the machine could solve all problems efficiently. To solve these difficult problems more effort has been focused on quantum and analogue computing which are more suitable to solve such problems. Quantum computers use quantum phenomena to compute, and analogue computers continuously solve a set of differential equations. By these definitions computers such as the D-Wave quantum computer are an example of both a quantum and analogue computer[122]. Here the focus is on analogue computers using classical physics, as they have the potential advantages of room temperature operation, portability and scalability.

## 7. Antiferromagnetics for analogue neuromorphic computing

Historically, the challenge for analogue computers was to find general purpose algorithms where digital algorithms are insufficient. The most common use of analogue computers is to solve complex differential equations efficiently with some research still ongoing[123]. Classical analogue computing has recently undergone a renewal, as new paradigms such as memcomputing, neuromorphic computing and probabilistic computing of probabilistic bits (p-bits) have been proposed to solve problems such as factorization, pattern recognition and “stochastic” Hamiltonians[124]–[127]. The outstanding issue in building these new analogue systems is the miniaturization of analogue components, which is something that is addressed in this work. Next we will focus on neuromorphic computing, which uses uniquely designed analogue, digital or mixed computers to simulate artificial neural networks (ANNs) with full or abstracted functionality of biological brains.

Artificial neural networks are remarkably proficient at quantifying different tasks that a human would consider to be unquantifiable. These ANN algorithms are almost always implemented in digital hardware and have granted computers the ability to produce art, master GO, translate language, operate vehicles and even generate general artificial intelligence[128], [129]. There are now a large variety of dedicated digital neuromorphic processors such as TrueNorth by IBM, Loihi by Intel and SpiNNaker by the University of Manchester. It is an open research question whether the full potential of biological neural networks can be achieved with digital architecture, but this seems unlikely as the functionality of the biological neurons is time dependent, extremely parallel, uses random noise and can be described as continuous differential equations. For these specific reasons analogue computers appear to be a more appropriate architecture.

As the conventional silicon building blocks for analogue circuits do not easily miniaturize, for a complete neuromorphic capable of learning, new materials systems are investigated. The most commonly suggested new materials for neuromorphic computers are oxide memristors which act as analogue resistive counters. For a recent and relevant review on memristors for analogue computing please refer to F. Caravelli et al. [130]. Interestingly, it appears that there are a group of AFM materials, such as CuMnAs and Mn<sub>2</sub>Au, which also act as electrically controllable counters which have improved endurance, fabrication reproducibility, fast switching rates, stray magnetic



## 7. Antiferromagnetics for analogue neuromorphic computing

field sensitivity and thousands of deterministic memory states. As the AFM counters are particularly nonlinear, the question of whether the AFM memory can be used to learn is not trivial. In this report we determine whether the nonlinear characteristics of the AFM counter prevent it from being implemented in an analogue learning circuit.

### **7.2 Biological and artificial neurons**

As the literature of neuromorphic computing heavily uses biological terms, it is important to understand the basics of neuron cell biology and how to apply them to digital and hardware based artificial neural networks. For the hardware of analogue neuromorphic computers, we will focus on all electrical networks.

#### **7.2.1 Neuron biology**

There are many types of human biological neurons, however, all neurons have similar properties[131], [132]. Each neuron cell has dendrites receiving information from other neurons[131]. The dendrites collect either excitatory or inhibitory incoming signals, which either respectively increase or reduce the probability that the neuron will produce an output signal. The cell body (soma) contains the nucleus of the neuron and other structures that maintain homeostasis of the cell[131], [132]. Both the soma and the dendrites are used to process the signals from the presynaptic neurons. The membrane potential, the electrochemical potential difference between inside and outside the cell, stores the specific state of the neuron electrochemically. If the membrane potential reaches a set threshold, an output spike signal is sent through the axon to the target neurons and the membrane potential reduces[131]. A single neuron can have thousands of different axon terminals connecting the neuron to different postsynaptic neurons. The interface where the signal from the emitting neuron, known as the presynaptic neuron, is transmitted to the target neuron, known as the postsynaptic neuron, is called the synapse. The information is physically transferred between neurons using neuro-transmitters. The connection strength of the synapse is one of the features that determines the effect of the presynaptic neuron on the postsynaptic neuron[131]. The strength of the synapse depends upon the history of activity between both the presynaptic and postsynaptic neurons. The exact learning mechanisms of the neuron cells are still being researched and depend on the cell type.

## 7. Antiferromagnetics for analogue neuromorphic computing

Known trainable features include membrane time constant, synapse strengths, thresholds and signal conduction delays[131].

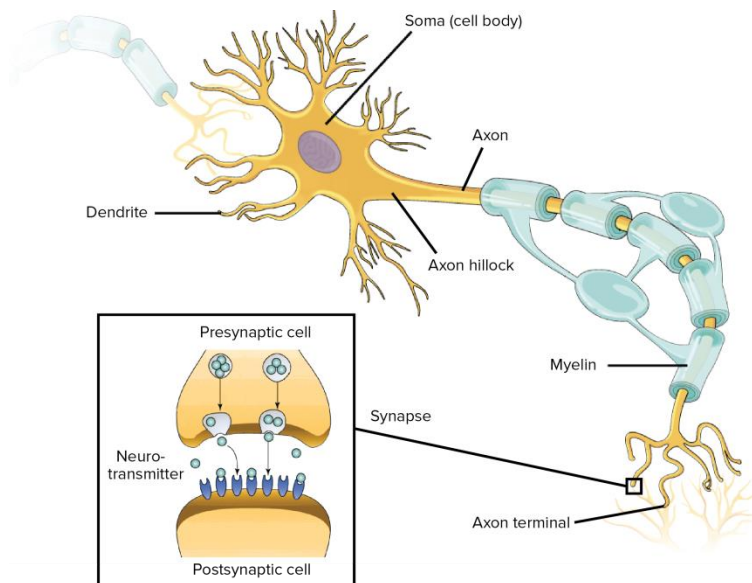


Figure 7-1: Structure of a neuron cell. Image adapted from Yael Avissar [132].

### 7.2.2 Artificial neurons

The artificial digital neuron is described mathematically as an activation function ( $f$ ) which maps the weighted sum of the discrete input values ( $x_i$ ) and bias value ( $b$ ) to a discrete output value ( $y$ ), i.e.  $y = f(b + \sum_i^n w_{j,i}x_i)$ . The synapse weights ( $w_{j,i}$ ) which connect the output of neuron  $i$  to the input of neuron  $j$  are analogous to the synapse strength between the presynaptic and postsynaptic neurons. The activation function used in applications depends upon the required computational speed and accuracy but an important aspect is maintaining nonlinearity. For example, single layer and deep neural networks with linear activation functions have identical model expressiveness which is not the case for nonlinear activation functions[133]. Common examples of activation functions include signum, sigmoid, heaviside step, rectal linear and hyperbolic tangent functions[129], [134].

An artificial analogue neuron can behave identically to a digital neuron during continuous time or to a more biologically plausible neuron model which simulates the membrane potential ( $v(t)$ ), which is a time dependent quantity that is dependent on the

## 7. Antiferromagnetics for analogue neuromorphic computing

history of the neuron output and input signals from other neurons and is directly related to the output of the neuron (Figure 7-2).

The membrane potential can be mathematically identical to the digital neuron just in continuous time  $v_j(t) = b + \sum_i^n z_{j,i}x_i(t)$ , or can be more biologically plausible where the membrane potential is defined as a differential equation dependent on the history of the neuron  $\frac{\partial v_j(t)}{\partial t} = g(b, z_{j,1..n}, x_{1..n}(t'), y_j(t'))$ . The output from analogue neurons can be a continuous differentiable signal and/or a spike train which propagates to the input of connected neurons via a variable impedance element ( $z_{j,i}$ ) which simulates the synapse weight. This work focuses on plausible routes to build an artificial variable impedance synapse using AFM and the exact details of the neuron circuitry are not discussed here. Possible neurons include an all CMOS neuron which consists of a leaky current integrator which outputs spike and zero resets the integrator when the integration reaches a set threshold, and Professor Datta Supriyo's p-bit neuron which stochastically outputs spikes with a probability proportional to the sigmoid of the sum of the input signals from the presynaptic neurons[127], [135].

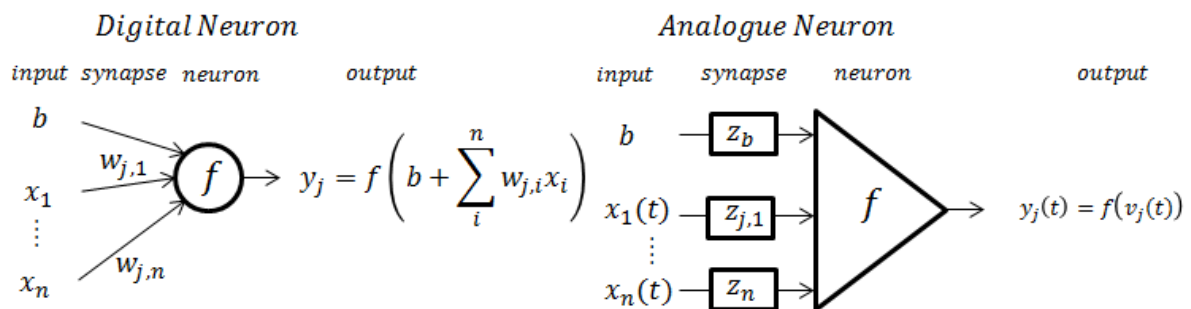


Figure 7-2: Digital and analogue artificial neurons used in artificial neural networks.

### 7.2.3 Artificial neural networks

Networks of neurons are generated by connecting the output of neurons to the input of other neurons or the same neuron. The properties of the networks are controlled by the number of neurons, activation function and network architecture[129]. Here the functionality and hardware implementations of network architectures is described.

#### 7.2.3.1 Feedforward network

Feedforward networks contain multiple hidden layers of neurons which connect the input layer of neurons to the output layer of neurons[136]. An example of a feed forward

## 7. Antiferromagnetics for analogue neuromorphic computing

artificial neural network with one hidden layer is seen in Figure 7-3. Deep neural networks are networks with many hidden layers. Deep neural networks have become pervasive because each additional hidden layer enables the network to predict more complex and abstract functions. An example of a single layer of an analogue neural network using a form of variable resistor, memristors, for the artificial synapse is seen in Figure 7-3. Multiple analogue layers could be attached in series to simulate a deep neural network. To compare the computational effectiveness of the suggested analogue neural network architecture to a digital computer, we compare the number of computations required to simulate the current through each of the memristors in the analogue computer. If the computer contains  $10^8$  memristors (memristor area of  $0.01\mu\text{m}^2$  on a  $1\text{mm}^2$  substrate), the output of each neuron can be discretized into 1ns intervals, and if each instance of current through the memristor is considered a floating point operation, the analogue computer would efficiently perform  $10^{17}$  flop digital computations which is on the same order as that of the world's fastest super computer.

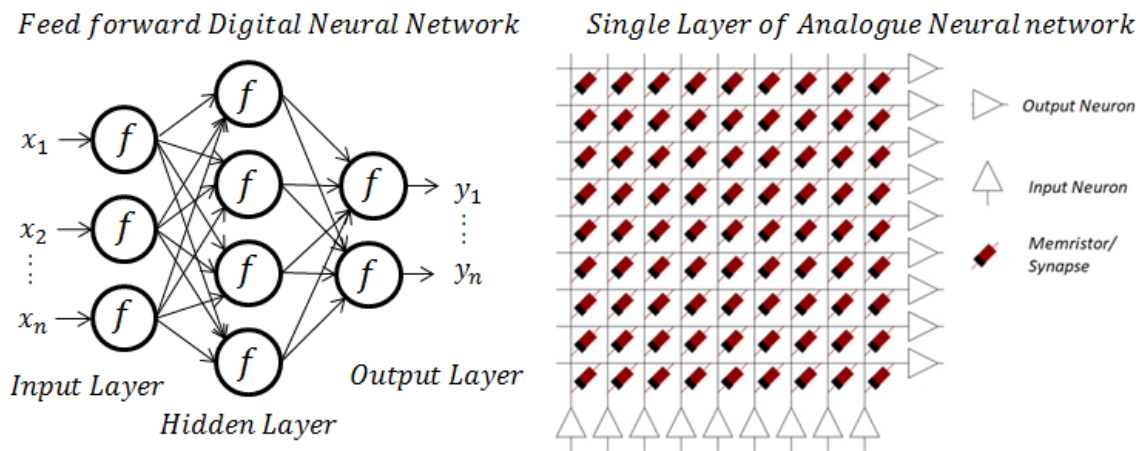


Figure 7-3: Left) Feed forward multilayer digital neural network and right) single layer analogue neural network. Image adapted from C. Zamarreno-Ramos et al. [137].

### 7.2.3.2 Convolution networks

Convolution neural networks perform a series of convolutions, nonlinear layers and pooling operations in order to generate a feature space which is an input to another neural network. The convolution layer convolves the inputs with specific kernels. The nonlinear layer applies an elementwise activation function and the pool layer performs a

## 7. Antiferromagnetics for analogue neuromorphic computing

down sampling operation. Convolution neural networks have been particularly useful in the field of image processing and are inspired by convolution neural networks used in biological neurons in the visual cortex of mammals[138]. The structure of convolutional neural networks can get rather complicated; for more information, please refer to *Practical Convolutional Neural Networks* by Sewak et al.[139]

### **7.2.3.3 Recurrent network**

Recurrent neural networks have neurons where the present state of the neuron is dependent on the previous states of the network. A possible route to achieve this is to connect the output layer of a feedforward network to an input of a neuron in the input layer. This enables recurrent neural networks to have temporal dynamics allowing them to use their internal memory to process a sequence of events, which makes them suitable for temporal tasks such as speech recognition or predicting the movement of objects across a series of images. Continuous recurrent neural networks are particularly suited for analogue ANNs as they operate in continuous time and direct electrical feedback can easily be achieved.

### **7.2.3.4 Reservoir network**

Reservoir neural networks contain a network of fixed interconnected neurons with either random or fixed synapse weights, called a reservoir, and an output layer to interpret the reservoir by sampling a subset of the reservoir neurons (Figure 7-4)[140]. Similar to recurrent networks, reservoir networks are suitable for temporal tasks. Reservoir networks are particularly interesting for analogue neuromorphic applications as learning does not occur by modification of the synapse weights in the reservoir and reservoir networks are mathematically equivalent to a collection of non-linear oscillators(Figure 7-4)[140]. These properties allow reservoir ANNs to be simulated in unintuitive systems such as electrical nanoscale spin-torque oscillators, optical m-z modulators, spatio-temporal photonic systems and physical buckets of water[140]–[143].

## 7. Antiferromagnetics for analogue neuromorphic computing

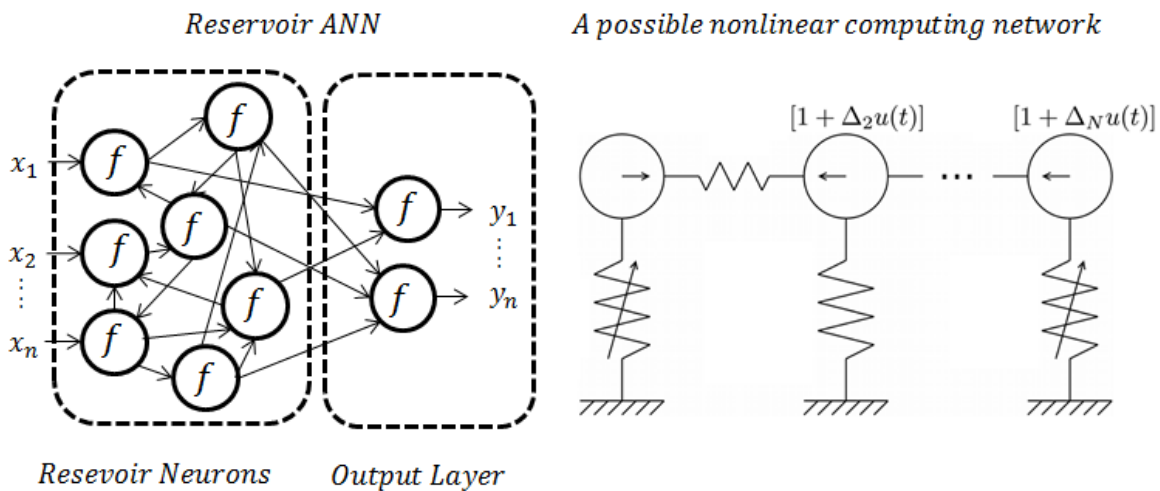


Figure 7-4: Left) Reservoir network using artificial neurons. Right) Schematic description of a nonlinear computing network. The  $N$  inertial masses (circles) arranged in a chain are coupled to neighbors by linear springs and to a substrate by a linear or non-linear spring, with damping. A harmonic forcing, with amplitude possibly modulated by coupling to the input signal  $u(t)$ , is imposed on the masses. Image adapted from C. Coulombe et al. [144].

### 7.2.3.5 Bayesian neural networks

Stochastic neural networks contain random variables built into the network[145]. This would include networks such as Markov Chain Neural Networks, Boltzmann machines or Bayesian neural networks. Here the focus is on Bayesian neural networks which have probabilistic synapse weights that are robust to over-fitting, can estimate uncertainty through a Monte Carlo simulation[56]. Furthermore, Yarin Gal et al. have demonstrated that Bayesian neural networks with Gaussian distributed probabilistic weights can be approximated by performing dropout on neurons, where dropout is a procedure used in ANNs to randomly exclude a neuron from a model[58]. Dropout could easily occur in an analogue network by continuously and randomly disconnecting a neuron using a stochastic tunnel junction as the random noise source[127].

### 7.2.4 Learning paradigms

In order for the neural networks to learn, the synapse weights of the neural network need to be appropriately updated. As learning algorithms in common digital neural networks can be implemented using only multiplication, addition and subtraction

## 7. Antiferromagnetics for analogue neuromorphic computing

operators, it is possible that some digital algorithms could be directly applied using analogue circuits. Here, the most common learning modalities in machine learning are discussed. In particular, time dependent spike algorithms which are not commonly implemented in digital applications as they are more suitable for analogue computers are investigated.

Unsupervised learning finds commonalities in unlabeled data and updates the model based on the absence or presence of the commonalities in new data. A commonly proposed unsupervised learning algorithm for neuromorphic computers with biological plausibility is spike time dependent plasticity (STDP)[146]–[152]. The basic STDP algorithm, seen in equation 7.1, determines that the change of the synapse weight ( $w_{i,j}$ ) between presynaptic ( $i$ ) and postsynaptic neurons ( $j$ ) is dependent on the time difference ( $t_i - t_j$ ) between the presynaptic and postsynaptic spikes and the learning curve ( $f$ )[149].

$$(7.1) \quad \Delta w_{i,j} = f(t_i - t_j)$$

The common implementation of the STDP algorithm in neuromorphic chips occurs because memristors and specific presynaptic and postsynaptic waveforms are capable of implementing STDP. The basic implementation of STDP using memristors, using a similar architecture as that in Figure 7-3, can be applied only to a single layer of neurons or used to train readouts for reservoir networks. However, simple STDP memristor networks are not capable of performing XOR classification[150], [153]. In this work it is demonstrated that STDP learning is possible for AFM based synapses. More complex STDP algorithms will be reviewed in the next sections on supervised and reinforcement learning.

Supervised learning maps input data to output data based on known input output data pairs. The process of learning occurs by modifying the set of synaptic weights between neurons and minimizing the cost function of the specific neural network. In certain spike algorithms such as SpikeProp and Remote Supervised Learning Method the timing of spike encodes the information and learning occurs through minimizing the timing error between an output spike and a desired target spike using multilayer STDP and/or backpropagation[154], [155]. The algorithms are difficult to implement in analogue

## 7. Antiferromagnetics for analogue neuromorphic computing

computers as precise timing and/or knowledge of previous states of the network are required when a learning event is triggered.

In a spike rate network (SRN) the output of a particular neuron is a train of Dirac-Delta pulses where the average spiking rate encodes the output value[156]. SRNs use rec-linear action functions and can be mathematically equivalent to digital artificial neural networks using rec-linear activation functions[129], [156]. In this report it is demonstrated that it is possible to build a multilayer spike rate network using AFM memory. The specific algorithm used was provided by Peter O'Connor et al. in their paper on Deep Spiking Networks[156].

### **7.2.5 Summary**

This section provided the fundamentals of how analogue neural networks work in nature, how to replicate these networks in hardware and how to implement different learning paradigms. Using this knowledge, the question of how to build an analogue computer, specifically the analogue synapses, is examined.

## **7.3 Analogue synapses**

Here we review possible hardware technologies capable of acting as controllable analogue synapses for electrical neural networks and compare the properties of these analogue synapses to antiferromagnetic memories to determine whether an antiferromagnetic based synapse could provide any benefit. A simple resistor could act as a synapse but will be excluded, as a resistor has no learning capabilities and cannot be updated. The electrical synapses reviewed include floating-gate MOSFETs similar to neuMOS, OLED inspired synapses, analogue electrically erasable programmable read-only memory (EEPROM) synapses as well as memristors.

The neuMOS floating-gate MOSFETs, referred to here as vMOS, were proposed in the mid-1990s as artificial neurons and recently they have been attracting attention as an artificial synapse in probabilistic computing[127], [157]. vMOS are variable voltage threshold MOSFETs where the voltage threshold is controlled by using n number of variable capacitors coupled to a MOSEFET with a floating gate. The voltage threshold scales linearly with the voltage applied to each of the capacitors. A single vMOS can be operated as a digitally controlled variable resistor. Similarly a complementary vMOS source-follower circuit acts as a voltage to voltage converter which can perform a



## 7. Antiferromagnetics for analogue neuromorphic computing

weighted sum of all the output voltages of the presynaptic neurons. The weighted sum is the input to the postsynaptic neuron. The weight and synapse strength are controlled by the specific capacitors connecting the presynaptic neuron to complementary vMOS using a network of programmable switches.

The OLED inspired synapse uses similar analogue transistor architectures, such as 2T1C, used in OLED transistor backplanes in order to control the current through the diode. However, instead of the transistor controlling the current through a diode like in an OLED display, the transistor controls the magnitude of the current from the presynaptic neuron to the postsynaptic neurons, therefore acting as a controllable synapse. To the best of the author's knowledge there is no reference to this specific architecture in the literature.

Interestingly, as OLED inspired and resistive vMOS synapses are passive components, it is feasible to stack MOSFETs as the transistors are not actively consuming power. An outstanding problem about both vMOS and OLED inspired design is that learning via direct feedback from the presynaptic and postsynaptic neurons is not possible, but for a lot of applications learning is not necessary. This will be addressed later in this work. Learning requirements will be discussed in further detail later in the report but for practical applications they might not be necessary.

Another plausible MOSFET based electric synapse uses electrically erasable programmable read-only memory (EEPROM), commonly used in flash memory, where a controlled amount of charge is stored in the floating gate[158]. The resistance of the MOSFET is then dependent on the charge of the floating gate allowing for a large number of analogue states. Unlike the digital to analogue synapses mentioned above, controlling the waveforms on the device allows the synapse to perform algorithm learning. As electrons are added to the gate through hot-electron injection with silicon dioxide, over time the silicon oxide layer degrades. This degradation is the major limiting factor for the future of both digital and analogue based EEPROM memories.

Memristors are the fourth fundamental passive circuit components where the conductance is dependent on the history of the current passing through the element[159]. In 2008, the first memristor devices were fabricated using  $\text{TiO}_2$  where the change in conductivity of the films was due to the migration of oxygen vacancies in the presence of an electric field over a minimum threshold[160]. Since 2007, more oxide,

## 7. Antiferromagnetics for analogue neuromorphic computing

organic, ferroelectric and carbon nanotube based memristors have been reported[102], [149], [150], [161]–[165]. Memristors are typically considered the natural synapse, as they are two terminal resistive devices that are capable of performing spike time dependent plasticity algorithms. Memristors perform STDP due to their inherent conductance change from constructive interference between the presynaptic and postsynaptic waveforms applied across the memristors, which results in a larger voltage differential across the memristor than either a single presynaptic or postsynaptic waveform[149]. It should be noted that memristor functionality can be completely replicated using CMOS circuits; however, fully CMOS memristors are active components that require large areas.

In comparing the memory properties of analogue EEPROMs and the memristive synapses capable of using feedback to learn, to the memory properties of antiferromagnetic memories, shown in Table 9, it appears there are certain aspects where AFM memories are superior. Antiferromagnetic memories have high endurance, high fabrication reproducibility, negligible sensitivity to stray fields, and reproducible memory states which suggest that the AFM memories could have unique advantages for specific applications. The details of AFM memories will be discussed in the following section.

Table 9: Properties of memristive devices.

Memory	Switch Time	Writing Current Density (Acm <sup>-2</sup> )	Memory Format	Endurance (Cycles)	Retention Time	Reproducibility	Readout	Sensitivity To Stray fields.
<b>EEPROM synapse</b>	ns		Analogue	10 <sup>5</sup>	10 years	low	Resistance	Yes
<b>Oxide Memristor</b>	5 ns to 500 μs	10 <sup>6</sup>	Analogue	10 <sup>5</sup> to 10 <sup>9</sup>	>1 yrs	Medium	Resistance	Yes
<b>Organic Memristor</b>	300 μs to 50 ms	1 to 10 <sup>4</sup>	Analogue	10 <sup>3</sup> to 10 <sup>8</sup>	~24 hr	Low	Resistance	Yes
<b>Ferroelectric Tunnel Junction Memristor</b>	>100 ns	10 <sup>4</sup> to 10 <sup>5</sup>	Analogue	>10 <sup>6</sup>	Unknown	Unknown	Resistance	Yes
<b>Magnetic Tunnel Junction</b>	>250 ps	10 <sup>6</sup> to 10 <sup>8</sup>	Binary	10 <sup>12</sup> to 10 <sup>15</sup>	>10 yrs	High	Resistance	Yes
<b>Antiferromagnetic Cruciform (CuMnAs)</b>	>100 ps	10 <sup>6</sup> to 10 <sup>8</sup> (Speed dependent)	Analogue	Unknown (Expected to be similar to MTJ)	hrs to yrs	High	Voltage	No

## 7. Antiferromagnetics for analogue neuromorphic computing

### **7.4 Antiferromagnetic counters**

Antiferromagnets are not easily controlled by external magnetic fields due to the inherent alternating directions of magnetic moments and zero net magnetization[166]. Current-induced internal fields whose sign alternates with the periodicity of the antiferromagnetic lattice can be enabled through relativistic quantum mechanics, enabling the rotation of the AFM spin axis[166]. By applying successive current pulses in AFM materials, such as CuMnAs and Mn<sub>2</sub>Au, in a specific orientation, the spin axis of the AFM tends to align with the orientation of the current pulse. Similarly, by applying current pulses in a perpendicular orientation to the domains tends to align the spin axis of the domains with the perpendicular current pulse. If one of the current pulse orientations is arbitrarily defined as generating positive AFM domain by detecting the relative number of AFM domains in a positive orientation, the AFM acts as a micron sized passive counter. The AFMs maintain their orientation for an extended period of time as the Curie temperature for CuMnAs and Mn<sub>2</sub>Au is greater than 100°C. In practice the read out of the relative number of AFM domains in CuMnAs and Mn<sub>2</sub>Au occurs by detecting the AFM transverse anisotropic magnetoresistance (AMR) by applying a current in plane with and rotated by 45° relative to the perpendicular current pulses and measuring the transverse voltage. As the transverse resistance signal, the ratio of transverse voltage to applied current, is on the order of tens of mΩ, amplification of the signal is required. It is conceivable that the amplifier could be removed using a tunnel junction as AFM tunnel junctions have been demonstrated. However, the feasibility of a room temperature deterministic AFM tunnel junction is still an open question. Later in this work we consider whether the implications of AFM tunnel junctions are possible. For more information on AFM counters please refer to the references[166]–[169]. In Figure 7-5 below, Schuler et al. demonstrate the electrical switching and reading out of the multiple AFM domains along with the required circuitry[170].

## 7. Antiferromagnetics for analogue neuromorphic computing

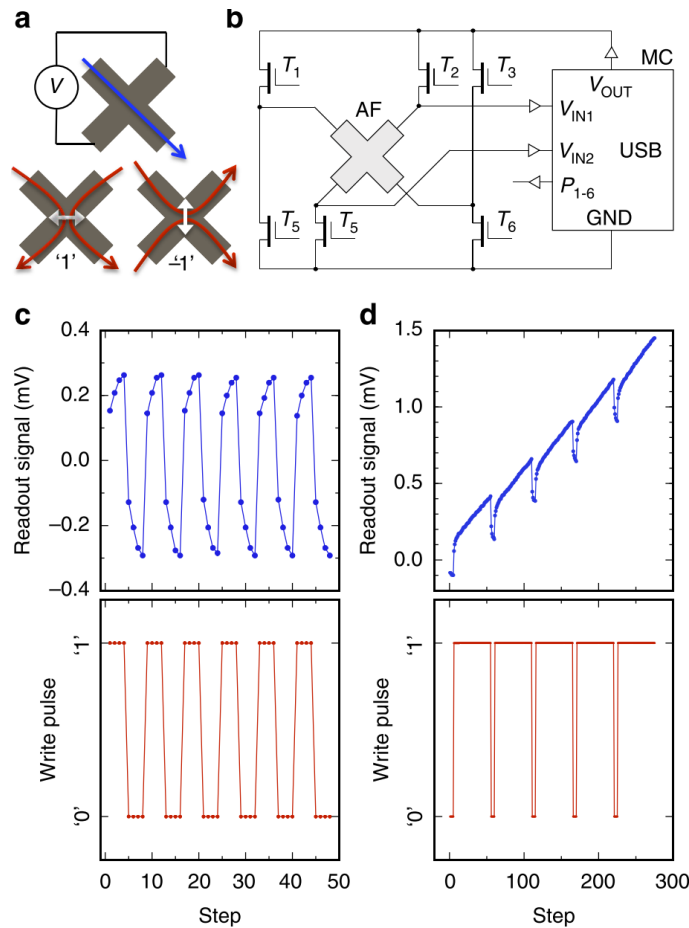


Figure 7-5: Antiferromagnetic multi-level memory bit-cell. (a) The readout current (blue arrow) and transverse voltage detection geometry; write pulse current lines (red arrows) labelled '1' and '-1' and the corresponding preferred AF moment orientations (white double-arrows). (b) Schematic of the circuitry controlling the write/read functions. Microcontroller (MC) supplies the AF bit-cell circuit through its adjustable voltage output  $V_{OUT}$ ; different writing and reading configurations are realized by switching transistors  $T_1$  to  $T_6$  controlled by digital outputs  $P_1$  to  $P_6$  of the MC; transversal voltage is sensed differentially by analogue voltage inputs  $V_{IN1}$  and  $V_{IN2}$  of the MC. GND labels ground. (c) A symmetric pulsing with repeated four write pulses with current lines along the  $[100]$  direction labelled '0' followed by four pulses with current lines along the  $[010]$  direction labelled '1' (red dots); corresponding readout signals (blue dots). (d) Same as (c) with the four '0' write pulses followed by fifty '1' pulses. All measurements. Image adapted from V. Schuler et al. [170]

In this work a similar device architecture inspired by Schuler et al. is used, where switching transistors controlled by feedback from the presynaptic and postsynaptic neurons control the current direction, magnitude and/or duration of the current pulses

## 7. Antiferromagnetics for analogue neuromorphic computing

in order to control learning[170]. The switching dynamics of the AFM are highly complicated as the particular domain is affected by the orientation of neighbouring domains due to magnetostriction, domain size, other boundaries and defects. As is evident in Figure 7-5 C) and D) the transverse voltage of the the CuMnAs does not scale linearly with the applied number of pulses. Furthermore, there is a significant non-linearity in the transverse voltage when the orientation of the current switches. Here a network of CuMnAs based synapses is simulated to determine whether the specific non-linearity prevents learning.

### 7.5 Methods

#### 7.5.1 How learning occurs in memristor analogue computers

The modeling performed in this dissertation is nearly identical to the work from Boyn et. al. which demonstrates learning through ferroelectric memristor synapses. As we apply the same methodology in our work and it applies generally to most other analogue neuromorphic computer designs, we will briefly discuss their STDP setup seen in Figure 7-6.

In Figure 7-6 a) the input neurons output a time dependent spiking signal with frequency proportional to that of the intensity of pixel value. The voltage signal then travels down corresponding blue wire. As the output neuron is originally held at ground, some of the voltage signal forms a current which travels to the right hand side where it is integrated by each output neuron. The magnitude of the current is inversely proportional to the resistance of the synapse which is the green element sandwiched between the red and blue wires and is a unique element for each input/output neuron pair. Once a sufficient charge has been integrated by the output neuron, it is no longer held at ground and produces a voltage spike which propagates to the left hand side along the corresponding red wire. After the first output neuron fires, the other output neurons are reset and the first spiking output neuron corresponds to the classification of the input image, as seen in Figure 7-6 c). When the output neuron outputs a voltage signal sending feedback to the synapse, the voltage drop across the synapse changes

## 7. Antiferromagnetics for analogue neuromorphic computing

dependent on the relative timing of the input and output neuron spikes as well as their corresponding waveform as shown in Figure 7-6 d). If the voltage signal goes below or above a set voltage threshold the synapse becomes more or less conductive causing the neuron to be more or less (respectively) likely to fire the next time the same pattern is applied to the input. Over time the network is able to recognize each pattern, as seen in Figure 7-6 b).

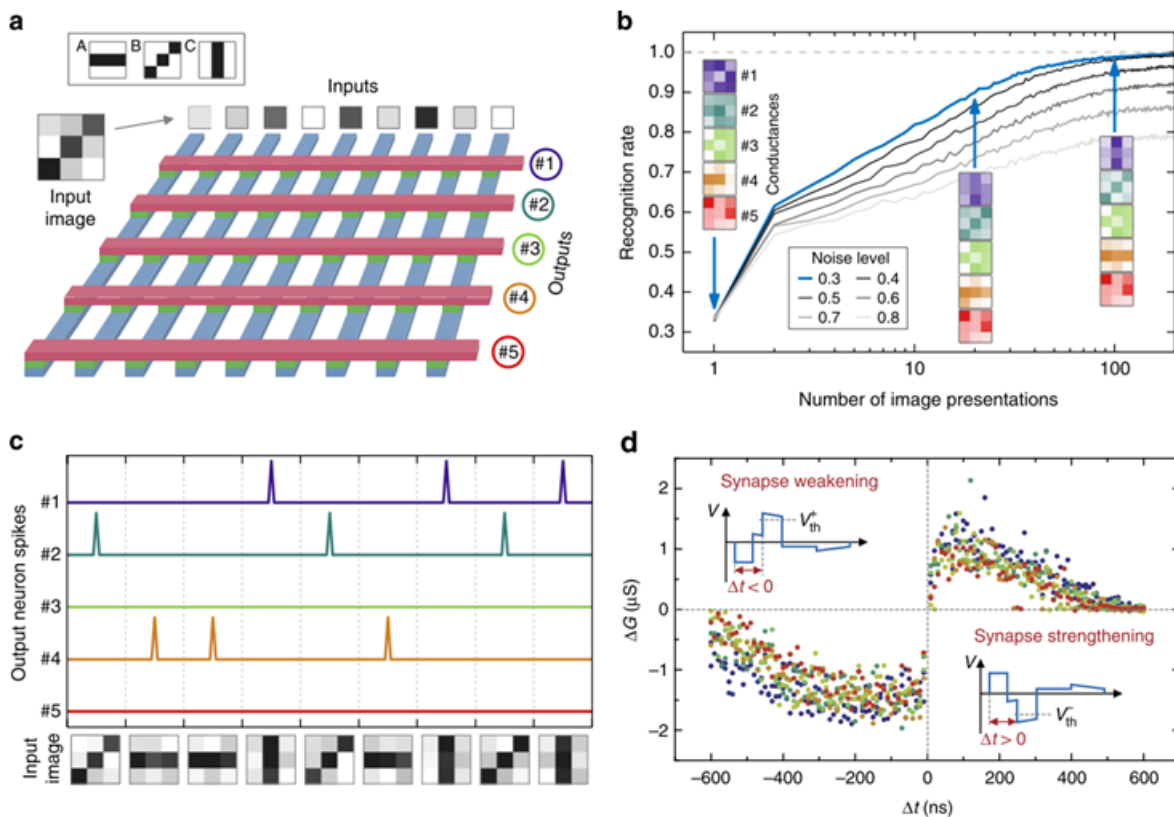


Figure 7-6: a) Simulated spiking neural network comparing nine input neurons connected to five output neurons by an array of memristors. The inputs are noisy images of the patterns to recognize: horizontal (A), diagonal (B) and vertical (C) bars in 3x3 pixel images. (b) Recognition rate as a function of the number of presented images for different noise levels. The colored images are conductance maps of the memristors in each line and their evolution for a noise level of 0.3 (blue). (c) Behavior of the network after successful learning. Neurons 1, 2, and 4 emit spikes when inputs C, B and A are presented, respectively.

## 7. Antiferromagnetics for analogue neuromorphic computing

### 7.5.2 Modeling AFM counters

Here an approximate analytical function to preliminarily model the functionality of the transverse readout of a CuMnAs cross bar is provided. The AFM is modeled as a uniform population of AFM domains where each domain requires different amounts of energy to switch. Here the additional energy required to add an additional state ( $\frac{dE}{dN}$ ) scales approximately linearly with each additional state  $N$ . As the AFM contains a population of domains in positive, negative and/or random states, the domains with the lowest switching energy are modelled in a different orientation than the applied pulse switches. If the applied energy is insufficient to change the orientation of a single domain, the domain changes to the applied orientation with a probability  $x/E(i)$ . This model agrees with experimental observations that the transverse AMR voltage scales as the square root of the number of applied pulses with the same energy[170]. Furthermore, when the current pulses switch orientations the model predicts a similar discontinuity in the transverse voltage.

### 7.5.3 Circuit modeling

To demonstrate learning using the nonlinear characteristics of AFM memories, the proposed neural networks using nonlinear AFM counting characteristics are simulated as described above by performing image recognition of a series of noisy 3x3 pixel images seen in Figure 7-7 in python. As these simulations are based on a paper by Boyn et al., demonstrating learning using ferroelectric synapses on a near identical pattern set, for comparison the same definition of added noise is used. The noise is a randomly generated number between 0 and the specified noise level. The noise is then added on top of the pixel values which has a value of 1. The noise level procedure is taken from Boyn et. al. in order to compare our results [149].

Learning occurs by successively re-exposing the network to a set of patterns. A single exposure is known as a training epoch, and learning is demonstrated by the network being able to distinguish the patterns. The simulated neural networks are all electrical networks where the neurons are connected via electrically controllable synapses, similar to all proposed electrical memristor networks. Initially, the CuMnAs counter is

## 7. Antiferromagnetics for analogue neuromorphic computing

set in a random state and learning occurs by feedback from the post and presynaptic neurons. All control switches (transistors), presynaptic neurons, post synaptic neurons and analogue components are ideal components.

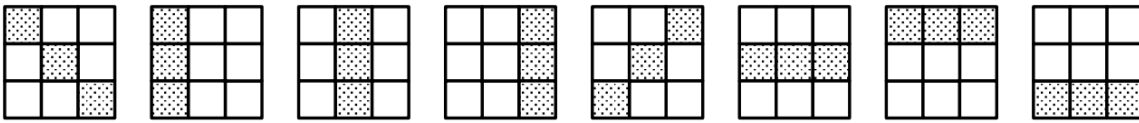


Figure 7-7: Training and testing set separate patterns.

In an STDP algorithm the patterns are unlabeled and the algorithm learns how to classify the patterns using unsupervised learning. As the goal of this simulation is to determine whether the electronics system are capable of learning, the test and the training set are the same set. This is not the typical approach used in the machine learning field, as the training and test sets are different sets, however, in the new field of analog neuromorphics demonstrating plausible routes to learning using fully electrical components is extremely difficult and therefore novel. To compare the SRN and STDP networks, even though the SRN is a supervised approach where the patterns are labeled, the test set is the training set.

All circuits simulated here have two operating cycles: read and run. During the read cycle, the state of the CuMnAs counter is converted to a voltage signal by controlling the current through the CuMnAs using control switches to measure the AMR. For the STDP and SRN networks the AMR voltage signal is amplified, and using control switches the amplified voltage is applied to one or more analogue transistors which act as resistive synapses. At the end of the read cycle the control switch connecting the amplifier to the analogue transistors is opened, which maintains the charge representing the weight of the resistive synapse in the transistor. The specific operation of the error-SRN will be discussed in the experimental section. For all simulated networks, during the run cycle the neurons communicate via the resistive synapse and the CuMnAs counter is updated via feedback from both the pre and post synaptic neurons. The input presynaptic neurons continuously integrate a current proportional to a unique pixel value with corresponding noise, and outputs a voltage spike when the integration reaches a set threshold which also resets the neuron integrator. The outputted voltage spikes of the



## 7. Antiferromagnetics for analogue neuromorphic computing

neurons bias the analogue transistors in the saturation regime and enable a current to flow from the specific presynaptic neuron to the postsynaptic neuron.

### **7.6 AFM synapse simulations**

Here the networks of CuMnAs based synapses are simulated to determine whether the specific non-linearity inherently prevents learning.

#### **7.6.1 Simulating spike time dependent plasticity**

Here STDP learning using antiferromagnetic memories is demonstrated. A diagram of the CuMnAs based synapse is observed in Figure 7-8. The state of the synapse weight is stored in the CuMnAs counter. The simulation consists of one feedforward layer with 9 input neurons and 8 output neurons. As mentioned previously, the input neurons integrate the input signal and generate a current signal that is integrated by the postsynaptic neurons. Furthermore, when the input neuron spikes, a feedback signal is sent to the CuMnAs counter. When the first output neuron spikes, feedback is sent from the specific output neuron to its respective synapse and lateral inhibition resets all other output neurons. The waveform of the feedback signals from the pre and post synaptic neurons can be adjusted to control the orientation of the net current through the CuMnAs counter and hence the number of positively oriented domains based on the relative timing of the spikes, which enables the network to learn. Two plots of the change in the net current through the CuMnAs counter, which are equivalent to the STDP learning curves, are presented in Figure 7-8. Here, the simulation results using the first learning curve are presented.

The results of the simulation, Figure 7-9, show the pattern recognition rate of the network increasing with successive training epochs with different noise levels. Learning is observed because after the network is successively exposed to the set of patterns, the recognition rate approaches 1, suggesting that the network is able to accurately recognize all of the different patterns. As the noise level increases, the recognition rate drops below optimal as the network is not able to completely distinguish the signals, which was also observed by Boyn et al. in their simulations[149]. The simulation results suggest that the nonlinear aspect of the CuMnAs counter does not inherently prevent STDP learning.

## 7. Antiferromagnetics for analogue neuromorphic computing

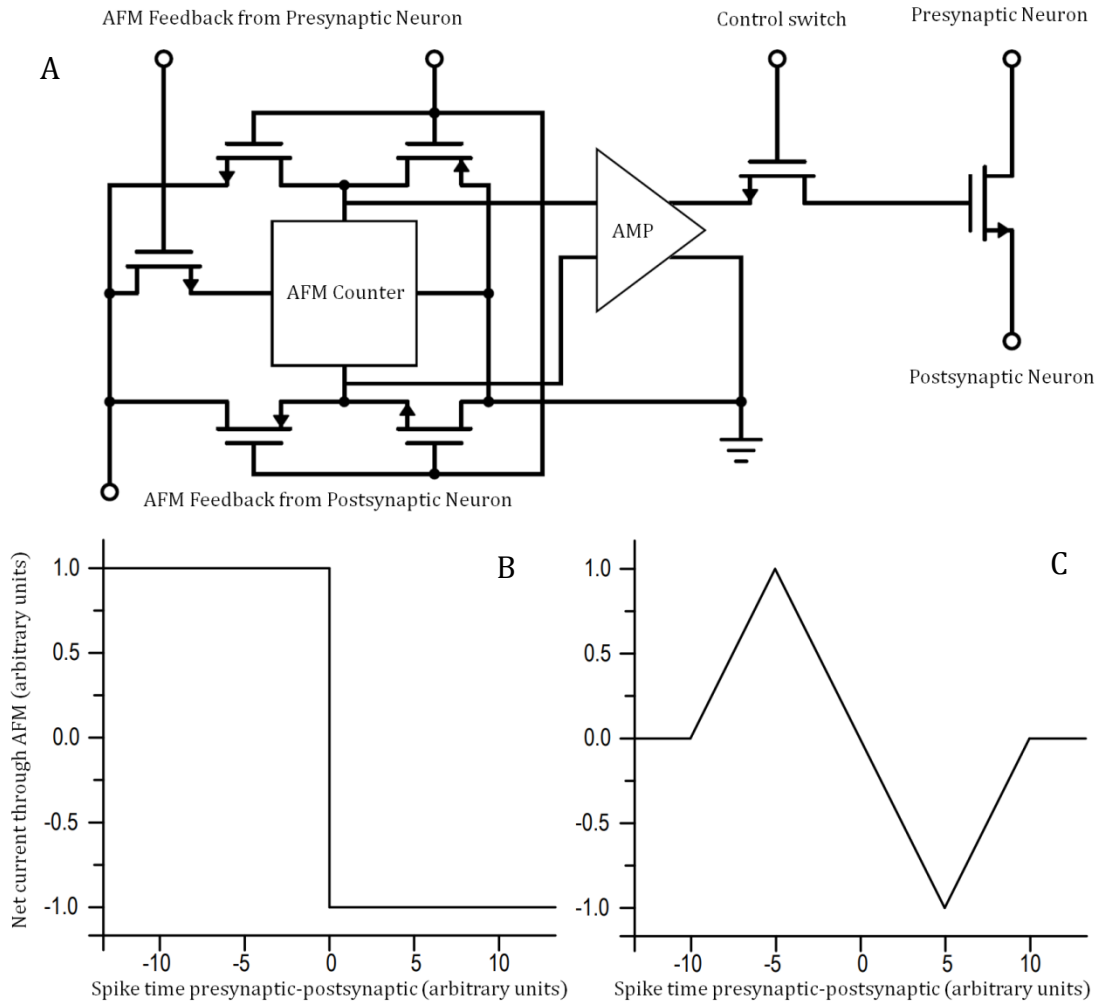


Figure 7-8: A) Circuit architecture for building an STDP AFM synapse. B) and C) are possible learning curves with the proposed architecture.

## 7. Antiferromagnetics for analogue neuromorphic computing

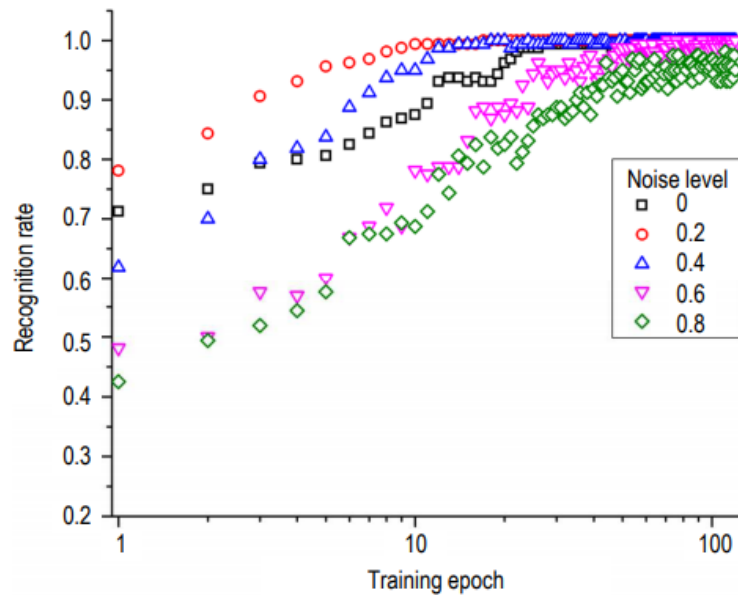


Figure 7-9: Recognition rate of simulated STDP AFM neural networks.

### 7.6.2 Multilayer spiking rate networks

Here, a simulated double layer SRN using antiferromagnetic synapses and the same algorithm as provided by O’Conner et al. in their paper on Deep spiking networks is demonstrated[149]. Similar to the STDP network, the signal propagates forward through the network using integration and fire neurons and learning occurs by feedback from the pre and post synaptic neurons. In addition to the circuitry used in the STDP network, an additional analogue transistor is added to the feedforward synapse to enable excitatory and inhibitory synapses, enabling XOR classification. Furthermore, a secondary synapse is added to enable multiple layer learning through back propagation. Supervised learning occurs in the SRN network by calculating the error of each of the output neurons for a particular training example; output neuron error is defined as the difference between the target and current spike rate of the output neurons. The error at each output neuron is then integrated by the same output neuron. Using identical procedures to forward propagate the signal in the spiking network, the network sends error spikes on a different set of synapses to back propagate the error throughout the network. During a back propagating spiking event a feedback signal is sent from the postsynaptic neuron with sign  $e$  to the AFM counter. In addition, a voltage feedback signal proportional to the time average presynaptic neuron spiking rate ( $\langle s \rangle$ ) is

## 7. Antiferromagnetics for analogue neuromorphic computing

constantly applied from the presynaptic neuron to the CuMnAs counter. As the postsynaptic neuron controls the orientation of the current through the CuMnAs counter, the weight modification is proportional to  $-\langle s \rangle \cdot e$ , which is the identical learning rule presented by O’Conner et al. for deep spiking networks.

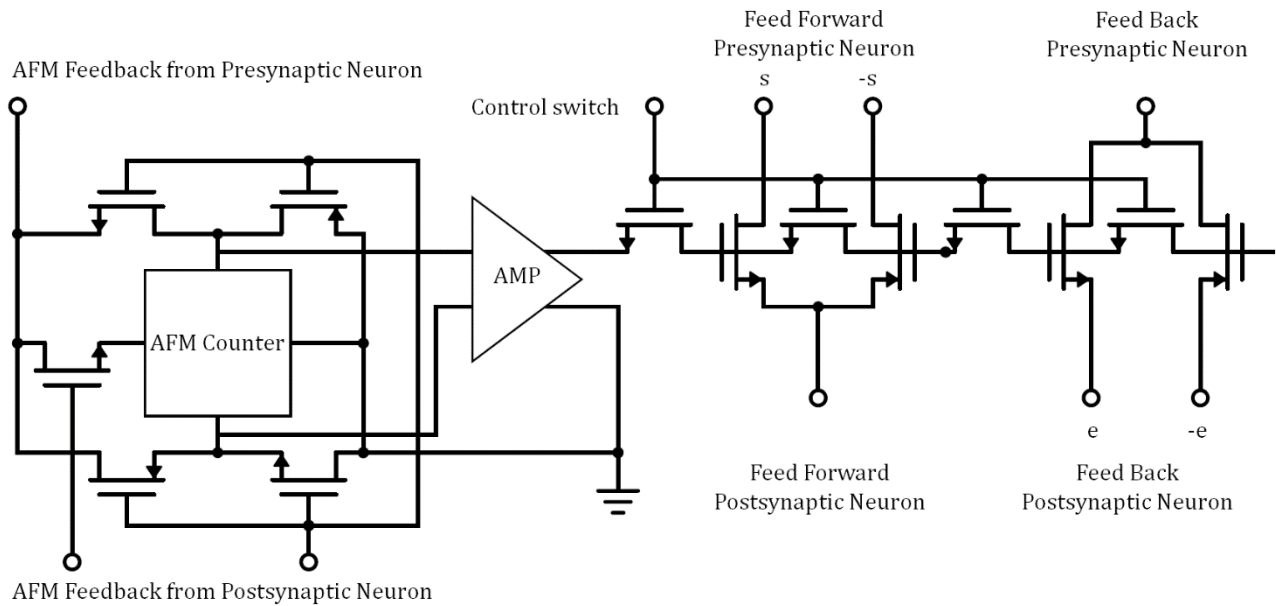


Figure 7-10: Circuit architecture for building an SRN AFM synapse.

The simulation consists of two feedforward layers with 9 input neurons, 9 hidden neurons and 8 output neurons. The results of the simulation, REF, show that the pattern recognition rate of the network increases with successive training epochs with different noise levels. Learning is observed as after the network is successively exposed to the set of patterns, the recognition rate approaches 1 and the network area is minimized, suggesting that the network is able to accurately recognize all of the different patterns. The simulation results suggest that the nonlinear aspect of the CuMnAs counter does not inherently prevent learning in multilayer spiking networks.

## 7. Antiferromagnetics for analogue neuromorphic computing

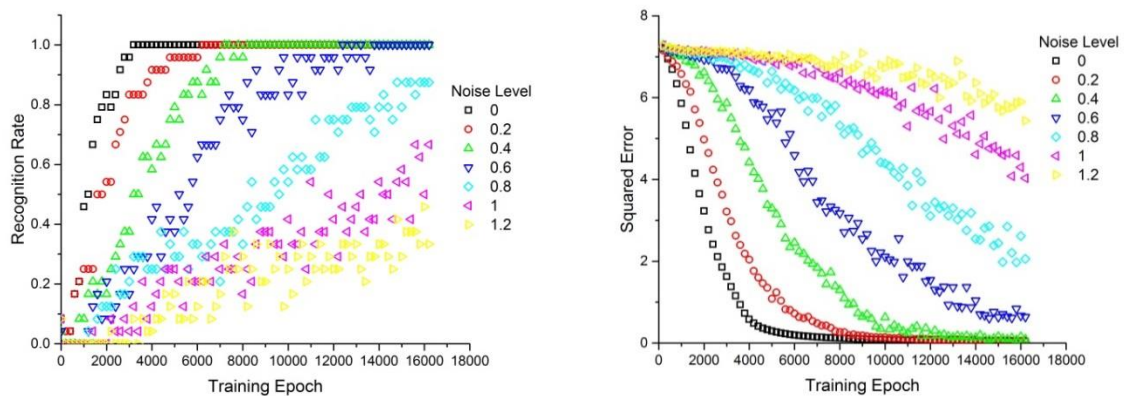


Figure 7-11: Recognition rate and squared error of a simulated SRN AFM neural network.

### 7.7 Conclusions and outlook of analogue neuromorphic computers

In summary, this chapter provides evidence that learning is possible in analogue neuromorphic computers with AFM analogue memories. As the AFM counter has unique features such as reproducible memory states and is not sensitive to stray field suggestions, AFM memories could fill unique applications where traditional memristors do not. The main limiting factor of miniaturization of the AFM synapse is the energy and current required to switch and read the AFM, in addition to the large analogue amplifier required to read out the AFM state. Nevertheless, it appears that STDP is more efficient at learning than SRN. This is not novel and it has been demonstrated that spike timed based algorithms can be far superior in certain applications and aspects, such as real time applications, where a quick learning rate is required[171]. The literature suggests that the temporal dimension of encoding in the spiked networks enables time dependent networks to produce compact representations of larger neural networks[171]. It should be noted that the SRN is mathematically equivalent to a conventional time digital neural network using rectified linear activation functions, so there are not any computational gains when implemented in continuous time. As the STDP algorithm implemented here is extremely simple, this further highlights the importance of researching more complex causal deep and recurrent time based algorithms which would be inefficiently implemented in digital but are naturally suited for analogue circuits[172]. This seems

## 7. Antiferromagnetics for analogue neuromorphic computing

achievable as the human brain is still the most powerful supercomputer and implements causal spike time based algorithms and analogue circuits are the natural, portable and room temperature platform to implement them.

Even though learning is feasible with AFM counters and other memristors, the specific future of the analogue neuromorphic computer is uncertain as there is not a clear consensus about direct applications where digital computers are insufficient. The long-term future of fully developed analogue computers is promising as analogue computers fundamentally use an appropriate basis function set to simulate biological and artificial neural networks. Therefore, it is conceivable that with the appropriate technology, analogue neuromorphic computers will fill a niche application alongside digital and quantum computers[173]. Here appropriate applications where neuromorphic computers could solve niche problems are suggested, such as improved continuous data acquisition and inference.

The quality and quantity of data used in artificial intelligence significantly limit the predictive capabilities of models. However, in continuous monitoring of real-world assets, extremely large quantities of data are generated and only a subset of the data is stored due to limited storage. Neuromorphic computing could provide a low power approach to perform continuous analysis of real time data that would otherwise be ignored.

To the best of the author's knowledge almost all of the analogue neuromorphic computers in the literature are focused on learning, however, in most applications of neural networks, such as performing inference in image recognition in autonomous cars or texture generation in computer graphics, the state of the synapses is not modified when the network is performing the inference. Google's first generation of tensor processing units took advantage of this aspect of neural networks and demonstrated large efficiency gains in performing inferences with only 8 bit precision[174]. Analogue computers should take a similar route, first demonstrating large computational gains through a low precision static network and then incorporating additional hardware to improve the precision and learn in situ. For example, a logical route to introduce

## 7. Antiferromagnetics for analogue neuromorphic computing

learning would be to place an STDP network at the output of a static network pipeline in order to provide fast real time learning using convoluted features generated by a static network.

The most novel insight of this work is that there are standard CMOS architectures likely capable of performing computationally demanding inferences. More focus should be placed on demonstrating large computational gains of static networks which could have a profound impact on edge computing.

### **Contributions**

Dr. Joerg Wunderlich and Dr. Deepak Venkateshvaran

Providing understanding of AFM

## 8 Conclusion and outlook

The goal of this chapter is to summarize the contributions this thesis has made to the understanding of solid state additives for stabilising semiconducting polymers and how this understanding applies to industrial applications and the future of organic electronics. Furthermore, the major hindrances of this work and routes to solve the problem are addressed.

In the search for understanding and expanding solid state molecular additives for stabilising polymer OFETs, a large collection of molecular additives with different functional groups and properties were tested as molecular stabilization additives. One of the key findings of this thesis is the discovery that solid state additives for stabilising semiconducting polymers at this time are limited to a small number of molecules with similar structures to TCNQ. This exhaustive search suggests that if filling the voids and hydrogen bonding are the rationale for the observed improvement, it is limited to a very small subset of molecules or other processes are responsible for the observed device improvement. This is relevant as it provides key insight that research should be focused on why and how TCNQ molecules interact with water to improve device characteristics.

In experimental and theoretical work presented in this thesis it was demonstrated that solid state additives with the appropriate LUMO level, with respect to that of the water-oxygen trap, create a trap free recombination pathway for electrons in the LUMO of organic semiconductors. The new recombination pathway results in the solid state additive improving light stress and PBS. Achieving solid state blends of molecular additives and polymers with minimal bias stress is complex as it appears that morphology/packing/diffusion of the additive in the semiconductor, intermolecular coupling of the OSC and additive and the relative energy of impurity and additive in the film influence the PBS of the OFET. This discovery that some molecular additives are capable of reducing PBS is relevant to analogue circuit applications such as OLED displays where maintaining a constant voltage threshold during operation is required.



The most significant discovery in this thesis is that the interaction regarding TCNQ improving the p-type OFETs completely correlates with a known chemical reaction between TCNQ and water, resulting in the formation of new chemical species. Even though the exact mechanism and chemical species are unknown, similar interactions occur between molecules with similar structure to TCNQ and water. This provides insight that dopants with similar structures, such as F4-TCNQ, could passivate beyond doping the polymer by interacting directly with the atmospheric defects. This thesis suggests these molecules should be labeled as reactive dopants. In addition, non-doping reactive molecular additives, such as (TCNQ, TCAQ, TCNE, DCAQ etc.), are a new family of doping molecules which do not inherently dope the OSC but chemically react with atmospheric species and dope the OSC by modifying the pH. This work suggests modification of the pH can result in an improvement in device characteristics without the negative consequences of high off currents which is undesirable for analogue circuit applications.

A common problem in organic electronics is only having experimental evidence with minimal theoretical models, minimal spectroscopic evidence and an immense parameter space to optimize with no theoretical guidance. In Chapter 7, Quantifying the search for molecular additives, we help to address this problem by applying machine learning to organic electronics. In Chapter 7, we demonstrated that machine learning algorithms can provide insight for selecting suitable molecular additives capable of improving device characteristics based on empirical results. To accelerate the development of OFETs in the future, machine learning algorithms should be used in parallel with conventional techniques to augment the discovery of new materials more efficiently.

Introducing only machine learning algorithms is perhaps still insufficient to efficiently achieve optimal device performance as insight from experts or artificial intelligence based on empirical results is limited by quality and quantity of the data. Achieving high quality and/or quantity of data in organic electronics is difficult as the device fabrication process is time consuming and probabilistic. As the device fabrication is probabilistic, the quality of data is limited by the quantity of data. To increase the quantity of data, researchers should explore high throughput automated fabrication systems.



# Appendix A

## A.1 Minimum and maximum equivalence of Kullback-Leibler divergence and evidence lower bound

In the following we will show that the derivation of minimization of the Kullback-Leibler divergence ( $D_{KL}$ ) of the variational distribution  $q_\theta(w)$  and the true posterior  $p(w|X, Y)$  with respect to  $\theta$  is equivalent to maximizing the model log evidence lower bound (ELBO),  $\log[p(Y|X)] = \int p(Y|X, w)p(w)dw$ , with respect to  $\theta$ .

First we determine the lower bound on the maximum of the model log evidence,

$$\log[p(Y|X)] = \log \int p(Y|X, w)p(w)dw = \log \int (q_\theta(w)/q_\theta(w))p(Y|X, w)p(w)dw$$

By applying Jensen's inequality,  $f(E[x]) \geq E[f(x)]$  as log is a concave function ( $f$ ).

$$\log[p(Y|X)] \geq \int q_\theta(w) \log \left[ \frac{p(Y|X, w)p(w)}{q_\theta(w)} \right] dw$$

The lower bound on the maximum of the model log evidence is seen in (A.1).

$$(A.1) \quad \log[p(Y|X)] \geq \int q_\theta(w) \log p(Y|X, w)dw - D_{KL}(q_\theta(w)||p(w))$$

Next we minimize  $D_{KL}(q_\theta(w)||p(w|X, Y))$

$$D_{KL}(q_\theta(w)||p(w|X, Y)) = \int q_\theta(w) \log[q_\theta(w)/p(w|X, Y)]dw$$

$$\text{As } p(w|X, Y) = p(w)p(X, Y|w)/p(X, Y)$$

$$= \int q_\theta(w) \log[p(X, Y)q_\theta(w)/p(w)p(X, Y|w)]dw$$

$$= \int q_\theta(w) \log[q_\theta(w)/p(w)]dw + \int q_\theta(w) \log p(X, Y)/p(X, Y|w)dw$$

$$\text{As } p(X, Y|w) = p(Y|X, w)p(X|w) = p(Y|X, w)p(X)$$

$$\text{Note independence: } p(X, w) = p(X)p(w)$$

$$\begin{aligned}
 &= D_{KL}(q_{\theta}(w)||p(w)) + \int q_{\theta}(w) \log[p(X, Y) / p(Y|X, w)p(X)]dw \\
 &= D_{KL}(q_{\theta}(w)||p(w)) - \int q_{\theta}(w) \log p(Y|X, w)dw + \int q_{\theta}(w) \log[p(X, Y)/p(X)]dw \\
 &= D_{KL}(q_{\theta}(w)||p(w)) - \int q_{\theta}(w) \log p(Y|X, w)dw + \log[p(Y|X)] \int q_{\theta}(w)dw \\
 &= D_{KL}(q_{\theta}(w)||p(w)) - \int q_{\theta}(w) \log p(Y|X, w)dw + \log[p(Y|X)] \\
 (A.2) \quad &\log[p(Y|X)] - D_{KL}(q_{\theta}(w)||p(w|X, Y)) = \int q_{\theta}(w) \log p(Y|X, w)dw - D_{KL}(q_{\theta}(w)||p(w))
 \end{aligned}$$

Therefore, as  $\log[p(Y|X)]$  is an unknown constant, minimizing  $D_{KL}(q_{\theta}(w)||p(w|X, Y))$  is equivalent to maximizing the ELBO (A.1) or the RHS of (A.2) with respect to  $\theta$ .

# References

- [1] A. J. Heeger, "The Nobel Prize in Chemistry 2000," Nobel Lecture, 2000.
- [2] R. A. Street and Book, *Hydrogenated Amorphous Silicon*, 1st ed. Cambridge: University of Cambridge, 1991.
- [3] M. I. Asghar, J. Zhang, H. Wang, and P. D. Lund, "Device stability of perovskite solar cells – A review," *Renew. Sustain. Energy Rev.*, vol. 77, no. April, pp. 131–146, 2017.
- [4] J. K. Jeong, H. Won Yang, J. H. Jeong, Y.-G. Mo, and H. D. Kim, "Origin of threshold voltage instability in indium-gallium-zinc oxide thin film transistors," *Appl. Phys. Lett.*, vol. 93, no. 12, p. 123508, 2008.
- [5] H. Sirringhaus, T. Sakanoue, and J. F. Chang, "Charge-transport physics of high-mobility molecular semiconductors," *Phys. Status Solidi Basic Res.*, vol. 249, no. 9, pp. 1655–1676, 2012.
- [6] S. Fratini, D. Mayou, and S. Ciuchi, "The Transient Localization Scenario for Charge Transport in Crystalline Organic Materials," *Adv. Funct. Mater.*, p. n/a-n/a, 2016.
- [7] A. Troisi and G. Orlandi, "Charge-transport regime of crystalline organic semiconductors: Diffusion limited by thermal off-diagonal electronic disorder," *Phys. Rev. Lett.*, vol. 96, no. 8, pp. 1–4, 2006.
- [8] S. Illig, A. S. Eggeman, A. Troisi, L. Jiang, C. Warwick, M. Nikolka, G. Schweicher, S. G. Yeates, Y. Henri Geerts, J. E. Anthony, and H. Sirringhaus, "Reducing dynamic disorder in small-molecule organic semiconductors by suppressing large-amplitude thermal motions," *Nat. Commun.*, vol. 7, p. 10736, 2016.
- [9] T. Kubo, R. Häusermann, J. Tsurumi, J. Soeda, Y. Okada, Y. Yamashita, N. Akamatsu, A. Shishido, C. Mitsui, T. Okamoto, S. Yanagisawa, H. Matsui, and J. Takeya, "Suppressing molecular vibrations in organic semiconductors by inducing strain," *Nat. Commun.*, vol. 7, p. 11156, 2016.
- [10] S. Fratini, S., Mayou, D., Ciuchi, "The transient localization scenario for charge transport in crystalline organic semiconductors," *Semiconductors*, vol. 6, no. 8, pp.

1–11, 2005.

- [11] D. Venkateshvaran, M. Nikolka, A. Sadhanala, V. Lemaury, M. Zelazny, M. Kepa, M. Hurhangee, A. J. Kronemeijer, V. Pecunia, I. Nasrallah, I. Romanov, K. Broch, I. McCulloch, D. Emin, Y. Olivier, J. Cornil, D. Beljonne, and H. Sirringhaus, "Approaching disorder-free transport in high-mobility conjugated polymers," *Nature*, vol. 515, no. 7527, pp. 384–388, 2014.
- [12] H. Sirringhaus, P. J. Brown, R. H. Friend, M. M. Nielsen, K. Bechgaard, B. M. W. Langeveld-Voss, a. J. H. Spiering, R. a. J. Janssen, E. W. Meijer, P. Herwig, and D. M. de Leeuw, "Two-dimensional charge transport in self-organized, high-mobility conjugated polymers," *Nature*, vol. 401, no. 6754, pp. 685–688, 1999.
- [13] V. I. Arkhipov, E. V. Emelianova, P. Heremans, and H. Bässler, "Analytic model of carrier mobility in doped disordered organic semiconductors," *Phys. Rev. B*, vol. 72, no. 23, p. 235202, 2005.
- [14] M. S. Freund, B. Deore, and Wiley InterScience (Online service), *Self-doped conducting polymers*. 2007.
- [15] M. Manceau, A. Rivaton, J. L. Gardette, S. Guillerez, and N. Lemaître, "The mechanism of photo- and thermooxidation of poly(3-hexylthiophene) (P3HT) reconsidered," *Polym. Degrad. Stab.*, vol. 94, no. 6, pp. 898–907, 2009.
- [16] Y. Aoyama, T. Yamanari, T. N. Murakami, T. Nagamori, K. Marumoto, H. Tachikawa, J. Mizukado, H. Suda, and Y. Yoshida, "Initial photooxidation mechanism leading to reactive radical formation of polythiophene derivatives," *Polym. J.*, vol. 47, no. 1, pp. 26–30, 2015.
- [17] J. B. Torrance, J. E. Vazquez, J. J. Mayerle, and V. Y. Lee, "Discovery of a Neutral-to-Ionic Phase Transition in Organic Materials," *Phys. Rev. Lett.*, vol. 46, no. 4, 1981.
- [18] I. Salzmann, G. Heimel, S. Duhm, M. Oehzelt, P. Pingel, B. M. George, A. Schnegg, K. Lips, R. P. Blum, A. Vollmer, and N. Koch, "Intermolecular hybridization governs molecular electrical doping," *Phys. Rev. Lett.*, vol. 108, no. 3, pp. 1–5, 2012.
- [19] H. Méndez, G. Heimel, S. Winkler, J. Frisch, A. Opitz, K. Sauer, B. Wegner, M. Oehzelt, C. Röthel, S. Duhm, D. Többens, N. Koch, and I. Salzmann, "Charge-transfer crystallites as molecular electrical dopants," *Nat. Commun.*, vol. 6, no. October, 2015.

- [20] P. Pingel, M. Arvind, L. Kölln, R. Steyrlleuthner, F. Kraffert, J. Behrends, S. Janietz, and D. Neher, "P-Type Doping of Poly(3-hexylthiophene) with the Strong Lewis Acid Tris(pentafluorophenyl)borane," *Adv. Electron. Mater.*, vol. 2, no. 10, pp. 1–7, 2016.
- [21] J. Panidi, A. F. Paterson, D. Khim, Z. Fei, Y. Han, L. Tsetseris, G. Vourlias, P. A. Patsalas, M. Heeney, and T. D. Anthopoulos, "Remarkable Enhancement of the Hole Mobility in Several Organic Small-Molecules, Polymers, and Small-Molecule:Polymer Blend Transistors by Simple Admixing of the Lewis Acid p-Dopant B(C<sub>6</sub>F<sub>5</sub>)<sub>3</sub>," *Adv. Sci.*, vol. 5, no. 1, pp. 1–10, 2018.
- [22] Y. Han, G. Barnes, Y. H. Lin, J. Martin, M. Al-Hashimi, S. Y. Alqaradawi, T. D. Anthopoulos, and M. Heeney, "Doping of Large Ionization Potential Indenopyrazine Polymers via Lewis Acid Complexation with Tris(pentafluorophenyl)borane: A Simple Method for Improving the Performance of Organic Thin-Film Transistors," *Chem. Mater.*, vol. 28, no. 21, pp. 8016–8024, 2016.
- [23] K. Sun, S. Zhang, P. Li, Y. Xia, X. Zhang, D. Du, F. H. Isikgor, and J. Ouyang, "Review on application of PEDOTs and PEDOT:PSS in energy conversion and storage devices," *J. Mater. Sci. Mater. Electron.*, vol. 26, no. 7, pp. 4438–4462, 2015.
- [24] A. G. Macdiarmid, J. C. Chiang, A. F. Richter, and A. J. Epstein, "Polyaniline: a new concept in conducting polymers," *Synth. Met.*, vol. 18, no. 1–3, pp. 285–290, 1987.
- [25] Q. Wang, C. C. Chueh, M. Eslamian, and A. K. Y. Jen, "Modulation of PEDOT:PSS pH for efficient inverted perovskite solar cells with reduced potential loss and enhanced stability," *ACS Appl. Mater. Interfaces*, vol. 8, no. 46, pp. 32068–32076, 2016.
- [26] L. Herlogsson, *Electrolyte-Gated Organic Thin-Film Transistors*. 2011.
- [27] A. Sedra and K. Smith, *Microelectronic Circuits*, Fifth Edit. New York: Oxford University Press, 2004.
- [28] H. H. Choi, K. Cho, C. D. Frisbie, H. Sirringhaus, and V. Podzorov, "Critical assessment of charge mobility extraction in FETs," *Nat. Publ. Gr.*, vol. 17, no. 1, pp. 2–7, 2018.
- [29] R. C. Chittick, J. H. Alexander, and H. F. Sterling, "The Preparation and Properties of

- Amorphous Silicon," *J. Electrochem. Soc.*, vol. 116, no. 1, p. 77, 1969.
- [30] E. Yousif and R. Haddad, "Photodegradation and photostabilization of polymers, especially polystyrene: Review," *Springerplus*, vol. 2, no. 1, pp. 1–32, 2013.
- [31] D. M. de Leeuw, M. M. J. Simenon, a. R. Brown, and R. E. F. Einerhand, "Stability of n-type doped conducting polymers and consequences for polymeric microelectronic devices," *Synth. Met.*, vol. 87, pp. 53–59, 1997.
- [32] H. T. Nicolai, M. Kuik, G. a. H. Wetzelaer, B. de Boer, C. Campbell, C. Risko, J. L. Brédas, and P. W. M. Blom, "Unification of trap-limited electron transport in semiconducting polymers," *Nat. Mater.*, vol. 11, no. 10, pp. 882–887, 2012.
- [33] K. Takimiya, T. Yamamoto, H. Ebata, and T. Izawa, "Design strategy for air-stable organic semiconductors applicable to high-performance field-effect transistors," *Sci. Technol. Adv. Mater.*, vol. 8, no. 4, pp. 273–276, 2007.
- [34] M. Nikolka, G. Schweicher, J. Armitage, I. Nasrallah, C. Jellett, Z. Guo, M. Hurhangee, A. Sadhanala, I. McCulloch, C. B. Nielsen, and H. Sirringhaus, "Performance Improvements in Conjugated Polymer Devices by Removal of Water-Induced Traps," *Adv. Mater.*, vol. 1801874, p. 1801874, 2018.
- [35] R. S. Ashraf, B. C. Schroeder, H. A. Bronstein, Z. Huang, S. Thomas, R. J. Kline, C. J. Brabec, P. Rannou, T. D. Anthopoulos, J. R. Durrant, and I. McCulloch, "The influence of polymer purification on photovoltaic device performance of a series of indacenodithiophene donor polymers," *Adv. Mater.*, vol. 25, no. 14, pp. 2029–2034, 2013.
- [36] P. A. Bobbert, A. Sharma, S. G. J. Mathijssen, M. Kemerink, and D. M. de Leeuw, "Operational Stability of Organic Field-Effect Transistors," *Adv. Mater.*, vol. 24, no. 9, pp. 1146–1158, 2012.
- [37] R. Di Pietro, D. Fazzi, T. B. Kehoe, and H. Sirringhaus, "Spectroscopic investigation of oxygen- and water-induced electron trapping and charge transport instabilities in n-type polymer semiconductors," *J. Am. Chem. Soc.*, vol. 134, no. 36, pp. 14877–14889, 2012.
- [38] Y. Zhao, W. Zhou, H. Tan, R. Fu, Q. Li, F. Lin, D. Yu, G. Walters, E. H. Sargent, and Q. Zhao, "Mobile-Ion-Induced Degradation of Organic Hole-Selective Layers in Perovskite Solar Cells," *J. Phys. Chem. C*, vol. 121, no. 27, pp. 14517–14523, 2017.



- [39] M. Kettner, mi zhou, J. Brill, P. W. M. Blom, and R. T. Weitz, "Complete suppression of bias-induced threshold voltage shift below 273K in solution-processed high-performance organic transistors," *ACS Appl. Mater. Interfaces*, p. acsami.8b13035, 2018.
- [40] P. L. Geissler, C. Dellago, D. Chandler, J. Hutter, and M. Parrinello, "Autoionization in liquid water," *Science (80-. )*, vol. 291, no. 5511, pp. 2121–2124, 2001.
- [41] M. Eigen and L. Maeyer, "Studies on the kinetics of neutralization," *Zeitschrift für Elektrochemie*, vol. 59, no. 10, 1955.
- [42] J. R. Cooper and R. B. Dooley, "Release on the Ionization Constant of H<sub>2</sub>O," 2007.
- [43] M. Nikolka, I. Nasrallah, B. Rose, M. K. Ravva, K. Broch, D. Harkin, J. Charmet, M. Hurhangee, A. Brown, S. Illig, P. Too, J. Jongman, I. McCulloch, J.-L. Bredas, and H. Sirringhaus, "High operational and environmental stability of high-mobility conjugated polymer field-effect transistors achieved through the use of molecular additives," *Nat. Mater.*, vol. 1, no. December, pp. 1–8, 2016.
- [44] G. Malliaras and R. Friend, "An organic electronics primer," *Phys. Today*, vol. 58, no. 5, pp. 53–58, 2005.
- [45] R. Griffiths and J. M. Hernández-lobato, "Constrained Bayesian Optimization for Automatic Chemical Design," no. Nips, 2018.
- [46] D. Duvenaud, D. Maclaurin, J. Aguilera-Iparraguirre, R. Gómez-Bombarelli, T. Hirzel, A. Aspuru-Guzik, and R. P. Adams, "Convolutional Networks on Graphs for Learning Molecular Fingerprints," *Dig. Asia-Pacific Magn. Rec. Conf. 2010, APMRC 2010*, pp. 1–9, 2010.
- [47] D. Rogers and M. Hahn, "Extended-connectivity fingerprints," *J. Chem. Inf. Model.*, vol. 50, no. 5, pp. 742–754, 2010.
- [48] C. Daskalakis, C. Tzamos, and M. Zampetakis, "A Converse to Banach's Fixed Point Theorem and its CLS Completeness," 2017.
- [49] W. Jin, R. Barzilay, and T. Jaakkola, "Junction Tree Variational Autoencoder for Molecular Graph Generation," 2018.
- [50] J. Gilmer, S. S. Schoenholz, P. F. Riley, O. Vinyals, and G. E. Dahl, "Neural Message Passing for Quantum Chemistry," 2017.

- [51] M. Rupp, A. Tkatchenko, K. R. Müller, and O. A. Von Lilienfeld, "Fast and accurate modeling of molecular atomization energies with machine learning," *Phys. Rev. Lett.*, vol. 108, no. 5, pp. 1–5, 2012.
- [52] G. Montavon, K. Hansen, S. Fazli, M. Rupp, F. Biegler, A. Ziehe, A. Tkatchenko, O. A. Von Lilienfeld, and K. Müller, "Learning Invariant Representations of Molecules for Atomization Energy Prediction," in *NIPS*, 2011, pp. 1–9.
- [53] A. Cameron, "Information Compression Of Molecular Representations Using Neural Network Auto-Encoders By," University of Prince Edward Island, 2017.
- [54] R. Gómez-Bombarelli, D. Sheberla, J. Aguilera-ipparraguirre, T. D. Hirzel, and R. P. Adams, "Automatic Chemical Design Using a Data-Driven Continuous Representation of Molecules," *ACS Cent. Sci.*, no. 4, p. 268–276, 2018.
- [55] F. Chollet, *Deep Learning with Python*. Shelter Island: Manning Publications Co, 2017.
- [56] Y. Gal, "Uncertainty in Deep Learning," *PhD Thesis*, no. October, p. 174, 2016.
- [57] R. M. Neal, "Bayesian Learning for Neural Networks," University of Toronto, 1995.
- [58] Y. Gal and Z. Ghahramani, "Dropout as a Bayesian Approximation: Representing Model Uncertainty in Deep Learning," *arXiv*, 2016.
- [59] P. I. Frazier, "A Tutorial on Bayesian Optimization," no. Section 5, pp. 1–22, 2018.
- [60] B. Cao, L. A. Adutwum, A. O. Oliynyk, E. J. Luber, B. C. Olsen, A. Mar, and J. M. Buriak, "How To Optimize Materials and Devices *via* Design of Experiments and Machine Learning: Demonstration Using Organic Photovoltaics," *ACS Nano*, vol. 12, p. acsnano.8b04726, 2018.
- [61] X. Sun, C. A. Di, and Y. Liu, "Engineering of the dielectric-semiconductor interface in organic field-effect transistors," *J. Mater. Chem.*, vol. 20, no. 13, pp. 2599–2611, 2010.
- [62] L. Chua, J. Zaumseil, J. Chang, and E. C. Ou, "General observation of n-type field-effect behaviour in organic semiconductors," *Nano Lett.*, vol. 434, no. March, pp. 194–199, 2005.
- [63] J. Veres, S. D. Ogier, S. W. Leeming, D. C. Cupertino, and M. S. Khaffaf, "Low-k Insulators as the Choice of Dielectrics in Organic Field-Effect Transistors TL," *Adv.*

- Funct. Mater.*, vol. 13 VN-r, no. 3, pp. 199–204, 2003.
- [64] S. Kim, K. Suzuki, A. Sugie, H. Yoshida, M. Yoshida, and Y. Suzuki, “Effect of end group of amorphous perfluoro-polymer electrets on electron trapping,” *Sci. Technol. Adv. Mater.*, vol. 19, no. 1, pp. 486–494, 2018.
- [65] T. T. Dao, T. Matsushima, and H. Murata, “Organic nonvolatile memory transistors based on fullerene and an electron-trapping polymer,” *Org. Electron. physics, Mater. Appl.*, vol. 13, no. 11, pp. 2709–2715, 2012.
- [66] H. Sirringhaus, “Reliability of Organic Field-Effect Transistors,” *Adv. Mater.*, no. 21, pp. 3859–3873, 2009.
- [67] L. Ma, P. Hu, H. Jiang, C. Kloc, H. Sun, C. Soci, A. A. Voityuk, M. E. Michel-Beyerle, and G. G. Gurzadyan, “Single photon triggered dianion formation in TCNQ and F4TCNQ crystals,” *Sci. Rep.*, vol. 6, p. 28510, 2016.
- [68] I. Nasrallah, “Investigating charge trapping effects in organic field-effect transistors,” University of Cambridge, 2015.
- [69] G. Socrates, *Infrared and Raman Characteristic Group Frequencies: Tables and Charts*, 3rd ed. Wiley, 2004.
- [70] M. Furuhashi and J. Yoshinobu, “Charge transfer and molecular orientation of tetrafluoro- tetracyanoquinodimethane on a hydrogen-terminated Si(111) surface prepared by a wet chemical method,” *J. Phys. Chem. Lett.*, vol. 1, no. 10, pp. 1655–1659, 2010.
- [71] M. A. Chamber and F. J. Montes, “TensorFlow: Large-Scale Machine Learning on Heterogeneous Distributed Systems,” *Plant Soil*, vol. 66, no. 3, pp. 353–360, 1982.
- [72] F. Pedregosa, R. Weiss, and M. Brucher, “Scikit-learn Machine Learning in Python,” vol. 12, pp. 2825–2830, 2011.
- [73] “RDKit: Open-Source Cheminformatics Software,” 2019. [Online]. Available: <http://www.rdkit.org>.
- [74] M. J. Keiser, “keras-neural-graph-fingerprint.” GitHub, 2018.
- [75] F. Chollet, “Keras.” GitHub, 2015.
- [76] R. Gómez-Bombarelli, J. Wei, D. Duvenaud, J. M. Hernández-Lobato, B. Sánchez-Lengeling, D. Sheberla, J. Aguilera-Iparraguirre, T. Hirzel, R. P. Adams, and A.

- Aspuru-Guzik, "chemical\_vae." GitHub, 2019.
- [77] T. Sterling and J. J. Irwin, "ZINC 15 - Ligand Discovery for Everyone," *J. Chem. Inf. Model.*, vol. 55, no. 11, pp. 2324–2337, 2015.
- [78] S. Kim, J. Chen, T. Cheng, A. Gindulyte, J. He, S. He, Q. Li, B. A. Shoemaker, P. A. Thiessen, B. Yu, L. Zaslavsky, J. Zhang, and E. E. Bolton, "PubChem 2019 update: improved access to chemical data," *Nucleic Acids Res.*, vol. 47, no. October 2018, pp. 1–8, 2018.
- [79] B. S. Ong and B. Keoshkerian, "11,11,12, 12-Tetracyanoanthraquinodimethane," *J. Org. Chem.*, vol. 49, no. 25, pp. 5002–5003, 1984.
- [80] \* Jun Li,†,‡ Guangwu Zhang,†,§ Daniella E. Holm,‡ Ian E. Jacobs,‡ Bin Yin,§ Pieter Stroeve,‡ Mark Mascall and 3 and Adam J. Moulé\*, "Introducing Solubility Control for Improved Organic P-Type Dopants," 2015.
- [81] Y. Karpov, T. Erdmann, I. Raguzin, M. Al-Hussein, M. Binner, U. Lappan, M. Stamm, K. L. Gerasimov, T. Beryozkina, V. Bakulev, D. V. Anokhin, D. A. Ivanov, F. Gunther, S. Gemming, G. Seifert, B. Voit, R. Di Pietro, and A. Kiriya, "High Conductivity in Molecularly p-Doped Diketopyrrolopyrrole-Based Polymer: The Impact of a High Dopant Strength and Good Structural Order," *Adv. Mater.*, pp. 6003–6010, 2016.
- [82] A. B. Padmaperuma and Padmaperuma, "Substituted Molecular &lt;i>p</i>-Dopants: A Theoretical Study," *Adv. Mater. Phys. Chem.*, vol. 02, no. 03, pp. 163–172, 2012.
- [83] Y. Washino, K. Murata, M. Ashizawa, S. Kawauchi, and T. Michinobu, "Creation of persistent charge-transfer interactions in TCNQ polyester," *Polym. J.*, vol. 43, no. 4, pp. 364–369, 2011.
- [84] I. E. Jacobs and A. J. Moulé, "Controlling Molecular Doping in Organic Semiconductors," *Adv. Mater.*, vol. 1703063, pp. 1–39, 2017.
- [85] A. Shin, S. J. Hwang, S. W. Yu, and M. Y. Sung, "Design of organic TFT pixel electrode circuit for active-matrix OLED displays," *J. Comput.*, vol. 3, no. 3, pp. 1–5, 2008.
- [86] W. Tang, J. Zhao, Y. Huang, L. Ding, Q. Li, J. Li, P. You, F. Yan, and X. Guo, "Bias stress stability improvement in solution-processed low-voltage organic field-effect transistors using relaxor ferroelectric polymer gate dielectric," *IEEE Electron Device Lett.*, vol. 38, no. 6, pp. 748–751, 2017.

- [87] T. Ashimine, T. Onoue, T. Yasuda, K. Fujita, and T. Tsutsui, "Parylene-C and high-k polymer bilayer gate dielectric for low-operating voltage organic field-effect transistors," *Mol. Cryst. Liq. Cryst.*, vol. 471, no. May, pp. 221–227, 2007.
- [88] R. Husermann and B. Batlogg, "Gate bias stress in pentacene field-effect-transistors: Charge trapping in the dielectric or semiconductor," *Appl. Phys. Lett.*, vol. 99, no. 8, 2011.
- [89] S. Ogawa, T. Naijo, Y. Kimura, H. Ishii, and M. Niwano, "Photoinduced doping effect of pentacene field effect transistor in oxygen atmosphere studied by displacement current measurement," *Appl. Phys. Lett.*, vol. 86, no. 25, pp. 1–3, 2005.
- [90] Y.-Y. Noh, J. Ghim, S.-J. Kang, K.-J. Baeg, D.-Y. Kim, and K. Yase, "Effect of light irradiation on the characteristics of organic field-effect transistors," *J. Appl. Phys.*, vol. 100, no. 9, p. 94501, 2006.
- [91] S. H. Jeong and C. K. Song, "Energetic distribution of interface states extracted from photo-conductance of organic thin film transistors," *Org. Electron. physics, Mater. Appl.*, vol. 15, no. 10, pp. 2599–2607, 2014.
- [92] R. Liguori, S. Aprano, and A. Rubino, "Metastable light induced defects in pentacene," *AIP Conf. Proc.*, vol. 1583, no. 9, pp. 212–216, 2014.
- [93] C. B. Park, "Investigation of the device instability feature caused by electron trapping in pentacene field effect transistors," *Appl. Phys. Lett.*, vol. 100, no. 6, pp. 1–4, 2012.
- [94] Y. Liang, G. Dong, Y. Hu, L. Wang, and Y. Qiu, "Low-voltage pentacene thin-film transistors with tantalum oxide gate insulators and their reversible light-induced threshold voltage shift," *Appl. Phys. Lett.*, vol. 86, no. 13, pp. 1–3, 2005.
- [95] O. D. Jurchescu, J. Baas, and T. T. M. Palstra, "Electronic transport properties of pentacene single crystals upon exposure to air," *Appl. Phys. Lett.*, vol. 87, no. 5, pp. 2003–2006, 2005.
- [96] C. S. S. Sangeeth, P. Stadler, S. Schaur, N. S. Sariciftci, and R. Menon, "Interfaces and traps in pentacene field-effect transistor," *J. Appl. Phys.*, vol. 108, no. 11, p. 113703, 2010.
- [97] M. Song, J. Seo, H. Kim, and Y. Kim, "Ultrasensitive Multi-Functional Flexible Sensors Based on Organic Field-Effect Transistors with Polymer-Dispersed Liquid

- Crystal Sensing Layers /639/301/1005/1007 /639/301/923 /120 /123 article," *Sci. Rep.*, vol. 7, no. 1, pp. 1–11, 2017.
- [98] S. Oae, "The Organic Chemistry of Superoxide," no. 1, pp. 385–390, 1977.
- [99] X. Niu, Y. Li, Y. Zhang, Q. Li, Q. Zhou, J. Zhao, and J. Wang, "Photo-oxidative Degradation and Protection Mechanism of Black Phosphorus: Insights from Ultrafast Dynamics," *J. Phys. Chem. Lett.*, vol. 9, pp. 5034–5039, 2018.
- [100] J. Li, G. Zhang, D. M. Holm, I. E. Jacobs, B. Yin, P. Stroeve, M. Mascal, and A. J. Moulé, "Introducing Solubility Control for Improved Organic P-Type Dopants," *Chem. Mater.*, vol. 27, no. 16, pp. 5765–5774, 2015.
- [101] M. Nikolka, "Device Physics of High Performance," University of Cambridge, 2015.
- [102] L. Müller, S. Rhim, V. Sivanesan, D. Wang, S. Hietzschold, P. Reiser, E. Mankel, S. Beck, S. Barlow, S. R. Marder, A. Pucci, W. Kowalsky, and R. Lovrincic, "Electric-Field-Controlled Dopant Distribution in Organic Semiconductors," vol. 1701466, pp. 1–7, 2017.
- [103] J. Li, C. W. Rochester, I. E. Jacobs, E. W. Aasen, and S. Friedrich, "The effect of thermal annealing on dopant site choice in conjugated polymers," *Org. Electron.*, no. 33, pp. 23–31, 2016.
- [104] C. N. McEwen and M. A. Rudat, "Fast radical reactions in a mass spectrometer ion source: radical addition to 7,7,8,8-tetracyanoquinodimethane," *J. Am. Chem. Soc.*, vol. 101, no. 21, pp. 6470–6472, 1979.
- [105] A. Cehak, A. Chyla, M. Radomska, and R. Radomski, "The Influence of Water and Oxygen on Stability of TCNQ Solution in Acetonitrile," *Mol. Cryst. Liq. Cryst.*, vol. 120, no. 1, pp. 327–331, 1985.
- [106] Y. Qi, U. Mazur, and K. W. Hipps, "Charge transfer induced chemical reaction of tetracyano-p-quinodimethane adsorbed on graphene," *RSC Adv.*, vol. 2, no. 28, pp. 10579–10584, 2012.
- [107] I. E. Jacobs, F. Wang, N. Hafezi, C. Medina-Plaza, T. F. Harrelson, J. Li, M. P. Augustine, M. Mascal, and A. J. Moulé, "Quantitative Dedoping of Conductive Polymers," *Chem. Mater.*, vol. 29, no. 2, pp. 832–841, 2017.
- [108] I. Salzmänn, G. Heimel, M. Oehzelt, S. Winkler, and N. Koch, "Molecular Electrical Doping of Organic Semiconductors: Fundamental Mechanisms and Emerging

- Dopant Design Rules," *Acc. Chem. Res.*, vol. 49, no. 3, pp. 370–378, 2016.
- [109] A. Mityashin, Y. Olivier, T. Van Regemorter, C. Rolin, S. Verlaak, N. G. Martinelli, D. Beljonne, J. Cornil, J. Genoe, and P. Heremans, "Unraveling the mechanism of molecular doping in organic semiconductors," *Adv. Mater.*, vol. 24, no. 12, pp. 1535–1539, 2012.
- [110] K. Kang, S. Watanabe, K. Broch, A. Sepe, A. Brown, I. Nasrallah, M. Nikolka, Z. Fei, M. Heeney, D. Matsumoto, K. Marumoto, H. Tanaka, S. Kuroda, and H. Sirringhaus, "2D coherent charge transport in highly ordered conducting polymers doped by solid state diffusion," *Nat. Mater.*, vol. 15, no. May, pp. 1–8, 2016.
- [111] M. C. Gossel, A. J. Duke, D. Brynn Hibbert, I. K. Lewis, E. A. Seddon, P. N. Horton, and S. C. Weston, "An investigation of the factors that influence the decomposition of 7,7',8,8'-tetracyanoquinodimethane (TCNQ) and its salts to, and structural characterization of, the  $\alpha,\alpha$ -dicyano-p-toluoylcyanoide anion," *Chem. Mater.*, vol. 12, no. 8, pp. 2319–2323, 2000.
- [112] M. Harris, J. J. Hoagland, U. Mazur, and K. W. Hipps, "Raman and infrared spectra of metal salts of  $\alpha$ ,  $\alpha$ -dicyano-p-toluoylcyanoide: non-resonant Raman scattering in tetracyano-p-quinodimethanide," *Vib. Spectrosc.*, vol. 9, no. 3, pp. 273–277, 1995.
- [113] H. Shiozawa, B. C. Bayer, H. Peterlik, J. C. Meyer, W. Lang, and T. Pichler, "Doping of metal-organic frameworks towards resistive sensing," *Sci. Rep.*, vol. 7, no. 1, pp. 1–8, 2017.
- [114] J. Li, G. Zhang, D. M. Holm, I. E. Jacobs, B. Yin, P. Stroeve, M. Mascal, and A. J. Moule, "Introducing Solubility Control for Improved Organic P - Type Dopants," *Chem. Mater.*, 2015.
- [115] D. Kiefer, A. Giovannitti, H. Sun, T. Biskup, A. Hofmann, M. Koopmans, C. Cendra, S. Weber, L. J. Anton Koster, E. Olsson, J. Rivnay, S. Fabiano, I. McCulloch, and C. Müller, "Enhanced n-Doping Efficiency of a Naphthalenediimide-Based Copolymer through Polar Side Chains for Organic Thermoelectrics," *ACS Energy Lett.*, vol. 3, no. 2, pp. 278–285, 2018.
- [116] B. Lüssem, C.-M. Keum, D. Kasemann, B. Naab, Z. Bao, and K. Leo, "Doped Organic Transistors," *Chem. Rev.*, p. acs.chemrev.6b00329, 2016.
- [117] M. P. Hein, A. A. Zakhidov, B. Lüssem, J. Jankowski, M. L. Tietze, M. K. Riede, and K.

- Leo, "Molecular doping for control of gate bias stress in organic thin film transistors," *Appl. Phys. Lett.*, vol. 104, no. 1, 2014.
- [118] I. E. Jacobs, F. Wang, Z. I. Bedolla Valdez, A. N. Ayala Oviedo, D. J. Bilsky, and A. J. Moulé, "Photoinduced degradation from trace 1,8-diiodooctane in organic photovoltaics," *J. Mater. Chem. C*, vol. 6, no. 2, pp. 219–225, 2018.
- [119] T. Jiang, W. Han, M. Maduke, and E. Tajkhorshid, "Molecular Basis for Differential Anion Binding and Proton Coupling in the Cl<sup>-</sup>/H<sup>+</sup> Exchanger ClC-ec1," *J. Am. Chem. Soc.*, vol. 138, no. 9, pp. 3066–3075, 2016.
- [120] J. Stejskal, M. Trchová, P. Bober, P. Humpolíček, V. Kašpárková, I. Sapurina, M. A. Shishov, and M. Varga, *Conducting Polymers: Polyaniline*, no. June. 2015.
- [121] D. R. Buckle, "2,3-Dichloro-5,6-dicyano-1,4- benzoquinone," in *Encyclopedia of reagents for organic synthesis*, no. 5, John Wiley & Sons, Ltd, 2005.
- [122] J. King, S. Yarkoni, J. Raymond, I. Ozfidan, A. D. King, M. M. Nevisi, J. P. Hilton, and C. C. McGeoch, "Quantum Annealing amid Local Ruggedness and Global Frustration," 2017.
- [123] N. Guo, Y. Huang, T. Mai, S. Patil, C. Cao, M. Seok, S. Sethumadhavan, and Y. Tsvividis, "Energy-Efficient Hybrid Analog/Digital Approximate Computation in Continuous Time," *IEEE J. Solid-State Circuits*, vol. 51, no. 7, pp. 1514–1524, 2016.
- [124] F. L. Traversa, P. Cicotti, F. Sheldon, and M. Di Ventra, "Evidence of an exponential speed-up in the solution of hard optimization problems," *Complexity*, vol. 2018, p. 13, 2017.
- [125] M. Di Ventra and F. L. Traversa, "Memcomputing: Leveraging memory and physics to compute efficiently," *J. Appl. Phys.*, vol. 123, no. 18, pp. 1–16, 2018.
- [126] K. Y. Camsari, S. Chowdhury, S. Datta, I. Introduction, Q. B. Law, B. Law, and V. Conclusions, "Scaled Quantum Circuits Emulated with Room Temperature p-Bits," *arXiv*, vol. 47907, pp. 1–9, 2018.
- [127] K. Y. Camsari, B. M. Sutton, and S. Datta, "p-Bits for Probabilistic Spin Logic," *Phys. Rev. X*, vol. 47907, no. September, pp. 1–10, 2017.
- [128] D. Hassabis, D. Kumaran, C. Summerfield, and M. Botvinick, "Neuroscience-Inspired Artificial Intelligence," *Neuron*, vol. 95, no. 2, pp. 245–258, 2017.



- [129] M. A. Nielsen, *Neural Networks and Deep Learning*. Determination Press, 2015.
- [130] F. Caravelli and J. P. Carbajal, “Memristors for the curious outsiders,” *Technologies*, pp. 1–42, 2018.
- [131] I. Levitan and Leonard Kaczmarek, *The Neuron: Cell and Molecular Biology*, 3rd editio. Oxford University Press, 2001.
- [132] Yael Avissar, *Biology*. Houston, Texas: OpenStax College, 2013.
- [133] A. M. Saxe, “Deep linear neural networks: A theory of learning in the brain and mind,” Stanford University, 2015.
- [134] C. Hurtes, M. Boulou, a. Mitonneau, and D. Bois, “Deep-level spectroscopy in high-resistivity materials,” *Appl. Phys. Lett.*, vol. 32, no. 12, p. 821, 1978.
- [135] X. Wu, V. Saxena, and K. Zhu, “A CMOS Spiking Neuron for Dense Memristor-Synapse Connectivity for Brain-Inspired Computing,” in *Neural Networks (IJCNN)*, 2015.
- [136] I. Goodfellow, B. Yoshua, and C. Aaron, *Deep Learning*. MIT Press, 2016.
- [137] C. Zamarreño-Ramos, L. A. Camuñas-Mesa, J. A. Perez-Carrasco, T. Masquelier, T. Serrano-Gotarredona, and B. Linares-Barranco, “On spike-timing-dependent-plasticity, memristive devices, and building a self-learning visual cortex,” *Front. Neurosci.*, vol. 5, no. MAR, pp. 1–22, 2011.
- [138] B. Y. D. H. Hubel and A. D. T. N. Wiesel, “Receptive fields, binocular interaction and functional architecture in the cat’s visual cortex,” *J. Physiol.*, pp. 106–154, 1962.
- [139] M. Sewak, R. Karim, and P. Pujari, *Practical Convolutional Neural Networks*, 1st ed. Mumbai: Packt Publishing, 2018.
- [140] B. Schrauwen, D. Verstraeten, and J. Van Campenhout, “An overview of reservoir computing: theory, applications and implementations,” *Proc. 15th Eur. Symp. Artif. Neural Networks*, no. April, pp. 471–82, 2007.
- [141] Y. Paquot, F. Duport, A. Smerieri, J. Dambre, B. Schrauwen, M. Haelterman, and S. Massar, “Optoelectronic Reservoir Computing,” *Sci. Rep.*, vol. 2, no. 1, p. 287, 2012.
- [142] Y. Shen, N. C. Harris, D. Englund, and M. Soljacic, “Deep learning with coherent nanophotonic circuits,” *2017 5th Berkeley Symp. Energy Effic. Electron. Syst. E3S 2017 - Proc.*, vol. 2018–Janua, pp. 1–2, 2018.

- [143] J. Bueno, S. Maktoobi, L. Froehly, I. Fischer, M. Jacquot, L. Larger, and D. Brunner, "Reinforcement Learning in a large scale photonic Recurrent Neural Network," *arXiv*, vol. 1, pp. 1–5, 2017.
- [144] J. C. Coulombe, M. C. A. York, and J. Sylvestre, "Computing with networks of nonlinear mechanical oscillators," *PLoS One*, vol. 12, no. 6, pp. 1–13, 2017.
- [145] M. Awiszus and B. Rosenhahn, "Markov Chain Neural Networks," *arXiv*, 2018.
- [146] T. Serrano-Gotarredona, T. Masquelier, T. Prodromakis, G. Indiveri, and B. Linares-Barranco, "STDP and sTDP variations with memristors for spiking neuromorphic learning systems," *Front. Neurosci.*, vol. 7, no. 7 FEB, pp. 1–15, 2013.
- [147] C. Clopath and W. Gerstner, "Voltage and spike timing interact in STDP - a unified model," *Front. Synaptic Neurosci.*, 2010.
- [148] Y. Babacan and F. Kaçar, "Memristor emulator with spike-timing-dependent-plasticity," *AEU - Int. J. Electron. Commun.*, vol. 73, pp. 16–22, 2017.
- [149] S. Boyn, J. Grollier, G. Lecerf, B. Xu, N. Locatelli, S. Fusil, S. Girod, C. Carrétéro, K. Garcia, S. Xavier, J. Tomas, L. Bellaiche, M. Bibes, A. Barthélémy, S. Saïghi, and V. Garcia, "Learning through ferroelectric domain dynamics in solid-state synapses," *Nat. Commun.*, vol. 8, p. 14736, 2017.
- [150] C. D. Schuman, T. E. Potok, R. M. Patton, J. D. Birdwell, M. E. Dean, G. S. Rose, and J. S. Plank, "A Survey of Neuromorphic Computing and Neural Networks in Hardware," *arXiv*, pp. 1–88, 2017.
- [151] J. S. Seo, B. Brezzo, Y. Liu, B. D. Parker, S. K. Esser, R. K. Montoye, B. Rajendran, J. A. Tierno, L. Chang, D. S. Modha, and D. J. Friedman, "A 45nm CMOS neuromorphic chip with a scalable architecture for learning in networks of spiking neurons," *Proc. Cust. Integr. Circuits Conf.*, pp. 2–5, 2011.
- [152] I. Sporea and A. Grüning, "Supervised Learning in Multilayer Spiking Neural Networks," *Neural Comput.*, vol. 25, no. 2, pp. 473–509, 2013.
- [153] X. Xie, H. Qu, G. Liu, M. Zhang, and J. Kurths, "An efficient supervised training algorithm for multilayer spiking neural networks," *PLoS One*, vol. 11, no. 4, pp. 1–29, 2016.
- [154] C. Paper and B. C. Wiskunde, "SpikeProp: backpropagation for networks of spiking neurons . SpikeProp : Backpropagation for Networks of Spiking Neurons,"

- in *ESANN 2000*, 2000, no. 8th European Symposium on Artificial Neural Networks.
- [155] F. Ponulak and A. Kasiński, “Supervised learning in spiking neural networks with ReSuMe: sequence learning, classification, and spike shifting,” *Neural Comput.*, vol. 22, no. 2, pp. 467–510, 2010.
- [156] P. O’Connor and M. Welling, “Deep Spiking Networks,” no. Nips, pp. 1–16, 2016.
- [157] T. Shibata and T. Ohmi, “A Functional MOS Transistor Featuring Gate-Level Weighted Sum and Threshold Operations,” *IEEE Trans. Electron Devices*, vol. 39, no. 6, 1992.
- [158] C. Hu, “The EEPROM as an Analog Memory Device,” vol. 36, pp. 1840–1841, 1989.
- [159] L. O. Chua, “Memristor—The Missing Circuit Element,” *IEEE Trans. Circuit Theory*, vol. 18, no. 5, pp. 507–519, 1971.
- [160] D. B. Strukov, G. S. Snider, D. R. Stewart, and R. S. Williams, “The missing memristor found,” *Nature*, vol. 459, no. 7250, pp. 1154–1154, 2009.
- [161] G. Indiveri, B. Linares-Barranco, R. Legenstein, G. Deligeorgis, and T. Prodromakis, “Integration of nanoscale memristor synapses in neuromorphic computing architectures,” *Nanotechnology*, vol. 24, no. 384010, 2013.
- [162] T. Prodromakis and C. Toumazou, “A review on memristive devices and applications,” *2010 IEEE Int. Conf. Electron. Circuits, Syst. ICECS 2010 - Proc.*, pp. 934–937, 2010.
- [163] H. Nili, S. Walia, S. Balendhran, D. B. Strukov, M. Bhaskaran, and S. Sriram, “Nanoscale resistive switching in amorphous perovskite oxide ( $a\text{-SrTiO}_3$ ) memristors,” *Adv. Funct. Mater.*, vol. 24, no. 43, pp. 6741–6750, 2014.
- [164] A. C. Torrezan, J. P. Strachan, G. Medeiros-Ribeiro, and R. S. Williams, “Sub-nanosecond switching of a tantalum oxide memristor,” *Nanotechnology*, vol. 22, no. 48, p. 485203, 2011.
- [165] T. Berzina, A. Smerieri, M. Bernab, A. Pucci, G. Ruggeri, V. Erokhin, and M. P. Fontana, “Optimization of an organic memristor as an adaptive memory element,” *J. Appl. Phys.*, vol. 105, no. 12, 2009.
- [166] P. Wadley, B. Howells, J. Zelezny, C. Andrews, V. Hills, R. P. Campion, V. Novak, F.

- Freimuth, Y. Mokrousov, A. W. Rushforth, K. W. Edmonds, B. L. Gallagher, and T. Jungwirth, "Electrical switching of an antiferromagnet," *Science (80-. )*, vol. 351, no. 6273, 2015.
- [167] K. Olejník, T. Seifert, Z. Kašpar, V. Novák, P. Wadley, R. P. Campion, M. Baumgartner, P. Gambardella, P. Nemeč, J. Wunderlich, J. Sinova, P. Kužel, M. Müller, T. Kampfrath, and T. Jungwirth, "Terahertz electrical writing speed in an antiferromagnetic memory," *Sci. Adv.*, vol. 4, no. 3, pp. 1–9, 2018.
- [168] J. Železný, H. Gao, K. Výborný, J. Zemen, J. Mašek, A. Manchon, J. Wunderlich, J. Sinova, and T. Jungwirth, "Relativistic néel-order fields induced by electrical current in antiferromagnets," *Phys. Rev. Lett.*, vol. 113, no. 15, pp. 1–5, 2014.
- [169] M. J. Grzybowski, P. Wadley, K. W. Edmonds, R. Beardsley, V. Hills, R. P. Campion, B. L. Gallagher, J. S. Chauhan, V. Novak, T. Jungwirth, F. Maccherozzi, and S. S. Dhesi, "Imaging Current-Induced Switching of Antiferromagnetic Domains in CuMnAs," *Phys. Rev. Lett.*, vol. 118, no. 5, pp. 1–5, 2017.
- [170] V. Schuler, X. Marti, and V. Nova, "Antiferromagnetic CuMnAs multi-level memory cell with microelectronic compatibility," *Nat. Commun.*, no. May, 2017.
- [171] S. Ghosh-Dastidar and H. Adeli, "Third Generation Neural Networks: Spiking Neural Networks," *Adv. Comput. Intell. Adv. Intell. Soft Comput.*, vol. 116, 2009.
- [172] F. J. Pineda, "Time Dependent Adaptive Neural Networks," *Adv. Neural Inf. Process. Syst.*, pp. 710–718, 1990.
- [173] R. P. Feynman, "Simulating Physics with Computers," *Int. J. Theor. Phys.*, vol. 21, pp. 467–488, 1982.
- [174] K. Sato, C. Young, and D. Patterson, "An in-depth look at Google's first Tensor Processing Unit (TPU)," *Google*, 2018. [Online]. Available: [https://cloud.google.com/blog/products/gcp/an-in-depth-look-at-googles-first-tensor-processing-unit-tpu?fbclid=IwAR1dYdfxi4kbsC\\_1X31grv2ZjNUIyoBoI4Zdeh7WjVn0oIW71hf\\_aUTMcZo](https://cloud.google.com/blog/products/gcp/an-in-depth-look-at-googles-first-tensor-processing-unit-tpu?fbclid=IwAR1dYdfxi4kbsC_1X31grv2ZjNUIyoBoI4Zdeh7WjVn0oIW71hf_aUTMcZo). [Accessed: 29-Nov-2018].